

Graphene Quantum Strain Transistors and Two-in-One Carbon Nanotube Quantum Transistors

Andrew Collins McRae

A Thesis
In the Department
of
Physics

Presented in Partial Fulfillment of the Requirements
For the Degree of
Doctor of Philosophy (Physics) at
Concordia University
Montréal, Québec, Canada

July 2018

© Andrew Collins McRae, 2018

CONCORDIA UNIVERSITY
SCHOOL OF GRADUATE STUDIES

This is to certify that the thesis prepared

By: **Andrew Collins McRae**

Entitled: **Graphene Quantum Strain Transistors and Two-in-One
Carbon Nanotube Quantum Transistors**

and submitted in partial fulfillment of the requirements for the degree of

Doctor of Philosophy (Physics)

complies with the regulations of this University and meets the accepted standards with respect to originality and quality.

Signed by the final examining committee:

_____ Chair
Dr. Rafik Naccache

_____ External Examiner
Dr. Peter Grutter

_____ External To Program
Dr. Xavier Ottenwaelder

_____ Examiner
Dr. Truong Vo-Van

_____ Examiner
Dr. Valter Zazubovits

_____ Supervisor
Dr. Alexandre Champagne

Approved by _____
Dr. Alexandre Champagne, Chair of Department

August 27th, 2018

Dr. André Roy, Dean of the Faculty of Arts and Science

Abstract

Graphene Quantum Strain Transistors and Two-in-One Carbon Nanotube Quantum Transistors

Andrew Collins McRae, Ph.D.

Concordia University, 2018

Graphene and carbon nanotubes are ideal for strain engineering in quantum nanoelectromechanical systems due to their long coherence lengths, mechanical strength, and sensitivity to deformations. Mechanical strain induces scalar ($\Delta\mu_\varepsilon$) and vector (\mathbf{A}) potentials, which directly tune the Hamiltonian, providing precise control of the energy, momentum, and quantum state of electrons in these materials. This strain-tunability could be used to completely suppress ballistic transmission in graphene quantum strain transistors (GQSTs), generate large pseudomagnetic fields ($\nabla \times \mathbf{A}$), or carry quantum information (valleytronics). Thus far, experimental challenges have prevented thorough exploration of quantum transport strain engineering (QTSE). To this end, we have constructed low temperature ($T \sim 1$ K) QTSE instrumentation. Incorporating fabrication methods for ultra-short (~ 10 nm), suspended carbon nanotube and graphene devices, we predict tunable uniaxial strains up to ≈ 1 –10% using this instrumentation.

We first determined the impact of ultra-short channel lengths on transport by measuring unstrained nanotube devices. These formed “two-in-one” quantum transistors with drastically different behaviour for electrons and holes. In a small bandgap nanotube (≈ 50 meV) we observed ballistic transport for electrons, and quantum dot (QD) behaviour for holes, while in larger bandgap nanotubes (≈ 300 meV), we measured asymmetric QD behaviour between electrons and holes. We showed that this transport asymmetry is caused by electron doping in the nanotube contacts, and is greatly enhanced in ultra-short devices. With these contact effects in mind, we developed a realistic applied theoretical model for transport in uniaxially strained ballistic GQSTs. We calculated conductivity for strained ballistic graphene, and found four transport signatures: gate-shifting of the data from the scalar potential, and strong suppression of conductivity, modification of electron-hole conductivity asymmetry, and a rich resonance spectrum from the vector potential. We calculated high on/off ratios $> 10^4$ in realistically achievable GQSTs at sufficient strains. Using our strain instrumentation, we measured transport in strained graphene, observing unambiguously the effects of strain-induced vector and scalar potentials. In graphene QDs, we observed gate-shifting of the charge states with strain, consistent with strong, strain-tunable pseudomagnetic fields. In a strained ballistic graphene device, we observed the four expected transport signatures discussed above, and using our model, we found good semi-quantitative agreement between theory and experiment.

Acknowledgments

Many people have helped to guide, push, and support me through this degree. I am so humbled by the generosity, kindness and wisdom of the people who are in my life, and I could not be more grateful. This is by no means a complete list of those who have helped bring this degree to fruition, but I only have a small space to write big thank-yous, so here they are.

Firstly, to my supervisor Alex, thank you so much for your unending help and flexibility for the completion of this degree. Although I was not physically in Montréal for a good portion of our work together, your guidance and advice always gave me direction and motivation to do high-quality experimental physics and explore the world around me. Your passion for physics is contagious and is what makes you a top-notch supervisor.

To the Champagne group, past, present (and future), thanks for all of your help, advice and support. But mostly, thanks for making me smile, laugh, and sometimes dance (depending on what music we have on in the lab). You guys make science fun, and I couldn't ask for a better group of people to work with: Joshua, Vahid, Jimi, Serap, Simeon, Marc, Matthew, Gareth, Israel, and Guoqing. I wish you all the best of luck. Also, a big thank you to the staff at Polytechnique Montréal for all of their help and advice with microfabrication.

I would also like to thank all of my good friends and family who helped to get me here, took care of me and kept me strong. Thanks to my best friends who can always cheer me up and make me laugh uncontrollably: Iain, Rory, Geoff, Chris, Marcus, Matt, Étienne, and Josh, as well as my too-many-to-name friends on the frisbee team. You guys are the best people I know, don't ever change.

A special thanks to my Montréal family: Geoff, Jennifer and Hollis for taking care of me while I was there. It's been such a pleasure to get to know you all better, and to watch Hollis grow up. I cannot put into words how appreciative I am for all you have done for me, and I am eternally grateful. I look forward to seeing you next time I am in Montréal!

To the Das Guptas: Cecilia, Swapan, and Camila, thank you for your love, kindness and support, and for making me feel like I am part of the family. I wouldn't be where I am today

without your help.

To Katie, little sister, I am so proud of you. Maybe a bit jealous that you got to be a doctor before I did, but we both made it eventually. Thanks for believing in me, and for offering your encouragement and advice. I wish you the best on the other side of the country, and I hope we can visit soon.

To Dad, Thanks for your unconditional love and support, your unending effort to make things better for your children and your sense of humour. I would not be who I am without your guiding influence, and, well, maybe some heredity too. I am forever grateful that you are always in my corner.

To Mom, thanks for watching over me. I remember your kindness and wisdom every day, and I know you would be very proud of me. I miss you.

Finally, the greatest thank you of all to my wife, Mica. Without your patience, love and support, I would be lost. Thank you for pushing me to succeed, and for always being there for me. We had a spectacular time together in (stunning) Scotland, and I am so proud that you have achieved your goal of becoming a vet. I am so happy with the life we have built together so far, and cannot wait to see what the future will hold for us.

Table of Contents

List of Figures	ix
List of Tables	xii
List of Abbreviations	xiii
Chapter 1	
Introduction: Strained Graphene and Carbon Nanotube QNEMS	1
1.1 Graphene and carbon nanotubes: a playground for QNEMS	2
1.2 Straining carbon nanoelectronic devices: recent experimental results	9
1.3 Organization of this thesis	12
Chapter 2	
Quantum Transport in Graphene and Carbon Nanotubes	16
2.1 Introduction	16
2.2 The physical and electronic structure of graphene	17
2.3 Diffusive and ballistic transport in graphene	21
2.3.1 Diffusive transport	21
2.3.2 Coherent electron transport	23
2.3.3 Ballistic transport of relativistic charge carriers	25
2.4 The physical and electronic structure of carbon nanotubes	31
2.5 SWCNT transport: FETs, SETs, and waveguides	33
2.5.1 SWCNT FETs	33
2.5.2 SWCNT SETs	37
2.5.3 SWCNT ballistic waveguides	42
2.6 Conclusions	43

Chapter 3

A Platform for Quantum Strain Electronics: Devices, Instrumentation, and Methods	44
3.1 Introduction	44
3.2 Fabrication of suspended graphene and SWCNT transistors	46
3.2.1 Wafer preparation for SWCNT growth and graphene deposition	47
3.2.2 Growing, locating, and sorting SWCNTs	52
3.2.3 Exfoliating, characterizing, and etching monolayer graphene	55
3.2.4 Contacting and suspending SWCNT and graphene devices	60
3.3 QTSE instrumentation strain-tunable low temperature transport measurements	65
3.3.1 QTSE assembly, construction, and integration with cryostat probe	65
3.3.2 Integrating thin-chip suspended devices with QTSE instrumentation	77
3.3.3 Wire bonding and preparing SWCNT devices for low temperature measurements	83
3.4 Electromigration, annealing, and measurement methods	86
3.4.1 Tailoring 10 nm scale suspended graphene junctions and quantum dots	91
3.4.2 Strain instrumentation calibration using Au tunnel junctions	93
3.5 Conclusions	95

Chapter 4

Giant Electron-Hole Transport Asymmetry in Ultra-Short Quantum Transistors	97
4.1 Introduction	97
4.2 Fabrication details, and transport measurements for five SWCNT transistors	99
4.2.1 SWCNT transistor band gaps from transport data	101
4.2.2 Ultra-short lengths of our SWCNT transistors from SEM and transport data	107
4.2.3 Suspended SWCNT-QD transistors with annealed contacts	109
4.3 Ultra-short suspended SWCNT-QD transistors with ballistic contacts	115
4.4 Giant $e - h$ charging energy asymmetry in 200 meV band gap SWCNT-QDs	117
4.5 Origin and length dependence of the electron-hole asymmetry	120
4.6 Conclusions	122

Chapter 5

Graphene Quantum Strain Transistors (GQSTs): an Applied Theory	124
---	------------

5.1	Introduction	124
5.2	Proposed experimental platform for strain engineering of 2D quantum transport	126
5.3	Applied theory of the strain engineering of transport in ballistic graphene . .	130
5.3.1	Strain-induced scalar and vector potentials in graphene	131
5.3.2	Transmission model for ballistic electrons in strained graphene	134
5.4	Conductivity signatures of strain-induced scalar and vector potentials	136
5.5	Graphene quantum strain transistors	140
5.6	Conclusions	142
 Chapter 6		
Experimental Evidence for Strain-Induced Scalar and Vector Potentials in Graphene		143
6.1	Introduction	143
6.2	Evidence for strain-tunable pseudomagnetic fields in graphene quantum dots	145
6.2.1	Suspended graphene quantum dots	145
6.2.2	Strained graphene QDs: evidence for tunable pseudomagnetic fields .	147
6.3	Suspended ballistic graphene: device geometry and electron transport	152
6.4	Strain-tunable transport in ballistic graphene: scalar and vector potentials .	154
6.4.1	Experimental measurement of the strain-induced scalar potential . . .	156
6.4.2	Experimental measurement of the strain-induced vector potential . .	158
6.5	Strained ballistic graphene: transport simulations	161
6.6	Conclusions	164
 Chapter 7		
Conclusions and Outlook		166
7.1	Main results	166
7.2	Outlook for quantum strain engineering in carbon QNEMS	174
 Bibliography		177
 Appendices		191
 Appendix A		
Details of Theoretical GQST Calculations		192

List of Figures

1.1	Strain instrumentation for ultra-short carbon nanoelectronic devices	2
1.2	Graphene and carbon nanotubes: crystal lattice and band structure	4
1.3	Strain-induced scalar and vector potentials	6
1.4	Fundamental interest and applications of strained graphene	7
1.5	Experimental methods for straining graphene and carbon nanotubes	11
2.1	The graphene crystal lattice	17
2.2	Graphene band structure	20
2.3	Diffusive transport in graphene	22
2.4	Ballistic transport in a graphene resonant electron cavity	24
2.5	Klein tunnelling in graphene	26
2.6	Carrier trajectories in a ballistic graphene device.	27
2.7	Transmission and transport in ballistic graphene	30
2.8	SWCNTs from rolled up graphene	32
2.9	SWCNT band structure	33
2.10	SWCNT field effect transistors	34
2.11	Schottky barriers in SWCNT transistors	35
2.12	The effect of metal work function and channel doping in SWCNT-FETs . . .	36
2.13	Quantum dot effective circuit	37
2.14	Single electron transistor energy level diagram	39
2.15	Calculated Coulomb blockade transport in SWCNT QDs	41
2.16	Fabry-Pérot resonances in SWCNTs	42
3.1	Applying mechanical strain with QTSE instrumentation	45
3.2	Fabrication goal geometry for SWCNT and graphene devices	47
3.3	Thick and thin Si wafer substrates	48
3.4	Backside wafer etching for gate contact	48
3.5	Photolithography procedure for alignment grids	50
3.6	Deposition of metal alignment grids on the blank wafer	51

3.7	Catalyst deposition and CVD growth of carbon nanotubes	53
3.8	Locating carbon nanotubes using a SEM	54
3.9	Determining CNT diameter using AFM	55
3.10	Graphene deposition and Raman spectroscopy	56
3.11	Etching graphene flakes for strained transport measurements	58
3.12	Contacting SWCNTs and graphene using EBL	61
3.13	Contacting the EBL pattern with 100 μm pads	63
3.14	Suspended Au, SWCNT, and graphene devices	64
3.15	Cryostat for low temperature measurements	66
3.16	Ultra-high vacuum sample space	68
3.17	QTSE cryostat probe overview	69
3.18	Original and modified probe designs for QTSE	69
3.19	Probe wiring and electronic connections for our QTSE set-up	70
3.20	Mechanical motion control of our QTSE set-up	72
3.21	Mechanical motion transfer from probe top to bottom	73
3.22	QTSE push screw for bending the thin chips	74
3.23	Sample holder for our QTSE set-up	75
3.24	QTSE set-up assembly in sample space	75
3.25	Maximum bending of Si chips in the QTSE set-up	76
3.26	Gating our suspended thin chips for QTSE measurements	78
3.27	Wire bonding the sample holder to thin chip devices	79
3.28	Assembling the QTSE set-up with thin chip samples	81
3.29	Loading the QTSE assembly in the cryostat probe	82
3.30	Wire bonding and loading SWCNT devices	84
3.31	Loading thick chips into the cryostat probe	85
3.32	Electromigration procedure for etching nanogaps in Au films	86
3.33	Electromigration circuit	88
3.34	Cleaning suspended SWCNT and graphene devices by annealing	89
3.35	dc measurement circuit	90
3.36	Tailoring 10 nm scale suspended graphene junctions and quantum dots	92
3.37	Strain calibration of our QTSE instrumentation using gold tunnel junctions	94
4.1	Ultra-short suspended nanotube quantum dot transistor fabrication	100
4.2	Ultra-short nanotube quantum dot transistors with annealed n-type contacts	102
4.3	$dI/dV_{\text{B}} - V_{\text{B}} - V_{\text{G}}$ data for the five studied SWCNT devices for E_{g} extraction	105

4.4	SEM images of the five SWCNT devices	107
4.5	Ultra-short nanotube quantum dot transistors with annealed suspended contacts	110
4.6	Schematic of the barriers between the naked and gold-covered SWCNT sections	112
4.7	Electron-hole transport asymmetry and ballistic contacts	114
4.8	Giant $e - h$ charging energy asymmetry in 200 meV band gap nanotube quantum dots	117
4.9	Extraction of addition and charging energies from each device vs. charge number.	119
4.10	Origin of the $e - h$ charging energy asymmetry.	121
5.1	Platform for uniaxial strain engineering of quantum transport in graphene .	127
5.2	Applied theory for uniaxial strain tuning of graphene's band structure	132
5.3	Applied theory for ballistic charge transport in strained graphene	135
5.4	Conductivity signatures of uniaxial QTSE in graphene	137
5.5	Graphene quantum strain transistors (GQSTs)	140
6.1	Suspended graphene quantum dots	146
6.2	Energy level shifts in strained graphene quantum dots	148
6.3	Strain-induced shifting of Coulomb diamonds in graphene QDs	151
6.4	False colour SEM images of a suspended graphene device	152
6.5	Ballistic transport in suspended graphene	153
6.6	Strain-tunable conductivity, and GQST signatures in graphene	156
6.7	Scalar potential gate-shift in strained graphene	157
6.8	Transport signatures of strain-induced vector potentials	159
6.9	Measured and calculated transport data for strained ballistic graphene . . .	162
7.1	Strain instrumentation for ultra-short carbon nanoelectronic devices	168
7.2	Ultra-short two-in-one quantum dot carbon nanotube transistors	169
7.3	Graphene quantum strain transistors: theory	171
7.4	Strained graphene nanoelectronic devices	173

List of Tables

4.1	Key parameters for the five SWCNT-QD transistors reported	99
4.2	Band gap of the SWCNT in each reported device	103
4.3	Channel lengths. L_{SEM} and L_{G} for all devices	108
4.4	Gate capacitance parameters, measured for the five studied SWCNT devices	109
4.5	Estimated barrier heights in each reported device	113
4.6	Electron-hole charging energy asymmetry ratios for the five studied SWCNT devices	118

List of Abbreviations

ac	Alternating Current.
AFM	Atomic Force Microscope.
AuTJ	Gold Tunnel Junction.
BNC	Bayonet Neill-Concelman.
BOE	Buffered Oxide Etch.
CAD	Computer Aided Design.
CNP	Charge Neutrality Point.
CNT	Carbon Nanotube.
CPD	Critical Point Drying.
CVD	Chemical Vapour Deposition.
CVI	C Virtual Instrumentation.
DAQ	Data Acquisition.
dc	Direct Current.
DI	Deionized.
e-h	Electron-hole.
EBL	Electron Beam (e-beam) Lithography.
EM	Electromigration.
FBZ	First Brillouin Zone.
FET	Field Effect Transistor.
FP	Fabry-Pérot.
GQST	Graphene Quantum Strain Transistor.
h-BN	Hexagonal Boron Nitride.
H.c.	Hermitian Conjugate.
IPA	Isopropyl Alcohol.
MEMS	Microelectromechanical Systems.
MIBK	Methyl Isobutyl Ketone.
MWCNT	Multi-Walled Carbon Nanotube.
NEMS	Nanoelectromechanical Systems.
PC	Personal Computer.
PDMS	Polydimethylsiloxane.
PMMA	Polymethyl Methacrylate.
QD	Quantum Dot.

QNEMS	Quantum Nanoelectromechanical Systems.
QTSE	Quantum Transport Strain Engineering.
RF	Radio Frequency.
RIE	Reactive Ion Etching.
rpm	Rotations per Minute.
SB	Schottky Barrier.
SCCM	Standard Cubic Centimetre per Minute.
SEM	Scanning Electron Microscope.
SET	Single Electron Transistor.
SLM	Standard Litres per Minute.
STM	Scanning Tunnelling Microscope.
SWCNT	Single Walled Carbon Nanotube.
TB	Tight Binding.
TPI	Threads per Inch.
UHV	Ultra-High Vacuum.
UV	Ultraviolet.
WKB	Wentzell-Kramers-Brillouin.

Chapter 1

Introduction: Strained Graphene and Carbon Nanotube QNEMS

By mechanically deforming nanoelectronic devices, we can study the rich physics of quantum nanoelectromechanical systems (QNEMS) which links together the quantum nature of electrons and mechanical motion at the mesoscale. Low dimensional carbon materials, such as graphene and carbon nanotubes (CNTs), are ideal QNEMS, due to their huge elastic deformation range [1], relativistic charge carriers [2], and strong electromechanical coupling [3, 4]. Despite numerous theoretical predictions of exotic physics in these materials, which could be unlocked with mechanical strain, this area of research remains largely unexplored experimentally. This is in part due to challenges in device microfabrication and experimental design in attaining large and tunable strains in nanoelectronic devices. In this thesis, we present our platform for achieving large and tunable strains ($\epsilon \approx 1\%$ – 10%) in nanoelectronic devices shown in Fig. 1.1(a), and present experimental data from both unstrained and strained ballistic graphene channels and carbon nanotube transistors, images of which are shown in Fig. 1.1(b) and (c) respectively.

We apply strain to our devices using instrumentation for quantum transport strain engineering (QTSE), compatible with low temperature ($T \sim 0.3$ K) transport measurements. The principle of operation is shown in Fig. 1.1(a): a push screw tunes the bending of the sample substrate, imparting a strain to the suspended channel of the devices. The transistor is electrically controlled by a source, drain, and gate electrodes. To achieve large strains, we require devices which are extremely short in length. In Fig. 1.1(b) and (c) we show false coloured scanning electron micrographs of nanofabricated graphene and ultra-short single-walled carbon nanotube (SWCNT) devices respectively. The source drain and gate electrodes

are visible, as well as the 100-nm graphene or 14-nm carbon nanotube channels respectively. Using our unique device fabrication techniques and QTSE instrumentation, we have studied electron transport to both set the stage and initiate the exploration of ultra-short carbon nanotubes and strained graphene QNEMS.

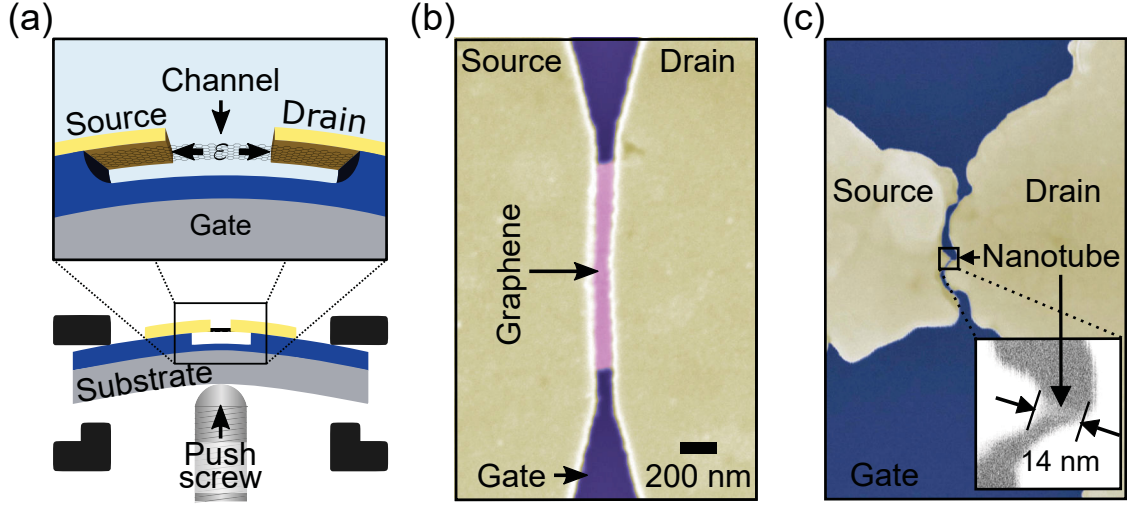


Figure 1.1: Strain instrumentation for ultra-short carbon nanoelectronic devices. (a) Schematic diagram of our QTSE instrumentation. (bottom) A push screw bends the sample substrate, imparting a strain on the suspended channel. (top) A more detailed view of the strained devices, showing the strained suspended channel, and source/drain/gate electrodes used for electron transport measurements. (b)–(c) False coloured scanning electron micrographs of suspended 100-nm graphene and 14-nm carbon nanotube devices respectively, with source, drain, and gate electrodes. The inset in panel (c) shows the nanotube channel in greater detail.

1.1 Graphene and carbon nanotubes: a playground for QNEMS

Classical electromechanics allows the conversion between mechanical and electrical energy. By creating nanoscale electromechanical devices, it becomes possible to study and harness the quantum nature of electromechanics. Quantum electronic circuits are of fundamental and practical interest, for studying coherent electron transport [5] and strong electron correlations [6], or for applications as single electron transistors [7], or spintronics, where information can be held and transferred in the electron spin, rather than charge [8]. A compelling reason to focus on quantum circuits is their proximity to real world applications, with coherent transport reaching the micron scale in room temperature devices [9]. This is unlike quantum

computing, another exciting area of research which requires extremely low temperatures to operate.

Adding mechanics to quantum electronic circuits provides additional functionality by exploiting the quantum nature of electronics and mechanics at the mesoscale. The electromechanical coupling fundamental to QNEMS, can be studied in quantum dot systems using tunnelling spectroscopy [3, 10], and has applications in extremely sensitive nanoelectromechanical systems (NEMS) sensors and actuators [11, 12], in mechanical qubits, where a buckled nanorod forms a two-state system which can be used for quantum computing [13], or for creating new types of devices for controlling and filtering the flow of electrons [14].

A powerful way to tune the behaviour of QNEMS is to use strain to mechanically deform devices. Strains can be applied statically, providing constant deformations, or dynamically by inducing oscillatory motion for time-dependent deformations (vibrons). The latter can be accomplished experimentally rather easily, using electronic control with alternating currents, which has spurred many studies on QNEMS resonators [10, 11, 15–17]. Static strains are much more difficult to detect experimentally, requiring large strains. However, the power of static strain is that we can freeze the mechanics of QNEMS to gain a deeper understanding of quantum electromechanical coupling. Static strains can tune the fundamental properties of nanomaterials, such as quantum capacitance [18], induce spin-orbit coupling [19], modify electron-vibron coupling [20], create pseudomagnetic fields [21], or lead to topological phases [22, 23].

Graphene and carbon nanotubes are ideal systems to study static quantum electromechanics due to their fantastic mechanical and electronic properties, and strong electromechanical coupling. Graphene is a two-dimensional material, composed of a single layer of carbon atoms in a honeycomb lattice, pictured in Fig.1.2(a). Carbon nanotubes, effectively one dimensional materials, are composed of a sheet of graphene rolled up on itself to form a cylindrical shell, pictured in Fig.1.2(b). Carbon nanotubes and graphene are extremely sensitive to mechanical deformation due to their single atom-thickness, as well as being mechanically robust and flexible due to the strong bonds between the sp^2 hybridized carbon atoms that make up their structures. In fact, graphene is one of the most mechanically robust materials known to man, theoretically allowing strains ($\varepsilon = \Delta L/L$) up to 20%–30% [1]. Carbon nanotubes are also extremely strong materials, found experimentally to allow strains up to 16% [24]. Moreover, graphene and carbon nanotubes can be essentially defect-free due to their strong bonding structures making them perfect candidates for linking together QNEMS experiments and theory [2].

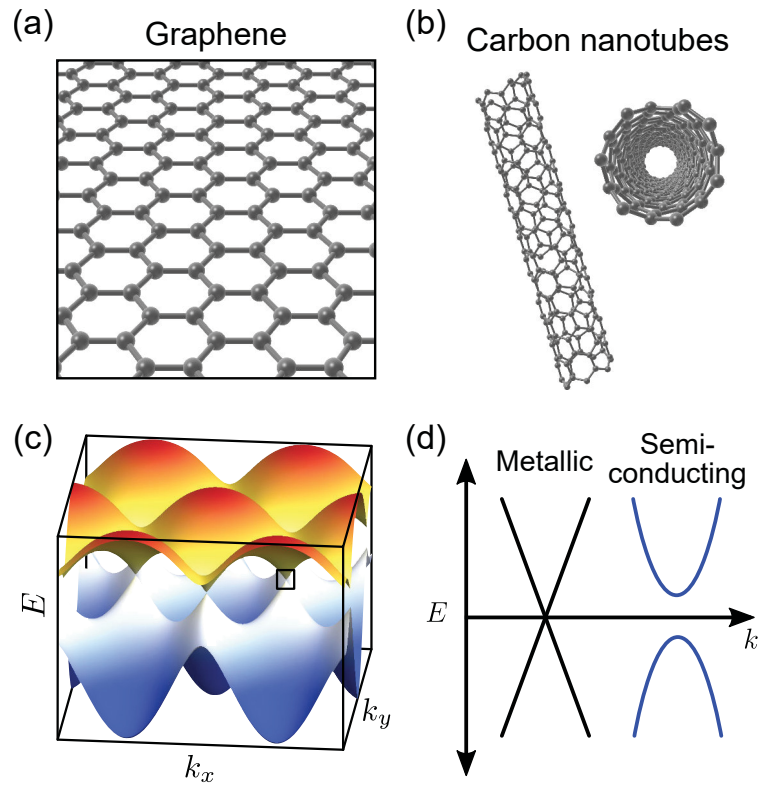


Figure 1.2: Graphene and carbon nanotubes: crystal lattice and band structure. (a) Graphene real-space crystal lattice. (b) Carbon nanotube real-space lattice. (c) Graphene band structure. The low energy dispersion (Dirac cone) is highlighted by the black box. (d) The carbon nanotube band structure can be metallic or semiconducting.

Graphene has intriguing electronic properties in addition to its astounding flexibility and elastic deformation range. We show graphene’s band structure in Fig.1.2(c). The valence (blue) and conduction (red) bands touch at a single point (the Dirac point) in the band structure, highlighted by the black rectangle in Fig.1.2(c) making it semimetallic. Graphene is remarkably conductive, with measured electron mobilities above $3,000,000 \text{ V}^{-1} \text{ s}^{-1}$ at 1.8 K, and with mean free paths up to $\ell \sim 1 \text{ }\mu\text{m}$ at room temperature [9]. This is promising for achieving room-temperature quantum circuits which are sensitive to electron scattering. These long mean free paths are made possible in part due to the linear dispersion relation about the Dirac point, making electrons behave relativistically in this material. This intrinsic property of the electrons in graphene can lead to novel “electron optics” devices, where the charge carriers (electrons or holes, “missing” electrons which can be thought of as positive quasiparticles) can be manipulated analogously to light, reflecting or refracting at potential boundaries [25]. It is the coupling between the robust mechanics and unique electronics that makes graphene ideal for QNEMS research.

We show the carbon nanotube band structure in Fig.1.2(d). While graphene has a semimetallic band structure, carbon nanotubes may be semimetallic or semiconducting depending on how they are rolled, making them more suitable for transistor applications [26,27]. In fact, a recent notable result is the advent of a computer made entirely from carbon nanotube transistors [28]. In the mesoscopic regime metallic nanotubes act as 1D waveguides, facilitating coherent transport [29], while semiconducting nanotubes act as single electron transistors [30].

The electronic band structure of graphene is highly sensitive to strain, leading to strong electromechanical coupling [4]. Specifically, strain induces scalar and vector potentials which act analogously to an electrostatic potential ($\Delta\mu_\epsilon$), and a magnetic vector potential (\mathbf{A}) respectively. In Fig. 1.3(a)–(b), we show a 3D view of the effect of the scalar potential on the low energy dispersion (Dirac cones) of the graphene band structure from Fig. 1.2(c). As strain is applied to graphene, the scalar potential causes an increase in work function, shifting the Dirac cones downward in energy. In Fig. 1.3(c)–(d), we show respectively zoomed out and zoomed in top-down views of the vector potential effect on graphene’s band structure. Indicated by the blue arrows, the vector potential shifts the positions of the Dirac points from the black circles ($\mathbf{K}^{(i)}$) in unstrained graphene, to the red circles ($\mathbf{K}_D^{(i)}$) in strained graphene. The dashed lines show the unstrained (black) and strained (red) first Brillouin zones. For the K and K' points, the vector potential points in opposite directions, making a two-level “quantum valley” system [4].

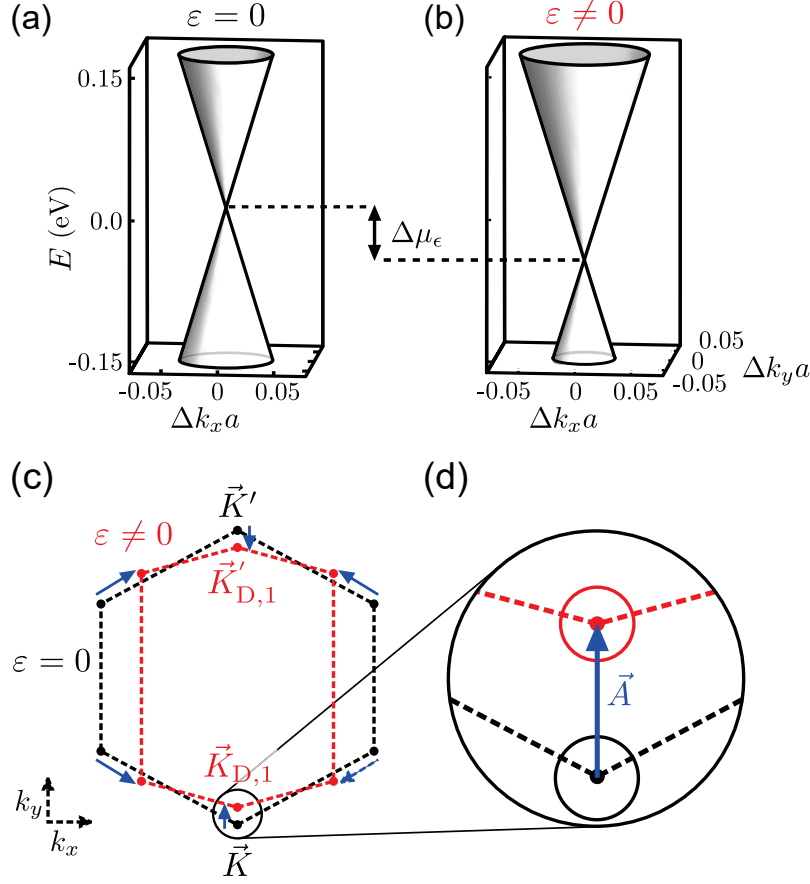


Figure 1.3: Strain-induced scalar and vector potentials. (a)–(b) Unstrained and strained low-energy dispersion of graphene. Strain induces a scalar potential ($\Delta\mu_\varepsilon$), which shifts the Dirac cone towards negative energy. (c) Momentum-space locations of the Dirac points in unstrained (\vec{K}' , black circles) and strained (\vec{K}_D , red circles). The dashed lines outline the first Brillouin zones of the unstrained (black) and strained (red) lattice, and blue arrows indicate the direction and magnitude of the vector potentials \vec{A} . (d) Shows a close-up view of the vector potential, representing the strain-induced shift of the Dirac point.

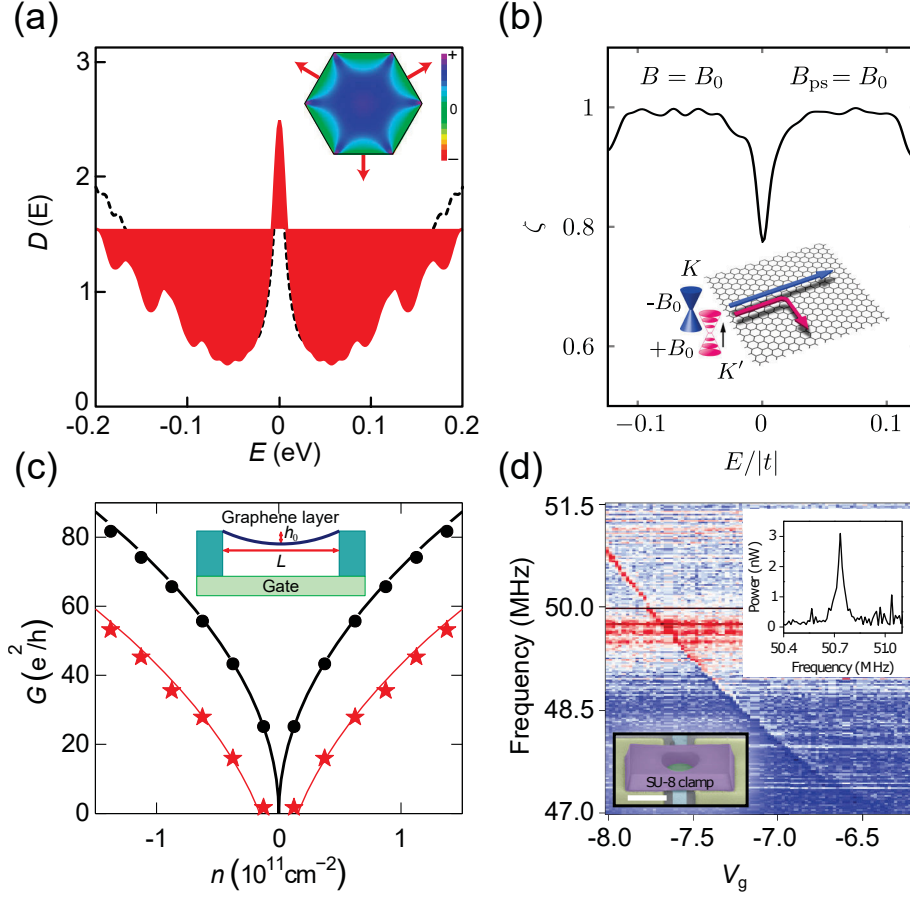


Figure 1.4: Fundamental interest and applications of strained graphene. (a) Inset: pseudo-magnetic fields $B_{ps} \sim 10$ T generated by triaxial (three axis) strain in graphene, indicated by the colour scale. Main panel: calculated density of states for unstrained graphene (blue, dashed), strained graphene (red, solid), showing Landau level formation as a result of triaxial strain. Figure adapted from Ref. [22]. (b) Valley polarization (ζ) as a function of energy in graphene with equal magnetic (B) and pseudomagnetic (B_{ps}) fields. Inset: The magnetic and pseudomagnetic fields add for one valley and cancel for the other, creating a valley filter. Figure adapted from Ref. [31]. (c) Calculated conductance vs. charge density in unstrained (black) and uniaxially strained (red) graphene, showing $G \rightarrow 0$ with strain. Inset: uniaxial strain mechanism in this device: electrostatic deflection of the graphene sheet (h_0). Figure adapted from Ref. [32]. (d) Strain-tunable graphene resonators. Bottom left inset: scanning electron microscope (SEM) image of a suspended graphene drum resonator. Main panel: oscillation power spectrum from the graphene resonator, whose resonance frequency is tunable through electrostatic strain using the gate voltage (V_G). Top right inset: line-cut from the main panel at $V_G = -8$ V showing resonance frequency in oscillation power spectrum. Figure adapted from Ref. [33].

The strain-induced vector potential can lead to exotic physics and exciting applications, examples of which we will now describe. Theoretically, large and tunable pseudomagnetic fields ($B_{\text{ps}} = \nabla \times \mathbf{A} \sim 10 \text{ T}$) are achievable with triaxial strains, allowing the quantum Hall effect and Landau level physics to be studied at room temperature [22, 34]. This theoretical prospect is shown in Fig. 1.4(a), adapted from Ref. [22]. The inset shows that triaxial strain in graphene generates strong, relatively uniform pseudomagnetic fields $B_{\text{ps}} \sim 10 \text{ T}$, as indicated by the colour scale. The main panel shows calculated density of states for unstrained graphene (blue, dashed) and strained graphene (red, solid), showing Landau level formation as a result of triaxial strain. This type of device could be used to study pseudomagnetic quantum Hall physics at room temperature, and topologically protected quantum circuits.

By combining real and pseudomagnetic fields it is theoretically possible to create a valley filter in graphene, where only electrons of a given valley could pass through the device [31]. This theoretical prospect is shown in Fig. 1.4(b), adapted from Ref. [31], where the valley polarization (ζ) is plotted as a function of carrier energy for equal magnitudes of magnetic ($B = B_0$) and pseudomagnetic ($B_{\text{ps}} = B_0$) fields. Polarization is nearly unity for a wide range of energies, indicating a robust valley filtering effect. The inset shows the mechanism of operation of this valley filter. Since the pseudomagnetic field has opposite sign for the two valleys, the sum of the magnetic and pseudomagnetic fields is $2B_0$ for one valley and 0 for the other. This introduces Landau gaps in the spectrum of one valley and not the other, allowing pure valley filtering. Such devices could pave the way for “valleytronics”, where information is encoded within the electron valleys, in analogy to electron spin in spintronics.

Even for $\nabla \times \mathbf{A} = 0$, as generated by uniaxial strains, a constant vector potential is predicted to change electron trajectories in graphene devices. For sufficient strains, this leads to generation of a transport gap, suppressing current completely in graphene [32, 35]. This theoretical prospect is shown in Fig. 1.4(c), adapted from Ref. [32], where calculated conductance is plotted as a function of charge density in unstrained (black) and uniaxially strained (red) data. A transport gap opens in the strained data, resulting in near-zero conductance at low charge density. The inset shows the proposed method of uniaxial strain, where electrostatic force from the gate electrode deflects the graphene sheet by an amount h_0 , imparting a small amount of uniaxial strain ($\sim 0.01\%$). These devices are predicted to have high on/off ratios for transistor behaviour in graphene; a long sought goal in graphene electronics research [36, 37]. We call these devices graphene quantum strain transistors (GQSTs). GQSTs have applications in extremely sensitive flexible and transparent strain

sensors [38], or in graphene integrated circuits [39].

By combining static and dynamic strains (oscillations), it is possible to create high frequency tunable NEMS resonators [16, 33]. Tunable frequency graphene NEMS have already been achieved, using electrostatic strain as shown in Fig. 1.4(d), adapted from Ref. [33]. The bottom right inset of this panel shows a graphene drum resonator, whose strain is tunable electrostatically using a global back-gate electrode. The main panel shows the oscillating power spectrum from this device, where blue is lower power and red is higher power. A clear resonance feature shifts in frequency with electrostatic strain applied by the gate. The top right inset shows the clear power spectrum resonance at $V_G = -8$ V. For smaller graphene resonators and with the application of large strains, oscillators in the THz range are theoretically possible [40], making for extremely sensitive and tunable mass or force sensors [11]. These high frequency graphene resonators could also act as pure valley current generators suitable for valleytronics applications [41]. This is caused by the time-dependent pseudomagnetic field generating a pseudoelectric field which has opposite sign for the different valleys.

In carbon nanotubes, strain has been shown to tune the bandgap, causing it to decrease or increase in size depending on tube chirality [42]. This leads to a strain-tunable conductivity, applicable for highly sensitive strain sensors [43]. Moreover, a strain-tunable bandgap is of fundamental interest in terms of QNEMS transistor engineering. Tuning the bandgap changes the heights of the tunnel barriers that form at the electrode/nanotube interfaces [44]. As such, strain can be used to continuously tune mesoscopic carbon nanotubes between 0D single electron transistors and ballistic 1D electron waveguides, which could be used for storing (quantum dot) or shuttling (quantum bus) quantum information. In addition, strain is also predicted to tune the fundamental physics of carbon nanotubes, increase the electron-vibron coupling in carbon nanotube quantum dots [20], and tune the quantum capacitance of nanotube devices [18]. Finally, as in graphene, combining static and dynamic strains can be used to generate tunable THz NEMS sensors for mass or force sensing applications [10, 11].

1.2 Straining carbon nanoelectronic devices: recent experimental results

Despite the wide range of exciting physics which could be unlocked with static strains in graphene and carbon nanotubes, this area of experimental physics remains largely unexplored. This is due to the complexity of the devices and instrumentation required to strain

nanoelectronic devices. Ideally, to study carbon nanotubes and graphene QNEMS, we require a system which can apply tunable, constant strains, and which is compatible with low temperature electron transport measurements. To our knowledge, no such system has been reported in literature for strained graphene and carbon nanotubes. However, some progress has been made in understanding strained transport in carbon nanotubes and graphene. Here we describe the recent results in strained graphene and carbon nanotube QNEMS from literature.

Constant strains have been induced by substrate topography [45, 48] or by creating nanobubbles or wrinkles in the graphene sheet [21] to study strong pseudomagnetic fields (≈ 300 T) in graphene. An example of this constant substrate induced strain, using boron nitride nanopillars, is shown in Fig. 1.5(a), adapted from Ref. [45]. A depiction of the deposition of graphene on the nanopillars is shown in the inset. The nanopillars stretched the graphene sheet, resulting in pseudo Landau level generation, measurable by differential conductance measurements shown in the main panel. The results from these studies are intriguing, but make thorough study of strain effects difficult, as these set-ups do not allow continuous and tunable strains. Large pseudomagnetic fields (~ 1000 T) have also been induced in graphene by creating a Gaussian bump in the sheet using proximity to a scanning tunnelling microscope (STM) tip, as shown in Fig. 1.5(b), adapted from Ref. [46]. In this study, the local density of states was changed by the large pseudomagnetic fields generated as tip currents were increased from 1–50 nA, measured by the STM tip itself, as shown in the right side of the panel. Despite these large pseudomagnetic fields from STM studies, the strain field is tightly localized and cannot be used for bulk transport measurements. In a similar vein, strain has been applied by pushing on graphene drumheads with atomic force microscope (AFM) tips [49], but this method is not compatible with low temperature transport measurements due to the difficulty in building low temperature AFM instrumentation and suspended devices, in addition to the non-uniform strain applied by the AFM tip. For Raman spectroscopy, and strained conductivity measurements, strains have been induced by putting graphene on stretchable substrates [47, 50], or using microelectromechanical systems (MEMS) comb drive actuators [51]. An example of a stretchable substrate graphene device is shown in Fig. 1.5(c), adapted from Ref. [47]. In the insets, we see that the graphene device is bendable and stretchable, while the main panel shows the resistance as a function of stretching up to 30% strain along the x and y axes. Despite their large degree of strain-tunability, stretchable substrates cause disorder in the graphene sheet and are not compatible with metal electrodes for low temperature measurements. As mentioned earlier,

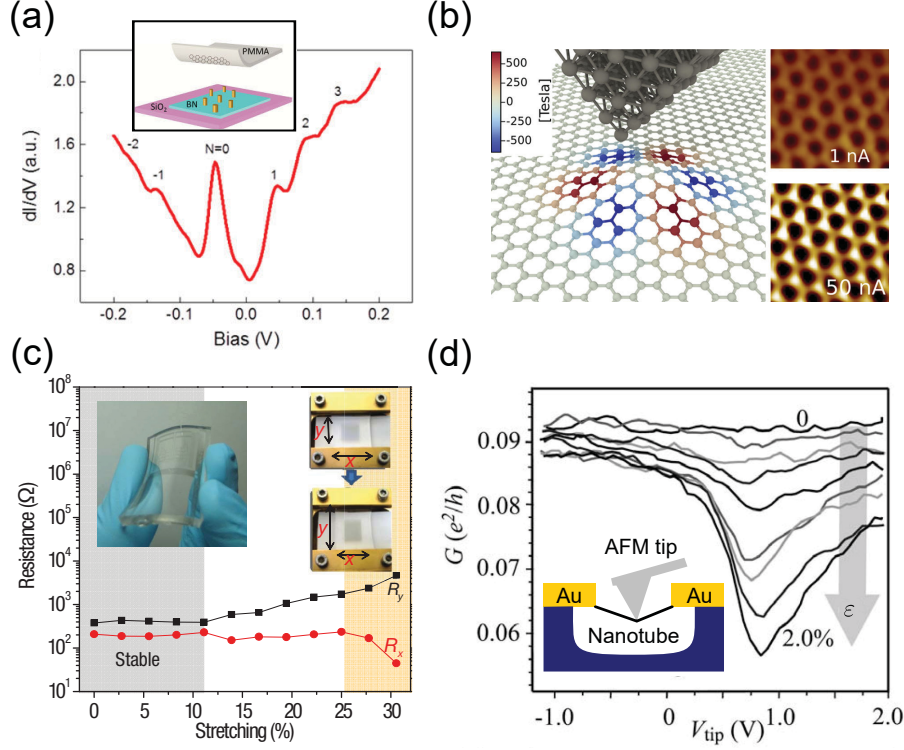


Figure 1.5: Experimental methods for straining graphene and carbon nanotubes. (a) Inset: constant substrate strain in graphene. Depositing a graphene sheet on boron nitride pillars imparts a constant strain. Main panel: differential conductance data as a function of bias voltage, showing pseudo-Landau levels (index N) from the constant substrate-induced strain. Figure adapted from Ref. [45]. (b) Locally strained graphene using STM. Extreme pseudo-magnetic fields ($B_{ps} \sim 1000$ T) were achieved by creating a Gaussian bump in graphene. STM images taken at tip current 1 nA and 50 nA (right), show the B_{ps} -modified local density of states. Figure adapted from Ref. [46]. (c) Tunable strain using flexible substrates. Top left inset: bendable graphene device on PDMS (Polydimethylsiloxane) substrate. Top right insets: controllably straining graphene along two axes. Main panel: Resistance change with strain in graphene on a flexible substrate with up to 30% strain. Figure adapted from Ref. [47]. (d) Straining carbon nanotubes using an AFM tip. Inset: Cartoon of a suspended nanotube device being strained by an AFM tip. Applying pressure with the tip strain. Main panel: Conductance decrease with tip voltage, indicating change in band gap with strain. Figure adapted from Ref. [42].

tunable electrostatic strains have been applied to suspended graphene sheets using a back gate electrode [33,52]. However, these strains are typically quite small $\sim 0.01\text{--}0.1\%$, and are not independent from the carrier density of the graphene sheet.

In individual carbon nanotubes, strain has most often been applied by using AFM tips. Extremely large strains ($\sim 16\%$) were achieved using a nanotube suspended between two AFM tips [24]. However, because AFM tips are generally non-metallic, this method does not allow for high-quality transport measurements. Conversely, by pushing on a suspended nanotube transistor with an AFM tip, bandgap opening and closing was measured by electron transport with strains up to 2.0% [42]. This result is shown in Fig. 1.5(d), adapted from Ref. [42]. The inset shows the strain-tuning mechanism using the AFM tip, while the main panel shows the change in conductance associated with the increasing band gap caused by strain from the AFM tip. Strains have also been applied to individual nanotubes by depositing them on flexible sheets, showing piezoresistive transport with strains $\lesssim 0.1\%$ [43]. However, these methods are not compatible with low temperature measurements, preventing the study of strained quantum transport in nanotubes.

1.3 Organization of this thesis

In this thesis, we will present our QTSE instrumentation and fabrication methods for low temperature electron transport measurements in ultra-short carbon nanotubes and strained graphene. We will show that our devices have ballistic contacts, a direct result of our unique fabrication processes. We will then show how these contacts create a strong electron-hole asymmetry in unstrained ultra-short carbon nanotubes, making two-in-one quantum transistors. With this theoretical understanding of our device contacts, we will develop a realistic applied theoretical model for transport in uniaxially strained graphene, highlighting the effects of the strain-induced vector and scalar potentials. Using these theoretical findings, we will show that we unambiguously observe the effects of strain-induced vector and scalar potentials through transport experiments on suspended graphene using our QTSE instrumentation. The remainder of the thesis is structured as follows.

In Chapter 2 we will present a general introduction to graphene and carbon nanotubes, and discuss their physical geometries. From its crystal lattice, we will derive the graphene band structure using the tight binding model, and show how this leads to relativistic electron propagation. We will discuss diffusive (semi-classical) and ballistic (quantum) transport in graphene, and distinguish between their transport features, providing the background

necessary to understand electron transport in strained graphene (Chapters 5 and 6). Finally, we will discuss electron transport in carbon nanotubes, highlight transport behaviour in field effect transistors, quantum dot transistors, and 1D electron waveguides. This will provide the background necessary to understand our experimental transport measurements of ultra-short two-in-one carbon nanotube quantum dots (Chapter 4).

In Chapter 3, we will detail our fabrication procedures for creating suspended graphene and carbon nanotube devices, starting from a blank Si/SiO₂ wafer which acts as our substrate and gate electrode. We will then discuss the design and construction of our QTSE instrumentation, used for applying large and tunable strains to these suspended devices. We then explain our unique feedback-mediated electromigration procedure, used to create ultra-short (10–100 nm) devices necessary to achieve large uniaxial strains ($\varepsilon \approx 1\text{--}10\%$), as well as our current-annealing procedure for cleaning them. Finally, we will present how we calibrate our QTSE set-up and measure its stability using metal point contacts which form a tunnel junction.

In Chapter 4, we focus on ultra-short carbon nanotube transistors. Although shorter device lengths are more desirable for larger strains, they are more susceptible to contact effects. Here, we describe the electron-hole asymmetric transport we observe in our devices. The magnitude of this effect is length-dependent, explaining why it has not been observed in the longer nanotubes studied previously [30]. This chapter is adapted from our publication in Nature Communications, see Ref. [53]. We will show that our electromigration procedure, used to create our ultra-short devices, also anneals the suspended metal films contacting the nanotube. We show that the annealed metal films allow coherent electron transport in the nanotubes underneath them, meaning that they effectively act as top gates to the metal coated nanotube sections. These coated nanotube sections act as source and drain leads contacting the naked nanotube channel, creating extremely short p-n junctions. These junctions are dependent on the band gap of the nanotube and govern the electron-hole asymmetry observed in our devices. In a nanotube with a small band gap ($E_g \approx 28\text{ eV}$), we find that electrons “see” the nanotube as a coherent 1D channel, while holes “see” it as a quantum dot. In devices with larger band gaps ($E_g \lesssim 300\text{ eV}$), we find that our ultra-short nanotubes behave as two-in-one quantum dots, where the energy required to add an electron or hole to the dot differs by a factor of ≈ 2 . We show that this effect is stronger in shorter devices, indicating that contact effects play a larger role in shorter devices. This must be considered during device design of our strained nanoelectronics.

In Chapter 5 we will discuss how uniaxial strain affects graphene devices from a theoretical

perspective. While strain-induced conductivity suppression in graphene has been predicted as early as 2008, requiring only small strains [32] and delivering high on/off ratios, it has not been observed experimentally. This is in part due to incomplete modelling of this strain transistor effect, leading to unrealistic predictions. In this chapter, we show how realistic strains can completely suppress conductivity resulting in the graphene quantum strain transistor effect, bridging this gap between theory and experiment. This chapter is adapted from a manuscript in preparation for submission to 2D Materials. We will expand on the tight binding derivation of the graphene band structure from Chapter 2 to include all strain effects. We calculate the resulting scalar and vector potentials which act on the charge carriers in graphene, being sure to include the contributions from distortion of the lattice which are often neglected [54,55]. From these vector potentials, and the Dirac Hamiltonian, we derive a realistic applied transmission model for strained graphene. In our model, we include the effects of the orientation of the crystal lattice, and contact doping which has been treated as negligible or infinite in previous studies, although it is not physically realistic. [32, 56]. Using the device geometries and QTSE parameters from Chapter 3, we show that graphene quantum strain transistors with high on/off ratios are realistically achievable. We highlight signatures from strained transport data which arise from the scalar and vector potentials, and can allow measurement of contact doping and crystal orientation of our devices.

In Chapter 6, we will present our experimental strained-transport data from graphene devices, measured using our QTSE instrumentation. We will first present transport data from strained graphene quantum dots, where we observed gate-shifts in the quantum energy levels, consistent with the generation of pseudomagnetic fields from non-uniform strains. We next present our transport data from a strain-tunable ballistic graphene channel. We confirm that annealing allows ballistic transport under the metal films in our devices by investigating coherent transport features in our data. We will then calibrate the strain in the graphene sheet by investigating the strain-induced scalar potential. Strong signatures of the scalar and vector potentials are present in our data, although we do not observe complete suppression of conductivity with strain causing: an overall decrease in conductivity, a change in the observed electron-hole asymmetry, and shifting of the coherent resonance peaks. From these signatures, we determine the device crystal orientation, contact doping, contact resistance, and intrinsic doping, showing a reasonable agreement between our calculations and the experimental data.

In Chapter 7, we will summarize the findings presented in this thesis and discuss potential future experiments in strained low dimensional materials, including graphene, carbon

nanotubes, and others, which could be made possible by our unique QTSE instrumentation.

Chapter 2

Quantum Transport in Graphene and Carbon Nanotubes

Our goal is to study strained carbon nanoelectronic devices and understand the fundamental physics that determines their behaviour. To build this understanding, we must first develop a background in quantum transport in graphene and carbon nanotubes. In this chapter, we will discuss the origin of the band structures that governs electron behaviour in these materials. This leads to a variety of transport regimes in single-walled carbon nanotubes (SWCNTs) and graphene that can be used to characterize their physical properties. We will use the background developed in this chapter to understand quantum dot and ballistic transport in our two-in-one ultra-short carbon nanotube transistors, and theoretical and experimental description of ballistic transport in graphene quantum strain transistors. This is a basic introduction to quantum transport in graphene and carbon nanotubes, and can be skipped by experts.

2.1 Introduction

In this chapter, we build up the theoretical background necessary for understanding electron transport in quantum carbon nanoelectronic devices. We first describe the physical structure of monolayer graphene: a single-atom-thick honeycomb lattice of carbon. We will then show how the physical lattice leads to graphene's peculiar band structure, with a linear dispersion relation at low-energy. The electron transport in graphene is governed by this band structure, which can be described by the Dirac Hamiltonian at low-energy, from which we derive the theoretical conductivity in the ballistic regime. With this understanding of graphene

transport in mind, we then shift focus to single-walled carbon tubes, a related carbon allotrope composed of a single rolled-up sheet of graphene. While graphene is effectively a 2D material due to sub-nm confinement in the out-of-plane direction, SWCNTs are effectively 1D structures due to their nm-scale diameters, and can be either semiconducting or metallic in nature. This can lead to a variety of interesting transport behaviours such as field effect transistors, single electron transistors, or 1D electron waveguides, which we will discuss at the end of the chapter.

2.2 The physical and electronic structure of graphene

We begin our theoretical description of graphene by showing its atomic structure and then deriving its band structure using the tight binding model. From this band structure we will determine the low-energy Hamiltonian, which we later use to derive conductivity in graphene.

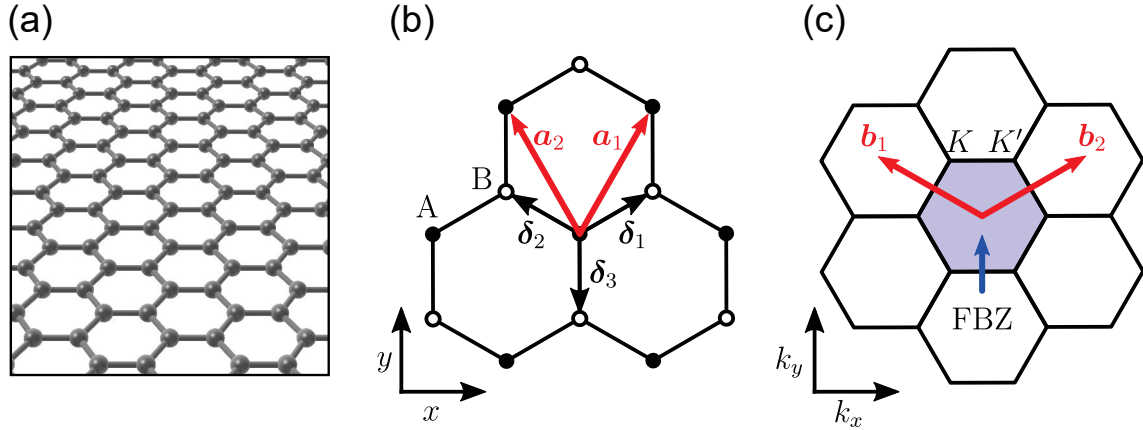


Figure 2.1: The graphene crystal lattice. (a) 3D rendered lattice of graphene, showing the honeycomb structure of carbon atoms, with the armchair edge along x -axis. (b) Real space hexagonal lattice of graphene with zigzag edge along the x -axis, showing two atom basis (A, B), nearest neighbour vectors δ_n , and primitive lattice vectors ($\mathbf{a}_1, \mathbf{a}_2$, red arrows). (c) Reciprocal lattice of graphene, corresponding to the real space lattice shown in (b), showing K and K' points in the corners of the first Brillouin zone, and reciprocal lattice vectors ($\mathbf{b}_1, \mathbf{b}_2$, red arrows).

Graphene is a two dimensional atomically thin crystal, formed from sp^2 hybridized carbon atoms, giving a honeycomb-like lattice [57]. The sp^2 hybridized carbon atoms form in-plane σ bonds with 3-fold rotational symmetry which give graphene its mechanical strength [57]. It is the remaining electrons in the out-of-plane π orbital which are free to flow through the lattice. In Fig. 2.1, we show the real-space graphene lattice. Fig. 2.1(a) shows a 3D render of the graphene lattice in real space, with the armchair direction running along the

x -axis. Fig. 2.1(b) shows a top-down illustration of a section of the graphene lattice, with the zigzag direction running along the x -axis. The graphene lattice is composed of two triangular sublattices, labelled A and B , and represented by the filled and open lattice points at the vertices of the hexagons. These are connected by nearest-neighbour vectors, $\boldsymbol{\delta}_n$. Atoms lying on the same sublattice are connected by the primitive vectors of the triangular lattice, \mathbf{a}_1 and \mathbf{a}_2 (red arrows). The carbon atoms in the graphene lattice have three nearest-neighbours, positioned 120° apart at a distance $a = 1.42 \text{ \AA}$. The nearest-neighbour vectors are [2]:

$$\boldsymbol{\delta}_1 = \frac{a}{2} (\sqrt{3}, 1), \quad \boldsymbol{\delta}_2 = \frac{a}{2} (-\sqrt{3}, 1), \quad \boldsymbol{\delta}_3 = a (0, -1), \quad (2.1)$$

and the primitive vectors of the triangular lattice are [2]:

$$\mathbf{a}_1 = \frac{a}{2} (\sqrt{3}, 3), \quad \mathbf{a}_2 = \frac{a}{2} (-\sqrt{3}, 3). \quad (2.2)$$

The carbon atoms of the graphene lattice have six next-nearest-neighbours which lie on the same sublattice, situated 60° apart at a distance $\sqrt{3}a$. The six next-nearest-neighbour vectors are given by the equations:

$$\boldsymbol{\delta}_{nm} = \boldsymbol{\delta}_n - \boldsymbol{\delta}_m, \quad n \neq m. \quad (2.3)$$

In Fig. 2.1(c) we show the reciprocal lattice, calculated from the real space primitive vectors. The figure shows the first Brillouin zone (FBZ) shaded in light blue, and reciprocal lattice vectors (red arrows) which are:

$$\mathbf{b}_1 = \frac{2\pi}{3a} (\sqrt{3}, 1), \quad \mathbf{b}_2 = \frac{2\pi}{3a} (-\sqrt{3}, 1). \quad (2.4)$$

Also shown in Fig. 2.1(c) are the two spatially asymmetric corners of the FBZ (analogous to a two-atom basis in real space), known as the K and K' points. The momenta of the three K points are: [2]:

$$\mathbf{K}_1 = \frac{4\pi}{3\sqrt{3}a} (1, 0), \quad \mathbf{K}_2 = \frac{4\pi}{3\sqrt{3}a} \left(-\frac{1}{2}, \frac{\sqrt{3}}{2} \right), \quad \mathbf{K}_3 = \frac{4\pi}{3\sqrt{3}a} \left(-\frac{1}{2}, -\frac{\sqrt{3}}{2} \right), \quad (2.5)$$

and the related K' points are $\mathbf{K}'_i = -\mathbf{K}_i$. We will see that these K and K' points have significance in graphene's band structure.

The band structure of graphene can be determined using the tight binding (TB) model. In

the second quantization, the TB Hamiltonian for graphene, accounting for only the nearest- and next-nearest-neighbours, is [2]:

$$H = -\gamma_0 \sum_{\langle i,j \rangle, s} \left(a_{s,i}^\dagger b_{s,j} + \text{H.c.} \right) - \gamma'_0 \sum_{\langle\langle i,j \rangle\rangle, s} \left(a_{s,i}^\dagger a_{s,j} + b_{s,i}^\dagger b_{s,j} + \text{H.c.} \right), \quad (2.6)$$

where $\gamma_0 \approx 2.7$ eV [2] and $\gamma'_0 = 0.1\gamma_0 \approx 0.3$ eV [58] are the nearest-neighbour and next-nearest-neighbour TB hopping energies respectively, $a_{s,i}^{(\dagger)}$ destroys (creates) an electron on sublattice A with spin s , b has an equivalent definition for sublattice B , and H.c. is the Hermitian conjugate of the other terms in the parentheses. To derive the band structure, we take the Fourier transform of the creation and annihilation operators giving the reciprocal TB Hamiltonian [59]:

$$H = -\gamma_0 \sum_{k,n} e^{-i\mathbf{k} \cdot \boldsymbol{\delta}_n} \left(a_k^\dagger b_k + \text{H.c.} \right) - \gamma'_0 \sum_{k, \langle n, m \rangle} e^{-i\mathbf{k} \cdot \boldsymbol{\delta}_{nm}} \left(a_k^\dagger a_k + b_k^\dagger b_k + \text{H.c.} \right), \quad (2.7)$$

from which we determine the dispersion relation [2, 59]:

$$E = \pm \left| \gamma_0 \sum_{k,n} e^{-i\mathbf{k} \cdot \boldsymbol{\delta}_n} \right| - \gamma'_0 \sum_{k, \langle n, m \rangle} \cos(\mathbf{k} \cdot \boldsymbol{\delta}_{nm}), \quad (2.8)$$

where the \pm sign refers to the valence and conduction bands. Electrons flow in the conduction band, while holes, missing electrons which can be equivalently thought of as positive quasi-particles, flow in the valence band. Substituting Eqs. 2.1 and 2.3 gives the simplified dispersion [2]:

$$E_{\pm}(\mathbf{k}) = \pm \gamma_0 \sqrt{3 + f(\mathbf{k})} - \gamma'_0 f(\mathbf{k}), \quad (2.9)$$

$$f(\mathbf{k}) = 2 \cos\left(\sqrt{3}k_x a\right) + 4 \cos\left(\frac{\sqrt{3}}{2}k_x a\right) \cos\left(\frac{3}{2}k_y a\right).$$

We plot graphene's band structure in Fig. 2.2, using Eq. 2.9. In Fig. 2.2(a), we show a 2D colour plot of the conduction band, with higher energy in red and lower energy in white, constant energy contours in black, and K and K' points. We show a 3D view of the full semimetallic band structure in Fig. 2.2(b). Here, the band structure has been rotated 90° for better visibility. A zoomed-in view of the low-energy band structure is shown in panel (c), where we see linear and isotropic dispersion, known as the Dirac cone. The points where the valence and conduction bands touch (making graphene a semimetal) are called

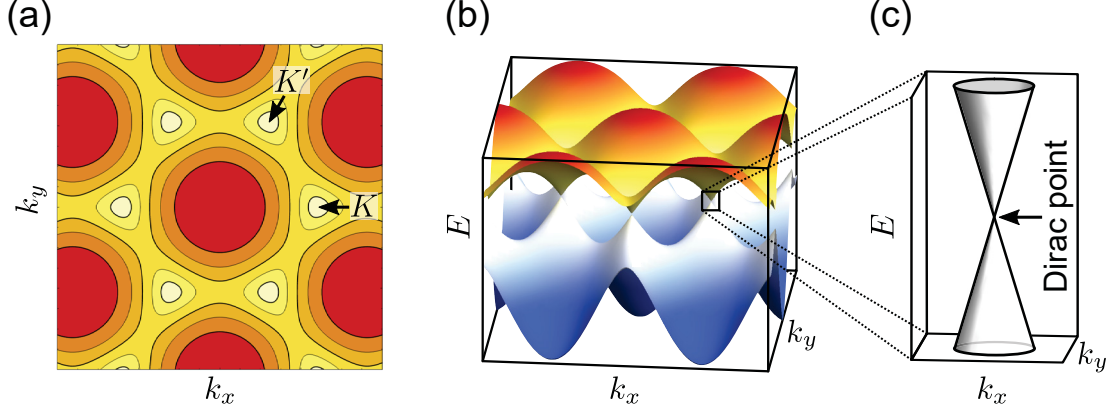


Figure 2.2: Graphene band structure. (a) Contour plot of the conduction band in graphene, showing the K and K' points at energy minima. (b) 3D plot of the full graphene band structure showing valence and conduction bands in blue and red respectively, with the graphene sheet rotated 90° for visibility. (c) Zoom-in on the Dirac cone; the low-energy linear graphene dispersion centered around the Dirac point.

the Dirac points. The Dirac points lie in the middle of the Dirac cones and coincide with the high symmetry K and K' points at the corners of the FBZ. The characteristic shape of graphene's band structure comes from the first term in Eq. 2.9, and is related to the nearest-neighbour (inter-sublattice) hopping. The second term in Eq. 2.9 arises from the next-nearest-neighbour (intra-sublattice) hopping, and sets the energy of the Dirac points, $E_D = E_{\pm}(\mathbf{K}^{(')}) = 3\gamma'_0$, but does not affect the shape of the low-energy dispersion.

We approximate the low-energy dispersion in the Dirac cones as being linear, giving a simplified relationship [2]:

$$E_{\pm}(\mathbf{k}) - E_D = \pm \hbar v_F \mathbf{k}, \quad (2.10)$$

where the Fermi velocity in graphene, $v_F = 3|\gamma_0|/2\hbar = 8.8 \times 10^5$ m/s, sets the slopes of the Dirac cone [2]. This linear dispersion is reminiscent of that for light, and leads to relativistic behaviour of the charge carriers (electrons and holes) in graphene. The charge carriers are Dirac fermions limited by v_F , in analogy to photons being limited by c , and are described by the Dirac Hamiltonian:

$$H = \pm \hbar v_F \boldsymbol{\sigma} \cdot \mathbf{k}, \quad (2.11)$$

where $\boldsymbol{\sigma}$ are the Pauli spin matrices:

$$\sigma_x = \begin{pmatrix} 0 & 1 \\ 1 & 0 \end{pmatrix}, \quad \sigma_y = \begin{pmatrix} 0 & -i \\ i & 0 \end{pmatrix}, \quad (2.12)$$

which indicate so-called pseudospin quantum number in Dirac systems, arising from the two

atom basis in graphene. The linear dispersion of the Dirac cones in graphene leads to a linear density of states [4]:

$$\rho_0(E) = \frac{2|E|}{\pi\hbar^2v_F^2}, \quad (2.13)$$

which allows us to calculate the charge carrier (electron or hole) density:

$$n = \text{sgn}(E) \frac{2|E|^2}{\pi\hbar^2v_F^2} = \text{sgn}(E) \frac{k_F^2}{\pi}, \quad (2.14)$$

where $k_F = E/\hbar v_F$ is the Fermi wave vector, and the sign of n is positive for electrons and negative for holes. This shows that $E \propto \sqrt{n}$ in graphene.

The linear dispersion is not the only aspect of the graphene band structure that makes it unique. The Dirac points at the K and K' corners of the FBZ are symmetrically inequivalent, although they have the same energy. The resulting two-fold degenerate quantum number is called “valley”, which in conjunction with the electron spins yields a 4-fold degeneracy for charge carriers in graphene. In addition, the two sublattices of graphene cause the electron and hole states of graphene to be linked together through their so-called “chirality”. We will explore this in the next section, and show that this is important for understanding ballistic transport in graphene.

2.3 Diffusive and ballistic transport in graphene

In this section, we show how quantum effects with measurable transport signatures arise from the linear dispersion and sublattice symmetry of graphene. For comparison, we will first discuss semi-classical diffusive transport in graphene, as it is measured experimentally at room temperature [60, 61]. We then show how graphene can behave analogously to an optical resonant cavity, showing Fabry-Pérot oscillations in conductivity. Finally, we account for the chirality of graphene charge carriers which links together particle and hole states to achieve the transmission equation for ballistic graphene.

2.3.1 Diffusive transport

In the diffusive transport regime, carriers undergo several scattering events while travelling across the graphene sheet. We show a schematic representation of diffusive transport in graphene in Fig. 2.3(a), where an electron travels between source and drain electrodes. An important concept here is the mean free path ℓ , which is the average distance an electron

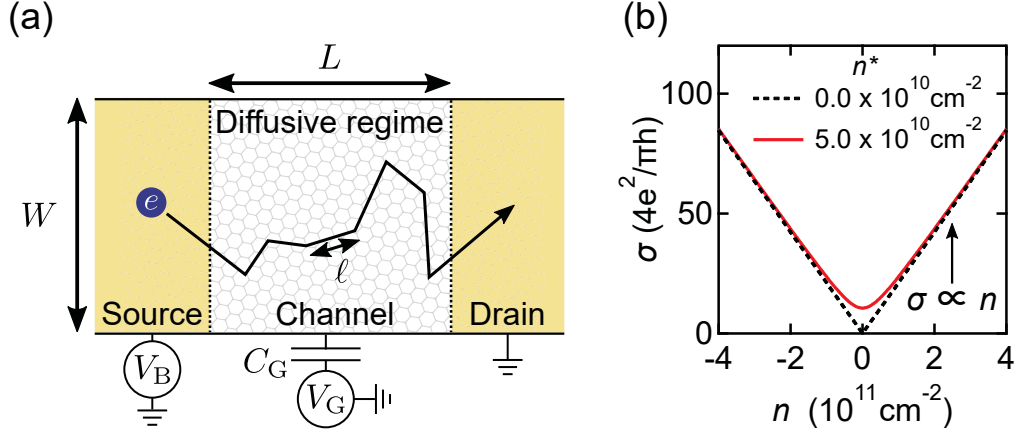


Figure 2.3: Diffusive transport in graphene. (a) Example carrier trajectory for diffusive transport in a graphene device of length L and width W with mean free path ℓ . The electronic measurement circuit is also shown, with bias voltage applied across the source and drain electrodes, and the carrier density in the channel, n , controlled by the gate voltage. (b) $\sigma - n$ data for a graphene sheet with $\mu = 65,000 \text{ cm}^2 \text{ V}^{-1} \text{ s}^{-1}$, with and without doping from spatial charge inhomogeneities.

travels between scattering events. The graphene sheet has dimensions L and W and mean free path $\ell < L$, leading to scattering events within the channel. A two-point circuit is also pictured, with bias voltage (V_B) applied across the source and drain electrodes to drive current flow across the device, and a gate voltage (V_G) to control carrier density in the sheet:

$$n = \frac{c_G V_G}{e}, \quad (2.15)$$

where c_G is the gate capacitance per unit area, and e is the elementary charge. Diffusive transport in graphene has been well studied, and follows the Boltzmann theory for conduction [61–63]. Screened Coulomb potential scattering in the graphene sheet leads to scattering times, τ , proportional to k_F , and gives conductivity, $\sigma = (2e^2/h)v_F k_F \tau \propto n$ [61]. This linear relationship between conductivity and carrier density in the diffusive regime is often expressed in terms of carrier mobility:

$$\sigma = |n|e\mu. \quad (2.16)$$

Electron mobility is therefore the measure of conductivity for different materials. Typical mobilities in graphene range from $15,000 \text{ cm}^2 \text{ V}^{-1} \text{ s}^{-1}$ on SiO_2 at room temperature [64], to $3,000,000 \text{ V}^{-1} \text{ s}^{-1}$ on hexagonal boron nitride (h-BN), another 2D material, at 1.8 K [9]. This makes graphene an extremely good conductor [65]. We plot $\sigma - n$ data in Fig. 2.3(b)

(black, dashed), using Eq. 2.16 with $\mu = 65,000 \text{ cm}^2 \text{ V}^{-1} \text{ s}^{-1}$. Theoretically, as n approaches zero, so does σ . Experimentally, however, conductivity never reaches zero due to the presence of extraneous charge carriers. These additional carriers come from thermal excitations and spatial charge inhomogeneities (also called electron-hole puddles) in the graphene sheet. The latter can be induced by substrate impurities, or naturally occurring corrugations in the graphene sheet [66,67]. Accounting for these additional carriers, the total charge carrier density in the graphene sheet is [63]:

$$n_{\text{tot}} = \sqrt{n^2 + n^{*2} + 4n_{\text{th}}^2}, \quad (2.17)$$

where n is the gate-induced carrier density, n^* is the carrier density induced by charge puddles, and $n_{\text{th}} = (\pi/6)(k_{\text{B}}T/\hbar v_F)^2$ is the thermally excited carrier density, with k_{B} , the Boltzmann constant. Substituting Eq. 2.17 into Eq. 2.16, we plot σ in Fig. 2.3(b) (solid, red), for $\mu = 65,000 \text{ cm}^2 \text{ V}^{-1} \text{ s}^{-1}$, with $n^* = 5 \times 10^{10} \text{ cm}^{-2}$ and $n_{\text{th}} = 0$. For $n \ll n^*$, the added impurities cause conduction at the Dirac point (conductivity minimum), while for $n \gg n^*$, the data converge to the $n^* = 0$ case.

Mobility can be related to the charge carrier mean free path in graphene [60]:

$$\ell = \frac{\mu \hbar \sqrt{\pi n}}{e}. \quad (2.18)$$

In h-BN encapsulated graphene, mean free paths as large as $\ell = 28 \text{ } \mu\text{m}$ have been measured at low temperatures ($T = 1.8 \text{ K}$) [9], and as large as $\ell \approx 1 \text{ } \mu\text{m}$ at room temperature [68]. This makes ballistic transport ($\ell > L$) realistically achievable in room temperature graphene devices. In the case of ballistic transport, there is no scattering in the channel and a quantum mechanical approach is necessary to determine transport behaviour.

2.3.2 Coherent electron transport

In ballistic graphene, there is no scattering in the channel. As a result, the charge carriers in a finite-width graphene channel have quantized transversal momenta. For a smooth-edged graphene channel, the transversal momentum for a single mode is [69]:

$$q_n = \frac{\pi}{W}(n + \frac{1}{2}), \quad (2.19)$$

where n is the integer index of the transversal mode, and W is the width of the graphene sheet. The number of energetically allowed modes in the channel is limited by the chemical

potential in the source/drain. We refer to this potential as the contact doping, $\Delta\mu_{\text{contact}}$ (not to be confused with the diffusive mobility μ), which determines the number of transversal modes [69]:

$$N_q = \text{Int} \left(\frac{\Delta\mu_{\text{contact}}}{\hbar v_F} \frac{W}{\pi} + \frac{1}{2} \right). \quad (2.20)$$

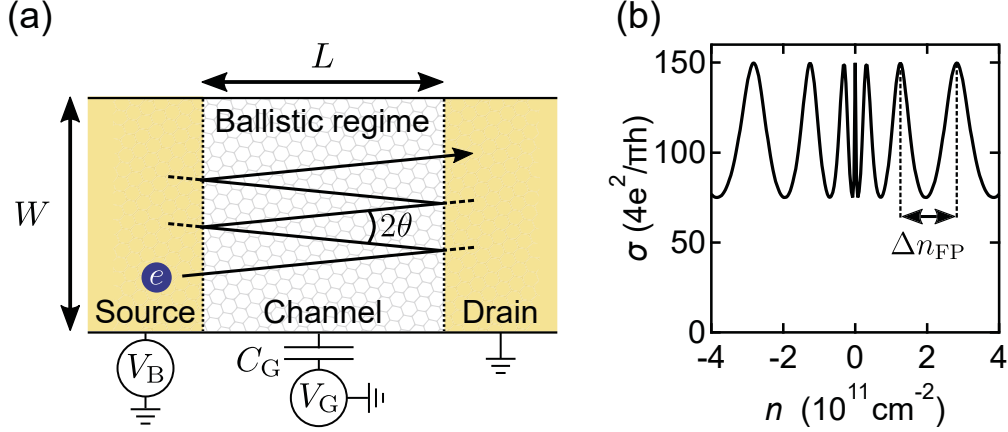


Figure 2.4: Ballistic transport in a graphene resonant electron cavity. (a) Example carrier trajectory for incidence angle θ coherent in ballistic graphene, showing transmission and reflection at the channel to source/drain boundaries. (b) $\sigma - n$ data, calculated using Eqs. 2.23 and 2.22, for a graphene sheet with $L = 100$ nm $W = 1000$ nm, contact doping $\Delta\mu_{\text{contact}} = 0.5$ eV and finesse $f = 1$, showing the spacing between resonant peaks.

A ballistic charge carrier travelling through a graphene device experiences no scattering in the channel, only reflection at the interfaces where the potential changes *i.e.* the junctions between the channel and the source/drain. This makes the graphene channel behave as a resonant Fabry-Pérot (FP) cavity for electrons. We show a schematic representation of transport in a ballistic graphene cavity in Fig. 2.4(a), with electron reflection at the interfaces between source/drain and channel, and angle of propagation of the electron in the channel, relative to normal incidence, $\theta = \sin^{-1}(q_n/k_F)$. This angle is important, as it determines the phase difference between propagating electrons in the channel [70]:

$$\Delta\varphi = 2k_F L \cos \theta. \quad (2.21)$$

By summing over all incidence angles, the transmission of the FP cavity is be calculated [70]:

$$T(\theta) = \frac{1}{1 + f \sin^2(\Delta\varphi/2)}, \quad (2.22)$$

where f is the finesse of the FP cavity, which depends on the specific transmission and

reflection coefficients at the two interfaces. To calculate the conductivity from transmission, we must sum over all energetically allowed transmission modes [69]:

$$\sigma = \frac{L}{W} \frac{4e^2}{h} \sum_{n=0}^{N_q-1} T. \quad (2.23)$$

In Fig. 2.4(b), we plot $\sigma - n$ using Eqs. 2.22 and 2.23 with $L : W = 100 : 1000$ nm, $f = 1$, and $\Delta\mu_{\text{contact}} = 0.5$ eV. Clear oscillations occur in the data, with peaks occurring for coherent, in-phase electrons, and troughs for destructive interference when the electrons are out-of-phase. The energy spacing between FP peaks can be determined from Eq. 2.22, and takes on a constant value:

$$\Delta E_{\text{FP}} = \frac{\pi \hbar v_F}{L \cos \theta}. \quad (2.24)$$

This corresponds to a density-dependent spacing between FP peaks:

$$\Delta n_{\text{FP}} = \frac{\pi}{L^2 \cos^2 \theta} + \frac{2\sqrt{\pi n}}{L \cos \theta}, \quad (2.25)$$

as shown by the black arrow in Fig. 2.4(b).

2.3.3 Ballistic transport of relativistic charge carriers

Although this picture of coherent transport in a 2D waveguide provides useful insight into carrier propagation in graphene, it does not account for the Dirac nature of the charge carriers necessary for a complete and accurate transmission model. Charge carriers in graphene are in a superposition over the A and B sublattices. This sublattice degree of freedom (A vs. B sublattice) is known as pseudospin, in analogy to the two-level electron spin. The phase from projecting wave functions onto the two sublattices is known as chirality, and defines a two-level pseudospin, with pseudospin up for sublattice A pointing parallel to the electron's momentum, and pseudospin down for sublattice B , pointing antiparallel to the electron's momentum [2, 4]. The chiral Dirac Fermions in graphene can be described by a single wave function with four components for the two valleys and two pseudospins. From quantum electrodynamics, this chirality links together electron and hole states. This is known as charge conjugation symmetry, and it allows a special tunnelling regime called Klein tunnelling [71].

We show a schematic representation of Klein tunnelling in Fig. 2.5, with initial conditions shown in Fig. 2.5(a). An electron with energy E and Fermi wave vector k_F , is incident on

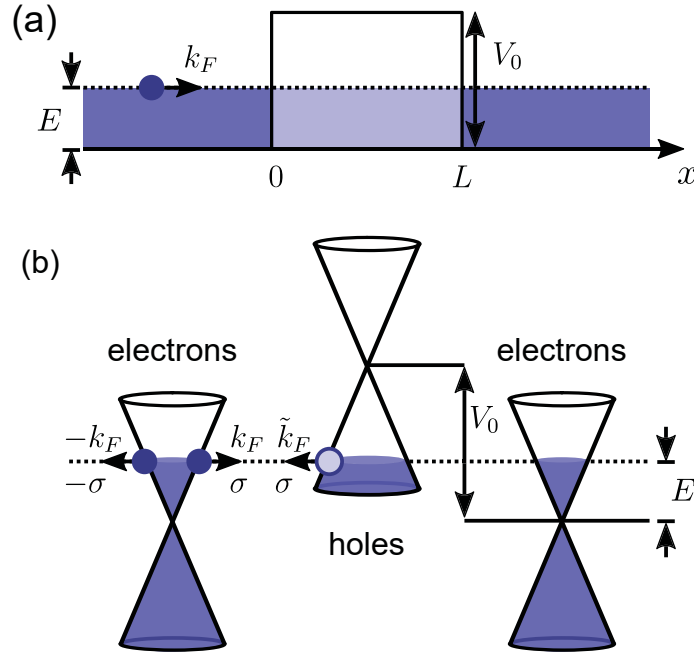


Figure 2.5: Klein tunnelling in graphene. (a) An electron with energy E and Fermi wave vector k_F incident on a potential barrier of height V_0 and length L . (b) Pseudospin, σ , is conserved across the barrier, when a right-moving electron with momentum k_F can become a left-moving hole with momentum \tilde{k}_F . Due to the Dirac nature of the carriers, this allows perfect transmission at normal incidence on a potential barrier.

a potential barrier of height V_0 and length L . For electron tunnelling in non-chiral systems, we would expect an exponential decrease in the electron wave function across the barrier. For Klein tunnelling, however, the barrier is completely transparent to normally incident electrons. We show the mechanism by which this occurs in Fig. 2.5(b). The opposite sides of the cones (upward downward slopes) have opposite pseudospins $\pm\sigma$, and opposite momenta. An electron incident on the barrier with Fermi wave vector k_F crosses into the potential barrier region. Upon entering the potential barrier, the right-moving electron becomes a left-moving hole in a potential well, with Fermi wave vector \tilde{k}_F while preserving its pseudospin. This is only possible because of graphene's charge conjugation symmetry. At the far end of the barrier, the reverse process occurs, with the hole becoming a right-moving electron once more. The net process results in greater overall transmission, and perfect transmission of normally incident carriers. This means that despite its excellent mobility, we cannot block the flow of current in graphene, making it unsuitable for transistor applications; a major obstacle for graphene-based electronics [37].

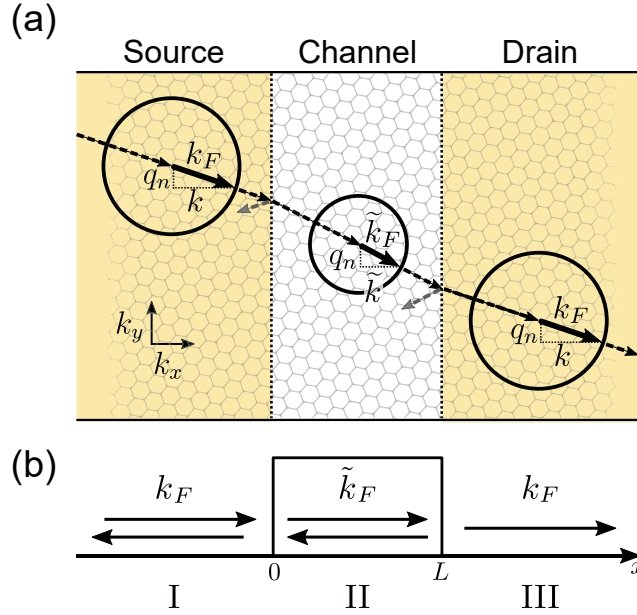


Figure 2.6: Carrier trajectories in a ballistic graphene device. (a) Fermi circles and momentum components for a single transmission mode in the channel and leads. The transversal momentum, q_n is conserved between the source/drain and the channel. This causes the momentum carriers to change from the leads to the channel. (b) Simplified carrier trajectory diagram, showing reflection and transmission in the three device regions, source (I), channel (II) and drain (III).

With the chiral nature of Dirac Fermions in mind, we will now derive ballistic transmission in graphene, following the methods from Ref. [69]. We begin by defining the ballistic

carrier trajectories. In Fig. 2.6(a) we show the Fermi circles with radii defined by the Fermi wave vectors, k_F and \tilde{k}_F , in the source/drain and channel respectively. As the boundary between the leads and channel runs along the y direction, the transversal momentum, q_n (defined in Eq. 2.19), is conserved across this boundary [32, 69]. This gives x components of momentum in the source/drain and channel $k = \sqrt{k_F^2 + q_n^2}$ and $\tilde{k} = \sqrt{\tilde{k}_F^2 + q_n^2}$ respectively. In Fig. 2.6(b), we show a simplified view of the carrier trajectories in graphene for the three regions of the device: source (I), channel (II) and drain (III), labelled by their respective Fermi wave vectors. The arrows indicate carrier propagation as a result of transmission and reflection at the boundaries of the graphene channel.

To derive the transmission equation for a ballistic graphene device, we begin with the Dirac equation [69]:

$$eV\Psi + v_F \begin{pmatrix} \boldsymbol{\sigma} \cdot \mathbf{p} & 0 \\ 0 & \boldsymbol{\sigma}^* \cdot \mathbf{p} \end{pmatrix} \Psi = E\Psi. \quad (2.26)$$

where the top and bottom parts of the matrix correspond to the K and K' valleys, and V is the potential. Substitution of plane wave test solutions $\Psi = e^{i(kx+q_ny)}$, the momentum operator $\mathbf{p} = -i\hbar\boldsymbol{\partial}$, and the Pauli matrices into Eq. 2.26 give the expanded form of the Dirac equation for graphene:

$$\hbar v_F \begin{pmatrix} eV & k - iq_n & 0 & 0 \\ k + iq_n & eV & 0 & 0 \\ 0 & 0 & eV & k + iq_n \\ 0 & 0 & k - iq_n & eV \end{pmatrix} = E. \quad (2.27)$$

This matrix has eigenvalues $E = \hbar v_F k_F$ as expected. The normalized eigenvectors of this matrix give four-part plane wave solutions to the Dirac equation:

$$\Psi_{n,k}(\mathbf{r}) = \chi_{n,k}(y)e^{ikx}, \quad (2.28)$$

$$\chi_{n,k}(y) = a_n \begin{pmatrix} 1 \\ z_{n,k} \\ 0 \\ 0 \end{pmatrix} e^{iq_n y} + a'_n \begin{pmatrix} 0 \\ 0 \\ z_{n,k} \\ 1 \end{pmatrix} e^{iq_n y} + b_n \begin{pmatrix} z_{n,k} \\ 1 \\ 0 \\ 0 \end{pmatrix} e^{-iq_n y} + b'_n \begin{pmatrix} 0 \\ 0 \\ 1 \\ z_{n,k} \end{pmatrix} e^{-iq_n y},$$

where the four eigenvectors have coefficients labelled to represent the combinations of A and B sublattices and K and K' valleys, and:

$$z_{n,k} = \pm \frac{\sqrt{k^2 + q^2}}{k - iq}. \quad (2.29)$$

We now apply boundary conditions to calculate the transmission. We separate the wave function into three regions, as defined in Fig: 2.6(b):

$$\Psi = \begin{cases} \Phi_{\text{I}} & \text{if } x < 0, \\ \Phi_{\text{II}} & \text{if } 0 < x < L, \\ \Phi_{\text{III}} & \text{if } x > L, \end{cases} \quad (2.30)$$

$$\Phi_{\text{I}} = \chi_{n,k} e^{ikx} + r_n \chi_{n,-k} e^{-ikx}, \quad (2.31)$$

$$\Phi_{\text{II}} = \alpha_n \chi_{n,\tilde{k}} e^{i\tilde{k}x} + \beta_n \chi_{n,-\tilde{k}} e^{-i\tilde{k}x}, \quad (2.32)$$

$$\Phi_{\text{III}} = t_n \chi_{n,k} e^{ik(x-L)}, \quad (2.33)$$

where r_n and t_n are the net mode-dependent reflection and transmission coefficients, and α_n and β_n are the coefficients for right-moving and left-moving carriers in the channel.

Due to valley and sublattice symmetry, we need only investigate a single eigenvector to derive a general solution. Setting the boundary conditions $\Phi_{\text{I}} = \Phi_{\text{II}}$ at $x = 0$, and $\Phi_{\text{II}} = \Phi_{\text{III}}$ at $x = L$ gives a system of equations:

$$\begin{pmatrix} 1 \\ z_{n,k} \end{pmatrix} + r_n \begin{pmatrix} 1 \\ z_{n,-k} \end{pmatrix} = \alpha_n \begin{pmatrix} 1 \\ z_{n,\tilde{k}} \end{pmatrix} + \beta_n \begin{pmatrix} 1 \\ z_{n,-\tilde{k}} \end{pmatrix}, \quad (2.34)$$

$$t_n \begin{pmatrix} 1 \\ z_{n,k} \end{pmatrix} = \alpha_n \begin{pmatrix} 1 \\ z_{n,\tilde{k}} \end{pmatrix} e^{i\tilde{k}L} + \beta_n \begin{pmatrix} 1 \\ z_{n,-\tilde{k}} \end{pmatrix} e^{-i\tilde{k}L}. \quad (2.35)$$

which we can solve for the final result, the total transmission in a graphene device [69]:

$$T_n = |t_n|^2 = \left| \frac{k\tilde{k}}{k\tilde{k} \cos[\tilde{k}L] - i(k_F \tilde{k}_F - q_n^2) \sin[\tilde{k}L]} \right|^2. \quad (2.36)$$

In Refs. [56, 69], the leads are modelled as having an infinite potential (infinite contact doping). This is equivalent to $k \rightarrow \infty$ for the low- n which have the highest transmission, and simplifies the transmission from Eq. 2.36:

$$T_n^\infty = |t_n|^2 = \left| \frac{\tilde{k}}{\tilde{k} \cos[\tilde{k}L] - i(\tilde{k}_F - q_n^2) \sin[\tilde{k}L]} \right|^2. \quad (2.37)$$

In Fig. 2.7(a), we show transmission as a function of incidence angle θ , as calculated from Eq. 2.37 for a ballistic graphene device with length $L = 100$ nm, and $W = 1000$ nm, and with channel carrier densities $n = 1 \times 10^{11} \text{ cm}^{-2}$ (red), and $n = 4 \times 10^{11} \text{ cm}^{-2}$ (blue). There is

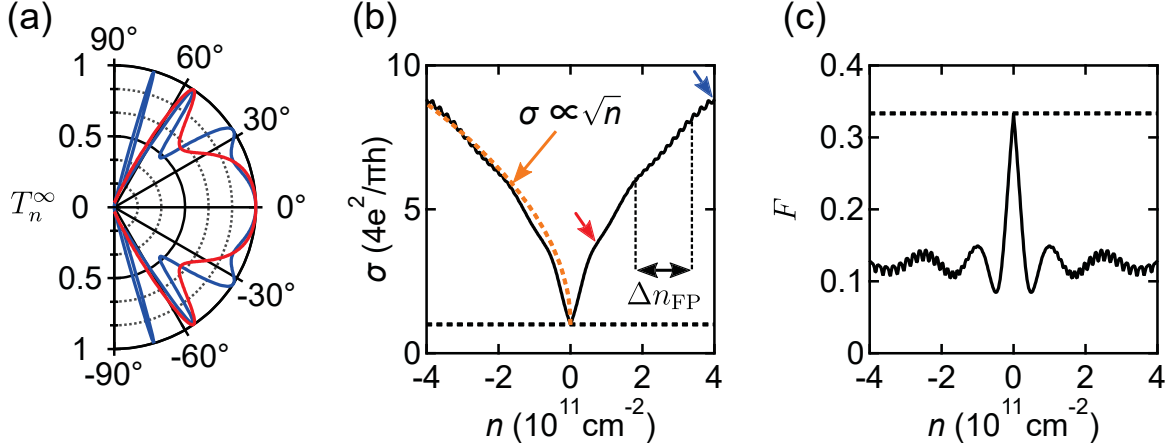


Figure 2.7: Transmission and transport in ballistic graphene. Device parameters: infinite contact doping, $L = 100 \text{ nm}$, and $W = 1000 \text{ nm}$. (a) Transmission probability for a ballistic graphene device. The red and blue curves correspond to channel carrier densities $n = 1 \times 10^{11} \text{ cm}^{-2}$, and $n = 4 \times 10^{11} \text{ cm}^{-2}$ respectively. (b) $\sigma - n$ data (black, solid) showing $\sigma \propto \sqrt{n}$ fit (orange, dashed), minimum conductivity $\sigma = 4e^2/\pi h$ (black, dotted). The black arrows show the Fabry P  rot carrier density spacing, and the red and blue arrows correspond to the channel dopings for the transmission plots in (a). (c) Fano factor as a function of n (black, solid), showing maximum value of $1/3$ (black, dashed) at the Dirac point.

100% transmission at normal incidence ($\theta = 0^\circ$) due to Klein tunnelling, while transmission drops to zero for $\theta = \pm 90^\circ$. The data show oscillations in transmission as a function of angle, arising from Fabry-P  rot resonances. Using Eqs. 2.37 and 2.23, we calculate conductivity of the device, shown in Fig. 2.7(b). FP resonances are visible in the data separated by Δn_{FP} (Eq. 2.25), the orange dashed line shows square-root fit of $\sigma \propto \sqrt{n}$ and the red and blue arrows point out the charge densities matching the transmission curves from Fig. 2.7(a).

Three major features in the conductivity data allow us to distinguish between quantum ballistic and semi-classical diffusive transport. The first is the shape of the conductivity curve. In diffusive transport, scattering by a screened Coulomb potential causes $\sigma \propto n$. In the ballistic case, however, $\sigma \propto \sqrt{n}$, due to the linear density of states in graphene, as shown in Eq. 2.14. The second is the presence of regular oscillations in the conductivity data, arising from carrier coherence in the FP cavity. In the figure, these are the wider oscillations, in the conductivity data, marked by the black arrow. The narrower oscillations at larger n correspond to mode opening, where the increasing Fermi level of the channel allows the propagation of an additional transport mode. The third is the minimum conductivity $\sigma_{\text{min}} = 4e^2/\pi h$. In ballistic transport, evanescent waves in the channel lead to finite conductivity at $n = 0$ [69] due to Klein tunneling (see Fig. 2.5), as opposed to the diffusive case where $\sigma = 0$ (for $n^* = 0$).

In addition to these three conductivity signatures, shot noise measurements can be used to confirm ballistic transport in graphene. Shot noise comes from the quantized nature of electrons, and has a characteristic distribution. The Fano factor, F , is a measure of that distribution and holds specific values for different transport regimes. For example, $F = 1$, when the shot noise follows a Poissonian distribution, as seen in tunnel junctions, while $F = 1/3$ in diffusive metallic wires [72]. F is therefore deeply related to the fundamental transport properties of a system. The Fano factor is calculated from the transmission:

$$F = \frac{\sum_{n=0}^{N_q-1} T(1-T)}{\sum_{n=0}^{N_q-1} T}. \quad (2.38)$$

We show the Fano factor as a function of carrier density in Fig. 2.7(c). F reaches a maximum value of $1/3$ at the Dirac point. This is indicative of sub-Poissonian shot noise, surprisingly matching the Fano factor for diffusive wires. This is due to “Zitterbewegung”, jittering motion from the relativistic quantum dynamics of Dirac fermions which causes interference between hole and electron states [69]. Sub-Poissonian shot noise is then an additional indicator of ballistic transport and relativistic charge carriers in graphene. We will now discuss how the electronic properties of graphene change when it is rolled up into a carbon nanotube.

2.4 The physical and electronic structure of carbon nanotubes

A carbon nanotube is simply a graphene sheet rolled up on itself, forming an atomically thin cylindrical shell. Carbon nanotubes can have enormous aspect ratios, with diameters of just a few nm and mm-scale lengths, making them effectively one dimensional structures [44]. Throughout this thesis, we will focus on single-walled carbon nanotubes for their simplicity, although double-walled and multi-walled carbon nanotubes (MWCNTs) consisting of multiple concentric nanotubes exist as well. In this section, we discuss how the electronic properties of the carbon nanotube arise from the band structure of graphene and the way the nanotube is rolled.

In Fig. 2.8 we show the physical make-up of a SWCNT. Fig. 2.8(a) shows the three classifications of wrapping in SWCNTs: zigzag, chiral, and armchair (dashed black lines). The wrapping vector, $\mathbf{C}_h = (n\mathbf{a}_1, m\mathbf{a}_2)$, defines this classification, shown for the zigzag case. Zigzag SWCNTs have $(n, 0)$, chiral nanotubes have (n, m) , and armchair nanotubes have (n, n) as their wrapping vectors. The translation vector, \mathbf{T} , runs parallel to \mathbf{C}_h , and defines

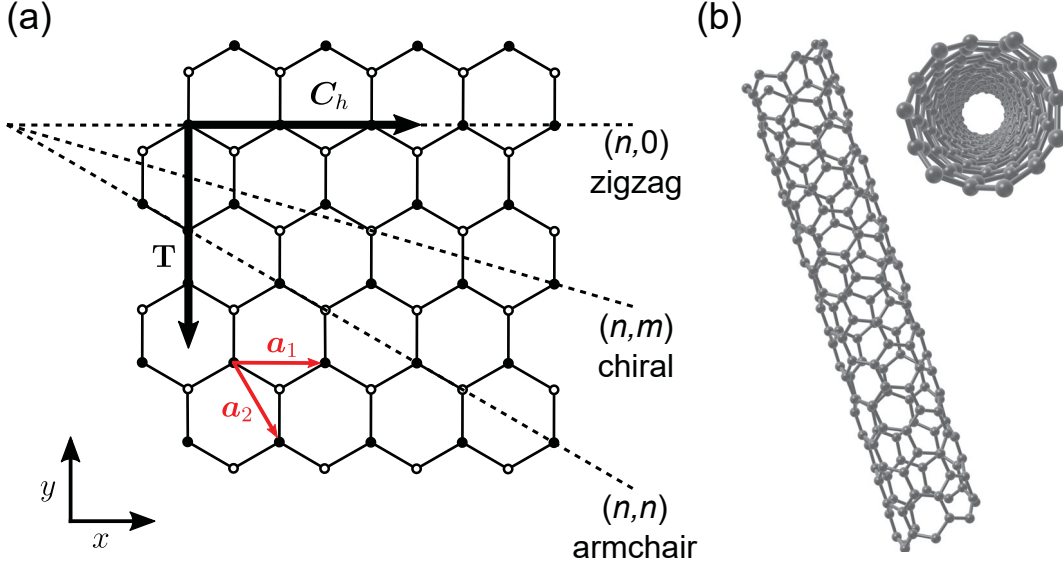


Figure 2.8: SWCNTs from rolled up graphene. (a) Real space graphene lattice showing primitive vectors (red arrows), wrapping vector, \mathbf{C}_h , and tube axis, \mathbf{T} for a zigzag $(n, 0)$ SWCNT. Also pictured are the wrapping vectors for chiral (n, m) and armchair (n, n) SWCNTs. (b) 3D render of a $(6, 1)$ chiral SWCNT, viewed from the side (left) and end (right).

the direction of the longitudinal axis of the nanotube [26]. Note, in the figure the primitive vectors have been rotated 120° from those shown in Fig. 2.1, but due to the 3-fold symmetry of the graphene lattice, these are equivalent. We show a 3D render of the structure of a $(n, m) = (6, 1)$ SWCNT as a 3D render in Fig. 2.8(b), with side and end views on the left and right respectively.

The rolling of the graphene sheet determines the SWCNT band structure, as shown in Fig. 2.9. As a result the periodic boundary condition along the circumference of the nanotube, the momentum along this direction, k_\perp , becomes quantized. This gives the SWCNT band structure: a vertical planar cut of the Dirac cone in the k_\parallel direction. The wrapping vector determines the position of this vertical cut in momentum space, leading to a metallic band structure (no bandgap) if the vertical plane crosses the Dirac point, or a semiconducting band structure (with a bandgap) otherwise. This is shown by the black and blue outlines respectively, corresponding to the SWCNT band structures shown in Fig. 2.9(b). A metallic band structure is expected for armchair nanotubes ($n = m$), and for zigzag or chiral nanotubes where $n - m = 3I$, where I is an integer [26]. All other nanotubes have bandgaps which depend on nanotube diameter, d , and chirality [73]:

$$E_g = \frac{2|q|\gamma_0 a}{d \cos(\theta)} - \frac{q\gamma_0 a^2}{3d^2 \cos^2(\theta)}, \quad (2.39)$$

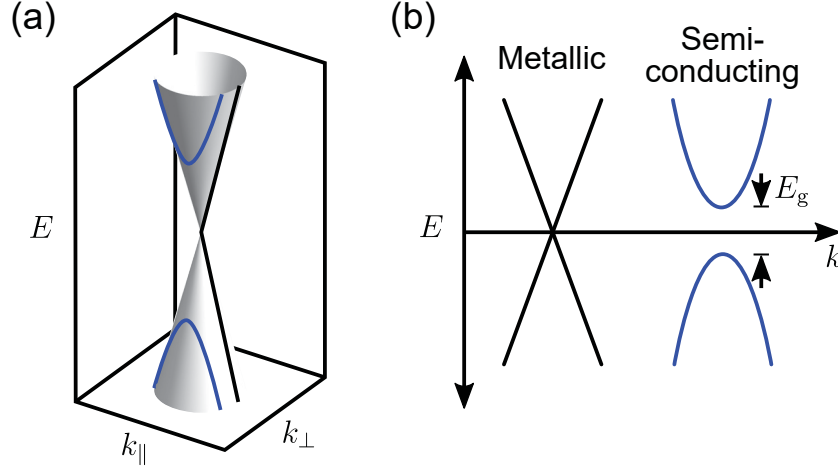


Figure 2.9: SWCNT band structure. (a) Dirac cone from the graphene band structure with planar cuts along k_{\parallel} , giving the SWCNT band structure. (b) Band structure for metallic and semiconducting SWCNTs, with zero, and finite bandgap (E_g) respectively.

where $q = 0, \pm 1$ is the remainder of $n/3$, and $d \cos(\theta) = (2n + m)\sqrt{3}a/2\pi$. The predicted band gaps from Eq. 2.39 are accurate for large d nanotubes with $E_g \sim 0.5$ eV [74]. However, in small d nanotubes, curvature-induced strains contribute to the band gap, producing band gaps $E_g \lesssim 0.1$ eV even in supposedly metallic SWCNTs [74, 75]. Next, we will show how this band structure affects transport in SWCNTs.

2.5 SWCNT transport: FETs, SETs, and waveguides

Transistor operation is possible in SWCNTs, unlike in graphene, due to their gapped band structure. SWCNTs can form a variety of types of transistor devices, from classical field effect transistors (FETs) to single electron transistor (SET) quantum dots (QDs) or ballistic 1D waveguides, depending on bandgap, device geometry and temperature [44]. In this section, we will discuss the conditions required to achieve these regimes, and show their transport behaviour.

2.5.1 SWCNT FETs

Carbon nanotube field effect transistors allow conductivity to be turned on or off simply by tuning the gate voltage. In Fig. 2.10(a), we show a SWCNT-FET in its off state. The transistor consists of metal source and drain electrodes (S , D) contacting a semiconducting SWCNT, and is constructed on a standard Si/SiO₂ wafer, with the degenerately doped Si layer acting as a global back gate electrode. A bias voltage is applied across the source

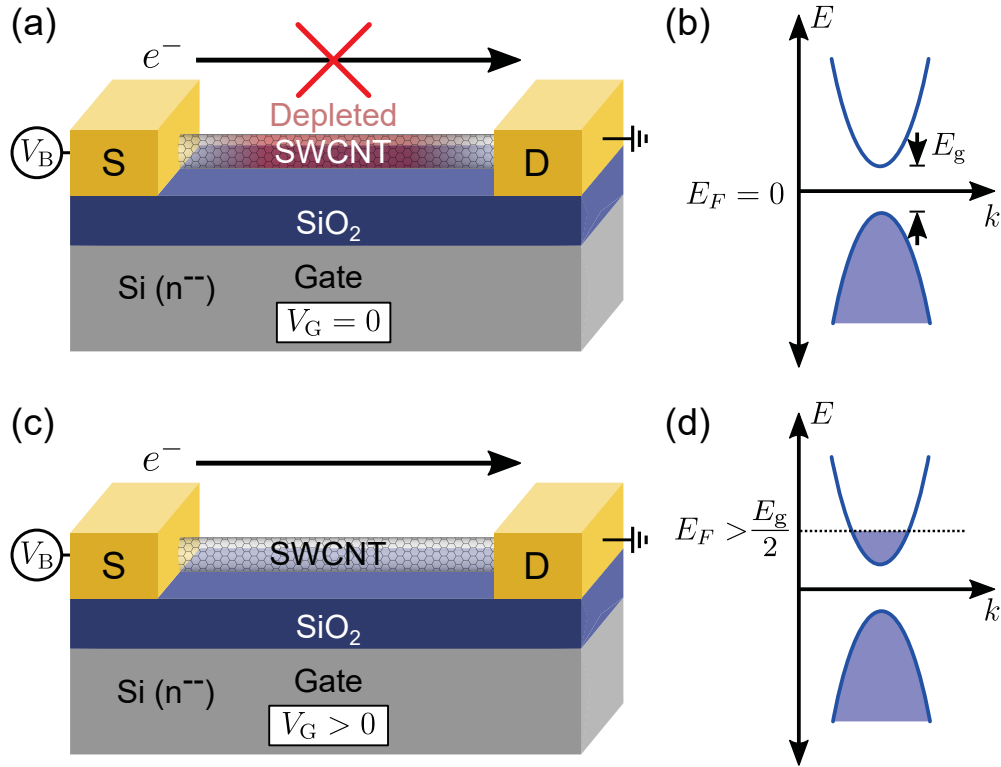


Figure 2.10: SWCNT field effect transistors. (a) Off state of a SWCNT-FET, showing current flow blocked by the depletion region in the SWCNT (red). The device consists of biased metal source/drain electrodes contacting the SWCNT device, on a Si wafer which acts as the back gate electrode. (b) Off state band alignment: the Fermi level lies within the band gap of the semiconducting SWCNT. (c) On state of a SWCNT-FET, showing current flow as a result of gating which induces carriers in the channel. (d) On state band alignment. The Fermi level is shifted into the conduction band by V_G .

and drain electrodes, and the channel potential is controlled by the gate. In the off state, the SWCNT is depleted of carriers (shown by the red region), and current cannot flow. In Fig. 2.10(b), we show the band diagram corresponding to the off state: the Fermi energy lies within the band gap of the nanotube and no states are available for transport. In Fig. 2.10(c)–(d) we show the SWCNT-FET in its on state, and the corresponding band diagram, respectively. With sufficient gate voltage, the Fermi energy leaves the band gap, entering the conduction band, populating the SWCNT channel with charge carriers and allowing the flow of current. For opposite gate voltage, the Fermi level of the nanotube enters the valence band, allowing on-state transport with holes.

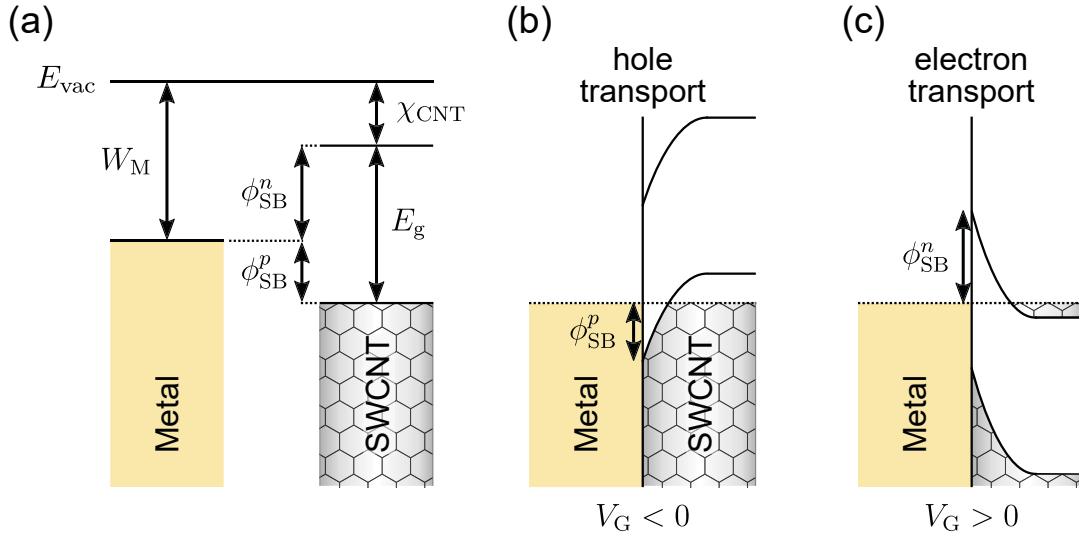


Figure 2.11: Schottky barriers in SWCNT transistors. (a) Separated metal and SWCNT band structures, showing the metal work function, W_M , SWCNT electron affinity, χ_{CNT} , and band gap, E_g with respect to the vacuum energy E_{vac} . These give the Schottky barriers for hole and electron transport, ϕ_{SB}^p and ϕ_{SB}^n respectively. (b)–(c) Schottky barrier formation in metal-semiconductor heterojunctions for hole and electron transport respectively. The band alignment depends on the gate voltage, which shifts the band structure in the channel.

The transport behaviour in SWCNT-FETs has been successfully modeled by treating the metal-semiconductor interfaces as Schottky barriers (SB), limiting the flow of current in the “on” state [76]. In Fig. 2.11(a), we show the metal and SWCNT band structures. The relevant parameters for determining the Schottky barrier heights with respect to the vacuum energy, E_{vac} , are shown: W_M , the metal work function, χ_{CNT} , the SWCNT electron affinity, and E_g the SWCNT bandgap. The Schottky barriers are different heights for holes and electrons, respectively [44]:

$$\phi_{\text{SB}}^p = \chi_{\text{CNT}} + E_g - W_M, \quad \phi_{\text{SB}}^n = -\chi_{\text{CNT}} + W_M. \quad (2.40)$$

In Fig. 2.11(b) and (c), we show the heterojunction band diagrams for hole ($V_G < 0$) and electron ($V_G > 0$) transport respectively. The bands of the carbon nanotube, whose energies are set by the Fermi energy in the channel, bend down at the interface, creating the Schottky barriers.

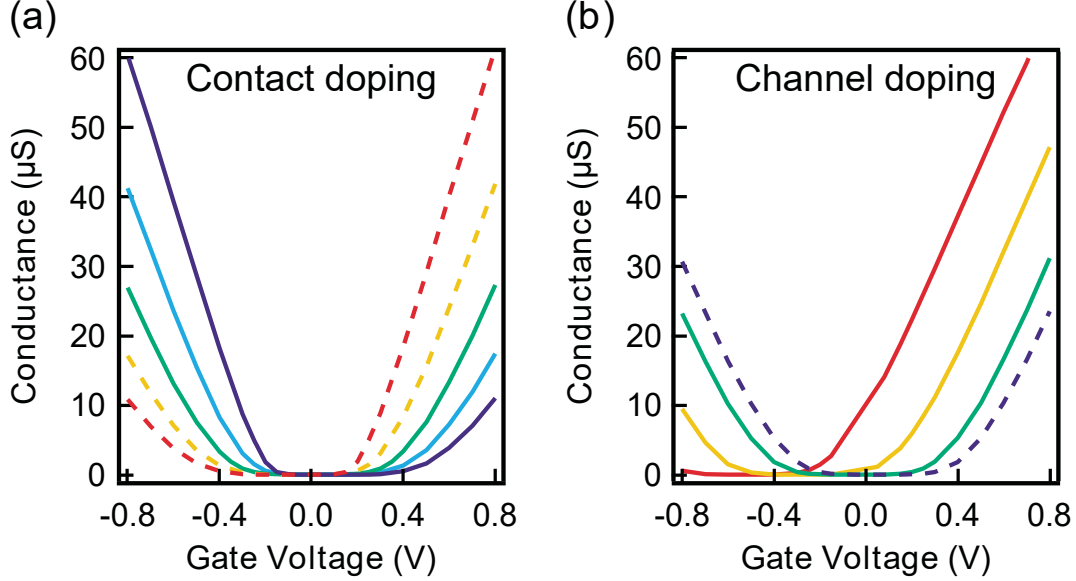


Figure 2.12: The effect of metal work function and channel doping in SWCNT-FETs. (a) Calculated conductance vs. gate voltage data for a SWCNT-FET at room temperature with different contact work functions. Contact doping changes the transport asymmetry, going from highly conductive electrons (red) to highly conductive holes (dark blue). Conductance is suppressed near $V_G = 0$ V; the off state of the transistor. (b) Calculated conductance vs. gate voltage data for a SWCNT-FET at room temperature for different channel dopings. Changing the channel doping causes the conductivity curves to shift in gate, but does not affect the electron-hole asymmetry about the center of the band gap. Figure adapted from Ref. [76].

The current flow in SWCNT Schottky barrier FETs is given by the Landauer formula [76]:

$$I = \frac{4e}{h} \int [f(E + eV_B) - f(E)]T(E)dE \quad (2.41)$$

where the drain electrode has been grounded, f is the Fermi distribution and $T(E)$ is the transmission probability, determined using the WKB (Wentzell-Kramers-Brillouin) approximation. Here, we spare the details of this calculation, but note that $T(E)$ depends both on the contact work function and the channel doping. We will now show calculated SWCNT-FET transport data and discuss the qualitative effects of the work function and channel doping. In Fig. 2.12, adapted from Ref. [76], we show the calculated SWCNT conductance ($G = \sigma W/L$) as a function of V_G . In Fig. 2.12(a), we show the effect of the metal work

function on the SWCNT transistor. In all cases we see transistor behaviour, where conductivity is tunable from zero near $V_G = 0$ V, to finite conductivity at higher $|V_G|$. If the metal work function matches that of the SWCNT channel (green curve), electron ($V_G > 0$) and hole ($V_G < 0$) conductance are symmetric. Progressively increasing the work function of the leads (light blue, dark blue) is equivalent to doping the leads with holes. This changes the relative heights of the Schottky barriers for electrons and holes, as shown in Eq. 2.40, and results in electron-hole asymmetric transport, with higher hole conductance. Conversely, decreasing the metal work function (yellow dashed, red dashed) results in higher conductance for electrons by the same logic.

In Fig. 2.12(b), we show the effect of extrinsic channel doping on the SWCNT transistor, occurring as a result of charged impurities on the SWCNT. The green curve shows the undoped case. As the concentration of n-type dopants is increased (yellow, red), the entire transistor curve shifts towards negative gate voltage, and the opposite for p-type dopants (blue, dashed). Channel doping increases the Fermi level in the channel, but does not affect the Schottky barriers. This gate-shifts the conductivity curves without altering their symmetry. The transport features presented here as a function of metal work function and channel contact doping are observed experimentally at room temperature [76]. This is consistent with thermally assisted tunnelling across Schottky barriers at the metal-nanotube interface. At low temperatures, thermally assisted tunnelling is not possible, and the tunnel barriers electronically isolate the SWCNT, forming a quantum dot (QD); a zero dimensional electronic structure with a discrete density of states.

2.5.2 SWCNT SETs

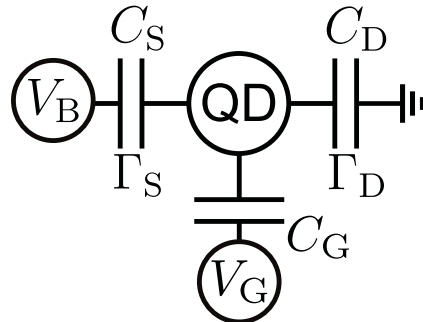


Figure 2.13: Quantum dot effective circuit. The quantum dot Fermi energy is controlled electrostatically through the gate capacitance by the gate voltage. A bias is applied across the QD, which has source and drain capacitances over the tunnel barriers with tunnelling rates Γ_S and Γ_D respectively.

We show the effective circuit for a quantum dot in Fig. 2.13. The QD is isolated by tunnel junctions with capacitances C_S and C_D , and tunnelling rates Γ_S and Γ_D at the source/drain interfaces respectively. The Fermi level of the QD is controlled by the gate voltage, capacitively coupled to the QD via C_G . The total energy of the QD with N charges is [77]:

$$U(N) = \sum_i^N E_i + \frac{(Ne)^2}{2C_\Sigma}, \quad C_\Sigma = C_S + C_D + C_G, \quad (2.42)$$

where E_i is the i^{th} energy level of the QD, and the second term is the Coulomb potential. This leads to the electrochemical potential of an electron on the quantum dot:

$$\mu_N = E_N + (N - \frac{1}{2}) \frac{e^2}{C_\Sigma} + e \frac{C_S V_B + C_G V_G}{C_\Sigma}, \quad (2.43)$$

where the last term describes the capacitive coupling of the electrodes to the dot in the case when the drain is grounded. From here we calculate the charge addition energy:

$$E_{\text{add}} = \mu_{N+1} - \mu_N = \Delta + E_C, \quad (2.44)$$

where the classical energy required to add a single electron to the system, known as the charging energy is [77]:

$$E_C = \frac{e^2}{C_\Sigma}, \quad (2.45)$$

and Δ is the energy difference between the orbitals of the QD, also known as the single particle energy spacing. This is akin to the quantized energies of the particle-in-a-box, and is determined by electronic potential of the QD. For metallic and semiconducting nanotubes, respectively:

$$\Delta = \frac{h v_F}{2L} \quad \Delta_n = \sqrt{\left(\frac{(n+1)h v_F}{2L}\right)^2 + \left(\frac{E_g}{2}\right)^2} - \sqrt{\left(\frac{n h v_F}{2L}\right)^2 + \left(\frac{E_g}{2}\right)^2}, \quad (2.46)$$

where n is the orbital index, and $v_F = 8.1 \times 10^5$ m/s is the Fermi velocity in SWCNTs. We note that this is a first order estimate of Δ , which depends on the shape of the confining potential and that various other formulae for Δ are required for more in-depth analysis [30]. Due to the 4-fold valley and spin degeneracy in SWCNTs, $\Delta = 0$ for all but every 4th energy state of the QD, although in the presence of inter-valley scattering, the valley degeneracy can be lifted, leading to $\Delta = 0$ for every 2nd state only [78].

SWCNT QDs are single electron transistors. An illustrative way to understand electron

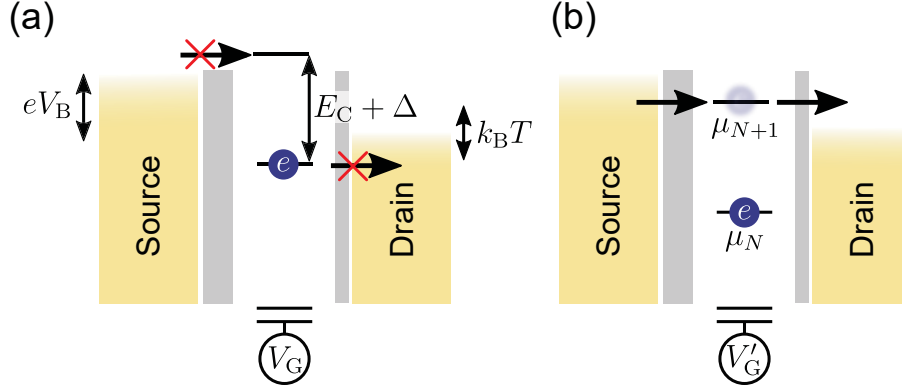


Figure 2.14: Single electron transistor energy level diagram. (a) SET “off” state, showing Fermi levels of the source and drain leads thermally smeared, and separated by the bias window eV_B , with asymmetric tunnel barriers (grey bars). The energy levels of the states in the channel (μ_N, μ_{N+1}) can be shifted up or down by the gate voltage, and have spacing $E_C + \Delta$. In this case, current cannot flow as there are no energy states within the bias window. (b) SET “on” state. Shifting the energy spectrum with V_G populates the bias window with a QD energy state, allowing the flow of current.

flow through SETs is through energy level diagrams. We show “off” and “on” states of a SET in Fig. 2.14(a) and (b) respectively. The source and drain Fermi energies, thermally smeared by the Fermi distribution at temperature T , and separated in energy by the bias voltage V_B . To be in the QD regime, these must satisfy $E_C + \Delta > k_B T$. Between the leads and the QD are asymmetric tunnel barriers, represented by gray bars. The states in the channel have energies μ_N and μ_{N+1} , which can be controlled by V_G and are separated by $E_C + \Delta$. As shown in Fig. 2.14(a), QD states which lie above the source/drain Fermi levels are energetically inaccessible and always unoccupied, while channel states which lie below the source/drain Fermi levels are always occupied. Neither of these permit the flow of current, putting the SET in the off state. By tuning the gate voltage, a state on the dot can be brought into the bias window, as shown in Fig. 2.14(b), allowing variable occupation of the dot and permitting the flow of current, putting the SET in the on state.

From the tunnelling rates, we can calculate the SET current [77]:

$$\frac{I}{e} = \frac{\Gamma_S \Gamma_D}{\Gamma_S + \Gamma_D} (f_D - f_S) \equiv \Gamma (f_D - f_S), \quad (2.47)$$

where f_S and f_D are the Fermi distributions at the source and drain lead, and μ_{N+1} is the

chemical potential the $N + 1$ electron:

$$\begin{aligned} f_D &= \left(1 + \exp \left(\frac{\mu_{N+1}}{k_B T} \right) \right)^{-1}, \\ f_S &= \left(1 + \exp \left(\frac{\mu_{N+1} + eV_B}{k_B T} \right) \right)^{-1}, \\ \mu_{N+1} &= -e \frac{C_G(V_G - V_G^0) + C_S V_B}{C_\Sigma}, \end{aligned} \quad (2.48)$$

where V_G^0 is the QD energy level offset, in terms of gate voltage. Between adjacent energy levels in the QD, this is related to the energy level spacing:

$$\Delta V_G^0 = \frac{E_C + \Delta}{e} \left(\frac{C_S + C_D}{C_G} + 1 \right) \quad (2.49)$$

In Fig. 2.15(a) we plot current as a function of gate and bias voltage using Eqs. 2.47 and 2.48 for four charge states (N to $N + 4$) on a 4-fold degenerate SWCNT QD. The calculation parameters are $\Gamma_S = \Gamma_D$, $\Gamma = 3$ GHz, $C_{S,D} = 1.0$ aF, $C_G = 0.1$ aF, $L = 50$ nm, $T = 4.2$ K, and $\Delta = 10$ meV. From the data, we see the Coulomb blockade pattern characteristic of SET transport, comprised of a series of diamond shapes. The white regions are the so-called Coulomb valleys, where conduction is disallowed, while the red and blue regions are the Coulomb peaks, where current flows forward or backward across the dot respectively. Each diamond represents a different number of electrons occupying the quantum dot, as shown by the grey numbering. On the right, we show the energy level diagrams which explain the different features of the blockade pattern, for forward or backwards currents. The heights of the diamonds (ΔV_B) are determined by E_C , every 4th diamond includes the energy contribution from Δ as well. The widths, ΔV_G , and negative (positive) slopes of the diamonds, are set by the gate and source (drain) capacitances, respectively:

$$\Delta V_G = \frac{e}{C_G}, \quad \Delta V_B = -\frac{C_G}{C_S} \Delta V_G, \quad \Delta V_B = \frac{C_G}{C_D + C_G} \Delta V_G. \quad (2.50)$$

We show vertical and horizontal cuts of the $I - V_B - V_G$ data in Fig. 2.15(b) and (c) along the red dashed and solid lines in panel (a) respectively. Fig. 2.15(b) shows $I - V_B$ data at constant $V_G = 2$ V. At low bias, the QD is in the Coulomb valley and no current flows. When the bias window becomes large enough to encompass an energy state, current flows through the device. These are off and on states of the SET. Fig. 2.15(c) shows $I - V_G$ data at constant $V_B = 5$ mV. As we vary the gate, energy states pass through the bias window

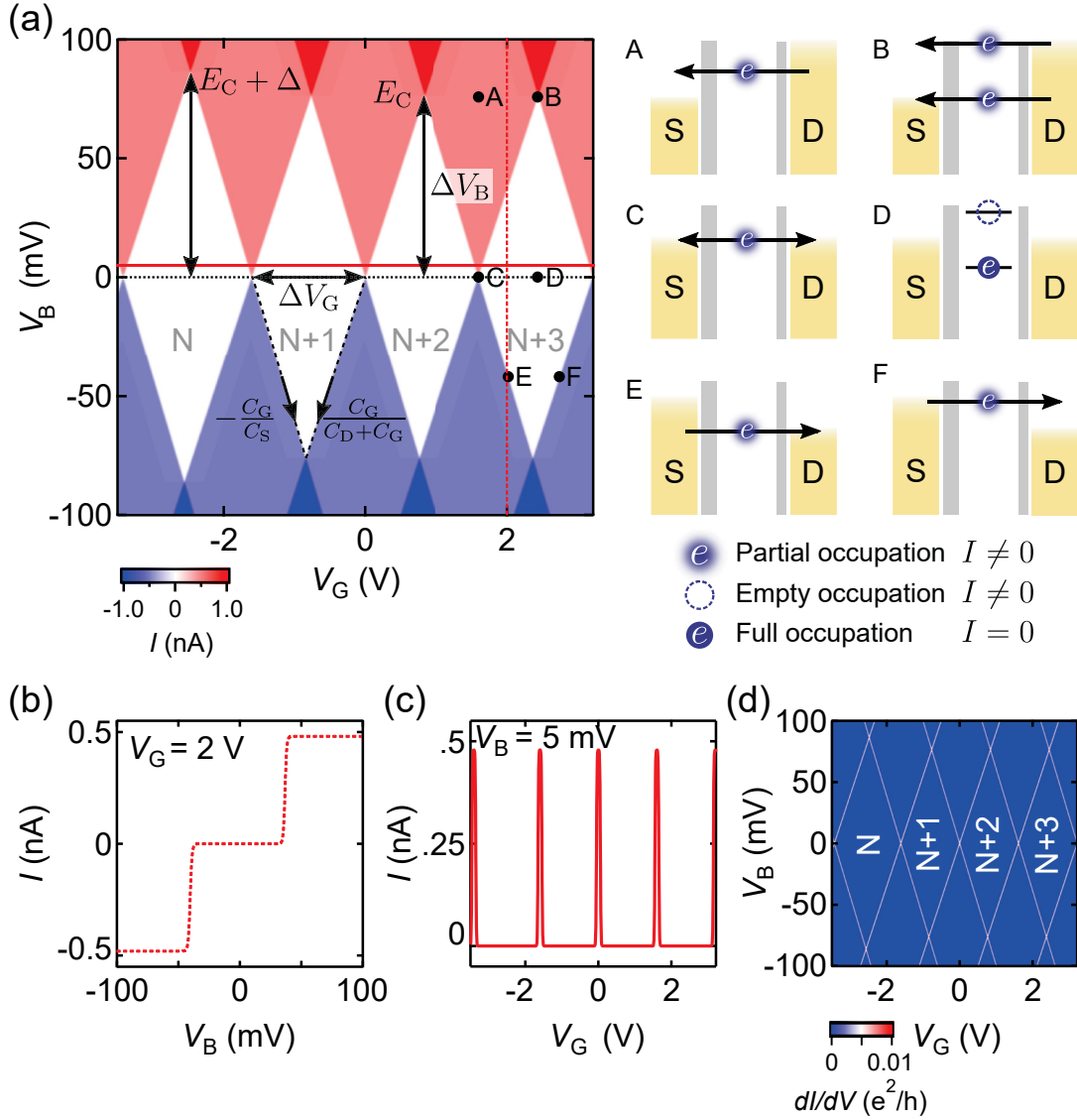


Figure 2.15: Calculated Coulomb blockade transport in SWCNT QDs, with calculation parameters: $\Gamma_S = \Gamma_D$, $\Gamma = 3$ GHz, $C_{S,D} = 1.0$ aF, $C_G = 0.1$ aF, $L = 50$ nm, $T = 4.2$ K, and $\Delta = 10$ meV. (a) $I - V_B - V_G$ data, showing Coulomb blockade diamonds (left). Each diamond represents an additional charge state on the QD. The heights of the four-fold degenerate diamonds (ΔV_B) are determined by E_C and Δ . The gate, source, and drain capacitances determine the widths and slopes in the diamond geometry. To the right, we show energy level diagrams corresponding to different points in the $I - V_B - V_G$ data, labelled A-F. (b) Bias cut along the dashed red line in (a), showing blocked transport at low V_B . (c) Gate cut along the solid red line in (a), showing peaks corresponding to QD states. (d) Differential conductance $dI/dV - V_B - V_G$ plot from the data in (a), showing sharp boundaries between the Coulomb peaks and valleys.

sequentially, giving a series of current peaks, and electronically imaging the density of states of the QD. In Fig. 2.15(c), we plot $dI/dV_B - V_B - V_G$ from the data in Fig. 2.15(a). For visibility of the Coulomb diamonds, it is often useful to differentiate the $I - V_B - V_G$ data, so that the constant plateaus of current become sharp lines.

We expect this SET behaviour in SWCNT devices with high tunnel barriers that strongly limit current flow, forming a 0D quantum dot. For lower, more transparent tunnel barriers, corresponding to metallic or small band gap nanotubes (see Eq. 2.40), the SWCNTs behave as coherent 1D Fabry-Pérot cavities [29]. The FP regime has much higher conductance and requires $\Delta > \hbar\Gamma > E_C$. These conditions are met for extremely short tunnel barriers which have large C_S and C_D , and giving very small E_C , from Eq. 2.45.

2.5.3 SWCNT ballistic waveguides

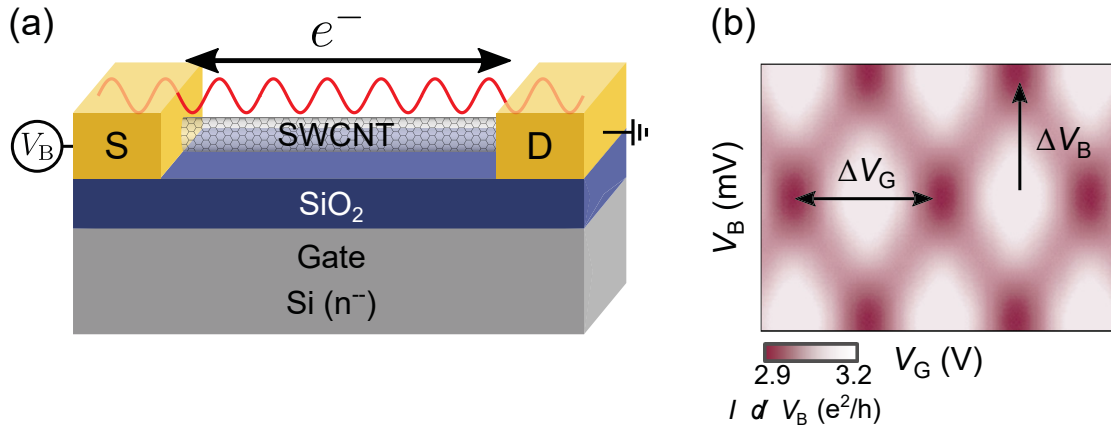


Figure 2.16: Fabry-Pérot resonances in SWCNTs. (a) Fabry-Pérot resonances arise due to semi-transparent tunnel junctions between the contacts and the graphene channel, allowing coherent electron transport in the channel. (b) Calculated $dI/dV_B - V_B - V_G$ data from Ref. [29] for an open quantum dot. Fabry-Pérot resonances are visible in both gate and bias directions with spacing ΔV_G and ΔV_B .

We show 1D electron waveguide behaviour in Fig. 2.16. Electrons form resonant standing waves in the SWCNT cavity, shown schematically in Fig. 2.16(a). Here, electrons reflect at the metal-SWCNT junctions, interfering to produce conduction oscillations, much like the FP resonances we discussed earlier in a 2D graphene cavity (Fig. 2.4). We show calculated $dI/dV_B - V_B - V_G$ data from Ref. [29] in Fig. 2.16(b), with gate and bias spacing between interferences ΔV_G and ΔV_B respectively. These interferences can be understood by the

electron phase shifts in the 1D SWCNT waveguide channel [29]:

$$\varphi_{1,2} = \frac{k_0 L}{2} \pm \left(\frac{e V_B L}{\hbar v_F} + \frac{\pi}{4} \frac{C_G V_G}{e} \right), \quad (2.51)$$

where the \pm symbol comes from the two electron valleys, and $k_0 = |\mathbf{K}| = |\mathbf{K}'| \approx 1.7 \text{ nm}^{-1}$. We expect constructive interference when the electron phase shift for a round-trip in the FP cavity is 2π , creating a standing electron wave in the SWCNT, leading to a conductance peak. The characteristic heights and widths of the FP interference pattern are given by the equations:

$$\Delta V_B = \frac{\Delta}{e} = \frac{\hbar v_F}{2Le}, \quad \Delta V_G = \frac{4e}{C_G}, \quad (2.52)$$

satisfying the round-trip phase condition for standing waves in the SWCNT waveguide. We have now seen how the Schottky barriers can lead to FET, quantum dot, or coherent 1D waveguide behaviour in SWCNT transistor devices.

2.6 Conclusions

In this chapter, we have set the groundwork for understanding the experimental transport data and theoretical calculations we will present in the remainder of the thesis. We have shown how the linear dispersion of the Dirac cones, and chiral nature of Dirac fermions in graphene, govern transport behaviour in both graphene and carbon nanotubes. The next step in our theoretical study of quantum electromechanics in carbon nanoelectronics is the inclusion of strain. Straining the hexagonal lattice causes significant changes to graphene's band structure, dramatically changing its transport behaviour, as we will see in Chapter 5. However, first there are some experimental considerations which must be addressed. Namely, we must discuss how to apply large and tunable strains to nanoelectronic devices in practice, and the ultra-short device geometries required for large strains depend on their contacts.

Chapter 3

A Platform for Quantum Strain Electronics: Devices, Instrumentation, and Methods

We aim to study the effects of strain in ultra-short graphene and carbon nanotube quantum nanoelectromechanical systems (QNEMS). However, it is non-trivial to design and build an experimental system for the application of large, tunable strains compatible with low temperature transport measurements. In this chapter, we detail our fabrication methods to create suspended ballistic graphene devices for strained transport measurements and ultra-short single-walled carbon nanotube (SWCNT) transistors. We then show our custom-built system for quantum strain transport engineering (QTSE) to apply large tunable strains ($\sim 1\text{--}10\%$), with independent control of mechanical strain and channel charge density at low temperatures. Finally, we discuss our methods for creating and measuring our ultra-short, clean carbon nanoelectronic devices with ballistic contacts using electronic circuits.

3.1 Introduction

As discussed in Chapter 1, strained carbon nanoelectronic devices form rich systems for studying quantum electromechanics, with applications for tunable high frequency nanoelectromechanical systems (NEMS) [10,11,15–17], valleytronics filters and current sources [34,41], high-quality transistors [35–37], and tunable two-in-one quantum transport systems [53]. However, little progress has been made towards experimental realization of strained carbon nanoelectronics despite their wide range of potential applications. This is in part due to

challenges in experimental design and practice involved in achieving large, tunable and reversible strains at the nanoscale, in a transport configuration, at the low temperatures where these strain effects are observable. To date, strained experiments in carbon nanoelectronics have been limited to: non-tunable strains induced by substrate geometry [45], non-uniform strains by pushing on the material directly [42], substrates which do not allow metallic contacts for transport measurements [50], or small electrostatically-induced strains, which do not allow independent tuning of the strain and charge density [52]. To overcome these limitations, we employ QTSE instrumentation for large and tunable strains compatible with low temperature transport, and independent from gate [79, 80].

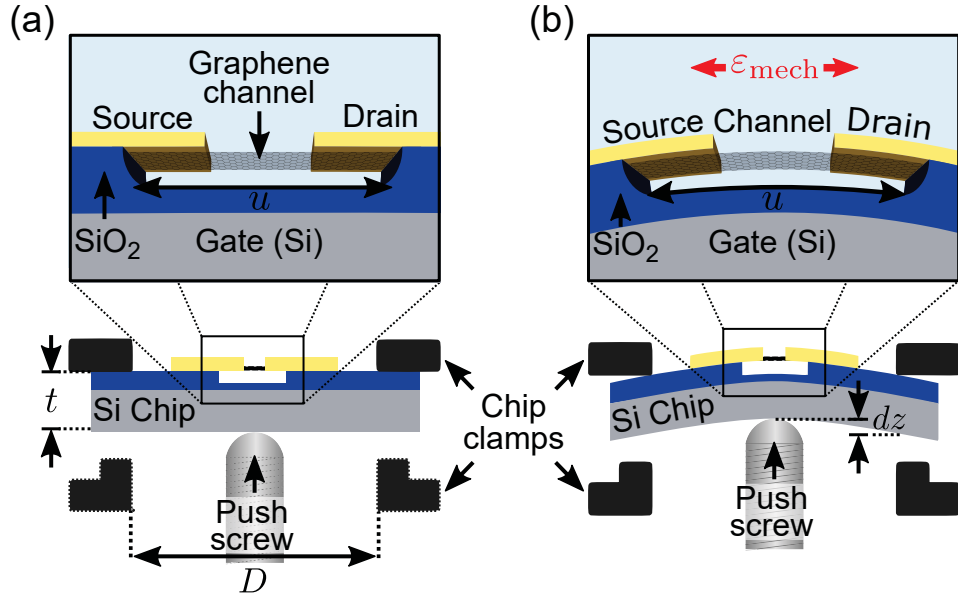


Figure 3.1: Applying mechanical strain with QTSE instrumentation. (a) A suspended device on a thin, flexible Si chip in the QTSE instrumentation before strain actuation. Suspended metal films form the source and drain, while the Si chip acts as a global back gate for transport measurements. The relevant geometric parameters for uniaxial strain are shown: D , the distance the chip clamps, t is the chip thickness, and u is the total undercut length. (b) Pushing on the chip by a vertical displacement dz causes it to bend. The suspended metal films act as lever arms, applying uniaxial mechanical strain ϵ_{mech} to the sample.

In Fig. 3.1(a)–(b), we show the operation of the 3-point QTSE set-up for unstrained and strained graphene devices respectively. A polished push screw bends the silicon chip which acts as a substrate and global back gate for our suspended devices. The suspended metal films, which form our source/drain electrodes for transport measurements, act as lever arms to apply large, tunable, and reversible strains to the suspended graphene channel. This lever arm effect is crucial, allowing small vertical displacements in the z direction to generate large in-plane strains. In this configuration, the theoretical lateral displacement applicable in our

system due to bending of the chip is [81]:

$$dx = \frac{3ut}{D^2} dz. \quad (3.1)$$

In Fig. 3.1, we label the relevant parameters: D is the distance between the clamps which hold the chip, t is the chip thickness, u is the length of the suspended part of the device including the metal films, and dz is the vertical displacement of the push screw. We predict that we can achieve tunable uniaxial strains up to $\varepsilon = 10\%$ using our QTSE set-up, for experimentally achievable device lengths ($L = 10 - 100$ nm). This is more than an order of magnitude greater than previous strained-transport systems which have typical strains $\lesssim 1\%$ [51, 52, 82]. While we focus on using our QTSE set-up for uniaxial strain in this thesis, our instrumentation is modular and extremely versatile for future studies of quantum electromechanics. We can modify the clamping of our devices for triaxial strain, use alternating current (ac) actuation of the gate for time-dependent strains, or include large magnetic fields ($B = 9$ T) to study large pseudomagnetic fields, high frequency tunable NEMS, or valley polarized transport [22, 31, 41].

In this chapter, we will first show how we fabricate QTSE-compatible, suspended SWCNT and graphene devices, used for studying ultra-short quantum dots and strained transport measurements. We will then detail the design and construction of our QTSE set-up and its integration with low-temperature transport instrumentation. We discuss our electronic measurement methods and final fabrication steps for creating ultra-short, extremely clean graphene and SWCNT devices before finally showing experimental calibration of strain in our QTSE set-up using gold point-contact devices.

3.2 Fabrication of suspended graphene and SWCNT transistors

In this section, we detail the microfabrication procedures used to build our suspended graphene and SWCNT devices. Each of our devices is unique, due to the nature of deposition of graphene and SWCNT growth. This means batch processing is not possible and each device must be constructed individually. While this process is challenging, time consuming, and results in low device throughput, it is necessary to create high-quality, aligned SWCNT and graphene devices for strained transport measurements.

In Fig. 3.2(a)–(b), we show our goal suspended device geometries for SWCNT break

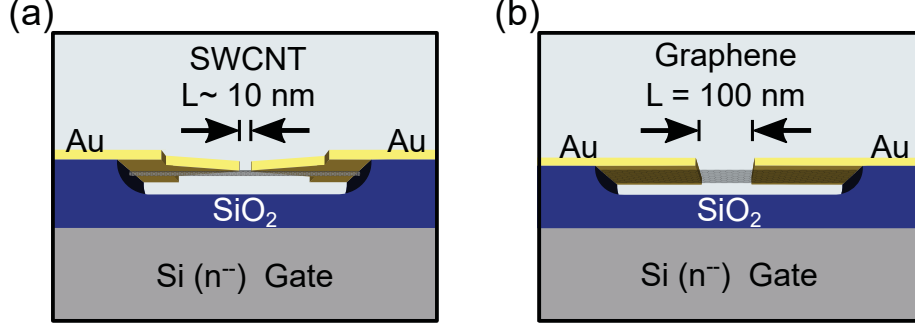


Figure 3.2: Fabrication goal geometry for SWCNT and graphene devices. (a) Ultra-short (~ 10 nm) suspended SWCNT device in a bowtie-shaped break junction geometry. (b) Suspended graphene device (≈ 100 nm) in a rectangular gap-junction geometry.

junctions (~ 10 nm) and graphene gap-junctions (≈ 100 nm) respectively. Suspended Au films contact the SWCNT or graphene, which are suspended over the Si/SiO₂ global back-gate. We outline the entire process, from the preparation of our Si/SiO₂ wafer substrates, and growth/deposition of SWCNTs and carbon nanotubes, to deposition of the Au leads and suspension.

3.2.1 Wafer preparation for SWCNT growth and graphene deposition

Here, we describe our wafer preparation fabrication procedures. We will show the thick and thin wafers we use for our graphene and SWCNT devices, and discuss how we remove unwanted thermal SiO₂ from the backside of the wafer, so that we may electrically control the Si global back gate. Finally, we discuss our process for depositing a gold alignment pattern on the wafers for locating SWCNTs and graphene.

In Fig. 3.3, we show the front, back, and side views of the thin (left) and thick (right) wafers used. These 4", $\langle 100 \rangle$, degenerately doped Si⁺⁺ wafers are covered on the front side by a layer of thermal SiO₂ with thickness $t_{\text{ox}} \approx 300$ nm. We use thin wafers for our QTSE devices as these are less rigid, allowing the chips to bend further without breaking (Fig. 3.1). These thin wafers are made by grinding the backside of standard wafers until they have the desired total thickness, $t = 200$ μm . However, these thin chips are much more fragile, resulting in lower device yields. For this reason, we used thicker wafers, with $t = 500\text{--}550$ μm , for initial measurements on SWCNTs to understand ultra-short transport (Chapter 4). For later studies on strained transport in graphene (Chapter 6), we used thin wafers compatible with the QTSE.

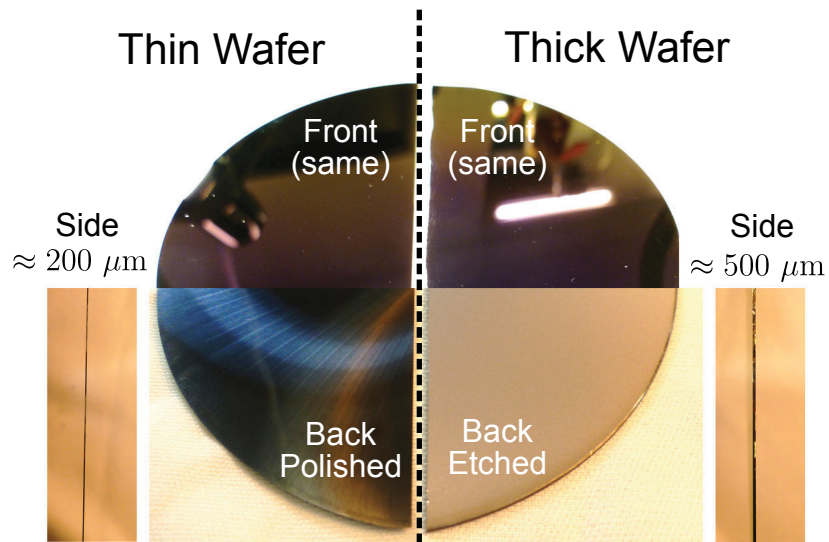


Figure 3.3: Thick and thin Si Wafer substrates. Thin (left) and thick (right) wafers with front, back, and side views. The thin wafer is made thin by grounding the backside.

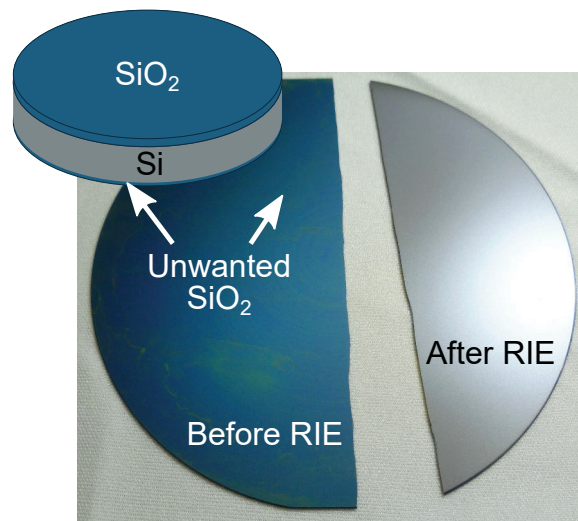


Figure 3.4: Backside wafer etching for gate contact. Unwanted oxide is removed from the wafer backside using oxygen plasma RIE, allowing electrical contact to the Si global back gate.

We control the electrostatic environment of our devices using the degenerately doped Si wafer as a global back gate. If any thermal oxide remains on the backside of the wafer, we cannot make good electrical contact to our gate, and must therefore remove it. In Fig. 3.4, we show part of a Si wafer, before and after reactive ion etching (RIE) the backside. RIE is a dry etching method in which we use radio frequency (RF) power to generate a plasma. The ionized gases of the plasma bombard the material in the RIE chamber. Depending on the chemical composition, and the gases used and the material in the chamber, this can cause directional etching. In our case, we use this method to remove the extraneous oxide from the backside of the wafer using the following recipe. Into the chamber, we flow 22.5 standard cubic centimetres per minute (SCCM) of CHF_3 and 2.5 SCCM of O_2 at a pressure of 100 mTorr. We then apply 300 W or RF power for 15 minutes. After this process, we confirm that the oxide is etched completely by ellipsometry or reflectometry. This can also be observed visually, as Si is matte and light grey in colour, while the oxide is dark blue and glossy (Fig. 3.4).

Next, we deposit gold grids on the surface of the wafer for the indexing of graphene flake and SWCNT positions. This step is done prior to deposition for graphene samples or after SWCNT growth, as the high temperatures ($\approx 1000^\circ\text{C}$) used in the latter approaches the melting point of gold. These grids will also be used later to align metal contacts on top of the samples using electron beam lithography (Fig. 3.12).

To define the grids, we use mask aligned photolithography in a clean room done under yellow filtered light to protect the sample from unwanted ultraviolet (UV) light exposure and dust. This process is detailed in Fig. 3.5(a). A layer of photosensitive polymer called photoresist is deposited on our wafer and selectively covered using a photolithography mask. The resist is exposed to UV radiation, which causes a chemical change in the resist which is not covered by the mask. The wafer is then developed in a remover solution which removes only the exposed photoresist. The details of this process are as follows. We coat a full 4" wafer with OIR-674-11 photoresist and spin it at 3000 rotations per minute (rpm) for 1 minute using a spin coater, giving an even $\approx 1.4\ \mu\text{m}$ resist layer. The resist-coated wafer is soft-baked at 90°C for one minute to partially harden and dry it. We then dice the wafer into vertical thirds using a diamond scribe to fit the photolithography mask. Scribing is done after spinning the resist to protect the wafer from particles released in the dicing process. The resist-coated wafer thirds are loaded into a Karl Suss MA6 mask aligner, along with our photolithography mask in preparation for UV exposure. As shown in Fig. 3.5(b), The mask consists of 5×3 grids which are $\approx 5 \times 5\ \text{mm}$ in size. The grid patterns consist of "L"

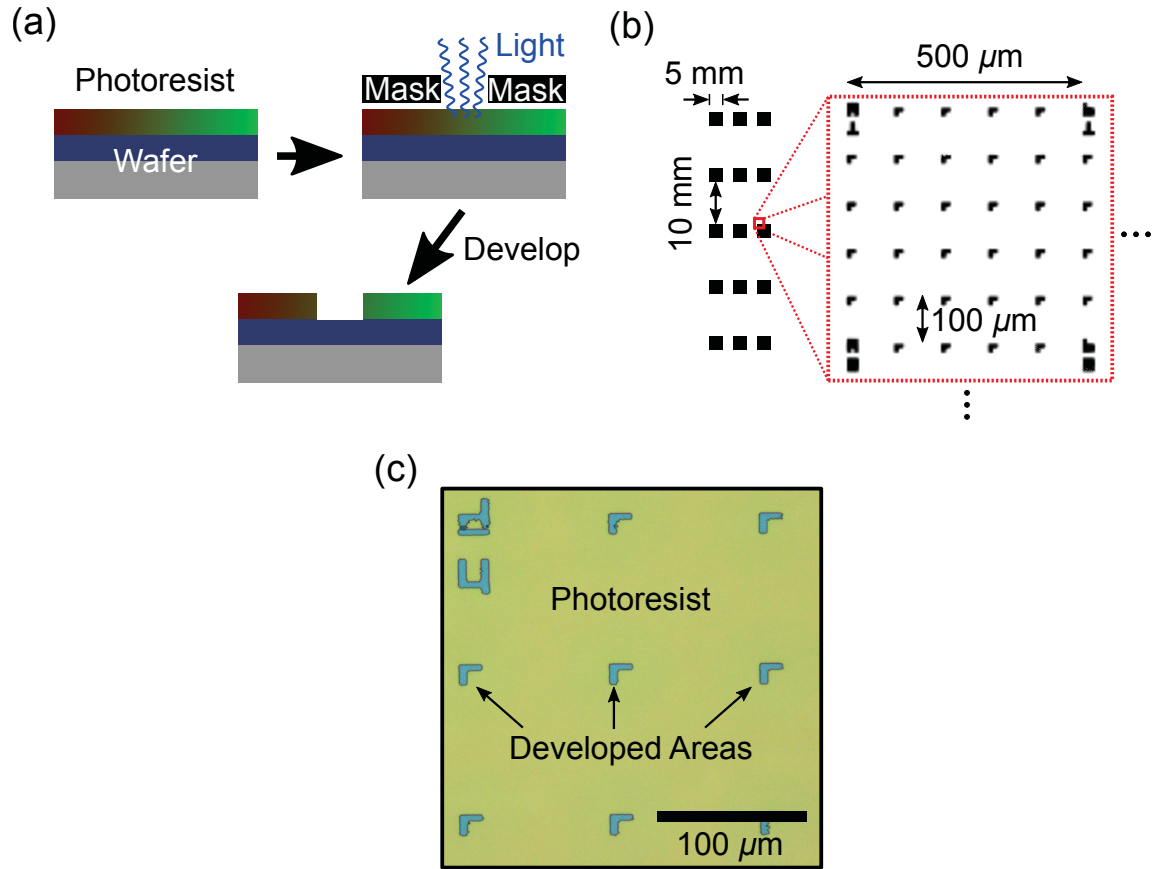


Figure 3.5: Photolithography procedure for alignment grids. (a) Photoresist is spun onto the wafer. A photomask blocks incident UV radiation. The resist is then developed, exposing the wafer. (b) The photomask grid alignment pattern, showing 15 sets of alignment grids, each with sets of “L” shaped grids of spacing $100 \times 100\ \mu\text{m}$, indexed by number and letter. (c) Optical image of the developed grid pattern, showing the grid-shaped holes in the resist where metal will be evaporated.

shapes, which are composed of two $15\text{ }\mu\text{m} \times 5\text{ }\mu\text{m}$ rectangles pointing along the x and $-y$ axes of the mask pattern, spaced $100\text{ }\mu\text{m}$ from one another in both dimensions. Every fifth grid point ($500\text{ }\mu\text{m}$) is given a letter index (A-I) for its x coordinate and a number index (1-9) for its y coordinate, giving each grid point an “address”.

Next, we bring the resist-coated $\frac{1}{3}$ -wafer into hard contact with our photomask to create sharp edges in the exposure pattern. We expose our wafer sections using a dose of 35 mJ/cm^2 of UV light from a Hg lamp to expose the photoresist through the mask. We then develop the exposed wafers, placing them in AZ-726-MIF developer and stirring gently for 50 seconds. This washes away the exposed resist, leaving a grid pattern of holes leading down to the oxide surface as shown in Fig. 3.5(c). After 50 seconds in the developer, we rinse the wafers with deionized (DI) water to stop the developing process.

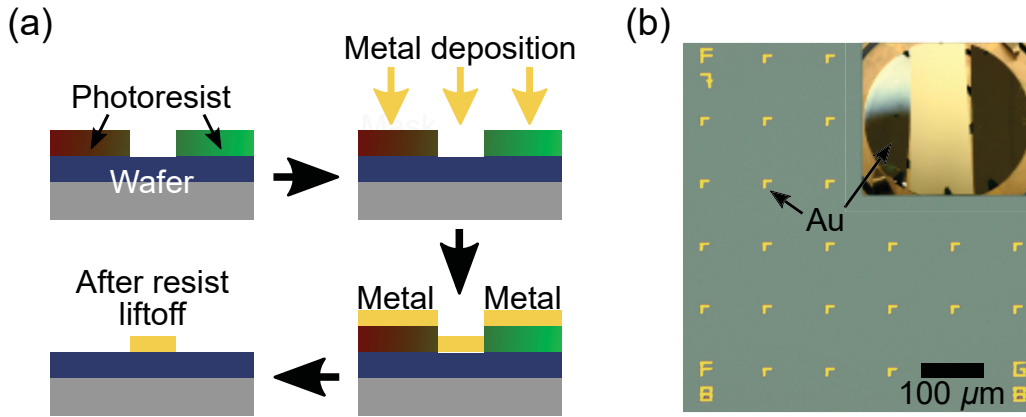


Figure 3.6: Deposition of alignment grids on the blank wafer. (a) Metal is deposited onto the developed photolithography pattern. After lift-off, the wafer is coated in a grid pattern of metal. (b) Optical microscope image of a section of the alignment grid pattern. The inset shows the entire wafer after metal deposition and before lift-off.

We use thermal evaporation to deposit metal grids onto the wafer, as described in Fig. 3.6(a). Metal is deposited onto the exposed photolithography pattern on the wafer. The photoresist and excess metal is then removed from the wafer, leaving behind the exposed pattern from the photomask. To thermally evaporate our metals, we apply large powers ($\sim 4\text{ A} \times 220\text{ V} = 880\text{ W}$) to a metal-containing filament or boat under vacuum ($P \sim \times 10^{-5}\text{ Torr}$) in a bell jar. Joule heating causes the metal to melt and evaporate, condensing on the wafer surface suspended above it. We deposit a 3 nm sticking layer of Cr, to adhere the Au to the SiO_2 , followed by 80 nm of Au, over the entire wafer. A gold-coated wafer is shown in the inset of Fig. 3.6(b). We use gold because it is inert and offers good contrast for imaging. After the evaporation is complete, we perform lift-off by soaking the metal-and-resist-coated wafer in an acetone bath on a hot plate at $60\text{ }^\circ\text{C}$, for 10 to 60 minutes.

The resist is removed from the surface, bringing the excess metal with it, and leaving behind the desired grid pattern on the surface, as shown in Fig. 3.6(c). To encourage complete lift-off, the surface of the wafer is sprayed with warm acetone, using a syringe. After lift-off, the wafer is rinsed with clean acetone and isopropyl alcohol (IPA), before being dried with dry N_2 gas, to remove any additional resist residues.

After the deposition of the Au grids, we dice the $\frac{1}{3}$ -wafers into smaller chips using a diamond scribe. We dice the thick chips to dimensions $\approx 5 \times 5$ mm so that they fit into our chip carriers (See Fig. 3.30), and the thin chips to dimensions $\approx 12 \times 5$ mm, to fit into the QTSE set-up (see Fig. 3.23). We dice our thick chips by scribing, then placing them on a glass slide such that they overhang along the scribe mark. We break the chips along the scribe mark by applying pressure to the chip on both sides of the overhang using plastic-tipped tweezers. For the thin chips, it is imperative to have pristine crystal edges to prevent shattering when they are bent, as any defects in the crystal edge can nucleate a fracture. As the thin chips are more fragile, we are able to dice them by pushing the scribe at a point on the edge of the chip. The chip dices naturally along the $\langle 100 \rangle$ axis of the Si wafer, perpendicular to the scribe point, giving a perfect crystal edge.

3.2.2 Growing, locating, and sorting SWCNTs

In this section, we will describe the chemical vapour deposition (CVD) growth of our carbon nanotubes on the prepared Si wafers. Then we will show how we locate them using a scanning electron microscope (SEM), and how we selectively choose single-walled carbon nanotubes based on their diameters, using an atomic force microscope (AFM). We grow our nanotubes directly on the Si wafer, after the backside etch, but before deposition of the metal grids. As stated in the previous section, we grow our nanotubes after the RIE backside etch of our wafers, but before the deposition of the Au alignment grids to protect them from the high temperatures used in CVD growth.

Using the same photolithography procedure described in Fig. 3.5(b), we deposit a sub-monolayer (6–8 Å) of Fe over a wafer in the same grid pattern, shown in Fig. 3.7, using magnetron sputtering. For this procedure, a plasma is created in the sputtering chamber and accelerated into an iron target, releasing iron particles which land on the wafer surface. To generate our plasma, we use Ar gas at 10 SCCM, 10 mTorr, and 150 mW, giving a deposition rate of ≈ 3.5 Å/min. We perform lift-off in acetone on a 60 °C hot plate as before, leaving “L” shaped islands of Fe on the wafer, which will act as a growth catalyst for the nanotubes during CVD. For future alignment with the Au grids, the positions of the iron grids are

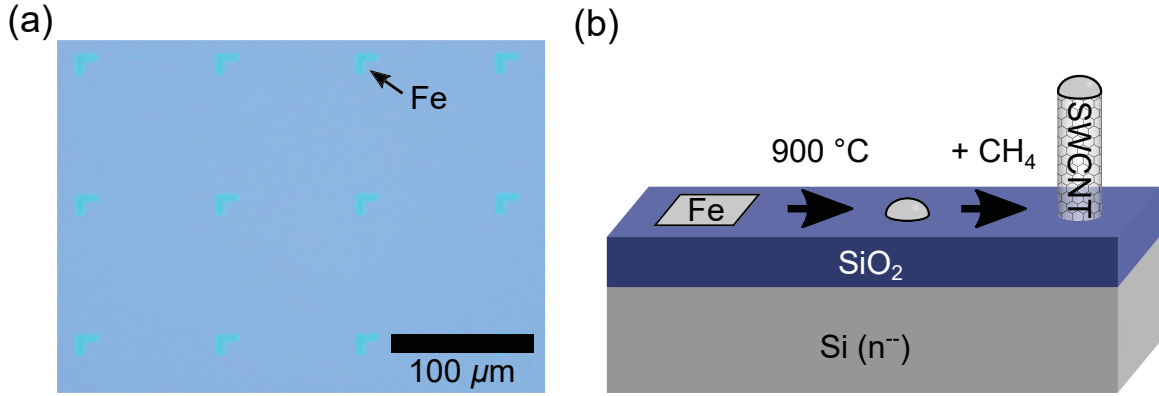


Figure 3.7: Catalyst deposition and CVD growth of carbon nanotubes. (a) Optical image of the 6–8 Å thick submonolayer of Fe, deposited on a Si wafer for catalyzing CNT growth. (b) When heated, the iron nanoparticles on the wafer form droplets which catalyze the growth of CNTs when exposed to methane.

marked on the wafer using a diamond scribe, as the iron becomes optically invisible after CVD.

We show the principle of CVD growth of carbon nanotubes (CNTs) in Fig. 3.7(b). The Fe catalysts are heated to form nanodroplets which catalyze nanotube growth from a methane feedstock gas. The full recipe for CNT growth follows. We load the sputtered wafers into the middle of a quartz tube in a high-temperature furnace. We first anneal the Fe catalyst islands at 900 °C in air. The temperature is then reduced to 500 °C and the wafers are annealed in an Ar environment with a flow rate of 0.1 standard litres per minute (SLM), while the temperature is raised back up to 900 °C. Hydrogen is then added to the quartz tube at a flow rate of 0.1 SLM, while the Ar is turned off for 20 minutes. The hydrogen “wets” the Fe nanoparticles to catalyze the growth of carbon nanotubes. At this point, the furnace temperature is raised to 970 °C. After waiting 3 minutes for stabilization, the CH₄ feedstock gas is added to the H₂ flow, at a rate of 0.2 SLM, for 45 minutes to grow the nanotubes. Subsequently, we stop the flow of these two gases, and restart the flow of Ar to avoid oxidation at high temperatures as the wafers are cooled. At this point, we deposit the gold alignment grids (Fig. 3.6) directly on top of the nanotube growth pattern, so that we may locate our nanotubes precisely on the wafer.

We image the nanotubes using a SEM, defining their positions based on their address in the Au grid. We show SEM images of single-walled and multi-walled carbon nanotubes in Fig. 3.8. It is well known that using SEM imaging deposits hydrocarbons on the imaged surface, which can be extremely detrimental to our carbon-based devices [83]. To ensure that we deposit as little carbon as possible on the nanotubes during SEM imaging, we image

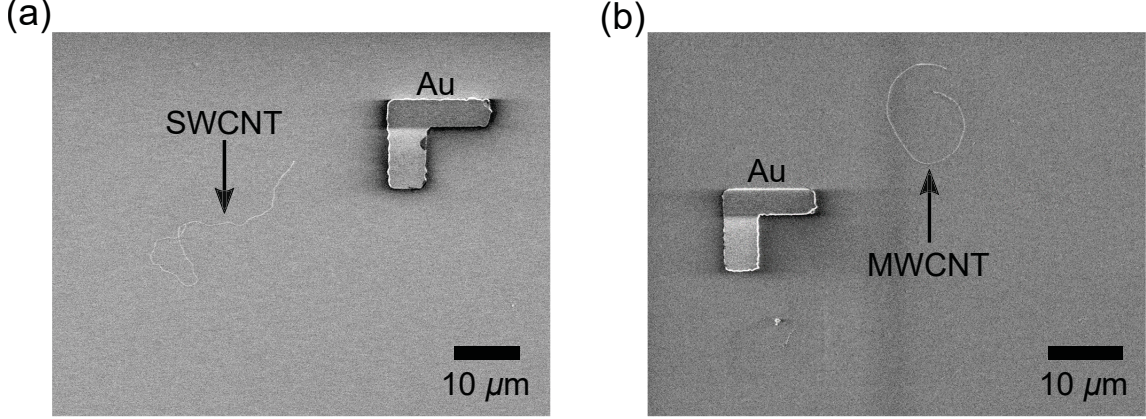


Figure 3.8: Locating carbon nanotubes using a SEM. (a) SEM image of a single-walled carbon nanotube next to a gold alignment mark. (b) SEM image of a multi-walled carbon nanotube next to a gold alignment mark.

them at low magnification ($700\times$) for as short a time as possible. We find that the ideal parameters for SEM imaging of SWCNTs are: accelerating voltage 1.0 keV, and current $10\ \mu\text{A}$, with working distance $\approx 6\ \text{mm}$. At this accelerating voltage the nanotubes are very easy to image; the nm-sized nanotubes appear to be microns in diameter due to charging effects [84]. We find that this method selectively images nanotubes with smaller band gaps $\lesssim 200\ \text{meV}$. For simplicity in transport measurements, we aim to study only single-walled carbon nanotubes. However, both single-walled and multi-walled carbon nanotubes are grown using this CVD approach. From experience, we have found that nanotubes with smaller ripples along their lengths tend to be single-walled. This is likely due to the lower structural rigidity of SWCNTs, compared to multi-walled carbon nanotubes (MWCNTs), leading to a smaller radius of curvature. We therefore limit our study to CNTs with very small ripples along their length. We capture high-quality SEM images of our candidate devices, ensuring that all four “L” shaped alignment marks are visible. This is necessary for the aligned deposition of metal electrodes on the nanotube (Fig. 3.12).

To ensure our addressed nanotubes are indeed single-walled, we perform AFM measurements. In Fig. 3.9(a)(b), we show AFM data from a SWCNT (diameter $1.0 \pm 0.5\ \text{nm}$) and MWCNT (diameter $7 \pm 1\ \text{nm}$). These are the same nanotubes as shown in Fig. 3.8(a) and (b) respectively. To capture high-quality images of our nanotubes, we use tapping mode AFM with a tip radius of $\approx 10\ \text{nm}$, ensuring the tips are clean through substrate imaging and perform ozone cleaning ($\approx 10\ \text{min}$) if necessary. We scan the AFM tip across a section of carbon nanotube, and measure its mean diameter. Van der Waals forces between the AFM tip and the nanotube can result in a reduced diameter measurement by up to $1\ \text{nm}$ [42, 85], and we

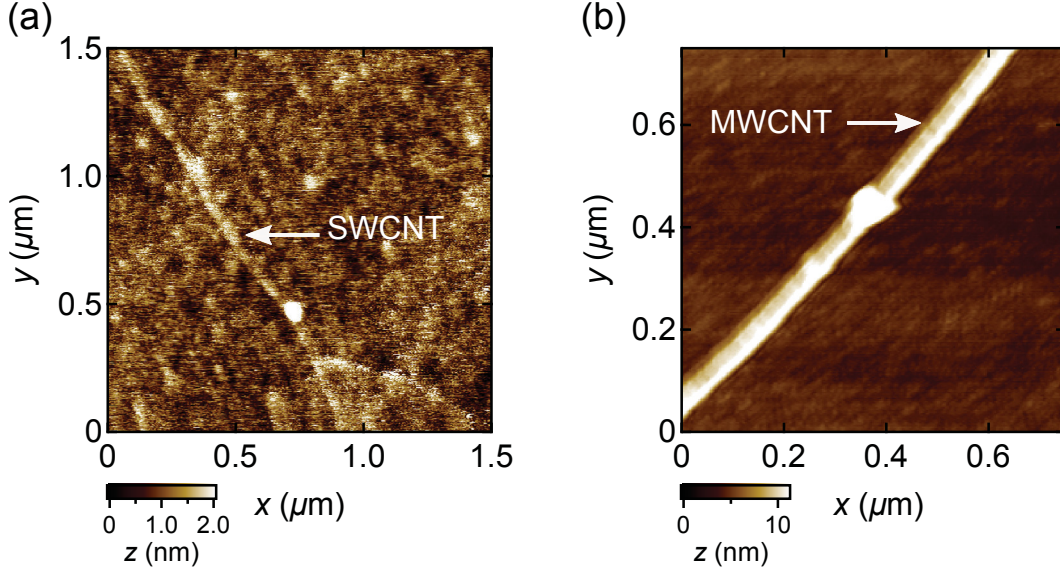


Figure 3.9: Determining CNT diameter using AFM. (a) AFM image of a single-walled carbon nanotube with measured diameter 1.0 ± 0.5 nm. (b) AFM image of a multi-walled carbon nanotube with measured diameter 7 ± 1 nm. These are the same nanotubes as shown in Fig. 3.8(a) and (b) respectively.

account for this in our calculations. We only use nanotubes with diameters $d \lesssim 2.0$ nm, as these are extremely likely to be single-walled [86]. As the remainder of the fabrication procedure for our suspended SWCNT devices is nearly the same as that for our suspended graphene devices, we will first show our procedures for the deposition and characterization of monolayer graphene.

3.2.3 Exfoliating, characterizing, and etching monolayer graphene

In this section, we discuss the procedure of depositing graphene flakes on our wafer substrates and then characterizing and etching them to shape. This is done through Scotch Tape exfoliation and optical imaging, followed by Raman spectroscopy to measure the number of graphene layers. The graphene is then shaped to the correct dimensions for studying strain-mediated transport using oxygen plasma RIE.

We use the Scotch Tape method for graphene exfoliation and deposition onto our Au-grid-covered thin chips, and then characterize the thickness of the flakes using Raman spectroscopy. This procedure is summarized in Fig. 3.10. We begin our deposition process with $\approx 2 \times 2$ mm flakes of high-quality Kish graphite, making them as thin as possible through cleaving using a razor blade, or by peeling off exterior layers using Scotch Tape. We take

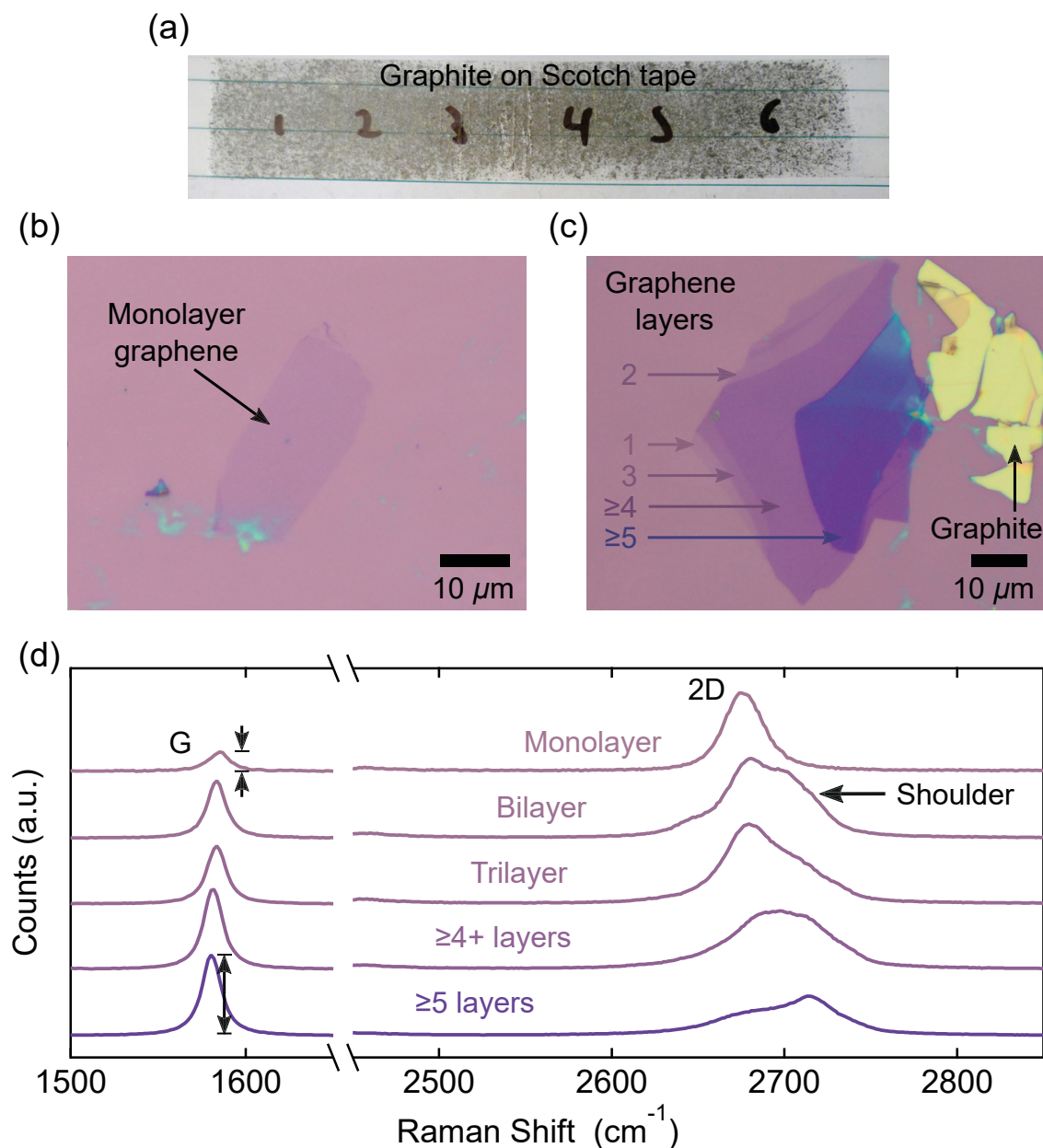


Figure 3.10: Graphene deposition and Raman spectroscopy. (a) Graphite-coated Scotch Tape, showing optimal flake density for large, sparse graphene deposition. The numbers indicate positions where graphene was deposited on six thin chips. (b) Optical image of a large monolayer graphene flake. (c) Optical image of exfoliated graphene/graphite of varying thickness. (d) Normalized and vertically offset Raman spectra for many thicknesses of graphene taken from the locations shown in panel (c), showing the evolution of the G and 2D peaks with number of layers. As the number of layers increases, the 2D peak broadens acquiring a shoulder (right, black arrow). The G peak becomes relatively larger as the number of layers increases (left, black arrows).

3–5 such thin flakes and place them in the middle of a 10×2 cm piece of Scotch Tape. The Scotch Tape is carefully folded and pressed 15 times, ensuring an even coating of graphite on the Scotch Tape, as shown in Fig. 3.10(a). A fresh piece of Scotch Tape with matching dimensions is then pressed against the original one 5 times, flipping 180° each time to remove excess graphite from the original tape. The original tape is then carefully pressed onto 4–8 of our thin silicon chips, and their positions numbered on the Scotch Tape, as shown in Fig. 3.10(a), and left to rest for 10 minutes. Van der Waals forces hold the graphene flakes on the SiO_2 substrate, and the Scotch Tape is carefully peeled off, leaving behind graphite and graphene flakes.

We use optical microscopy at a magnification of $50\times$ to locate monolayer candidates. We show in Fig. 3.10(b) that monolayer graphene is nearly transparent against the SiO_2 substrate and in 3.10(c), we show a graphene flake with many different layer thicknesses. Increasing the number of graphene layers causes the structure to become more opaque in optical imaging, going from light purple for monolayer graphene, to dark purple for few-layer graphene, and opaque yellow for graphite. We select monolayer graphene candidates based on transparency and colour. We capture high-quality optical images of our candidate devices, ensuring that all four “L” shaped alignment marks are visible. This is necessary for the aligned deposition of metal electrodes on monolayer graphene (Figs. 3.11 3.12).

To ensure that our deposited flakes are monolayer graphene, we study them using Raman spectroscopy. In Fig. 3.10(d), we show Raman data from the different thicknesses of the flake in Fig. 3.10(c). We collect the Raman spectrum at a single point on the graphene flake, using a 532 nm laser with $25 \mu\text{W}$ power and 50 second exposure time. The Raman spectra of single and multi-layer graphene are extremely well understood [87, 88] and the relevant Raman peaks for determining thickness are the so-called G and 2D peaks. The G peak occurs near 1582 cm^{-1} and comes from in-plane optical phonons. The 2D peak occurs near 2700 cm^{-1} , and arises from second order optical phonon processes. The 2D peak is composed of a single Lorentzian in monolayer graphene, but is composed of many offset Lorentzian peaks in multilayer graphene, as a result of inter-layer phonon coupling [87]. This provides two signatures for determining whether or not a graphene flake is monolayer. Qualitatively, monolayer samples have a single, well defined 2D peak, while bilayer or multilayer graphene samples tend to have 2D peaks with two maxima, or with a large shoulder, as indicated by the black arrow on the right of Fig. 3.10(d). In monolayer graphene, the 2D peak is larger than the G peak, while in many-layer graphene the G peak is much larger than the 2D peak, as indicated by the black arrows on the left of Fig. 3.10(d). Quantitatively, the expected

ratio of the integrated intensity $G/2D$ is ≈ 0.18 for monolayer graphene, while for bilayer graphene this ratio is closer to ≈ 0.32 , increasing for more layers. Thus, by investigating the Raman spectra we can qualitatively and quantitatively ensure that our graphene flakes are monolayer.

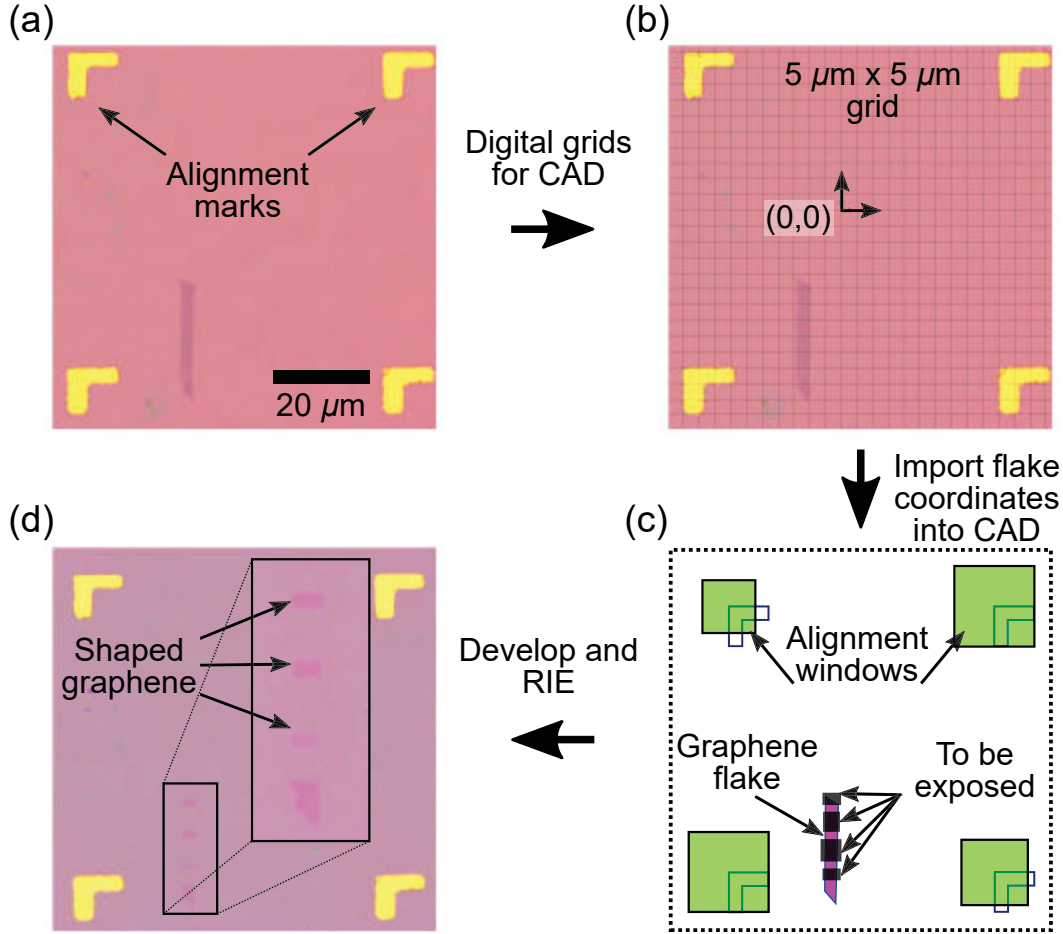


Figure 3.11: Etching graphene flakes for strained transport measurements. (a) Optical image of a bilayer graphene flake within an alignment grid pattern, digitally rotated and scaled for proper alignment and dimensions. (b) Digital grid ($5 \times 5 \mu\text{m}$), added to the image in (a), for determining the coordinates of the graphene flake. (c) CAD, drawn by importing the graphene flake coordinates from (b). This design will be exposed in the e-beam resist to create exposed sections of the flake and make graphene rectangles along the long axis of the chip. The windows in the corners are used to align the CAD to the flake during patterning. (d) Optical image of the shaped graphene flake in (a), after EBL exposure, development, and oxygen plasma.

For strained graphene measurements, we require that our metal films coat a large portion of the graphene flake to reduce contact resistance [89]. For reference, these devices will have an ideal final device length $L = 100 \text{ nm}$ following exposure of the contacts (see Fig. 3.12). We

also require flakes with a large aspect ratio $W \gg L$, to reduce the effects of the disordered graphene edges on transport [69]. Finally, as uniaxial strain is applied along the length of the $\approx 12 \times 5$ mm thin chips, we require these graphene flakes to be aligned with the chip orientation. As these conditions are rarely met naturally through deposition, we must etch our graphene flakes into the desired geometry. Our ideal flake geometry is ≈ 1 μm wide and 5–10 μm long, and aligned along the chip orientation. The process of etching the flakes to the desired geometry is shown in Fig. 3.11. To define our flake geometry, we use a method similar to photolithography called electron beam lithography (EBL), wherein an electrosensitive resist is used and patterned using an electron beam (e-beam) before development, in conjunction with oxygen plasma RIE.

We begin the EBL process by cleaning our chips with acetone and IPA, blowing them dry with N_2 gas, before spin coating with the e-beam resist. We coat the chips with PMMA A4 (polymethyl methacrylate 4% in anisole) and using a spin coater, spin at 3000 rpm for 1 minute to give a 200 nm layer of resist. We then bake the chips on a hot plate for 15 minutes at 170 $^\circ\text{C}$. After spinning, we investigate the graphene flakes using optical imaging to ensure that spinning has not shifted or removed the monolayers.

We next use computer aided design (CAD) to draw the e-beam patterns, which will be selectively exposed by the e-beam writer. We first use Olympus Analysis software to rotate and scale an optical image containing the four “L” marks and graphene flake, so that it is square, with 100 μm spacing between the “L”s. This is shown in Fig. 3.11(a) for a bilayer graphene flake. Defining the origin as the midpoint between the top-left corners of the four “L”s, we use the Olympus Analysis software to draw a 5×5 μm Cartesian grid over the image, as shown in Fig. 3.11(b). This gives us a properly rotated and scaled digital map to measure the points along the periphery of the graphene flakes. Importing these coordinates into the Raith e-Line Pro software, we define the sections of the graphene flake we wish to expose, as shown in Fig. 3.11(c). In addition to the exposure sections, the CAD design contains manual alignment windows, used to image the “L”s and properly align the CAD to the chip during patterning. From dose tests, we find that the ideal electron beam dose is ≈ 250 $\mu\text{C}/\text{cm}^2$.

Once our CAD is complete, the resist-covered samples are loaded in the e-beam writer. To achieve a high-quality exposure, we first adjust the stigmator and focus of the beam so that 10 nm contamination spots are clearly visible, and measure the beam current immediately before exposure. For high resolution patterning, we expose our samples using an aperture size of 10 μm (working current ≈ 20 –40 pA), working distance of 10 mm, acceleration voltage of

20 kV, and expose at a magnification of $700\times$ with a $142.9 \times 142.9 \mu\text{m}$ write-field size. After exposure, the samples are developed using MIBK (methyl isobutyl ketone). The exposed samples are swirled slowly (≈ 0.5 Hz) in a solution of 1:3 MIBK:IPA for 30 seconds to develop the resist, followed by methanol for 15 seconds to remove the developer, and finally placed in IPA for 30–60 seconds to remove the methanol. The chips are then dried with N_2 .

Next, we use oxygen plasma RIE to etch away the exposed graphene in the e-beam pattern as oxygen plasma removes organic, carbon-based materials. Since graphene is atomically thin, it is etched away much more quickly than the organic e-beam resist. We use RIE parameters: 19 SCCM O_2 at 200 mTorr and 150 W for 6 seconds. After RIE, we perform the standard lift-off procedure in acetone on a 60°C hot plate to remove any unwanted PMMA, leaving behind an ideally shaped monolayer graphene flake for strained transport measurements. There is one caveat to this etching method. Oxygen plasma creates extremely rough edges, and defects in the exposed graphene [90]. Because our final sample geometry satisfies the condition $W \gg L$, these edge effects will not affect the ballistic transport we aim to study [69]. However, edge defects weaken the structural integrity of the graphene sheet [51]. We found that many of our devices shaped using this method were ripped or damaged after suspension and wire bonding (see Section 3.2.4). It is possible that this tearing occurred as a result of edge defects from the oxygen plasma etching, but future study of this phenomenon is necessary to avoid this problem and ensure high device yields.

3.2.4 Contacting and suspending SWCNT and graphene devices

At this stage in the process, we have produced two types of samples: SWCNTs, located and measured by SEM/AFM (see Section 3.2.2), and monolayer graphene flakes, located and measured using optical microscopy and Raman spectroscopy (see Section 3.2.3). The next stage in our fabrication is to contact these samples with metal electrodes that we can access on a macroscopic level, and then suspend them for clean transport measurements in ultra-short SWCNTs, and strained transport measurements in graphene. In this section, we will detail the fabrication steps involved in this process.

The next fabrication step is to deposit aligned μm -scale electrodes on our SWCNT and graphene devices, which we accomplish using EBL. This process follows a similar procedure to the EBL steps used for etching the graphene flakes (Fig. 3.11). On the thick chips, we use a bilayer e-beam resist for easier lift-off, composed of 300 nm copolymer EL9 (9% in ethyl lactate) under 200 nm PMMA A4, while on the thin chips, we use a PMMA A4 monolayer resist for higher resolution patterning. For both e-beam resists, we spin at 3000 rpm for

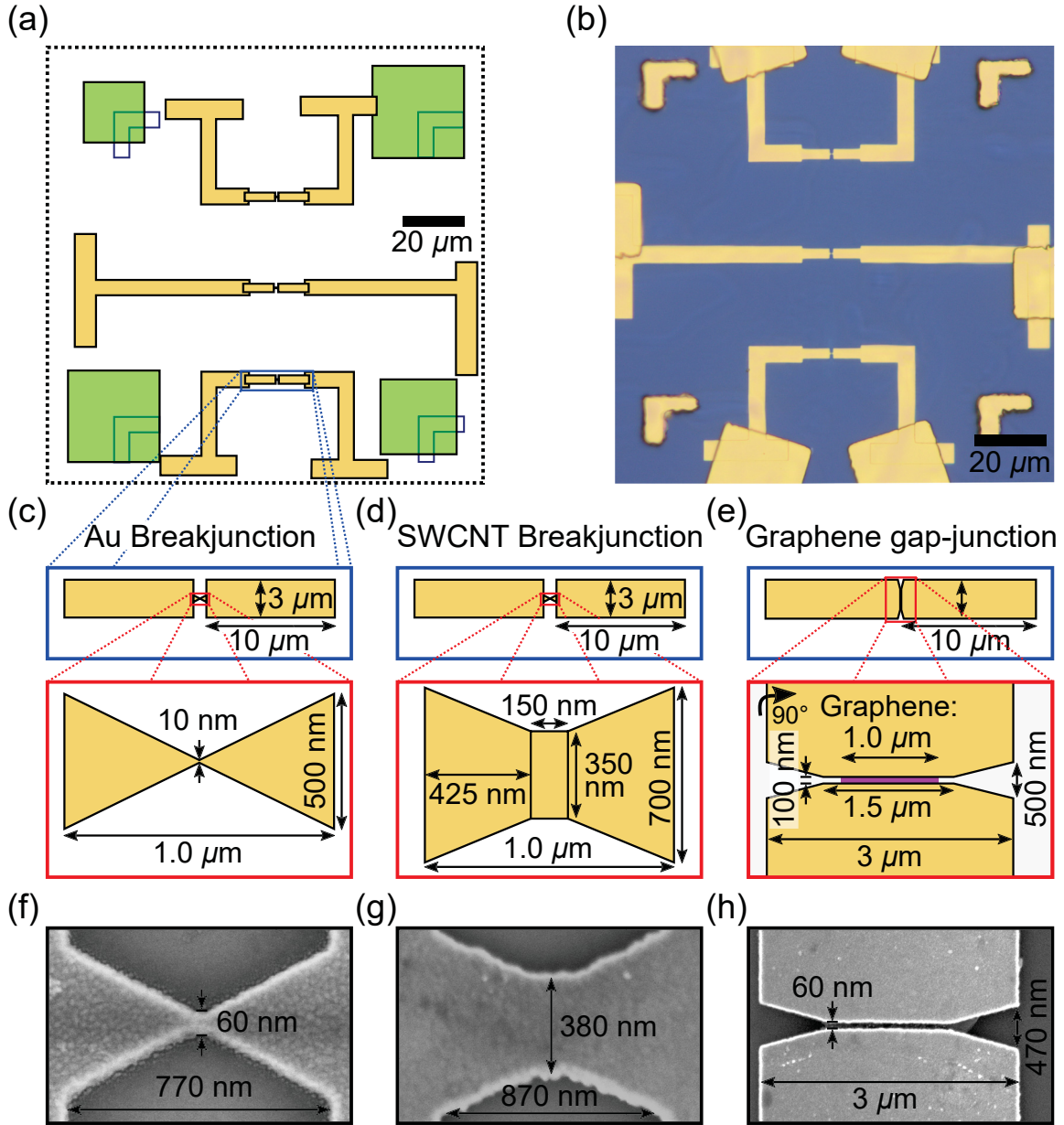


Figure 3.12: Contacting SWCNTs and graphene with Au electrodes using EBL. Full CAD image for three Au tunnel junction devices, showing six 10 μm -scale electrodes. (b) Optical image of the electrodes shown in (a) after exposure, development, evaporation of 80 nm Au, and lift-off. (c)–(d)–(e) Zoom-in on the middle of CAD designs for the 1 μm -scale and 100 nm-scale electrodes to form our Au and SWCNT bowtie-shaped junctions, and rectangular graphene gap-junctions respectively, with relevant dimensions. (f)–(g)–(h) SEM images of the three different device geometries corresponding to the CAD designs in (c)–(d)–(e). Actual dimensions differ slightly from the CAD due to proximity effects and purposeful overdosing of the e-beam pattern. Zoom-in of panel (e), and panel (h) rotated 90° for visibility.

1 minute and bake for 15 minutes at 170 °C. As before, we build a Cartesian map of our devices to draw our contacts in a CAD file. In general, larger-dosed exposures are required for smaller pattern shapes as the proximity effect is reduced. From dose tests, we find that the required doses for our exposure patterns range from $\approx 200\text{--}420\text{ }\mu\text{C}/\text{cm}^2$.

In Fig. 3.12, we show representative CAD design files for gold tunnel junctions (AuTJs) — which will be used for strain calibration of our QTSE set-up (Fig. 3.37)— SWCNT break junction devices, and graphene gap devices. In our designs, we ensure that the electrodes have good overlap with the devices, and avoid constrictions to reduce line resistance. In Fig. 3.12(a) we show the full device design for a AuTJ pattern, designed to match our 6-point photolithography pattern for macroscopic device contact (see Fig. 3.13). In Fig. 3.12(b), we show an optical image of this pattern after exposure, development, evaporation of 80 nm Au and lift-off, illustrating the high fidelity of the EBL process. Fig. 3.12(c)–(e) shows the CAD designs for the bowtie-shaped AuTJs and SWCNT break junctions, and rectangular graphene gap junctions respectively, with defined electrode dimensions at the μm and 100-nm scales. We note that our bowtie junctions fully house and protect the devices underneath them, and are used to create ultra-short devices for electromigration (Section 3.4), while the gap junctions are exposed and ready to measure immediately

After exposure and development of our electrode pattern, we deposit 40–120 nm of pure Au using thermal evaporation (Fig. 3.6), with thinner Au layers used for the break junctions for easier electromigration, and thicker Au layers used for the QTSE devices for contact rigidity. We emphasize that we use no sticking layer, to ensure pristine metal contact to the graphene or SWCNT. We perform lift-off in hot acetone as before. Fig. 3.12(f)–(h) shows SEM images of the exposed electrodes after lift-off for the cases in Fig. 3.12(c)–(e) respectively, showing actual device dimensions. These differ slightly from the CAD design dimensions as a result of proximity effects and purposeful overdosing to ensure total exposure. For break junction devices, we may investigate the quality and dimensions of the EBL exposure using a SEM, but in gap junctions we cannot SEM these devices as the electron beam collects carbon from volatile organic contaminants (fabrication residues) in the vacuum chamber and deposits them on the surface. To SEM image our gap junction devices, we expose a duplicate gap junction pattern elsewhere on the chip, and image this “dummy” pattern to infer EBL quality and dimensions of the real devices.

In break junction devices, we can rid the chips of excess resist residues and carbon from SEM imaging using an oxygen plasma RIE, as the Au electrodes protect the underlying device. We use 20 SCCM O_2 at 200 mTorr and 200 W for 3 minutes to clean the chips. This

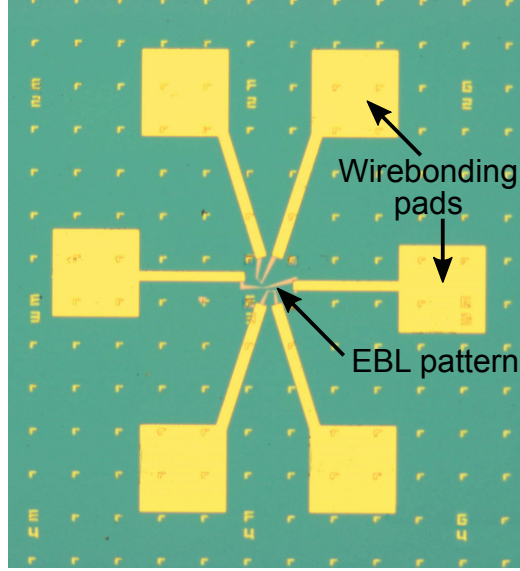


Figure 3.13: Contacting the EBL pattern with $100\ \mu\text{m}$ pads. Optical image of a 6-point photolithography pattern used to contact the small EBL pattern and provide large contacts for wire bonding.

step is not possible in the gap junctions, where it would etch away the SWCNT or graphene. From our $10\ \mu\text{m}$ -scale device electrodes, we now connect $100\ \mu\text{m}$ -scale contacts for wire bonding. The 6-point $100\ \mu\text{m}$ -scale electrode pattern is shown in Fig. 3.13, contacting the much smaller EBL pattern in the middle. We prepare these larger electrodes using photolithography with the same resist, exposure and development procedure as in Section 3.2.1. We optically align the 6-point electrode pattern on the photomask with the EBL pattern in the mask aligner. After exposure and development, we thermally evaporate a $3\ \text{nm}$ Cr sticking layer and $80\text{--}100\ \text{nm}$ Au, and perform lift-off in hot acetone.

With the large electrodes deposited, we now suspend our devices using a wet buffered oxide etch (BOE) to remove the supporting oxide beneath them. The gold films mask the oxide beneath them, protecting the wide contacts from collapsing, while the channel becomes suspended by the BOE. We first perform an additional RIE cleaning of the break junction chips to remove residue from the photoresist: $20\ \text{SCCM}\ \text{O}_2$ at $200\ \text{mTorr}$ and $200\ \text{W}$ for 3 minutes. At this point, we measure the oxide thickness using ellipsometry or reflectometry to calibrate our etch. If any excess water is present in our BOE solution, it can drastically alter the etch rate. As such, we bake all of our chips at $120\ ^\circ\text{C}$ for 5 minutes on a hotplate before the BOE. We use 49% HF in a 1:7 buffer solution with NH_4F . We find that the oxide etch rate is roughly linear at $70\ \text{nm}/\text{min}$ by ellipsometry and reflectometry measurements. To wet etch our samples, we place them in the BOE solution, ensuring there are no bubbles on

the chip which would prevent even etching. Once the etch is complete, we transfer the chips to three successive DI water baths to ensure that no acid remains, and leave the samples in the final bath. For SWCNTs on thick chips, we etch for approximately two minutes to a depth of ≈ 130 nm, to achieve complete suspension while leaving a thick layer of insulating oxide to reduce gate leakage (current flow through the insulating oxide layer). For the QTSE thin chips, we necessitate a long undercut u to generate large strains (see Eq. 3.1). We must therefore etch as much as possible while avoiding sample collapse and gate-leakage. We etch our graphene gap devices for approximately 3 min, removing ≈ 200 nm of oxide.

Because liquid surface tension during evaporation is strong enough to collapse our break junctions, we perform a step of critical point drying (CPD). The samples are transferred from the DI water bath to IPA. The samples are then loaded into the IPA-filled critical point drier. During the CPD process, liquid CO_2 displaces the IPA in the chamber. The temperature and pressure are modified so that the liquid CO_2 enters the critical phase, then the gaseous phase, circumventing the liquid-gas transition and preventing device collapse. At this point, we measure the oxide thickness with ellipsometry or reflectometry once more to determine the total oxide etch depth (t_0), and remaining oxide thickness (t_{ox}).

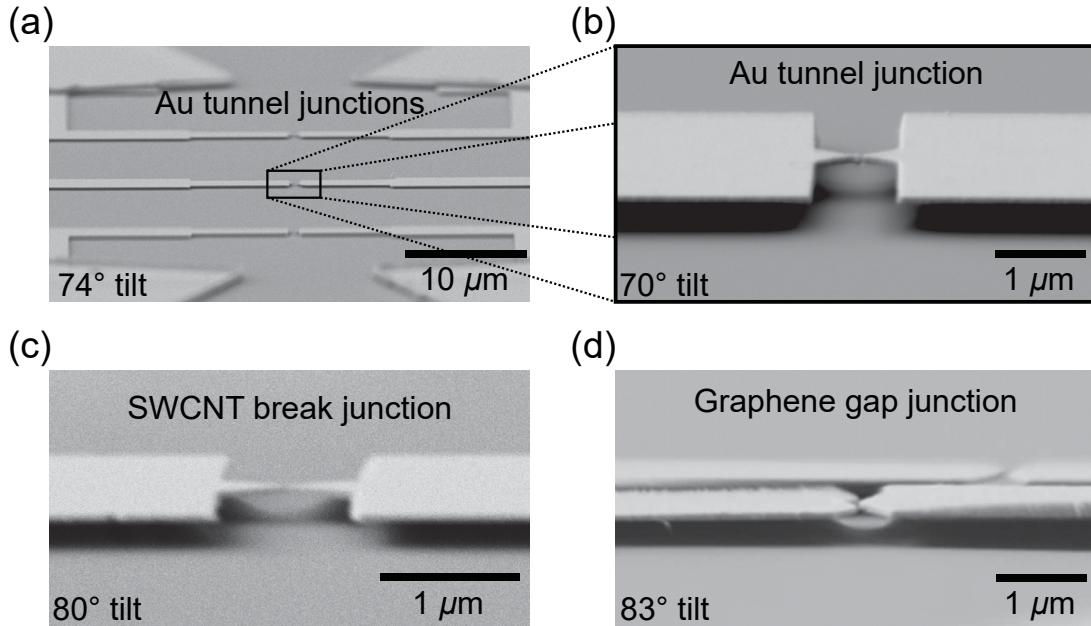


Figure 3.14: Suspended Au, SWCNT, and graphene devices. (a)–(b) Zoomed out and zoomed in tilted SEM images of suspended Au break junctions to be used for strain calibration. (b)–(c) Tilted SEM images of a SWCNT break junction and a graphene gap junction respectively, showing that these devices are fully suspended and not collapsed.

We now determine the quality of the suspension using tilted SEM imaging, obtaining

images such as those shown in Fig. 3.14. In the figure, we show example tilted SEM images of the AuTJs, SWCNT break junctions and graphene gap devices. The channels in the middle of the devices are clearly suspended based on the visible shadows in Fig. 3.14. For tilted imaging, the samples are carefully loaded on a 60° support stage inside of a SEM with a tilting stage. We image our break junction devices and “dummy” gap device structures at tilts of 75° – 83° , to ensure that they are indeed suspended and not collapsed. From tilted imaging, we can estimate the undercut length of our devices. For a 200 nm vertical etch, we generally find $u \approx 800$ – 1200 nm for our CAD patterns. At this point in the fabrication process, we have produced suspended gold break junctions housing SWCNT samples and graphene gap-junction devices like those shown in Fig. 3.2, achieving our goal geometry for strain-tunable carbon nanoelectronics. In the next section, we will discuss how we build our QTSE set-up for large and tunable uniaxial strains in these devices.

3.3 QTSE instrumentation strain-tunable low temperature transport measurements

We have constructed instrumentation for the application of extremely large and tunable strains ($\sim 10\%$) to nanoelectronic devices for low temperature transport measurements. In conjunction with our suspended device geometry (shown schematically in Fig. 3.1), this QTSE set-up can be used to tune our nanoelectronics systems and explore new physics. In this section we detail the design and construction challenges in building QTSE instrumentation. We first show how we incorporate our QTSE assembly with low temperature instrumentation. Next, we show the final fabrication steps to incorporate our suspended thin-chip samples into this geometry. Finally, we will briefly contrast these final preparations for our QTSE thin chips, to the thick chip set-up used previously to study transport in ultra-short SWCNTs.

3.3.1 QTSE assembly, construction, and integration with cryostat probe

For high-quality transport measurements, we require low temperature instrumentation and ultra-high vacuum (UHV) to reduce thermal fluctuations and keep devices free of disorder. To meet these criteria, we use an existing cryostat probe that we modified for mechanically tunable transport measurements. Here, we will briefly discuss the low-temperature, UHV

characteristics of the probe before showing our modifications for simultaneous mechanical actuation and electronic measurement. We will then show the QTSE used for bending our thin chips in detail.

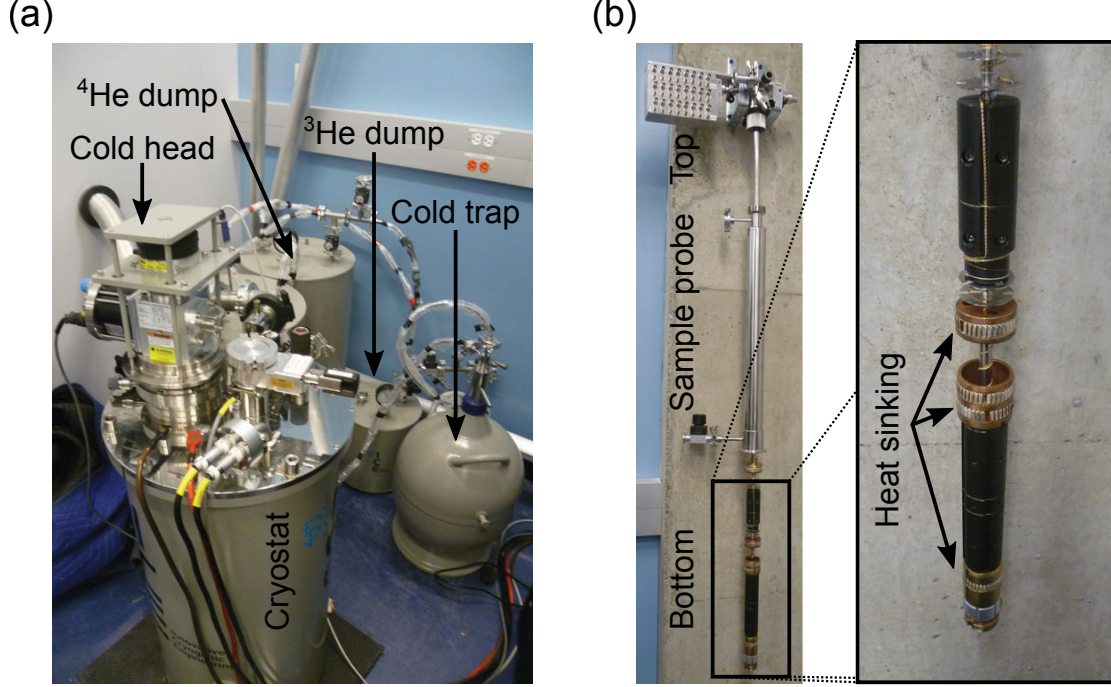


Figure 3.15: Cryostat for low temperature measurements. (a) Cryogen-free ^3He sorption cryostat, showing the cold head which cools the cryostat, and the ^4He and ^3He circuits used to reach $T = 0.3$ K (b) Cryostat probe. The mechanical actuation and electronic readout are accomplished at the top of the probe, while samples are loaded into the bottom, for low temperatures. We show a zoom-in on heat sinking “springy fingers” used to cool the sample probe inside the cryostat.

Low temperatures ($T < 4$ K) are required for high-quality measurements of low-energy quantum effects by eliminating thermal excitations and fluctuations. In Fig. 3.15(a)–(b), we show our cryostat and sample probe respectively, used for low temperature measurements. We use a ^3He cryogen-free sorption cryostat, capable of reaching temperatures down to 0.3 K. The principle of operation is as follows. The cold head expands compressed ^4He , cooling the cryostat. A second ^4He loop (cleaned through the liquid nitrogen cold trap) is cooled to liquid by proximity to the cold head inside the cryostat, and flows through a needle valve into the 1K pot, which is vacuum pumped to reach $T \approx 1.3$ K. The 1K pot condenses ^3He around the sample space inside the cryostat, which is pumped by a chemical sorption pump, cooling the sample space to $T = 0.3$ K. Inside the cryostat is a bipolar 9 T superconducting magnet, for study of magnetic field effects. The sample probe, shown in Fig. 3.15(b) consists

of control and readout instrumentation at the top, while the sample space lies in the bottom. When inserted into the cryostat, the heat sinking “springy fingers”, shown in the zoom-in of panel (b), make thermal contact to the cryostat, cooling the sample in the sample space.

We require ultra-high vacuum ($P \sim 10^{-7}$ Torr) inside the sample space to ensure clean, undoped transport in our devices. We show the vacuum sealing of the probe in Fig. 3.16. At the bottom of the probe, the sample space is kept under vacuum through a cone seal, consisting of precisely mating male and female tapered cone pieces, shown in Fig. 3.16(a). The male piece plugs the sample space, shown in Fig. 3.16(b), from the bottom, giving the assembled probe configuration shown in Fig. 3.16(c). An aluminum retainer nut holds the cone seal in place. The vacuum space runs from the sample space at the bottom of the probe along its length to the top of the probe, which is shown in Fig. 3.16(d). The vacuum space opens up inside the top of the probe, and an O-ring forms the top seal with a metal plate to cap it. An inlet and vacuum valve allow the pumping and sealing of the full vacuum space, applying UHV to the sample space.

The existing low temperature and UHV system in the cryostat provided limitations for our QTSE assembly design. When incorporating our QTSE instrumentation, we were careful not to disrupt the low temperature, UHV characteristics of the cryostat probe. We show the completely assembled QTSE cryostat probe in Fig. 3.17. The probe is controlled mechanically and electronically at the top, and remains well heat-sunk and leak proof down its length. Major changes were made to the wiring and construction of the sample holder and probe.

For strained transport measurements, we need to transmit mechanical turning motion as well as electric current down the length of the probe, to turn the push screw which bends the chip, and perform electronic measurements of our samples respectively. This requires non-trivial design and construction for compatibility with low temperature instrumentation. We show two QTSE designs to accomplish this in Fig. 3.18, with the original design in panel (a) and the modified design in panel (b). In the original design of the probe, a single rod provided heat sinking and mechanical stability to the wires, as well as carrying mechanical turning motion down the length of the probe. This design had two major flaws. Namely, extra slack in the wiring was necessary at the top and bottom of the probe to allow it to turn. With loose wires around the mechanically rotating parts, it was possible that the wiring could get caught and the insulation (or even the wires themselves) destroyed by mechanical motion. Secondly, this design required disassembly of the top and bottom of the probe every time a sample was loaded. An improved design is shown in Fig. 3.18(b). In this case, separate

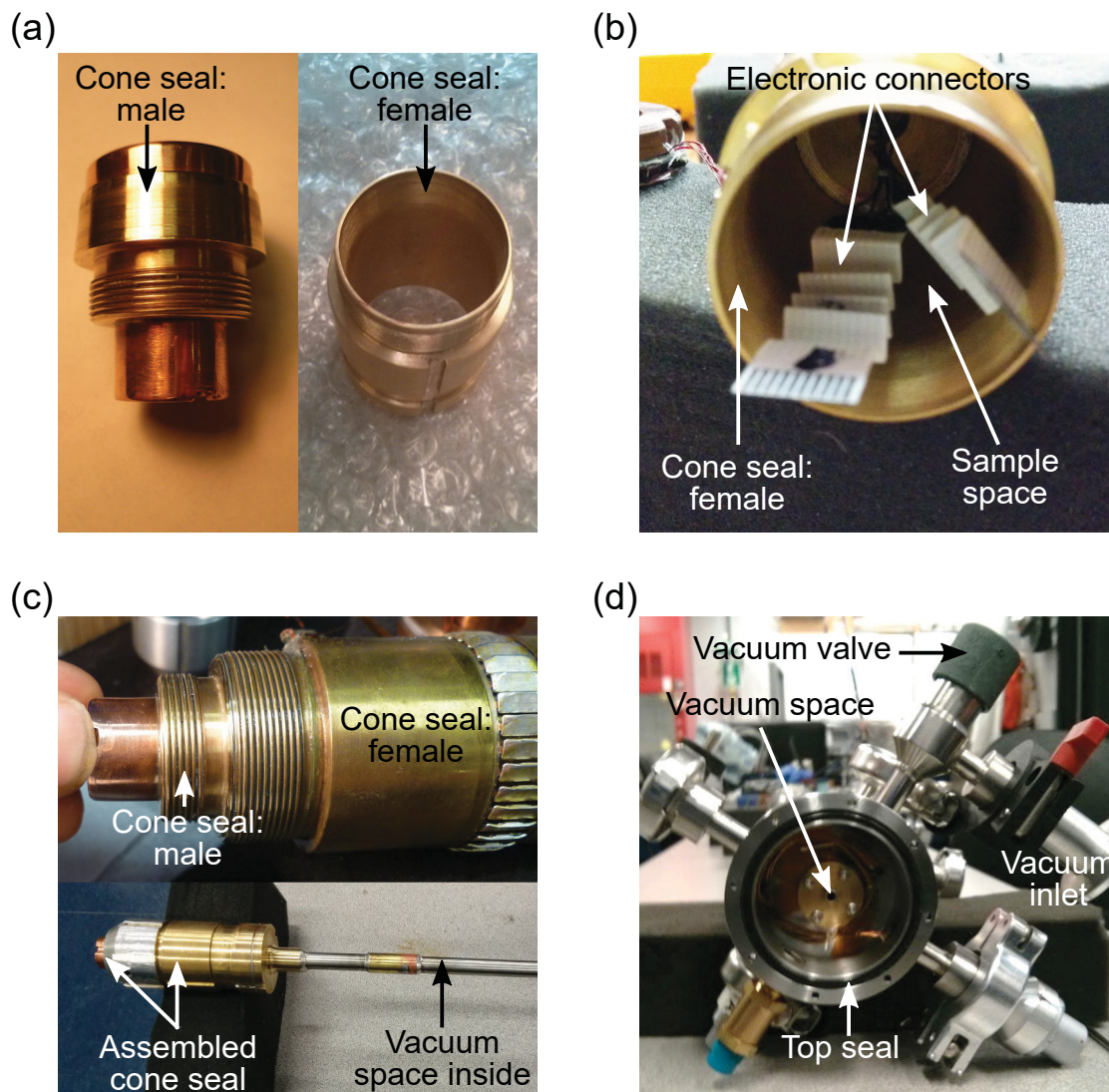


Figure 3.16: Ultra-high vacuum sample space. (a) Male and female parts of cone seal used to vacuum seal the sample space. (b) UHV sample space in the cryostat probe and female cone seal. Electronic connectors also shown. (c) The assembled cone seal, shown in detail (top) and with aluminum retainer nut for holding the cone seal in place (bottom). The vacuum space runs from the sealed sample space up to the top of the probe. (d) Opened top of the probe, showing O-ring top seal, the continuation of the vacuum space which runs the length of the probe, and the vacuum inlet and valve used for pumping.

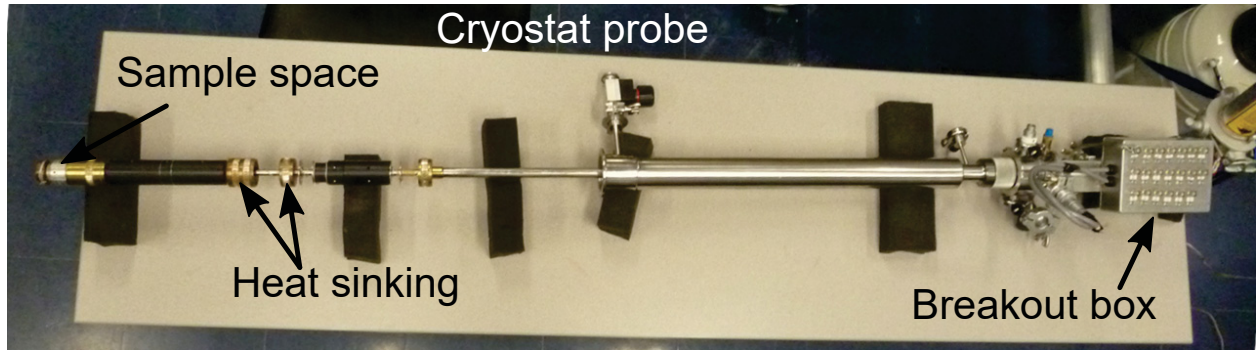


Figure 3.17: QTSE cryostat probe overview. The cryostat probe was modified for strained low temperature measurements. The probe is mechanically and electronically controlled from the top, at room temperature, while the sample itself is measured and strained inside the bottom of the probe at low temperature.

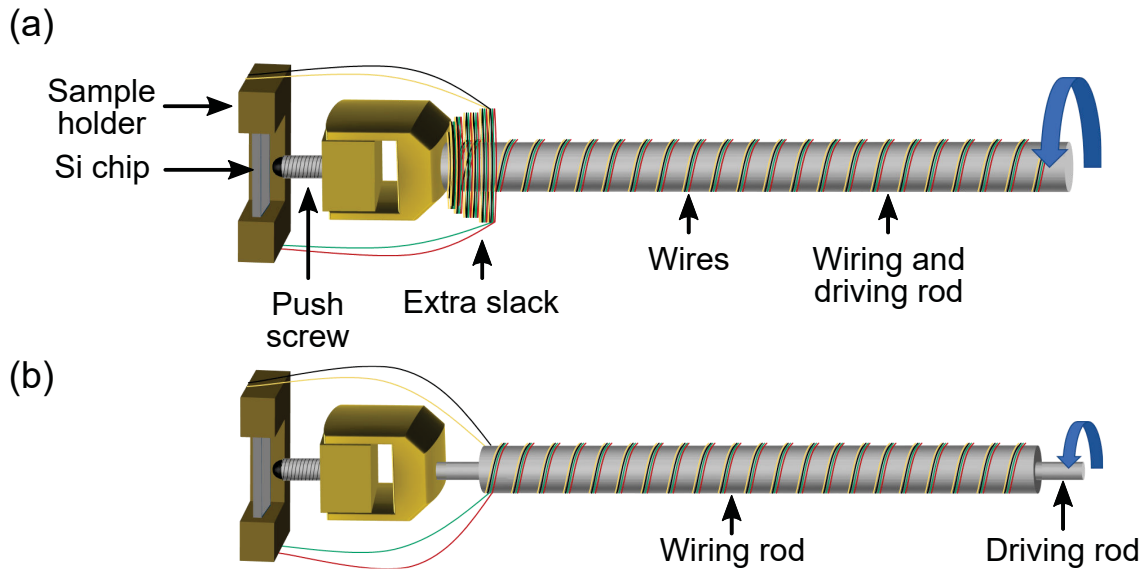


Figure 3.18: Original and modified probe designs for QTSE. (a) Original probe design: a single rod for both electronic and mechanical control involving excess slack in the wiring to allow rotational driving. (b) Modified probe design: separate rods for mechanical and electronic control, with static wiring rod and mechanically actuated driving rod.

coaxial rods carry the wiring and mechanical motion with the static wiring rod not requiring extra slack in the wires, and more efficient sample exchange from the bottom only. Through careful machining and rewiring, we constructed the QTSE probe with the second design, as detailed below.

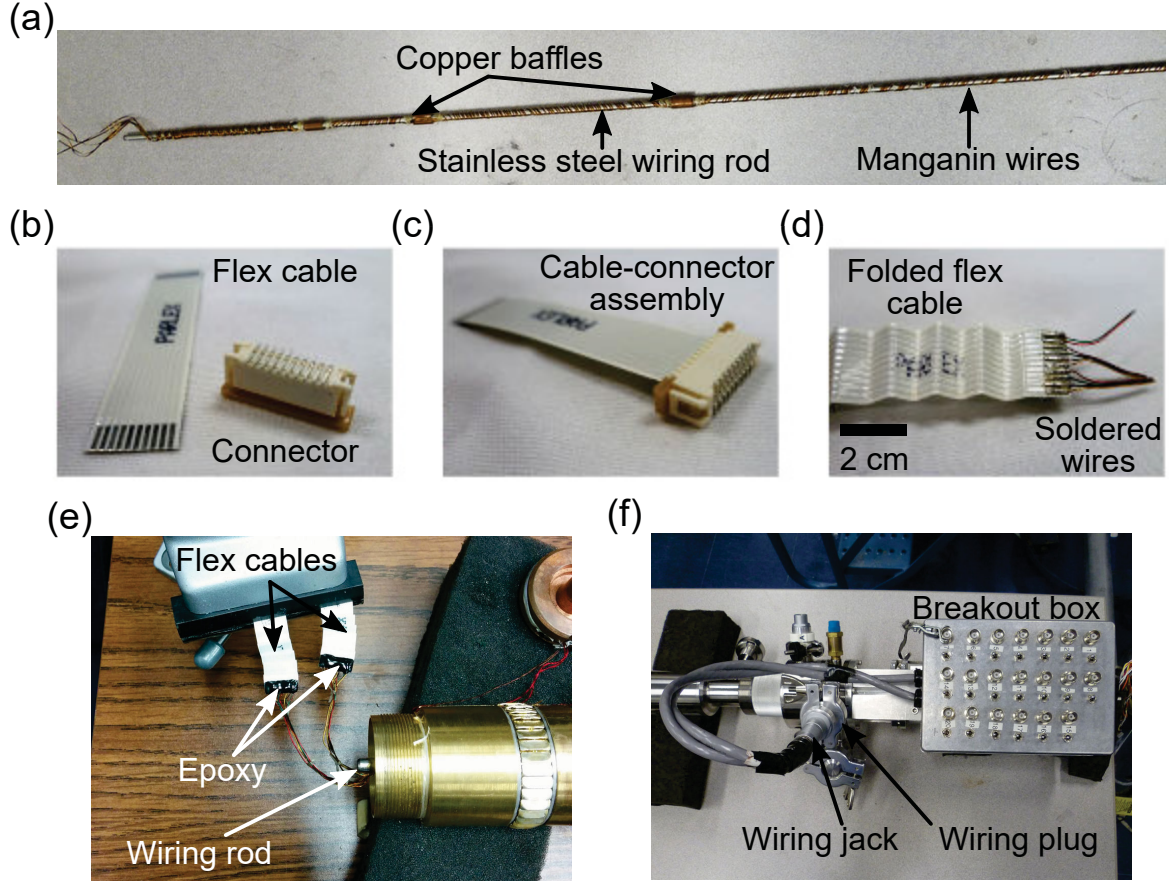


Figure 3.19: Probe wiring and electronic connections for our QTSE set-up. (a) Wiring inside sample probe, consisting of 20 Manganin wires on the wiring rod. Copper baffles are used for heat sinking. (b) Flat flex cable and flex cable connector. (c) Flex cable inserted into connector, mechanically locked using brown wing tabs. (d) Folded flex cable for spring effect, and soldered for electrical connection. (e) Flex cable connectors for contacting the sample, soldered to the internal wiring of the probe and epoxied for insulation and mechanical stability. (f) Breakout box mounting on sample probe for connecting our external measurement circuits to the devices inside through the wiring jack and plug.

The full wiring system of the QTSE probe is shown in Fig. 3.19. The wiring rod is shown in Fig. 3.19(a), with 20 Manganin wires running down its length. For the wiring rod, we used a hollow rod of stainless steel, which has poor heat conductivity, to reduce the heat load on the cryostat. For heat-sinking the wires, we used copper baffles on the lower end of the wiring tube. For electrical connection between the Manganin wires and the

sample, we needed robust, flexible, and detachable connections to survive the mechanical motion of the QTSE system, and allow the frequent changing of samples. To satisfy these requirements we used flex ribbon cables and connectors, shown separately and connected together in Fig. 3.19(b) and (c) respectively. These 10-pin flex cables and connectors have a locking mechanism (brown wing tabs) to ensure strong mechanical connections. As the flex cables remain connected to the wiring inside of the sample space, we required a system for their extension and retraction. We achieved this by “accordion folding” the flex cables into springs. In Fig. 3.19(d) we show an accordion folded flex cable, created by making four 13 mm long folds along the 51 mm long flex cables. Fig. 3.19(d) also shows Manganin wires soldered to the flex cables. This procedure was used to make connections from the wiring rod to the flex cables, with great care so as not to melt the plastic insulation of the flex cables. In Fig. 3.19(e), we show the electrical connections at the bottom of our probe. We partially removed the wiring rod for access to the bottom of the 20 Manganin wires which run along its length. After soldering these to the folded flex cables, we put Stycast, a black two-part insulating epoxy, over the solder connections for insulation, protection and mechanical stability. In Fig. 3.19(f), we show the electronic connections at the top of the probe. The Manganin wires at the top of the wiring rod were soldered to 20 pins in a vacuum sealed plug. We constructed a 20-pin BNC (Bayonet Neill-Concelman) connector breakout box which connects to the wires in the plug through a jack, making BNC connections to the flex cables at the bottom of the probe. Each BNC connection on the breakout box is connected to a switch, allowing the connections at the bottom of the probe to be “hot” (connected to the BNC connectors), or grounded. This allows us to protect samples from unwanted electrical discharge while they are not being measured. With the static wiring connections between the BNC breakout box and the flex cables, along the length of our hollow wiring rod, we have built a working electronics system for the QTSE set-up and now shift focus to the mechanics.

The system for driving mechanical motion in our QTSE instrumentation is shown in Fig. 3.20. A stepper motor is controlled through a driver by custom written CVI (C virtual instrumentation) software. The top of the QTSE probe, showing the motor assembly, is shown in Fig. 3.20(a). The stepper motor scaffolding was attached to the top of the probe, supporting the breakout box and motor assembly. The motor is controlled through an RS-232 connection and is attached to a 100:1 gearbox for fine control of rotational motion. The motor drives a small rod which passes through a rotational sealed vacuum feedthrough, passing rotational motion into the probe while preserving its vacuum seal. The motor motion

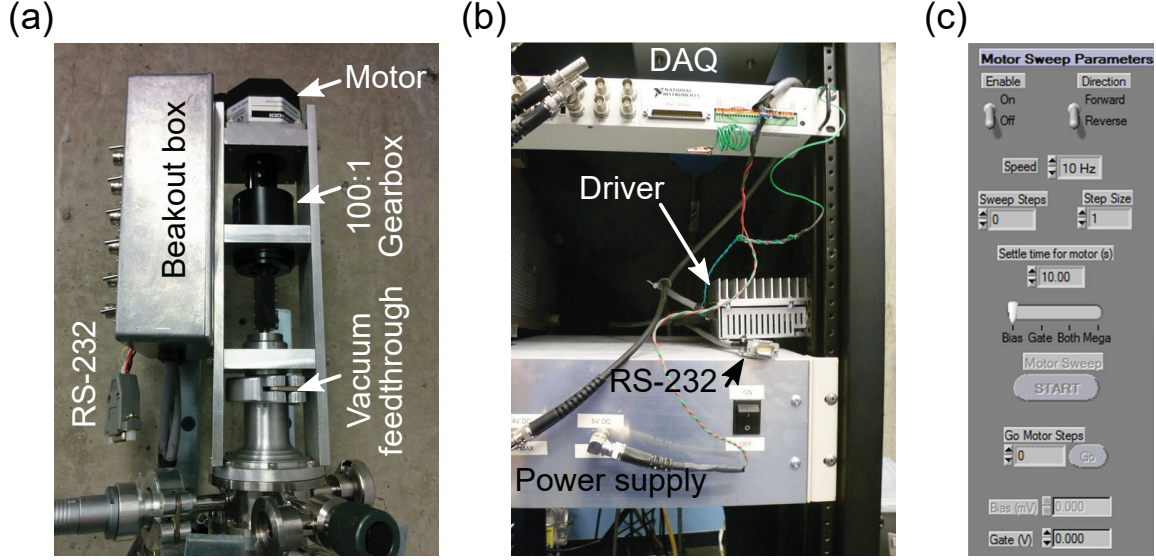


Figure 3.20: Mechanical motion control of our QTSE set-up. (a) Two-way stepper motor and 100:1 gear box for extremely fine motor control with support scaffolding and RS-232 connector. (b) Power supply and driver for stepper motor, controlled by the DAQ with RS-232 connector output. (c) Custom-built software interface for automated control of the mechanical turning of the motor.

control set-up is shown in Fig. 3.20(b). This consists of 24 V and 5 V power supplies for the motor and driver. Mechanical motion is programmed by PC (personal computer) through the data acquisition (DAQ) hardware with RS-232 output to connect directly to the motor. We show the relevant part of our motor control user interface in Fig. 3.20(c), written in CVI for automated measurement and motor control. Here, we have programmed controls for the stepper motor and measurement sweep parameters. From top to bottom, the controls allow the motor to be turned on or off, set the direction of rotation, set the speed of rotation, and set a settle time for the motor between sweeps. This panel provides control to perform various gate and bias sweeps while measuring current, at incrementally increasing motor positions, allowing transport measurements integrated with tunable automated motion of the motor.

Once full motor control was established, we needed to translate this mechanical motion down the cryostat probe into the sample space. We show how this was accomplished in Fig. 3.21. In the inset of Fig. 3.21(a), we show the machined brass connector which attaches the vacuum feedthrough rod (controlled by the motor) to the driving rod, which sits inside the wiring rod, as shown in the main panel. The driving rod is free to rotate inside of the wiring rod and, as shown in Fig. 3.21(b), is connected to a brass driving fork at the bottom of the probe. The custom-built driving fork was designed to fit the sample space and apply

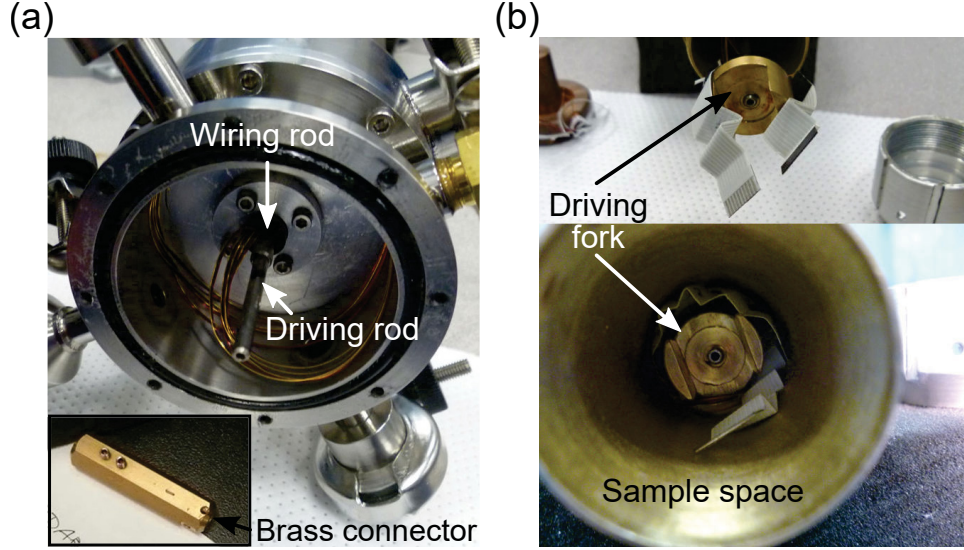


Figure 3.21: Mechanical motion transfer from probe top to bottom. (a) View from the top of the probe, showing the driving rod, passing through the wiring rod down to bottom of the stick. The inset shows the brass connector for clamping the motor rod to the driving rod. (b) A driving fork at the bottom of the mechanical rod is used to apply torque. The driving fork is pictured here, pushed out of the probe for visibility (top), and sitting in its normal position inside the sample space (bottom).

torque to the push screw (see Fig. 3.22). In the top of Fig. 3.21(b), we show the driving fork pulled outside of the sample space for better visibility. In the bottom of the figure, we show the driving fork in its normal position inside the sample space. The folded flex cables lie on either side of the rotating fork.

The driving rod is used to turn the push screw which bends our suspended thin chips in the QTSE set-up. We show the push screw in Fig. 3.22. To build the push screw assembly, we began with a precision 100 threads-per-inch (TPI) stainless steel screw from Thorlabs, shown in Fig. 3.22(a). A ball bearing is inset into the screw tip to form a spherical pushing surface. For each turn of the screw, the tip of the screw advances $254 \mu\text{m}$. We epoxied this screw into a brass block using Stycast, as shown in Fig. 3.22(b). This fork block was machined to fit snugly into the driving fork (Fig. 3.24(b)) to avoid any wobble in the screw motion. To avoid electrical contact between the metal screw tip and the Si back gate of our chips, we coated the ball bearing with Stycast insulating epoxy. To ensure a smooth and even coating of the epoxy, we outgassed the epoxy in a vacuum chamber after thoroughly mixing. A drop of the smooth epoxy was placed on the tip of the ball bearing, and the entire fork block assembly spun at 3000 rpm for 35 seconds on the spin coater before leaving the epoxy to dry. We show the smooth epoxied tip in greater detail in Fig. 3.22(c). The tip of

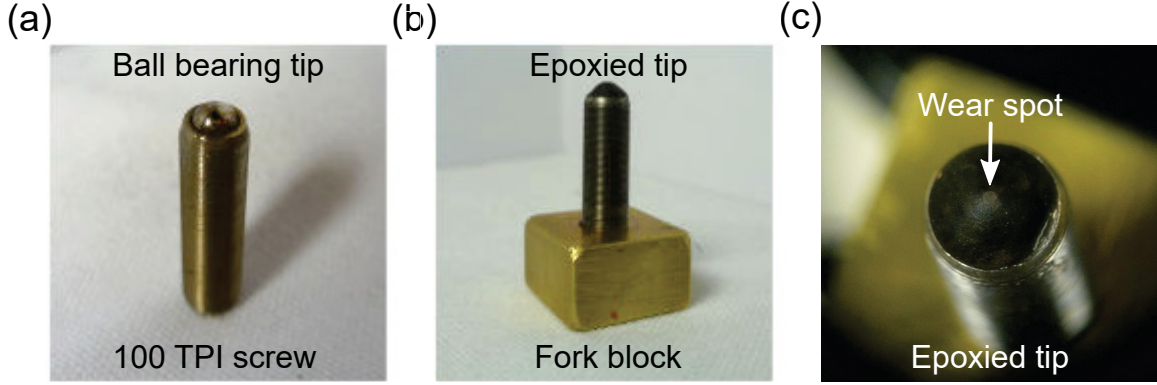


Figure 3.22: QTSE push screw for bending the thin chips. (a) 100 threads-per-inch push screw with ball bearing tip. (b) The same push screw from (a), epoxied into the brass fork block and with Stycast epoxy on the tip for electrical insulation. (c) Close-up view of the epoxied screw tip, showing its smoothness. After several rounds of pushing motion, a spot on the tip of the screw is worn down.

the epoxy is flattened into a wear spot from repeated rotational friction against the backs of our thin chips.

We have shown how we transferred electronic signals and mechanical motion from the top of our cryostat probe to the bottom. We now discuss how we connected these to our samples. The final major piece of the QTSE set-up is the sample holder, which holds the thin chips inside of the sample space, provides mechanical clamping for the chip bending, and makes electrical connections between the sample and the probe wiring. The sample holder geometry and construction are shown in Fig. 3.23. Panels (a) and (b) show front and back views of the “U” shaped sample holder, custom machined from phenolic resin. We designed this shape to allow the push screw to make unobstructed contact to the back of the Si chip. Here, the inner distance of the “U”, D , is extremely important for the application of strain, as can be seen from Eq. 3.1. For our sample holders, we designed this distance to be $D = 8.18$ mm, to provide reasonable spacing for the 5×5 mm Au grid pattern, and fit easily inside the sample space. We designed a slit in the “U” holder for the insertion of Si chips, and vertical screw holes to allow chips to be clamped in place. We tapped screw holes in the back of the holder as well, for rigid attachment to the QTSE scaffolding in the sample space. Flex cable connectors were epoxied onto the sides of the sample holder using Stycast, as shown in Fig. 3.23(c). We made sure to epoxy these connectors as level as possible for wire bonding. In Fig. 3.23(d), we show the complete sample holder with a loaded, device-containing Si chip.

With all of the electronic and mechanical pieces of the QTSE in place, we now show

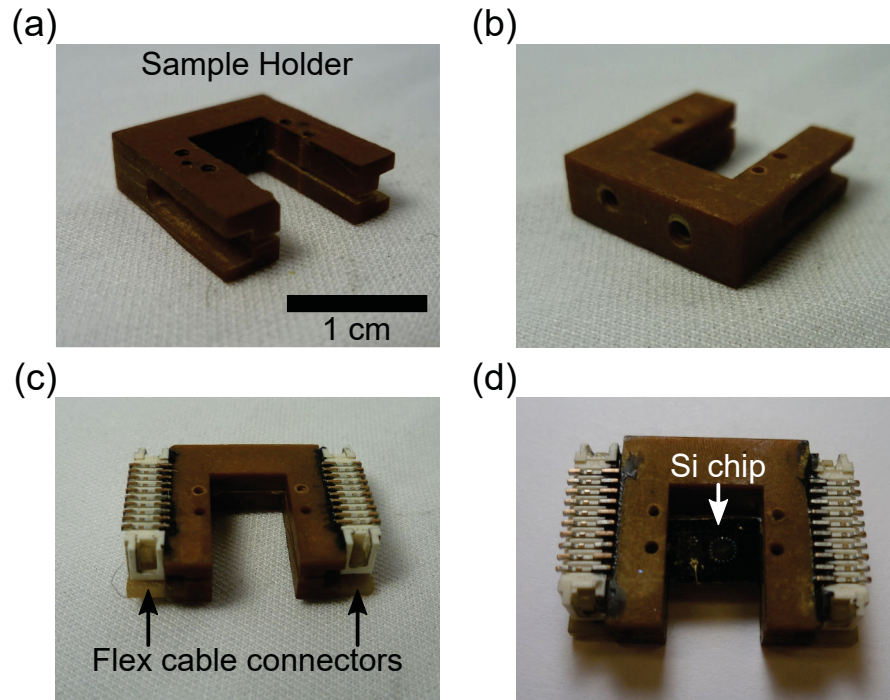


Figure 3.23: Sample holder for our QTSE set-up. (a)–(b) Front and back view of phenolic sample holder base, showing the slit for chip insertion and screw holes for clamping. (c) Sample holder with epoxied flex cable for connection to the sample probe wiring. (d) Sample holder containing a Si chip with devices, showing how the thin chip sits in the QTSE sample holder.

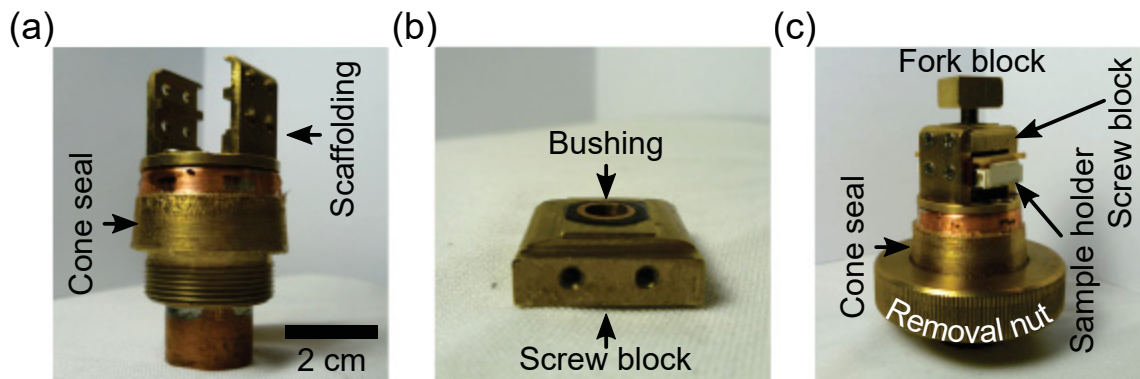


Figure 3.24: QTSE set-up assembly in sample space. (a) Cone seal with scaffolding. (b) Screw block with epoxied bushing. (c) Fully assembled QTSE assembly with screw block, fork block, and sample holder in the scaffolding on the cone seal. Large brass nut for removing cone seal from the probe.

how they come together inside the sample space for strained transport measurements. Rigid clamping of all of the pieces is crucial here, as μm -scale wobble of the screw or sample can lead to significant uncertainty in our measurements. In Fig. 3.24(a), we show the cone seal with QTSE scaffolding rigidly screwed on top. We must preserve the cone seal structure to maintain UHV inside the sample chamber. The brass scaffolding was custom machined with slits and screw holes for the retention of the sample holder and screw block. The screw block is shown in Fig. 3.24(b). It is composed of a smooth brass piece with threaded holes for clamping on either side. In the middle of the screw block, we epoxied a Thorlabs 100 TPI threaded phosphor bronze bushing to perfectly match the push screw to prevent wobbling. We show the full QTSE assembly in Fig. 3.24(c). The sample holder and fork block are held into the QTSE scaffolding by screws, and the push screw is threaded into the screw block. The large brass removal nut included in the image is for removing the male cone seal out of the female socket.

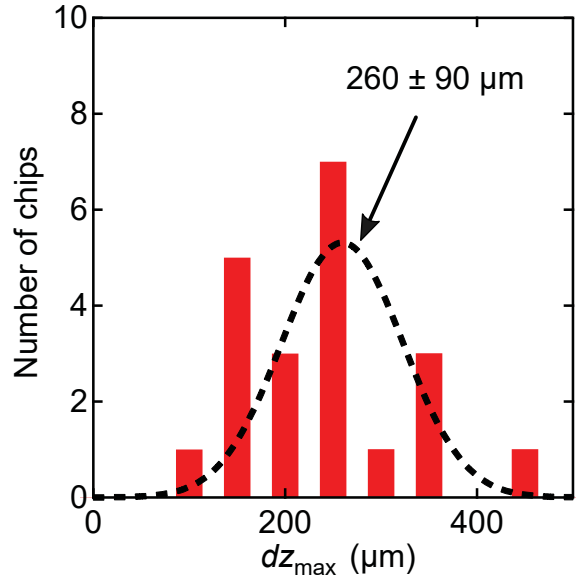


Figure 3.25: Maximum bending of Si chips in the QTSE set-up. Histogram showing maximum applicable screw displacement before breaking the chip at room temperature.

With the QTSE system fully constructed, we tested the chip-bending capabilities of this assembly. It is important to know the maximum allowed pushing distance of the screw, dz_{max} to predict the uniaxial strain applicable by our QTSE set-up, as can be seen from Eq. 3.1. This maximum displacement is reached when the push screw builds enough stress in the Si chip that it shatters. Using the complete QTSE assembly, we repeatedly loaded blank thin chips, and turned the push screw manually until the breaking point. In Fig. 3.25, we show a histogram of dz_{max} for breaking 21 thin chips at room temperature. We find

$dz_{\max} = 260 \pm 90 \text{ } \mu\text{m}$ for our QTSE set-up. The wide error margin shows that dz_{\max} is heavily chip dependent; any defects in the chip will nucleate cracks for smaller dz , causing the chip to shatter.

Using Eq. 3.1, along with the QTSE geometry and fabrication details discussed above, we calculate the theoretical mechanical strain applicable by our set-up. We summarize these parameters: $D = 8.18 \text{ mm}$ is the clamping distance set by the sample holder geometry (Fig. 3.23), $t \approx 200 \text{ } \mu\text{m}$ is the thickness of the chip (Fig. 3.3), $u \approx 1 \text{ } \mu\text{m}$ is the length of the suspended part of the device including the metal films (Fig. 3.14), and $dz_{\max} = 260$ is the maximum vertical displacement of the push screw, as determined above. Using Eq. 3.1, this gives a lateral stretching of $dx = 2.3 \pm 0.9 \text{ nm}$, and a displacement ratio $\approx dx/dz = 9 \times 10^{-6}$. Using achievable device lengths for electromigrated break junctions ($L = 10\text{--}100 \text{ nm}$, see Section 3.4), this corresponds to extremely large mechanical strains $\epsilon_{\text{mech}} \approx 2\text{--}20\%$, nearly reaching the deformation limit of graphene ($\sim 20\%$) [1]. Experimentally, Eq. 3.1 often overestimates the applied strain by roughly a factor of two [79]. Even accounting for this, strains of $\approx 1\text{--}10\%$ are still extremely significant compared to the $< 1\%$ strains achieved using other methods [51, 52, 82]. With these large and tunable strains readily attainable in our QTSE set-up, we have produced an ideal system for the testing and measuring of carbon quantum electromechanical devices. We now turn to completing the device fabrication for our thin chip devices, and integrating this with our QTSE instrumentation.

3.3.2 Integrating thin-chip suspended devices with QTSE instrumentation

From the completed QTSE instrumentation, we know the physical limitations and requirements for low temperature strained transport measurements on thin chip devices. In this section we discuss the last stages of our sample fabrication for thin chips, detailing the gating, wire bonding and loading of these thin chips for integration with the QTSE sample probe.

Because we need to push on the backside of our chips to bend them, the chips themselves must be suspended in the sample holder. This leads to challenges in gating our devices. We show our QTSE gating process in Fig. 3.26, in which we connect the Si global back gate on the backside of the chip, to the front of the chip for wire bonding (Fig. 3.27). To gate our samples, we expose an empty 6-point pattern (no EBL pattern inside) near the edge of the chip during photolithography of big pads for the real devices (see Fig. 3.13), performing evaporation and lift-off along with them. We thoroughly mix a two-part conductive epoxy (EPO-TEK H20E), and carefully apply it to the middle of the empty 6-point pattern using

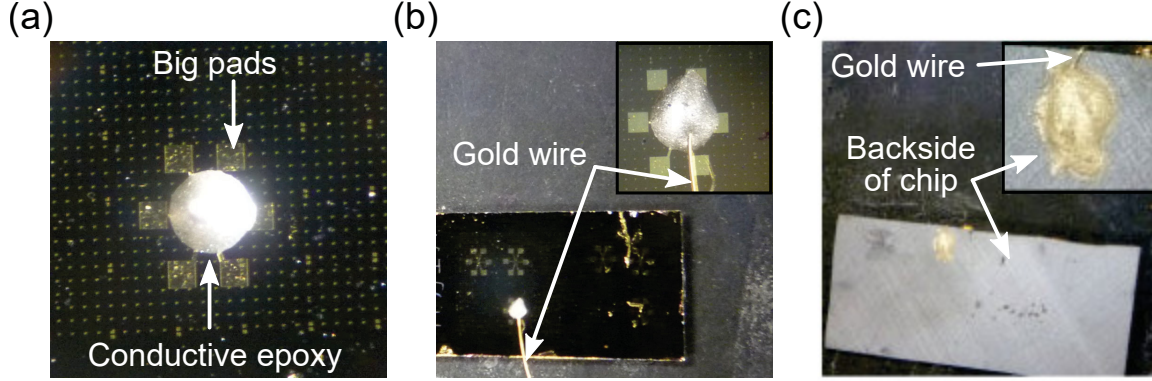
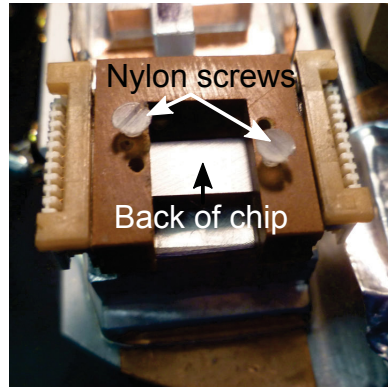


Figure 3.26: Gating our suspended thin chips for QTSE measurements. (a) A drop of conductive epoxy on a blank 6-point pattern, shorting the pads together while leaving space for wire bonding. (b) Gold wire inserted into the drop of conductive epoxy for connecting to the backside of the chip. The inset shows a zoom-in of gold wire in epoxy. (c) Backside connection from gold wire to Si back gate. The inset shows a zoom-in of epoxy on backside of chip.

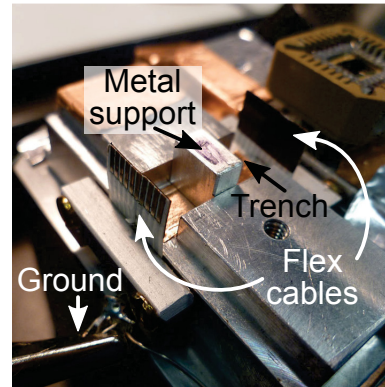
a wooden applicator. The result is shown in Fig. 3.26(a). The epoxy shorts together the six contact pads, while leaving them exposed for wire bonding later (Fig. 3.27). We next insert a gold wire (20 μm diameter) into the epoxy droplet as shown in Fig. 3.26(b), zoom-in of the epoxy droplet shown in the inset. The chip is then placed on a hot plate at 100 $^{\circ}\text{C}$ for 10 minutes to cure the epoxy. Once the epoxy is dry and the Au wire is mechanically and electronically connected to the topside of the device, we epoxy this wire to the backside of the chip to connect it to the gate, as shown in Fig. 3.26(c), zoom-in of the epoxy spot shown in the inset. To accomplish this, we flip the chip upside down, the devices are protected by the raised bump of epoxy on the front side. The free end of the gold wire is epoxied onto the backside of the chip, using the same epoxy, connecting the Si global back gate to the empty 6-point pattern on the front of the chip and allowing us to gate our sample. It is imperative that we use as little epoxy as possible during this process so that we do not change the uniform structure of our thin chips for predictable bending motion. In addition, the positioning of this epoxy on the backside is crucial. It should be far from the middle of the chip to avoid getting in the way of the point-of-contact for the push screw which will bend the chip, but not so far that it interferes with the clamping of the chip at the edges of the sample holder.

Once our chip has been gated, we carefully insert it into our sample holder (Fig. 3.23). The thin chips are manipulated using carbon-tipped tweezers so as not to scratch them. The chip must be inserted with the samples as close to the middle of the “U” shape as possible,

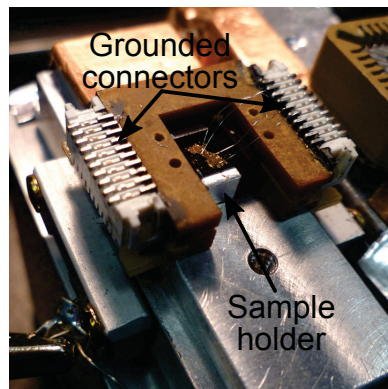
(a)



(b)



(c)



(d)

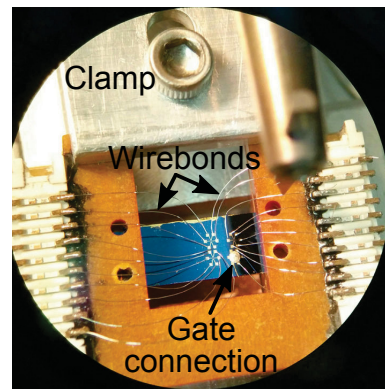


Figure 3.27: Wire bonding the sample holder to thin chip devices. (a) Old chip clamping system: nylon screws push on the back of the chip, clamping it for bonding. (b) New chip clamping system: a moveable metal support block braces the chip in the sample holder against the wire bonding jig. The support block sits in a trench, with grounded flex cables on either side to connect to the sample holder. (c) Sample holder loaded onto the grounded connectors a metal support block, showing wire bonds to thin Si chip coated with gold. (d) Close-up view of a real wire bonded sample with 20 wire bonds and gate connection through the conductive epoxy.

and keeping the samples parallel to the strain axis (perpendicular to the arms of the “U”), all while positioning the chip away from the outer edges of the sample holder, and positioning the epoxy away from the inner edges and center of the sample holder. This will ensure that strain is applied uniformly along the correct direction, and that non-uniform stress is not applied to the sample by the edges, or the conductive epoxy bump. Once we have achieved the proper positioning of the chip, we must hold it in place for wire bonding. This is shown in Fig. 3.27. We originally used two to four small nylon screws to clamp the chip to the sample holder from the underside, as shown in Fig. 3.27(a). Over the fabrication of many samples, we discovered that this method sometimes resulted in chip breakage due to non-uniform rigid clamping and pressing with the bonder tip. In addition, we noticed static build-up in the nylon screws which is dangerous for our extremely sensitive devices. We show our new clamping design and wire bonding jig which resolved these issues in Fig. 3.27(b). A small grounded, aluminum metal support block was machined to fit the sample holder and wire bonding jig. This was placed in a trench in the bonding jig to support the suspended chip and allow easy displacement. This small block is moveable and can accommodate different chip and epoxy positions in the jig. For wire bonding, it is important that the chip carrier pins be grounded at all times to protect the samples from electrostatic discharge. We position two fully grounded flex cables on either side of a trench to allow dual contacting of the flex cable connectors on the sample holder (Fig.3.23).

In Fig. 3.27(c), we show the sample holder, loaded into the wire bonding jig. For high-quality wire bonding, we use clamps to keep the sample holder in place. In Fig. 3.27(d), we show the clamped sample holder with wire bonds contacting the 6-point patterns as well as the epoxied gate connection to the backside of the chip. To ensure strong bonds, we lightly roughen the flex cable connector pins using 600 grit sandpaper before bonding. For wire bonding, we use a Westbond 7400A wedge bonder. As the wire bonds act as antennae to the sample, we must be very careful about static discharge, and the user and tweezers must both remain grounded at all times. We bond aluminum wires (diameter $25\ \mu\text{m}$) from the pins on the chip carrier to our samples and the gate through the large pad 6-point pattern. These bonds are made by pressing the bonder tip into a metal surface and applying an ultrasonic pulse which softens the metal and the wire, causing them to bond together. We use power/time settings: 750/650, 550/550 for the first bond to the flex cable connector pin, and the second bond to a pad on the 6-point pattern respectively. Lower power/time settings are used for the actual chip to reduce the likelihood of gate leakage. As the chip sits far below the level of the connecting pins and the pins are only on two sides of the chip carrier,

we must carefully plan out and implement our bonds, often necessitating 90° turns in the bonds, which are non-trivial to make. It is imperative that the bonding be done correctly the first time, as re-bonding often causes defects in the oxide layer, resulting in gate leakage.

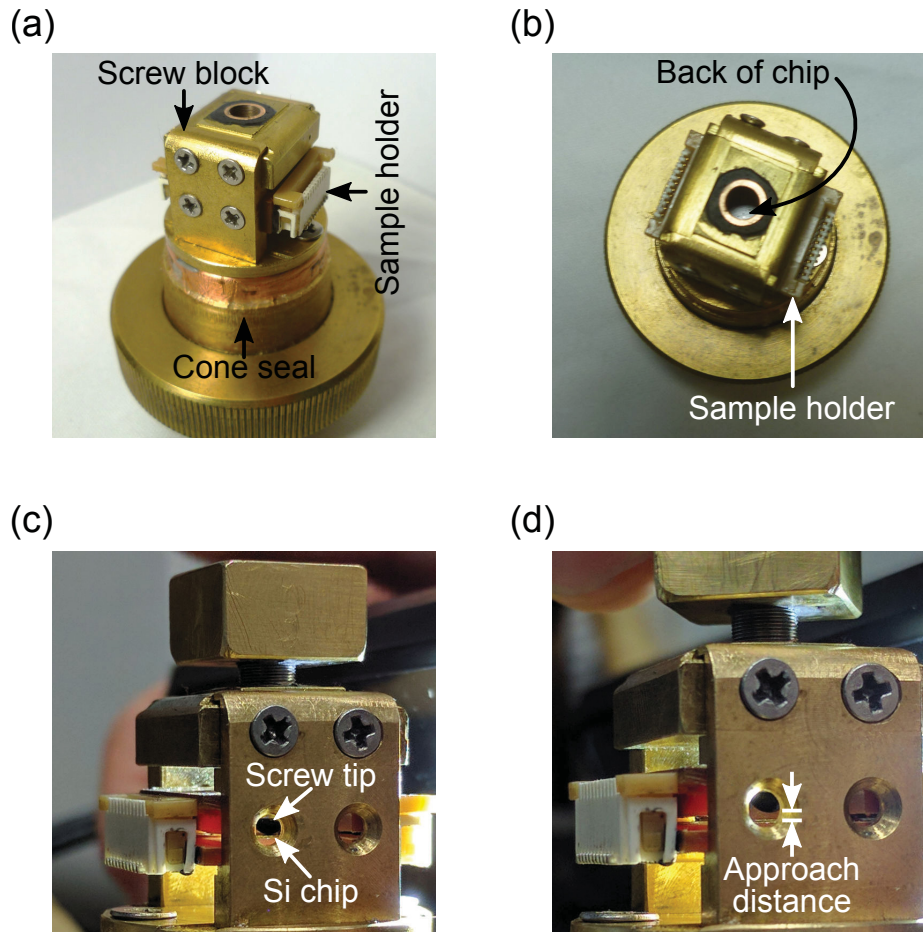


Figure 3.28: Assembling the QTSE set-up with thin chip samples. (a) Sample holder inside QTSE assembly without push screw. (b) Top-down view of the QTSE assembly from (a), showing the centered backside of Si chip visible through the hole in the screw block. (c) Close-up view of the QTSE assembly with the tip of the push screw touching the backside of the Si chip, loaded in the sample holder. (d) Same as (c), but with the push screw retracted to a visible approach distance.

Next, the bonded chip and sample holder are carefully removed from the grounded wire bonding jig and the nylon screws are removed, if used. The chip is now held in place in the sample holder by the many wire bonds attached to the connectors. We now load the sample holder into the QTSE assembly, as shown in Fig. 3.28. The wire bonded sample holder is inserted, contact-side down, into the QTSE scaffolding, shown in Fig. 3.28(a). We take extreme caution while manipulating the sample holder so as not to disrupt or remove the Al wires, and ensure that we are grounded to prevent static discharge from damaging

our devices. Once the sample holder is screwed in place, we inspect the back of the chip through the screw hole in the top of the assembly, as shown in Fig. 3.28(b). Here, we ensure that the chip is centred, and that there is no epoxy in the path of the screw tip. The push screw is then threaded into the screw block, and screwed downward until some resistance is felt, indicating that the screw tip has made contact with the back of the chip. This can be seen visually in a through-hole in the QTSE scaffolding in Fig. 3.28(c), where the screw tip is touching the back of the Si chip. To ensure that the chip does not break during loading into the cryostat probe, we back the screw off from the contact point, setting an approach distance, as shown in Fig. 3.28(d). Normally we use an approach distance of one full turn ($254\text{ }\mu\text{m}$).

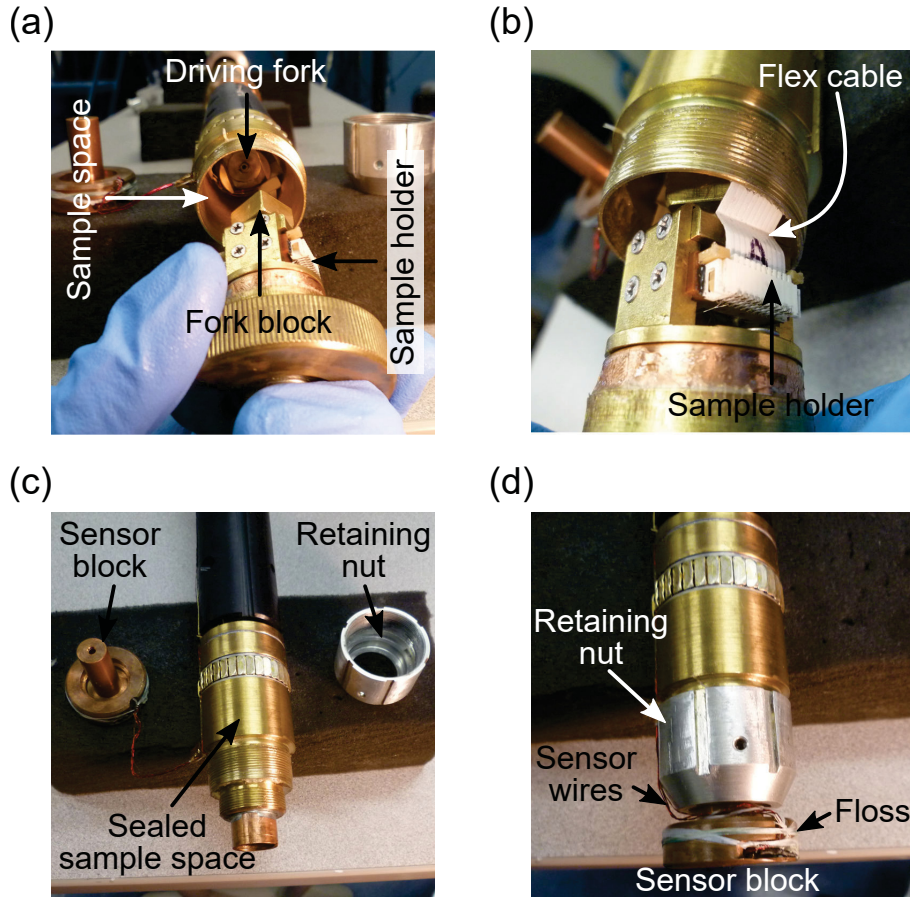


Figure 3.29: Loading the QTSE assembly in the cryostat probe. (a) Fork block to be aligned with driving fork to match the QTSE assembly to the cryostat probe. (b) The grounded flex cables are inserted into the connectors on the sample holder for electrical contact to our devices. (c) The QTSE set-up is inserted into the probe to vacuum seal the sample space. (d) The fully assembled bottom of the cryostat probe with retaining nut and sensor block attached.

We now insert the sample holder and QTSE assembly into the cryostat probe, as shown in Fig. 3.29. This is done cautiously so as not to damage the wire bonds or the wiring connected to the flex cables. First, we visually align the fork block to the driving fork, shown in Fig. 3.29(a), so that these mate when the cone seal is inserted into the sample space. Next, we straighten the grounded flex cables and partially insert the QTSE assembly into the sample space. We connect the flex cables one by one into the connectors on the sample holder, locking them in place using the wing tabs, as shown in Fig. 3.29(b). We next look inside the sample space to ensure the connecting wires are not tangled in the driving fork which turns the screw, and then apply vacuum grease to the cone-seal to prepare for insertion into the sample space. We confirm alignment between the fork block and the driving fork inside the sample space and fully insert the QTSE assembly fully into the sample space, making minute adjustments to ensure the fork block enters the driving fork. The resulting sealed sample space is shown in Fig. 3.29(c), with the aluminum retaining nut for keeping the cone seal in place and copper sensor block, containing a heater and temperature sensors for temperature measurement and control. In Fig. 3.29(d), we show the fully assembled bottom of the probe with retaining nut and sensor block attached. The sensor wires are tied down using dental floss.

After loading our samples, we perform three initial tests on our samples at room temperature. We first check the electrical continuity to determine the resistance of our samples and ensure they are not broken. We then ensure the samples have gate dependence. Finally, we ensure there is no gate leakage between the sample electrodes and the back gate. Gate leakage arises from electron tunnelling between the contact pads on top of the oxide, and the back gate underneath it. If the devices do not pass these three tests, we load a new chip into the QTSE probe. Otherwise, we prepare our samples for measurements. Using a turbomolecular pump and leak detector, we ensure the sample space is leak tight and pump the sample space down to $P \sim 10^{-7}$ Torr. The QTSE probe is now ready for insertion into the cryostat for low temperature strained transport measurements.

3.3.3 Wire bonding and preparing SWCNT devices for low temperature measurements

In this section, we describe the bonding and loading procedure for our SWCNT devices on thick chips. As these devices do not allow strain actuation, we load them into a separate cryostat probe, with no QTSE instrumentation. We pick up the fabrication of these samples from where we left off in Section 3.2: suspended bowtie shaped Au break junctions housing

SWCNTs, and contacted by the 6-point pattern.

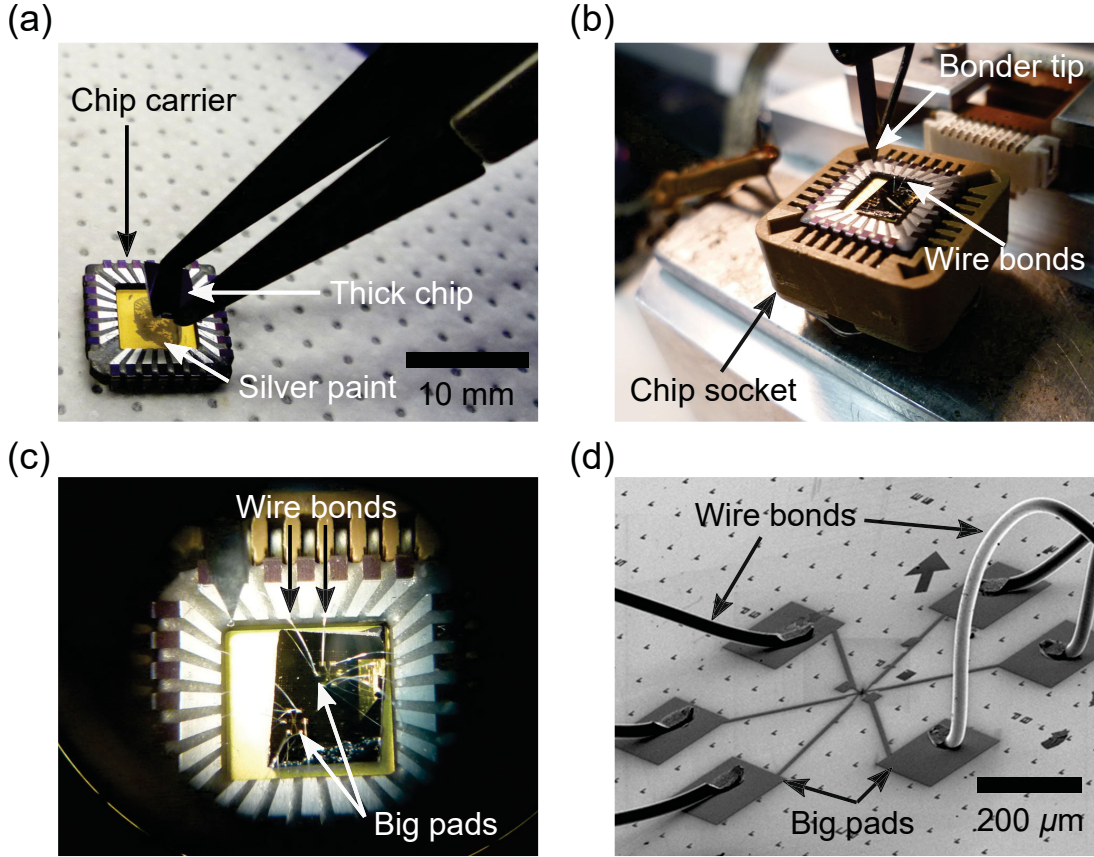


Figure 3.30: Wire bonding and loading SWCNT devices. (a) Installing a thick chip on the chip carrier using silver paint. (b) The loaded chip carrier in a grounded chip socket for wire bonding. Al wire bonds and the bonder tip also shown. (c) Close-up view of the Si chip, with big pads from the 6-point pattern visible and bonded to the chip carrier. (d) Tilted SEM image of the wire bonds attached to the six point pattern. Image courtesy of Vahid Tayari.

In Fig. 3.30(a), we show the process of loading a thick chip with SWCNT devices into the chip carrier. We use 28-pin chip carriers to house our thick silicon chips. These serve both for connecting our devices to the wiring of the cryostat probe, and for gating our devices through the conductive chip carrier substrate. We use silver paint to mechanically and electronically connect the chip carrier to the backside of the chip. Care must be taken not to push the silver paint onto the contacts during this stage, as this shorts them together.

The next step is to wire bond the big pads on the chip, which are connected to our SWCNT break junction devices, to the contact pins on the chip carrier. Our wire bonding set-up for thick chips is shown in Fig. 3.30(b). Again, the user, tweezers, and chip carrier must be grounded to protect the samples. We carefully press the chip into a socket with all

pins grounded. Using the same wire bonding procedure as discussed above, we connect the chip carrier pins to the big pads on the chip, which are connected to our samples, and to the chip carrier substrate, which is connected to our back gate. We use bonder power/time settings of 650/650 for both bonds. In Fig. 3.30(c), we show a close-up view of the wire bonds connecting the chip carrier pins to the big pads on the chip surface, and completing our macroscopic electronic connections to our nanoscale electronics devices. In Fig. 3.30(d), we show a tilted SEM image of the Al wire bonds connected to the big pads, courtesy of Vahid Tayari.

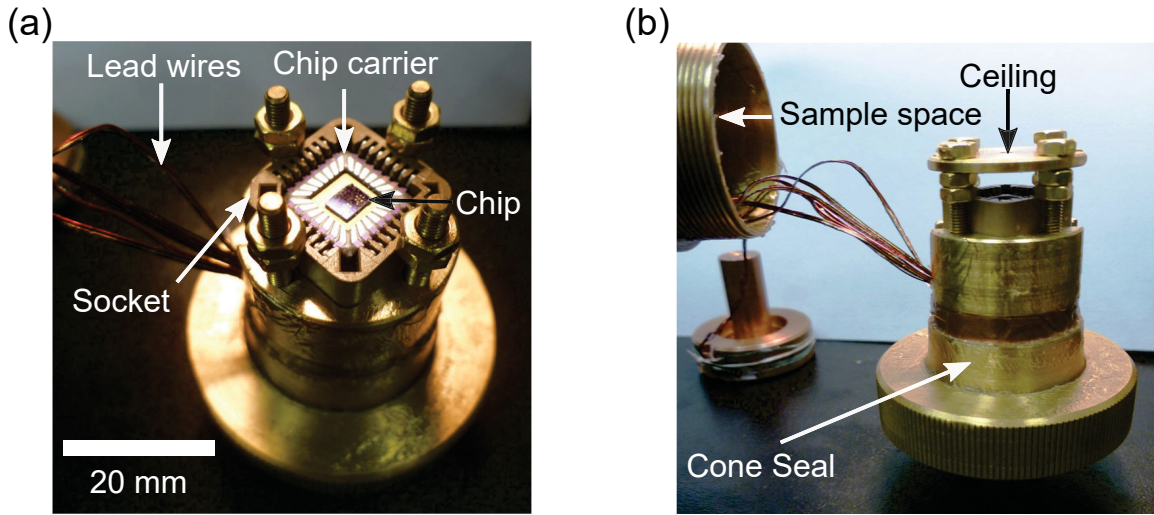


Figure 3.31: Loading thick chips into the cryostat probe. (a) Overview of the cryostat probe with breakout box at the top connected to the socket at the bottom inside the sample space. (b) Sample loaded inside the chip carrier socket, electronically connected through lead wires. (c) A ceiling plate is put over the sample to protect it. The assembly is inserted into the cryostat probe, sealing the vacuum space with a cone seal.

Once we have fully wire bonded connections to our devices, we carefully remove the chip carrier from the wire bonding set-up and load it into the cryostat probe, where it will be placed under vacuum ($P \sim 10^{-7}$ Torr) and brought to low temperature ($T \sim 0.3$ K) for transport measurements. The thick chip loading procedure and sample holder assembly are shown in Fig. 3.31. Fig. 3.31(a) shows the thick chip with SWCNT devices, loaded into the sample holder of the non-QTSE cryostat probe. The wire bonded chip carrier is pressed into the chip carrier socket, which is connected to lead wires that we use to measure our samples. Fig. 3.31(b) shows the fully assembled sample holder, with the cone seal to vacuum seal the sample space and a protective ceiling to protect the wire bonds inside the sample space. The cryostat probe is now ready to be inserted into the cryostat for electronic fabrication steps (electromigration and annealing), and low temperature transport measurements discussed

in the following section.

3.4 Electromigration, annealing, and measurement methods

We have now shown the full sample fabrication and loading procedures for low temperature measurements, in both strained and unstrained devices, on thin and thick chips respectively. Once these devices have been loaded into the cryostat, we perform final electronic fabrication steps, and measure the devices. In this section, we will detail our electromigration method for producing Au point contacts and ultra-short (~ 10 nm) SWCNT transistors. We then show how we clean our devices using Joule heating (annealing), and detail our measurement circuits for high-quality transport experimentation. Finally we will show how we can use these measurement methods along with electromigrated gold tunnel junctions, to calibrate the strain-tunability of our QTSE instrumentation

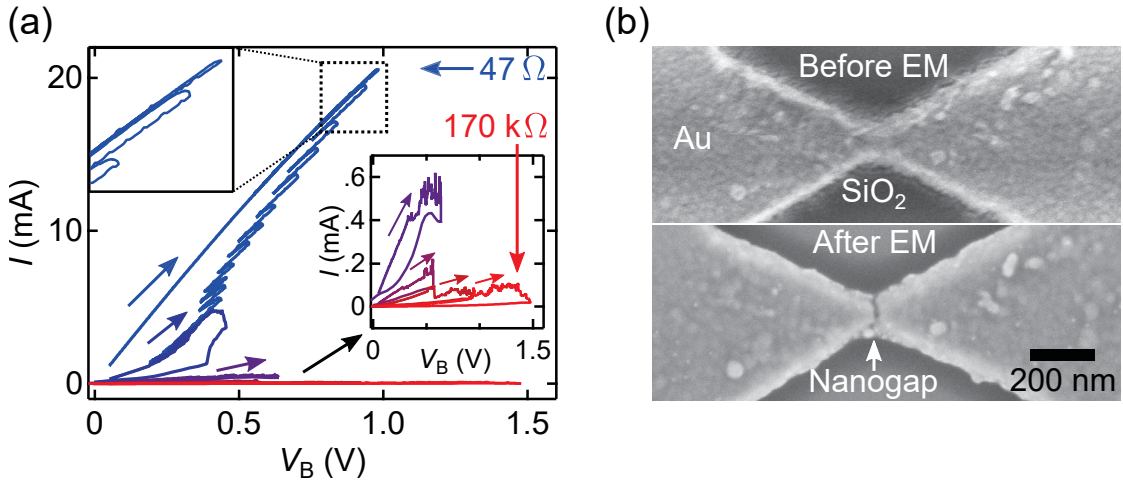


Figure 3.32: Electromigration procedure for etching nanogaps in Au films. (a) $I - V_B$ data, taken at $T = 1.3$ K showing a 6-step electromigration process, beginning with a feedback-mediated electromigration (blue) for a 47Ω gold tunnel junction, and followed by 5 breaking steps, finally reaching the red curve tunnel junction with $170 \text{ k}\Omega$ resistance. Left inset: detail of the feedback-mediated electromigration. Right inset shows a zoom-in of the low current data for electromigration steps 3–6. (b) SEM images of the device electromigrated in (a), before and after electromigration, showing the etched nanogap.

To create nm-scale devices, we perform feedback-mediated electronic etching of metallic nanowires. This process, called electromigration (EM), is the final step in our fabrication process for break junction devices. This process has been described in detail in literature

[40,91]. In Fig. 3.32 we give a summary of our electromigration procedure. We apply a bias voltage across the source and drain electrodes to pass large currents (~ 10 mA) through the narrow metal constriction of the break junction, causing significant Joule heating, up to ~ 500 °C [92]. The high-momentum electrons passing through the heated junction push the hot metal nuclei out of the constriction. This is a runaway process, much like a fuse breaking, and left unchecked, the EM will create a μm -sized gap, and destroying devices housed inside the break junction (*e.g.* SWCNTs). However, we can control this process by decreasing the voltage immediately when the resistance changes. In Fig. 3.32(a), we show data collected during this feedback-mediated EM process for a suspended AuTJ (see Fig. 3.14(b)), at $T = 1.3$ K. The feedback-mediated electromigration (blue curve) chips away at the constriction slowly, narrowing it. Up to $R \approx 200$ Ω , we control the feedback iteratively based on a percent change in resistance. However, for higher R this approach does not work, and we must perform a single feedback step based on the absolute value of R , which we call a breaking step. For each breaking step, we increase this feedback resistance by roughly a factor of 2. In Fig. 3.32(a), five breaking steps follow the initial electromigration step, going from blue to red and increasing the resistance of the junction from 47 Ω to 170 k Ω . The insets of the figure show the migration (left) and breaking (right) steps in more detail. This increase in resistance arises through the introduction of a nanogap in the Au nanowire. In Fig. 3.32(b), we show SEM images of the AuTJ before (top) and after (bottom) electromigration. A clear nanogap is formed in the junction by the electromigration. The nanogap appears to be closed from the SEM image due to thermal expansion of the metal point contacts as the sample is warmed to room temperature for imaging. The width of the constriction in this device is ≈ 100 nm. We find that we have better control over the EM for devices with thinner Au films and narrower constrictions, because there is less material to electromigrate.

We show our feedback-mediated electromigration circuit in Fig. 3.33. We apply a bias voltage across the break junction source and drain using a Keithley 2400 in series with a low pass filter to prevent voltage spikes. In the later stages of the EM process ($R > 200$ Ω), we use an Ithaco 1211 current preamp output to the DAQ for high-quality current measurements. However, the Ithaco is not rated for high currents (> 10 mA), so in the early stages of the EM, we use a small resistor in parallel with a Stanford SR560 voltage preamp to amplify the current. The output voltage and input current are measured by the computer, which computes R in real-time for feedback-mediated EM. Using our electromigration techniques, we are able to create gold point contacts or ultra-short SWCNT and graphene devices using

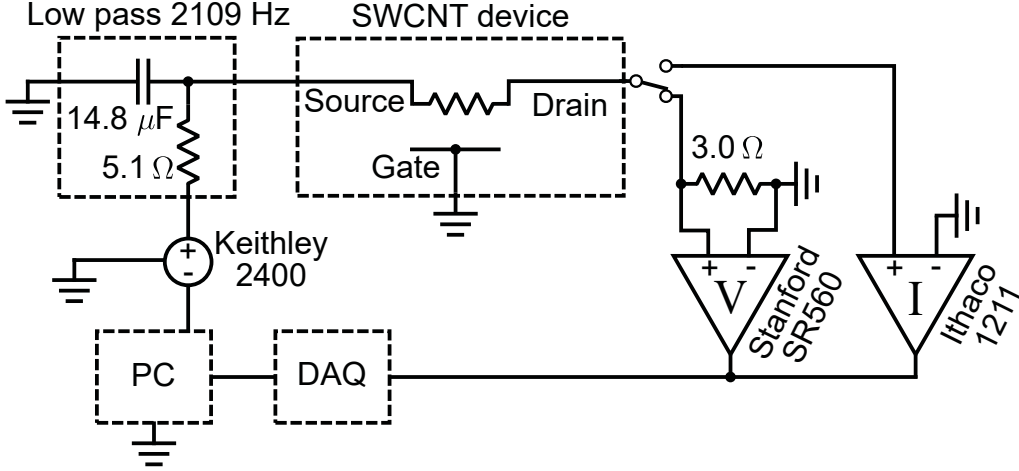


Figure 3.33: Electromigration circuit. The computer controls the voltage applied to the device by constantly measuring the resistance of the device. In the first stages of the electromigration, we must use a resistor and voltage pre-amp to measure current as the current preamp is not rated for such high currents (> 10 mA).

bowtie-shaped break junction geometries [40, 91].

At this stage in our fabrication procedure, we have one of two types of devices in sample probes at low temperature: suspended and electromigrated ultra-short SWCNT break junction devices on thick chips, or suspended graphene gap junctions on thin chips. Our final fabrication process is to clean these devices using current annealing. It is well known that residues from the fabrication procedure have a strong effect on transport in graphene and carbon nanotubes, introducing charge impurities and defects in the crystal structure, which affect electron transport. It is possible to remove these residues by heating the samples to bake them off. This process is known as annealing and not only removes fabrication residues, but has also been shown to heal defects in the lattice and reduce contact resistance [93, 94]. To current anneal our samples, we use the same circuit as used for electromigration (Fig. 3.33) with automatic feedback disabled. We apply large currents to our samples, cleaning them by Joule heating.

We show annealing data for SWCNT and graphene devices in Fig. 3.34. In Fig. 3.34(a), we show a typical annealing curve for ultra-short, suspended SWCNT transistor. To perform current annealing in our SWCNTs, the bias voltage is ramped up across the sample, increasing current flow and dissipating power in the device. In Fig. 3.34(a), we show a single annealing step at $4 \mu\text{W}$ for 10 minutes, after which the voltage is ramped back down to zero. In Fig. 3.34(b), we show $I-V_G$ data for this sample before (blue) and after (red) the annealing step shown in Fig. 3.34(a). After annealing, we measured a shifted conductance spectrum

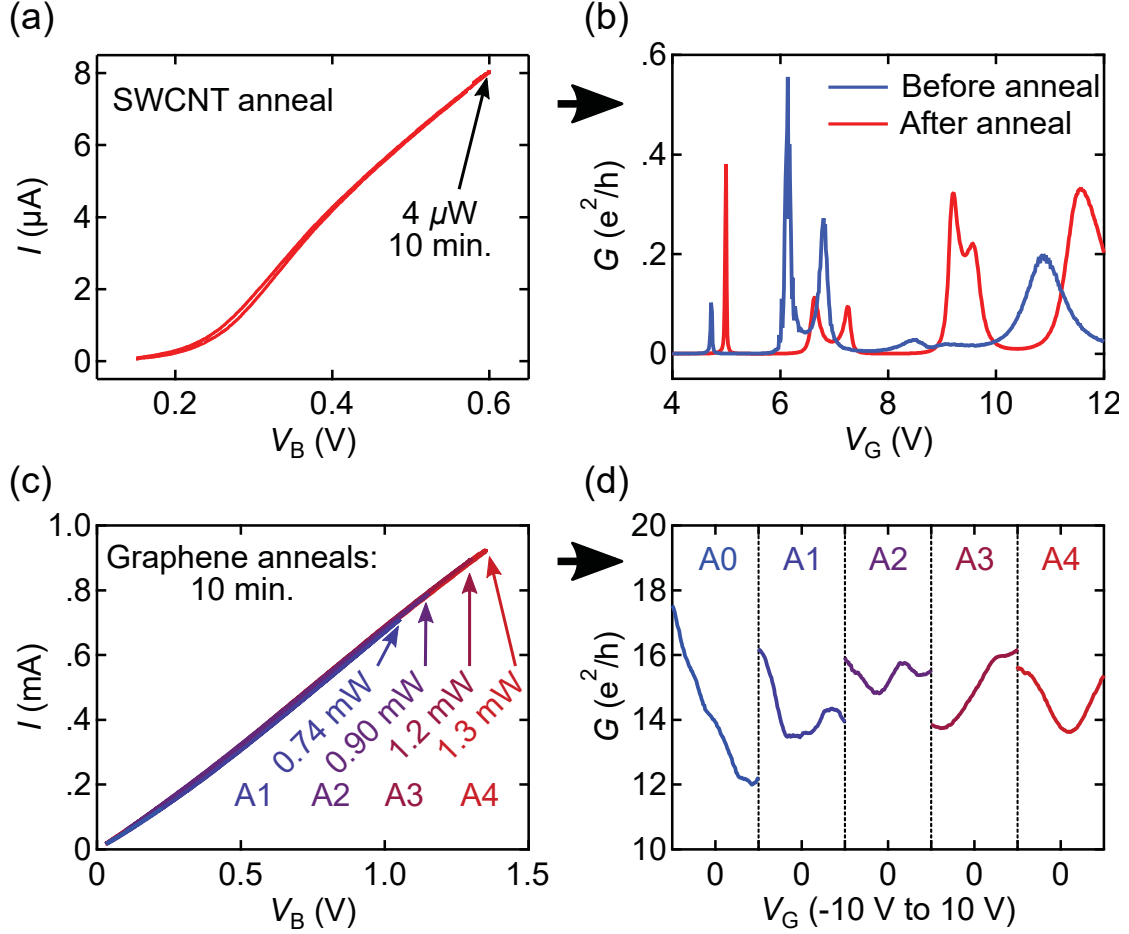


Figure 3.34: Cleaning suspended SWCNT and graphene devices by annealing. (a) $I - V_B$ annealing curve for an ultra-short SWCNT device. This device was annealed at 4 μW for 10 min. (b) $I - V_G$ data from SWCNT before (blue) and after (red) the anneal shown in (a). The peaks shift, change shape, and become smoother, indicating that annealing has cleaned the device. (c) $I - V_B$ annealing curves for a suspended graphene device. Here, we show four anneals (A1–A4) of increasing power from blue to red. (d) Horizontally offset $I - V_G$ data ($V_G = -10$ V to 10 V) from the graphene device in (c) for different anneals. For higher annealing power, the curves become smoother, and the conductivity minimum (Dirac point) shifts towards $V_G = 0$ V. All data collected at 1.5 K.

with more numerous, smoother peaks, indicating that it has been cleaned. In Fig. 3.34(c) we show the annealing process for a graphene gap junction with four annealing steps (A1–A4) ranging from 0.74 mW (A1, blue) to 1.3 mW (A4, red). In Fig. 3.34(d), we show $I - V_G$ data from zero annealing (A0, blue), and for each step of the anneal in Fig. 3.34(c). For higher power, the $I - V_G$ data becomes smoother, indicating that we are cleaning the graphene device. In addition, for increasing annealing power we see the conductivity minimum (Dirac point) shift from $V_G > 0$ to $V_G < 0$ before finally settling near $V_G = 0$. This is a result of the successively higher annealing powers first cleaning the graphene sheet from n-type dopants, and then p-type dopants, likely water and resist residues. We stop annealing when a clear Dirac point has emerged near $V_G = 0$. Typically this corresponds to the point where the $I - V_B$ annealing data shifts from curving upwards, to curving downwards, as exemplified by the red curve (A4) shown in Fig. 3.34(c).

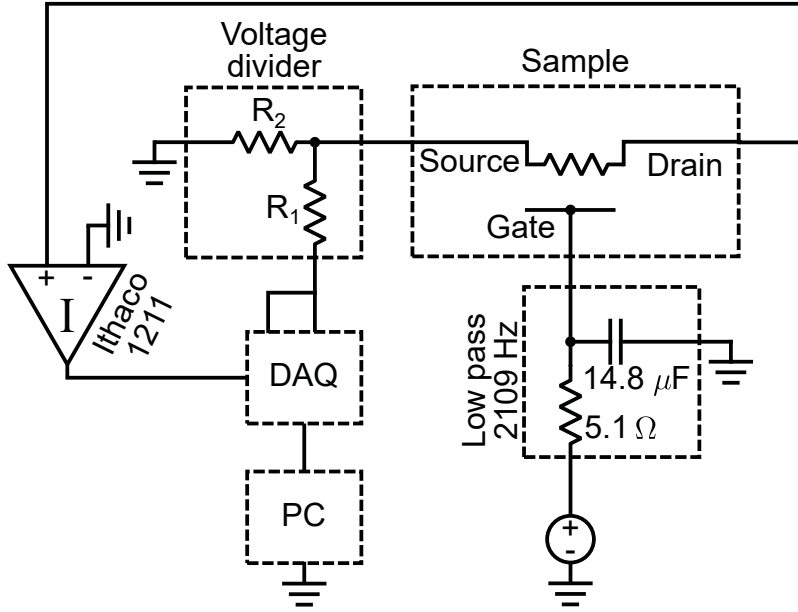


Figure 3.35: dc measurement circuit, optimized for reliable low-noise measurement of current as a function of bias and gate voltage.

After annealing, our fabrication process is complete for all devices. We now describe our two-point measurement methods for high-quality data acquisition. In Fig. 3.35, we show our dc (direct current) circuit, for measuring current flow in our samples as a function of bias and gate voltages. For our measurements, we aim to both protect the sample and reduce noise as much as possible. The user must always be grounded to prevent any static discharge from destroying the samples, and additionally we ground our samples at all times when not in use. We use a DAQ to apply bias voltage through a voltage divider, increasing our digital voltage

resolution and reducing ambient noise. We use a Keithley 2400 voltage supply to apply voltages to our sample gate through a low pass filter to prevent voltage spikes. We measure current from the drain electrode amplifying the signal through an Ithaco 1211 current preamp and sending the output to the DAQ. We use this measurement circuit to collect all of the experimental data shown in the remainder of this thesis.

3.4.1 Tailoring 10 nm scale suspended graphene junctions and quantum dots

I have made substantial contributions to other ongoing research projects. For the project described below, my contributions led to a publication in Nano Letters [40] on using our electromigration procedure to tune the shape, geometry, and transport regime (ballistic or quantum dot) of our suspended graphene devices. This research is applicable to our studies on electron transport in strained graphene, as the strain field uniformity and magnitude depend heavily on device geometry.

Creating ultra-short graphene devices opens up the possibility of studying ballistic transport, strain-engineering, electromechanical coupling and ultra-high-frequency NEMS. We fabricated 10-nm scale suspended graphene devices using our custom feedback-mediated electromigration methods. We showed that, not only can we control the length of the suspended graphene devices through careful selection of the electromigration parameters, but also their shape. We showed that both ballistic and quantum dot transport are possible in these devices. This research is summarized in Fig. 3.36.

In Fig. 3.36(a), we show a false coloured SEM image of a graphene break junction with $L \approx 6$ nm, and $W \approx 60$ nm formed using a low power electromigration breaking step, $P_{\text{Break}} = 2.7$ mW. The device has very regular, symmetric edges as a result of this low power breaking step. We find that the device lengths are roughly proportional to $P_{\text{Break}}^{1/2}$ in electromigrated devices from 6 to 55 nm long. In Fig. 3.36(b), we show resistivity calculated from $I - V_{\text{B}}$ curves from 8 devices, electromigrated with $P_{\text{Break}} < 5$ mW, with black circles and red squares corresponding to devices electromigrated at 4.2 K and 1.5 K respectively. The longer devices have resistivities near the upper limit, $\rho = \pi h/4e^2$, indicating ballistic transport. In shorter devices, the resistivities are lower, as contact effects play a larger role. We find that the shape of the channels for higher power breaking electromigrations ($P_{\text{Break}} > 10$ mW) arises due to tearing of the graphene sheet, as shown in Fig. 3.36(c). This occurs as a result of stronger downward electrostatic force between the graphene sheet and the back gate, due to the high voltages applied during high power electromigrations.

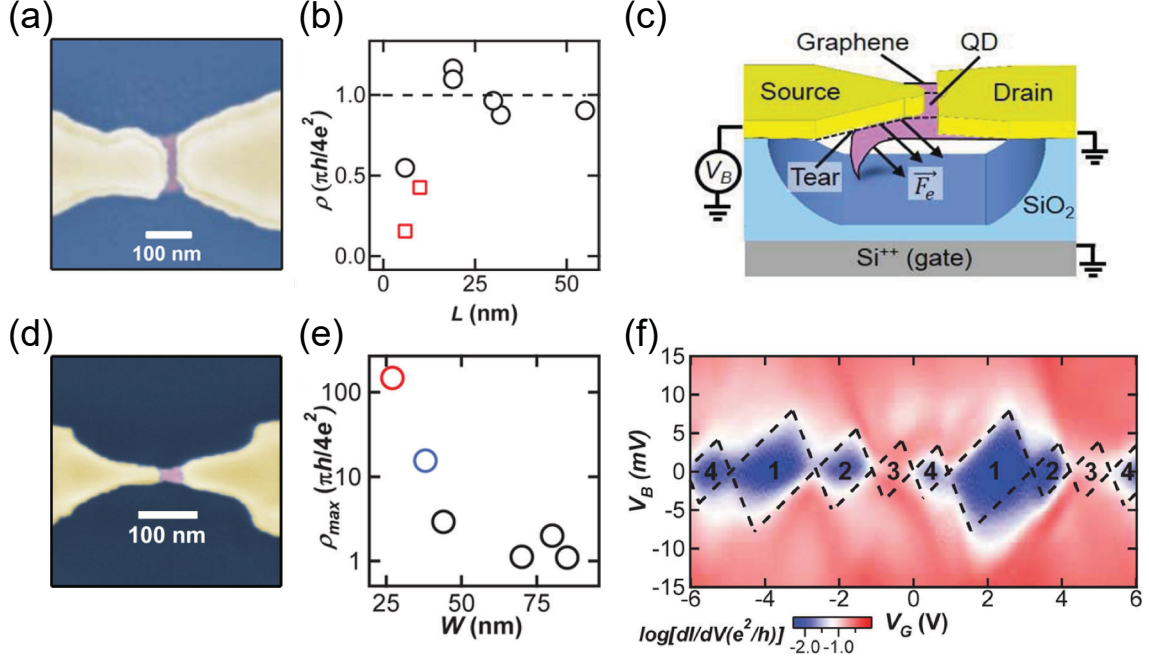


Figure 3.36: Tailoring 10 nm scale suspended graphene junctions and quantum dots. For more details, see main text. (a) False colour SEM image of a $L \approx 6$ nm graphene device, formed by low power breaking electromigration. (b) Resistivity data from low power electromigrated devices, showing ballistic transport in longer devices. (c) Tearing mechanism which shapes the graphene flakes in high power breaking. (d) False colour SEM image of a $W \approx 27$ nm graphene device, formed by high power breaking electromigration. (e) Resistivity data from low power electromigrated devices, showing ballistic transport in wider devices. (f) Quantum dot transport data from the device shown in (c).

By engineering the shape of the gold contacts and choosing the electromigration power, the width of the junctions can be tailored. In Fig. 3.36(d) we show a false coloured SEM image of a graphene break junction device formed using a high power electromigration breaking step, $P_{\text{Break}} = 14.4$ mW with $L \approx 40$ nm, and $W \approx 27$ nm. This device has asymmetric contacts, and has been torn electrostatically to its current shape. Using this electrostatic tearing method, we find that we can controllably form devices from 100 nm down to 27 nm in width. In Fig. 3.36(e), we show that the maximum resistivity for graphene devices electromigrated at high power, showing that wider graphene devices are ballistic, while more narrow ones have higher resistivity. Investigating transport data from this device in Fig. 3.36(f), we see that the lateral confinement in this graphene device causes it to form a quantum dot.

Thus, we show that we can tune the dimensions, and therefore the transport behaviour, (quantum dot vs. ballistic) in graphene devices using our electromigration methods. These methods could be applied to other 2D materials, and are of interest for studying electromechanical coupling strain engineering, ultra-high-frequency NEMS, and ballistic transport.

3.4.2 Strain instrumentation calibration using Au tunnel junctions

Before using our QTSE instrumentation for measurements, we must first test its operation and calibrate its motion. Here, we briefly go over our strain calibration method, done using electromigrated and suspended AuTJs on thin chips, showing strain tunable resistance and extremely good mechanical stability.

We calibrate the mechanical strain in our QTSE set-up using gold tunnel junctions as shown in Fig. 3.37. The concept behind this calibration method is shown in Fig. 3.37(a)–(b), where bending the Si chip in the QTSE set-up causes an electromigrated AuTJ point contact to open up further into a tunnel junction. As tunnelling is exponentially dependent on the tunnel barrier length, we expect to measure exponentially suppressed current (increased resistance), as we bend our thin chips. Quantitatively, the tunnel junction resistance is [95]:

$$R \propto e^{2\kappa x}, \quad \kappa = \frac{\sqrt{2m_e\phi_{\text{Au}}}}{\hbar}, \quad (3.2)$$

where $m_e = 9.109 \times 10^{-31}$ kg is the electron mass, and $\phi_{\text{Au}} \approx 5.1\text{--}5.5$ eV is the work function of gold [79, 96]. To calibrate the applicable strain in our QTSE set-up, we measured a suspended and electromigrated AuTJ at $T = 1.3$ K. In Fig. 3.37(c), we plot resistance R as a

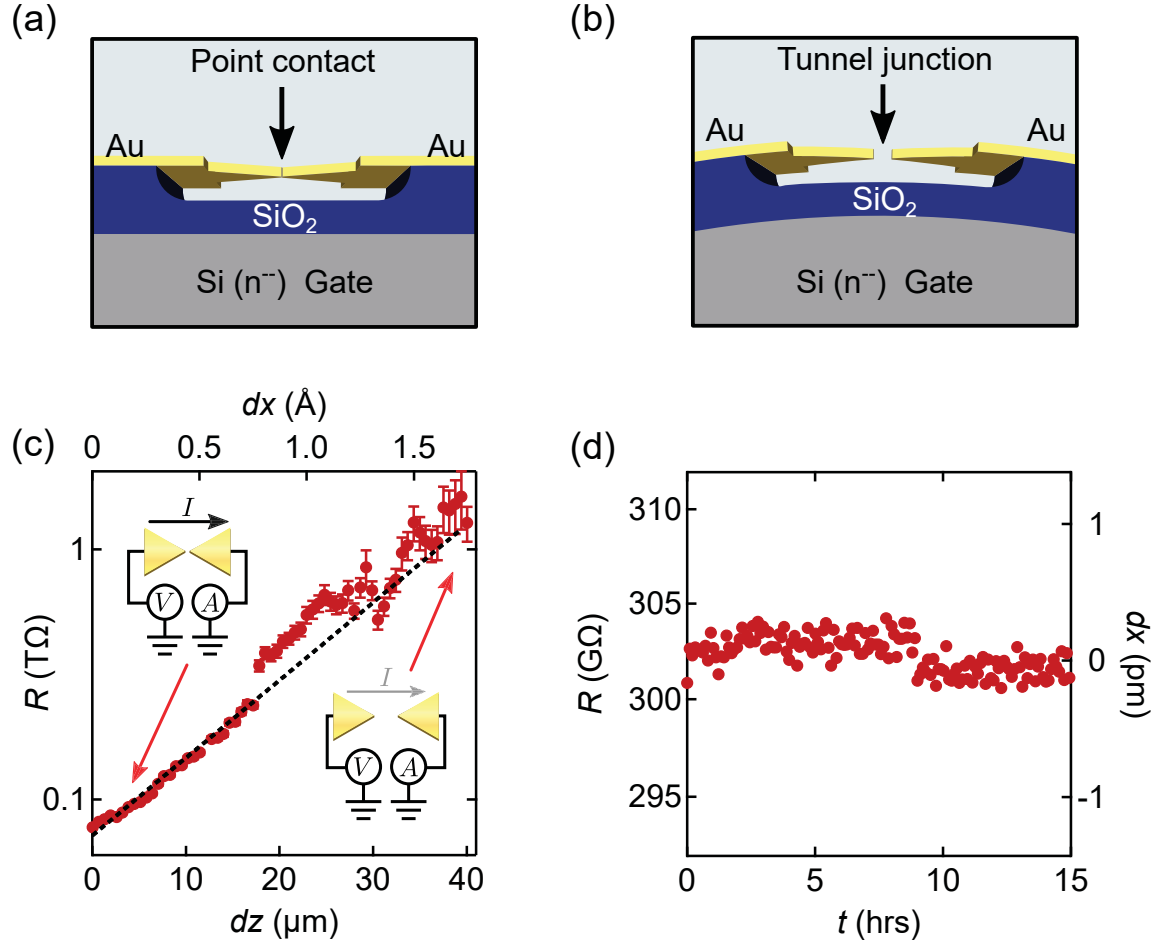


Figure 3.37: Strain calibration of our QTSE instrumentation using gold tunnel junctions. (a)–(b) Principle of operation for tunnel junction strain calibration. A metal point contact is stretched apart by the QTSE creating a tunnel junction, with exponential sensitivity. (c) $R - dz$ data for a suspended gold tunnel junction, showing strain-tunable resistance, calculated from individual $I - V_B$ curves. An exponential fit is overlaid in black, giving the change in tunnel junction spacing dx plotted on the top axis. (d) Stability test of the AuTJ in (c), showing pm stability over a 15 hour period.

function of vertical displacement of the push screw dz with an exponential fit (black, dashed) using Eq. 3.2. The insets show cartoons of the tunnel junction circuits with shorter tunnel junctions allowing more current (left), and longer tunnel junctions allowing less (right). Each R data point represents a linear fit of $I - V_B$ data at a different motor position. Small deviations from the linear fit arise from the atomically imperfect shape of our electromigrated tunnel junctions. We calculate $dx/dz = 3.1\text{--}6.6 \times 10^{-6}$ from exponential fits of $R - dz$ data from several gold tunnel junctions. We use the midpoint value of $dx/dz = 4.5 \times 10^{-6}$, to determine the change in tunnel barrier length dx , plotted on the top axis of Fig. 3.37(c). Comparing to the theoretical value of $dx/dz \approx 9.0 \times 10^{-6}$ for our set-up (Section 3.3) our calibrated strain results are roughly a factor of two smaller. This outcome matches that from previous QTSE measurements [79].

It is important to ensure mechanical stability in our QTSE set-up for long term measurements of our samples. We perform stability tests on our QTSE using electromigrated AuTJs. In Fig. 3.37(d) we show the stability of our QTSE set-up over a 15 hour period from the same device as in panel (c). These data were taken near the middle of the vertical displacement range of dz shown in 3.37(c). Each data point represents a linear fit of $I - V_B$ data at a different time. Using Eq. 3.1, we calculate pm stability in the tunnel junction, indicating that thermal fluctuations and mechanical vibrations are well isolated in our QTSE instrumentation.

3.5 Conclusions

In this chapter, we have shown our fabrication methods for producing clean and suspended ultra-short SWCNT transistors and ballistic graphene gap junctions. These are compatible with strain-tunable low temperature transport measurements made possible by our custom-built QTSE set-up. We showed that we can apply significant and tunable uniaxial strains $\sim 1\text{--}10\%$ in suspended nanoelectronic devices. These large uniaxial strains could be used for extreme tuning of conductivity in SWCNTs, through bandgap modification, and in graphene through the graphene quantum strain transistor effect (discussed in Chapter 5), for making extremely high-quality integrated circuits or strain sensors.

Our QTSE instrumentation is extremely modular and can be used to study a wide variety of physical effects in different materials. Uniaxial strains could be used to study tunable THz NEMS in SWCNTs and graphene [10, 40]. Changing only our fabrication geometry

to clamp a graphene sheet at three equally spaced points, rather than two, our QTSE set-up could be used to impart triaxial strains for the study of large pseudomagnetic fields in graphene [22]. These large fields could allow the study of room temperature Landau level physics [45], valley polarized transport for valleytronics applications [31] and topological phases in graphene [97]. In addition to monolayer graphene, our QTSE set-up is applicable to study quantum electromechanics in a plethora of other strain-sensitive 2D materials. For example, strain could be used in twisted bilayer graphene near the so-called magic angle, where strain could be used to tune the strength of a superconducting phase [98]. Strain could also be used for band gap modulation in transition metal dichalcogenide monolayers, such as MoS₂ or WS₂ [99], or phosphorene [4] for engineering tunable 2D heterostructures. We expect to use our custom-built QTSE instrumentation to probe novel physics in a wide variety of materials and configurations, to gain a deeper understanding of quantum electromechanics in nanoelectronics systems.

Chapter 4

Giant Electron-Hole Transport Asymmetry in Ultra-Short Quantum Transistors

Short length scales are necessary for achieving large strains in carbon quantum nanoelectromechanics. In this chapter, we describe the dramatic difference between electron and hole behaviour we observe in ultra-short carbon nanotubes. These devices form two-in-one quantum transistors, with ballistic/quantum dot behaviour for electrons/holes in small bandgap nanotubes, and as two quantum dots with different charging energies for electrons and holes in large bandgap nanotubes. This electron-hole asymmetry arises as a result of electron doping of the ballistic nanotube leads by the gold films coating them. The work presented in this chapter was adapted from Giant electron-hole transport asymmetry in ultra-short quantum transistors, Andrew McRae *et al.*, Nature Communications, **8**:15491 (2017) [53].

4.1 Introduction

An important feature of ultra-clean (intrinsic) single-walled carbon nanotube (SWCNT) channels is that a small gate voltage can tune them from n-type (electron-doped) to p-type (hole-doped) devices. A large electron-hole transport asymmetry would enable dual functionality quantum SWCNT transistors with drastically different characteristics under electron or hole doping. Unfortunately, the intrinsic transport properties of SWCNTs are mostly electron-hole ($e - h$) symmetric [30, 100], and thus the two types of transport are redundant. Nevertheless, quantum SWCNT devices can be engineered to create an $e - h$

transport asymmetry. This is achieved for instance in SWCNT quantum dot (QD) transistors whose tunnel barrier heights depend on whether the channel is n or p doped. Such a transport asymmetry has been demonstrated in ultra-clean devices with channel lengths ranging from a few hundreds to 100 nanometers [101, 102]. Downsizing ultra-clean $e - h$ asymmetric SWCNT transistors to 10 nm would create quantum dots which can be toggled between two vastly different charging energies. They would be useful to explore fundamental nanoelectromechanical systems (NEMS) physics [10, 11, 103–105] and qubits [100, 106–108] at energy scales close the ones in single-molecules [109, 110] or to create THz bolometers [111] which are sensitive to two different wavelength ranges (one for each E_C). Additionally, a large $e - h$ transport asymmetry in SWCNT transistors could allow them to act as both active logic elements (QDs) for hole doping and interconnects (quantum bus) for electron doping. This dual functionality is needed to create reconfigurable logic circuits which can be programmed with gate voltages [112], and would support the development of commercial SWCNT electronics [28].

Here, we demonstrate the capability to engineer a giant $e - h$ charging energy and conductance asymmetry in ultra-clean (single QD or ballistic) suspended SWCNT channels whose lengths range down to 14 nm. Ultra-clean SWCNTs used to explore many-body physics and quantum bits have previously been limited to channel lengths above 100 nm [101, 103, 106–108, 113–115]. The key feature of our fabrication is to use an annealed-gold film as an electrostatic gate directly deposited on a SWCNT (no dielectric spacer). This n-dopes the gold-covered SWCNT sections which then act as contacts to the naked channel. These gold gates create extremely sharp barriers at the contact-to-channel interfaces (few-nm wide), and these barriers have different heights whether the channel is n or p doped. We measured transport in five devices under both electron and hole doping of their channels, and at temperatures ranging from 1.3 to 295 K. In a small gap SWCNT device (Device A), E_C 's for electrons and holes differ by orders of magnitude. When this device's channel is p-doped, it forms a 102 nm-long low-disorder QD. When the channel is n-doped, the device becomes a one-dimensional waveguide where carriers can travel ≈ 330 nm without losing their phase coherence. In the four devices whose band gaps $E_g \gtrsim 200$ meV the charging energy asymmetry ratio η_{e-h} of the charging energies for holes, E_C^h , and electrons, E_C^e ranges from 1.5 to 2.6. We demonstrate that when we bias appropriately these QDs, a modest gate voltage switches their charge transport from QD to quasi-ballistic. We show that the $e - h$ charging asymmetry scales inversely with channel length and the SWCNT's band gap. The giant $e - h$ asymmetry allows us to very significantly increase E_C^h , while reducing E_C^e , for a

given channel length and band gap. The charging energies of our shortest device (Device B) exceed 100 meV, demonstrating the potential for room temperature operation.

4.2 Fabrication details, and transport measurements for five SWCNT transistors

Device	E_g (meV)	L_{SEM} (nm)	L_G (nm)	$\eta_{\text{e-h}}$
A	28 ± 5	111 ± 5	102 ± 5	above 100
B	270 ± 50	14 ± 3	7 ± 5	2.6
C	190 ± 20	42 ± 7	46 ± 8	1.5
D	250 ± 20	16 ± 4	13 ± 5	2.1
E	170 ± 50	24 ± 8	15 ± 5	2.5

Table 4.1: Key parameters for the five SWCNT-QD transistors reported. E_g is the band gap extracted from transport data, L_{SEM} the channel length measured via scanning electron microscope (SEM), L_G the channel length from transport data, and $\eta_{\text{e-h}} = E_C^{\text{h}}/E_C^{\text{e}}$ is the measured charging energy asymmetry between electron and hole doping of the quantum dots.

In Table 4.1, we list for the five studied devices, the following key parameters: band gap E_g as extracted via QD transport, channel length L_{SEM} measured via SEM imaging, channel length L_G extracted from QD transport data, and ratio $\eta_{\text{e-h}}$ of the charging energies for holes, E_C^{h} , and electrons, E_C^{e} . Figure 4.1 summarizes the fabrication and contact geometry of our suspended SWCNT devices [10,91]. We first fabricated suspended gold-on-SWCNT break junctions. Figure 4.1(a) shows a tilted SEM image of break junction with L_{sus} indicating the length over which the gold is suspended. The substrate (blue) is used as a global back-gate electrode. The gold break junctions are suspended using a buffered oxide etch (BOE) which removes the SiO_2 underneath the central portion of the bowtie-shaped junctions. We measured the suspension length, L_{sus} , of 19 samples prepared with the same BOE etching recipe as for our reported devices. The results are shown in Figure 4.1(b). The mean suspension length is $L_{\text{sus}} = 350 \pm 70$ nm.

The final fabrication step is to create a nm-long naked SWCNT channel in the center of the gold break junction. To do so, we used a previously reported feedback-controlled electromigration (EM) procedure [10,40] summarized in section 3.4, and shown specifically for a SWCNT device in Fig. 4.1(c), where a bias voltage, V_B , is applied between the source

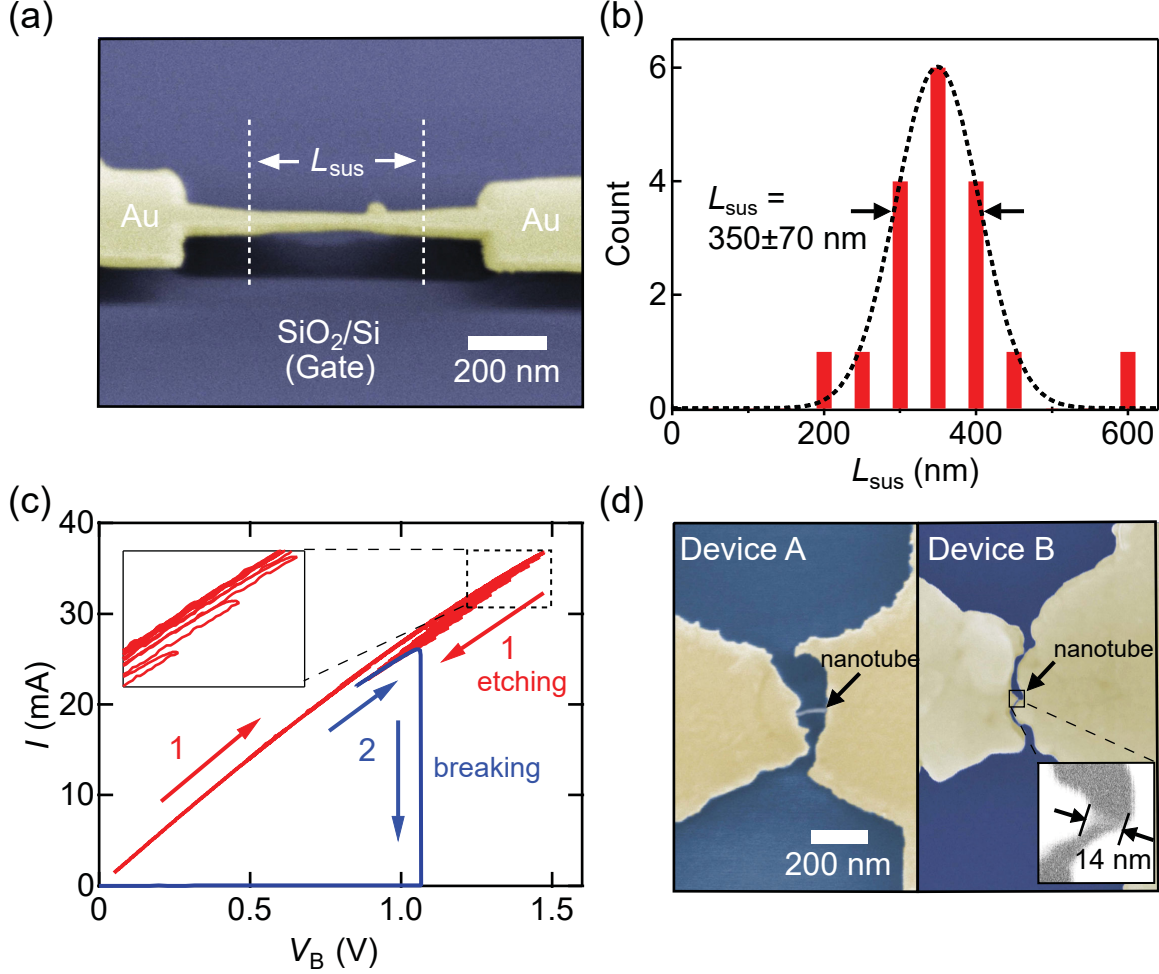


Figure 4.1: Ultra-short suspended nanotube quantum dot transistor fabrication. (a) Tilted scanning electron microscope (SEM) image showing a suspended gold break junction fabricated on top of a single-walled carbon nanotube (SWCNT). The break junction is suspended over a length $L_{\text{sus}} \approx 350$ nm. The back plane (blue) is used as a global back-gate. (b) Histogram of 19 suspended devices with buffered oxide etching depths of 130 to 143 nm (closely matching the parameters for our reported devices). The mean suspension length is $L_{\text{sus}} = 350 \pm 70$ nm. (c) The $I - V_B$ electromigration (EM) data for a gold-on-SWCNT break junction at $T = 4$ K, showing the process to (1) narrow the junction and (2) create a naked nanotube channel. (d) SEM images of Devices A and B after EM. The naked channels are visible and their lengths are $L_{\text{SEM}} = 111$ and 14 nm, respectively.

and drain gold electrodes. This EM process exposes a short naked SWCNT channel. Figure Fig. 4.1(d) shows top-view SEM images of Devices A and B whose channel lengths are respectively 111 ± 5 nm and 14 ± 3 nm. We note that the fabrication process of our ultra-clean SWCNT devices is compatible with the optical measurement of the SWCNT chirality [116,117] prior to the gold deposition. Such ultra-clean SWCNT transistors with a known tube chirality could lead to breakthroughs in SWCNT physics [100].

Figure 4.2(a) shows the current-gate voltage, $I - V_G$, characteristics at $T = 1.3$ K for Devices A (black) and B (red). The EM not only uncovers short naked SWCNT channels, but also anneals them such that the QDs in the channels are nearly undoped [10] with their charge neutrality point (CNP) close to $V_G = 0$. The inset of Fig. 4.2(a) shows the Fermi level position in the channel under electron or hole doping. The current (conductance) is much higher when the back gate n-dopes rather than p-dopes the channel. This is consistent with the suspended gold film (top gate) n-doping the SWCNT sections it covers, and that these SWCNT-under-gold sections act as contacts to the channel. We emphasize that we use pure gold films, without any adhesion layer, to create clean SWCNT-Au interfaces. Gold's work function is very close to the threshold, ≈ 5.4 eV, where physisorbed metal films switch from n-doping to p-doping graphene [96] and SWCNTs [118,119]. While gold normally p-dopes SWCNTs, it is well documented that annealing gold removes oxygen from the film and changes its work function [76] such that it becomes n-doping. Fig. 4.2(b) shows transport data from Device B after annealing (suspended gold is n-doping), and Fig. 4.2(c) shows transport data in the same sample after it was re-exposed to oxygen (suspended gold is p-doping). In Fig. 4.2(b), we observe Coulomb blockade diamonds corresponding to a SWCNT-QD whose charge occupation number is controlled by V_G . We note that the current (conductance) is much higher for electron occupation of the QD ($V_G > 0$ V) than for hole occupation of the QD ($V_G < 0$ V). This indicates that the contacts (SWCNT sections under the suspended gold) are n-doped. To acquire the data in Fig. 4.2(c), Device B was warmed up to 295 K and exposed to air to undo the effects of annealing. The transport data show a much higher conductance for hole rather than electron doping of the QD, indicating that the contacts are now p-doped. Fig. 4.2(d) highlights the difference between n and p doping of the contacts by showing $I - V_G$ data extracted at $V_B = 15$ mV from Figs. 4.2(b)–(c).

4.2.1 SWCNT transistor band gaps from transport data

From transport data, it is possible to extract the band gaps and lengths of our SWCNT transistors, as reported in Table 4.1. These parameters are extremely important for our

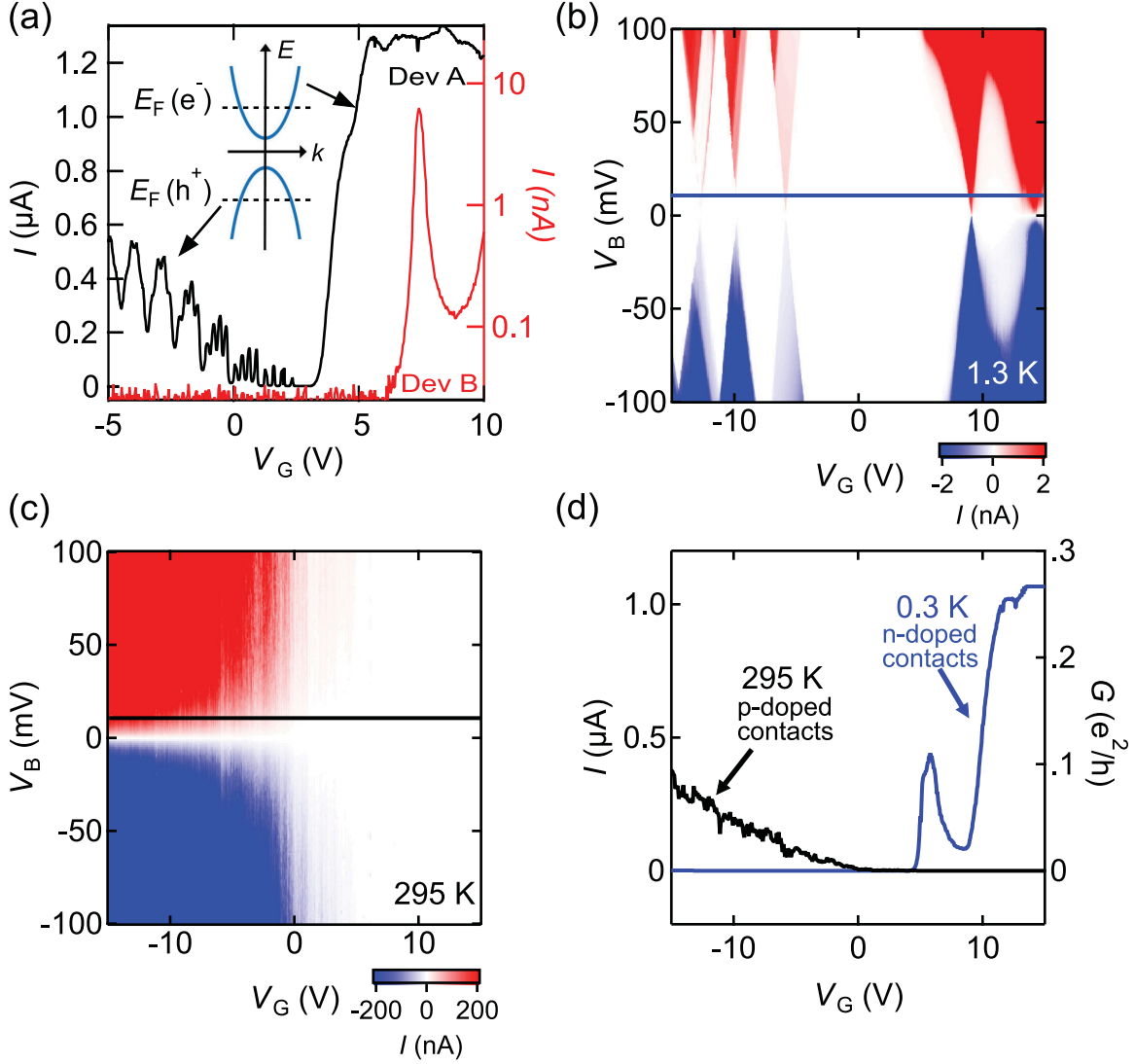


Figure 4.2: Ultra-short nanotube quantum dot transistors with annealed n-type contacts. (a) $I - V_G$ transistor data from Devices A (black) and B (red), at $T = 1.3\text{ K}$ and $V_B = 10\text{ mV}$. We measured a much higher conductance for positive V_G . This indicates that the suspended gold, annealed during the EM, n-dopes the underlying tube. (b)–(c) $I - V_B - V_G$ data from Device B at 1.3 K and 295 K , showing n-doped and p-doped contacts to the SWCNT channel, respectively. The horizontal lines at $V_B = 15\text{ mV}$ correspond to the data in (c) which show higher conductance for electrons at 1.3 K (blue data, annealed gold), and higher conductance for holes at 295 K (black data, oxygen-exposed gold).

analysis of the observed $e - h$ asymmetry. We show differential conductance data for the five devices we report on in Fig. 4.3. To determine the band gaps E_g of the tubes, we use data at the charge neutrality point ($N = 0$) corresponding to the tallest Coulomb blockade diamond. The band gap of a given nanotube can be determined from the following equation:

$$E_g = E_{\text{add}}^{N=0} - E_C - \Delta, \quad (4.1)$$

where E_g is the band gap, $E_{\text{add}}^{N=0}$ is the height of the $N = 0$ diamond, E_C is the charging energy, and Δ is the single particle energy spacing. The contributions of E_C and Δ are often negligible [30], but in our ultra-short devices they are too large to be ignored. These quantities are measured from the Coulomb diamonds in Fig. 4.3. The measured values for E_g , $E_{\text{add}}^{N=0}$, $E_C^{N=-1}$, and Δ^h for all five devices are summarized in Table 4.2 below. Details about the extraction of $E_{\text{add}}^{N=0}$, $E_C^{N=-1}$, and Δ^h are discussed below.

Device	E_g (meV)	$E_{\text{add}}^{N=0}$ (meV)	$E_C^{N=-1}$ (meV)	Δ^h (meV)
A	28 ± 8	79 ± 8	39 ± 2	12 ± 1
B	270 ± 50	450 ± 50	120 ± 10	60 ± 10
C	190 ± 50	230 ± 50	36 ± 4	7 ± 4
D	250 ± 20	410 ± 20	140 ± 3	18 ± 6
E	170 ± 50	280 ± 50	109 ± 7	-

Table 4.2: Band gap of the SWCNT in each reported device. We determine the band gap, E_g , from the parameters $E_{\text{add}}^{N=0}$, $E_C^{N=-1}$, and Δ^h extracted from Fig. 4.3, and using Eqs. 4.2 and 4.4.

The $E_{\text{add}}^{N=0}$ values are the heights of the $N = 0$ diamonds in Fig. 4.3. When the $N = 0$ diamond is too tall to be measured directly, we measure the slopes of the diamonds edges to extract its height. E_C and Δ are carrier type dependent, and we use the hole values because they show less dependence on the number of carrier inside the QD and better represent the $N = 0$ values. The value of $E_C^{N=-1}$ is measured directly from the height of the $N = -1$ diamonds. In a SWCNT-QD showing a 4-fold degenerate diamond pattern (Device A), Δ is given by the difference between E_{add} (diamond height) for an $N = 4n$ diamond and a $N = 4n \pm 1$ diamond [100]:

$$\Delta_{\text{4fold}} = E_{\text{add}}^{N=4n} - \frac{1}{2} (E_{\text{add}}^{N=4n+1} + E_{\text{add}}^{N=4n-1}). \quad (4.2)$$

For Device A, using Eq. 4.2 we find, $\Delta^h = 12 \pm 1$ meV. Because this tube is nearly metallic,

(small band gap), we use the single particle energy spacing for a metallic nanotube [29],

$$L = \frac{\hbar v_F}{2\Delta} \quad (4.3)$$

This gives a device length of 140 ± 10 nm. Considering that Eq. 4.3 is only an approximation for Device A, this length is in reasonable agreement with the SEM measured length of 111 ± 5 nm. It confirms that the channel length when the QD is doped with holes corresponds to the naked SWCNT channel visible in Fig. 4.1(d) and Fig. 4.4.

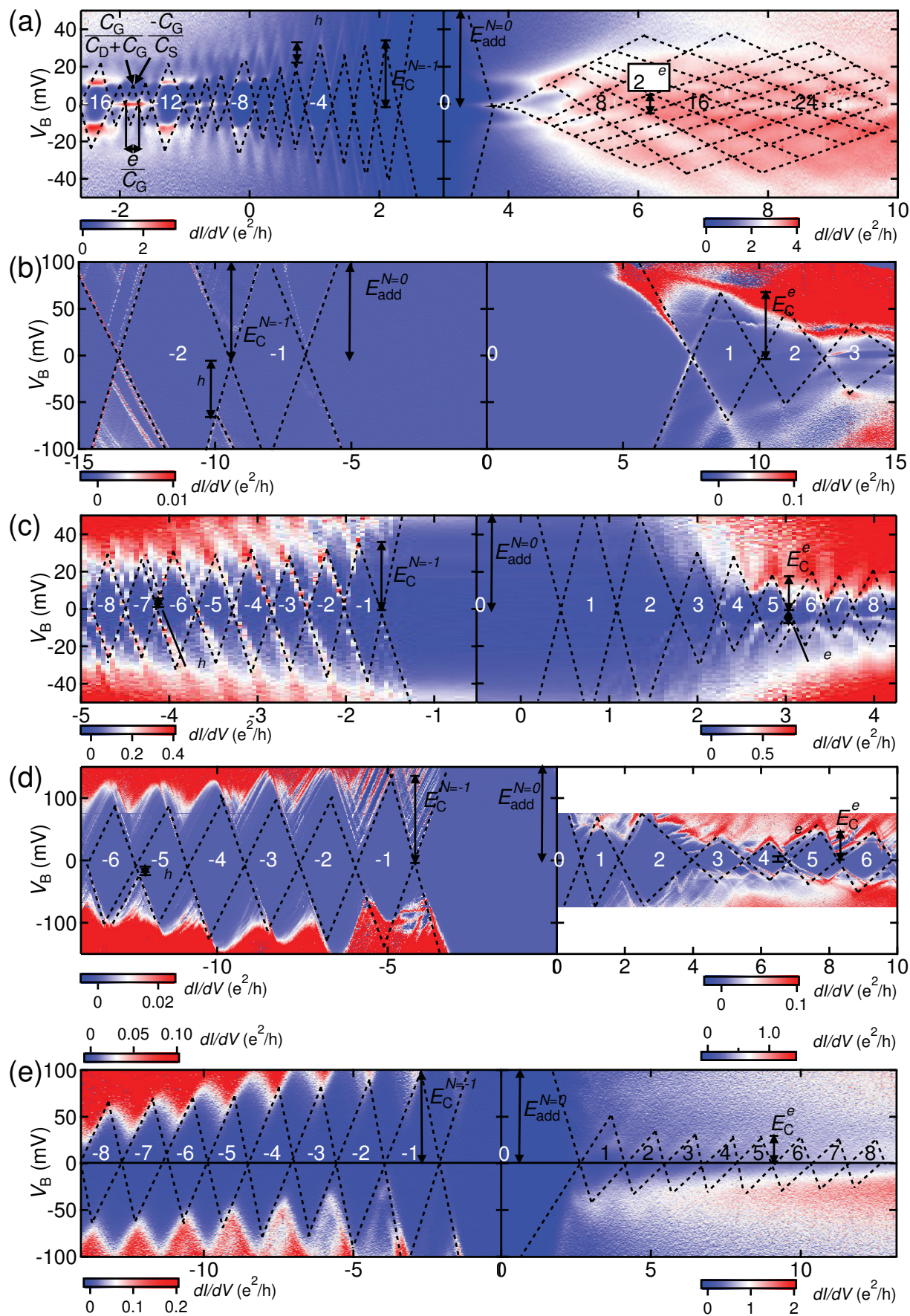


Figure 4.3: (Previous page) $dI/dV_B - V_B - V_G$ data for the five studied SWCNT devices for E_g extraction. (a)–(e) Devices A, B, C, D, and E respectively. $T = 1.3$ K for Devices A, B, C, $T = 4$ K for Device D, and $T = 50$ K for Device E.

When the channel of Device A is electron doped, its transport behaviour no longer shows Coulomb Blockade (Fig. 4.3, right hand side), but rather Fabry-Pérot (FP) oscillations. The spacing of the first set of maxima around $V_B = 0$ gives the energy level spacing, and we find $\Delta^e = 5 \pm 1$ meV. Using Eq. 4.3 gives a FP cavity length of 330 ± 70 nm, which is vastly different from the naked SWCNT channel length (section 4.2.2) but matches the length of the suspended gold gates (Figs. 4.1(b), 4.5).

For 2-fold degenerate QD devices such as Device C and D, Δ is given by Eq. 4.4 below,

$$\Delta_{\text{2fold}} = E_{\text{add}}^{N=4n} + E_{\text{add}}^{N=4n+2} - \frac{1}{2} (2E_{\text{add}}^{N=4n+1} + E_{\text{add}}^{N=4n-1} + E_{\text{add}}^{N=4n+3}). \quad (4.4)$$

In Device C, we measure for hole and electron deltas: $\Delta^h \approx \Delta^e \approx 7$ meV, and in Device D, $\Delta^h \approx \Delta^e \approx 18$ meV. We note that the Δ 's show that the QD channel length is the same for electrons and holes. We do not know the exact shape of the QD confinement potential, because the devices are very short and have significant contact doping. A rough estimate of the device length can be calculated using the measured Δ and a harmonic potential [30], as shown in Eq. 4.5. These lengths are in agreement with the more precise measurements presented below.

$$\Delta = \hbar \sqrt{\frac{4E_g}{m_{\text{eff}}L^2}}, \quad m_{\text{eff}} = \frac{[(\hbar v_F/2L)^2 + (E_g/2)^2]^{3/2}}{(v_F E_g/2)^2} \quad (4.5)$$

4.2.2 Ultra-short lengths of our SWCNT transistors from SEM and transport data

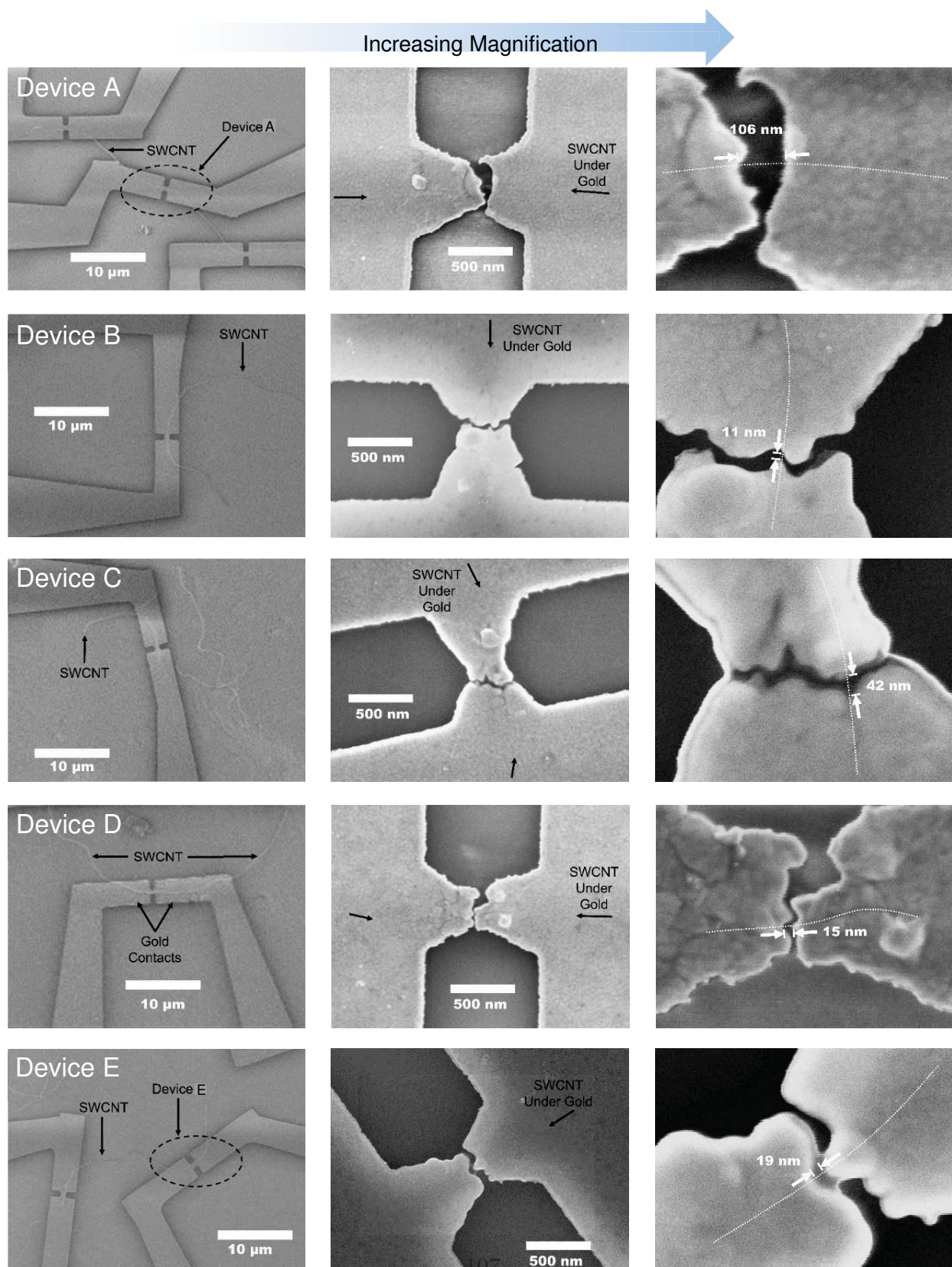


Figure 4.4: (Previous page) SEM images of the five studied SWCNT devices. The device names are on the left, and the magnification of the images increases from the left to the right column. The rightmost images show the SWCNT channels of each device (the dashed lines are guides to the eye).

To analyze our data, it is important to accurately determine the lengths of our ultra-short nanotube channels. We combine information from SEM images and Coulomb diamonds to determine the length of our SWCNT quantum dots.

We captured high resolution SEM images of our devices at nearly all stages of their fabrication. Note that the naked channels were only imaged after the transport data were acquired. In Fig. 4.4, SEM images of each device are shown on a separate row. The images in the left column are superpositions of SEM images before and after deposition of the gold contacts. These before and after deposition images were aligned using the positions of protruding SWCNTs and alignment markers. Using the positions of the nanotubes before metal deposition, we can locate the tube positions after EM (right column). We drew dashed lines on Fig. 4.4 to indicate the SWCNT positions. From the right column images, we measured the lengths of the naked SWCNT channels, L_{SEM} , and summarize the results in Table 4.3.

Device	L_{SEM} (nm)	L_{G} (nm)
A	111 ± 5	102 ± 5
B	14 ± 3	7 ± 5
C	42 ± 7	46 ± 8
D	16 ± 4	13 ± 5
E	24 ± 8	15 ± 5

Table 4.3: Channel lengths. L_{SEM} and L_{G} for all five SWCNT devices studied.

From the widths of the Coulomb diamonds (Fig. 4.3), we determined the gate capacitance of each device using $C_{\text{G}} = e/\Delta V_{\text{G}}$, where ΔV_{G} is the width of the odd Coulomb diamonds and e is the elementary charge. The capacitance of a back-gated SWCNT devices is modeled as a wire over a plane using:

$$\frac{C_{\text{G}}}{L_{\text{G}}} = \frac{2\pi\epsilon}{\cosh^{-1} \frac{t}{r}}, \quad (4.6)$$

where L_{G} is the length of the wire, ϵ is the permittivity of the insulator, t is the thickness of the insulator, and r is the radius of the wire. In our devices, the dielectric spacer is made of

two thin films in series: vacuum and SiO₂. For Device A, $C_G = 0.59 \pm 0.04$ aF, $t_{\text{ox}} = 202$ nm, $t_0 = 126$ nm, and $r \approx 3$ Å. The gate capacitance is given by [10]:

$$\frac{C_G}{L_G} = \frac{2\pi\epsilon_{\text{ox}}}{\frac{\epsilon_{\text{ox}}}{\epsilon_0} \cosh^{-1} \frac{t_0}{r} + \cosh^{-1} \frac{t_0+t_{\text{ox}}}{r+t_0}} \quad (4.7)$$

Where ϵ_{ox} , ϵ_0 are the permittivities, and t_{ox} , t_0 the thickness of the oxide and vacuum spacers respectively.

We measured the oxide thickness using ellipsometry before and after the buffered oxide etch, and measured the nanotube diameter using an atomic force microscope (AFM). The relevant device parameters for capacitance modeling are summarized in Table 4.4. Using these values and Eq. 4.7, we calculated the electrostatic lengths, L_G , of the SWCNT-QD which are summarized in Table 4.3 above. We note that AFM tends to underestimate SWCNT diameters, and thus the measured radius values, r , should be considered as lower bounds. However, the calculated values of L_G depend only very weakly on precise values of r .

Device	C_G (aF)	t_{ox} (nm)	t_0 (nm)	r (Å)
A	0.59 ± 0.04	202	126	≈ 3
B	0.05 ± 0.01	170	134	≈ 3
C	0.41 ± 0.07	169	139	≈ 13
D	0.11 ± 0.01	172	135	≈ 8
E	0.12 ± 0.01	170	134	≈ 5

Table 4.4: Gate capacitance parameters, measured for the five studied SWCNT devices. These parameters are used in Eq. 4.7 to determine the electrostatic lengths, L_G , of the SWCNT QDs.

The gate capacitance, C_G , was extracted by averaging over all odd diamonds for $|V_G| > 6$ V, where the widths are roughly constant and unaffected by the quantum energy level spacing Δ . Comparing the values of L_G to L_{SEM} in Table 4.3 we see a strong agreement.

4.2.3 Suspended SWCNT-QD transistors with annealed contacts

With this knowledge of the lengths and band gaps of our devices, we can investigate the contact effects in our ultra-short SWCNT-QDs in greater quantitative detail. Close inspection of the gold surface reveals that the suspended portion of the gold film changes texture after the EM, as shown in In Fig. 4.5(a). We corroborate the suspension lengths of our devices by

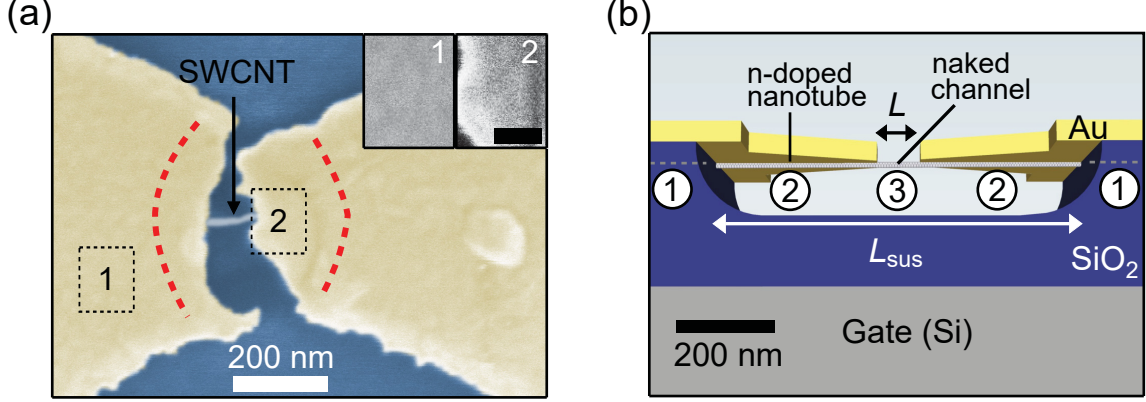


Figure 4.5: Ultra-short nanotube quantum dot transistors with annealed suspended contacts. (a) False colored top-view SEM image of Device A, showing not annealed (1) and annealed (2) sections of the film corresponding to the on-substrate and suspended sections of the break junction. Insets 1 and 2 correspond to the boxes in the main panel and show the film texture after the EM, for the on-substrate and suspended gold, respectively. Black scale bar is 100 nm and applies to both insets. (b) Geometry of our suspended SWCNT transistors. The labels 1, 2, and 3 refer respectively to the disordered on-substrate nanotube sections, the n-doped gold-covered suspended SWCNT sections, and the naked SWCNT channel.

investigating this texture. During the gold electromigration (EM), the portion of the gold film which is substrate-supported is heat-sunk and not annealed. This substrate-supported gold film shows a standard polycrystalline texture, as shown in inset 1 of Fig. 4.5(a). During the EM, Joule heating raises the temperature of the suspended gold to a few hundred degrees Celsius [92] and anneals the gold into a more uniformly textured film as shown in inset 2 of Fig. 4.5(a). The boundaries of this gold texture change are shown in the main panel of Fig. 4.5(a) (Device A) with dashed red lines. Using these boundaries to measure the suspension length, we find a good agreement with the length from tilted SEM (Fig. 4.1(b)).

The electronic interactions between an ultra-clean SWCNT and gold are weak [120] and the density of states in the SWCNT is unaffected by the gold film. This is because SWCNT electronic wavefunctions have large wavevectors, and the conservation of momentum suppresses the tunnelling matrix elements between these high-momentum states and gold states [121]. It follows that the injection length for an electron to tunnel between gold and the SWCNT is very long (μm) [120, 122]. Electrostatic disorder leads to stronger SWCNT-gold interactions and shorter injection lengths [120, 121]. This knowledge is necessary to describe the electron transport in the gold covered sections of our SWCNTs, and the device design shown in Fig. 4.5(b). The gold film covering the SWCNT sections ① is thermally anchored to the substrate, and not annealed during the EM process. This leaves the sections ① acting as diffusive (disordered) contacts where the gold-SWCNT coupling is stronger [120]

and most of the electrons are injected from gold into the SWCNT [29, 114, 123, 124]. The suspended gold film covering the tube sections labeled ② is annealed as evidenced from both transport data and the film texture (Fig. 4.2(a), Fig. 4.5(a)). Finally, the naked SWCNT channel labelled ③ is thoroughly annealed by the EM process [10, 91] and can be doped with either holes or electrons via V_G . The data presented below will demonstrate that the charge transport is ballistic in both sections ② and ③ of the SWCNTs, and that $e - h$ asymmetric tunnel barriers form where the two sections connect.

The left hand side of Fig. 4.6(a) shows an example of the band diagram for the SWCNT contacts (sections ②), and the right hand side shows the bands in the naked channel (section ③). The dashed lines indicate the positions of the Fermi energies $E_{F,1}$ and $E_{F,2}$ in each section, and their shifts $\Delta E_{F,1}$ and $\Delta E_{F,2}$ away from the center of the band gap. The band gap has the same value in both SWCNT sections since they belong to the same tube. The carbon nanotube's (CNT's) electron affinity, χ_{CNT} , is defined as the energy between the bottom of the conduction band and the vacuum energy, E_{vac} . On the left side of Fig. 4.6(a), gold transfers charges to the SWCNT and moves $E_{F,1}$ up from the center of the gap. The exact amount of doping varies depending on the crystalline orientation of the gold as well as the quality of annealing (oxygen content). The relevant values of $\Delta E_{F,1}$ for our devices are reported to range from 0.05 to 0.2 eV [118, 119, 122, 126, 127], and we use a median value of 0.12 eV to draw our band diagrams. The gold film can also modify the nanotube's electron affinity by $\Delta\chi$. This shift is expected to be 0.03 – 0.05 eV [119, 126], and we use 0.05 eV to draw the bands in our devices. These parameters correctly predict several features of the data below, such as the presence or absence of a barrier, the sign of the $e - h$ charging energy asymmetry, and correlate with the magnitude of the asymmetry. Moreover, the discussion and conclusions below remain valid over the range of reported $\Delta E_{F,1}$ and $\Delta\chi$ values. The Fermi energy of the naked SWCNT channel, $E_{F,2}$, can be tuned using V_G . The gating efficiency of the back gate (dielectric of 130 nm vacuum plus 170 nm SiO_2) is much weaker than the gating efficiency of the gold film (top gate) which is only three angstroms away from the SWCNT [119]. This means that the back gate does not significantly affect $E_{F,1}$, but only effectively tunes $E_{F,2}$. This is confirmed by the transport data below showing that the lengths (confinement) of the SWCNT-QDs are independent of V_G . At the junctions between the tube sections ② and ③, these band diagrams in Fig. 4.6(a) and (c) for hole and electron transport are brought into contact and equilibrate to form homojunctions.

Using Andersons rule [125], we draw the approximate shape and height of the barriers forming at the homojunctions between the gold-covered and bare SWCNT suspended sections

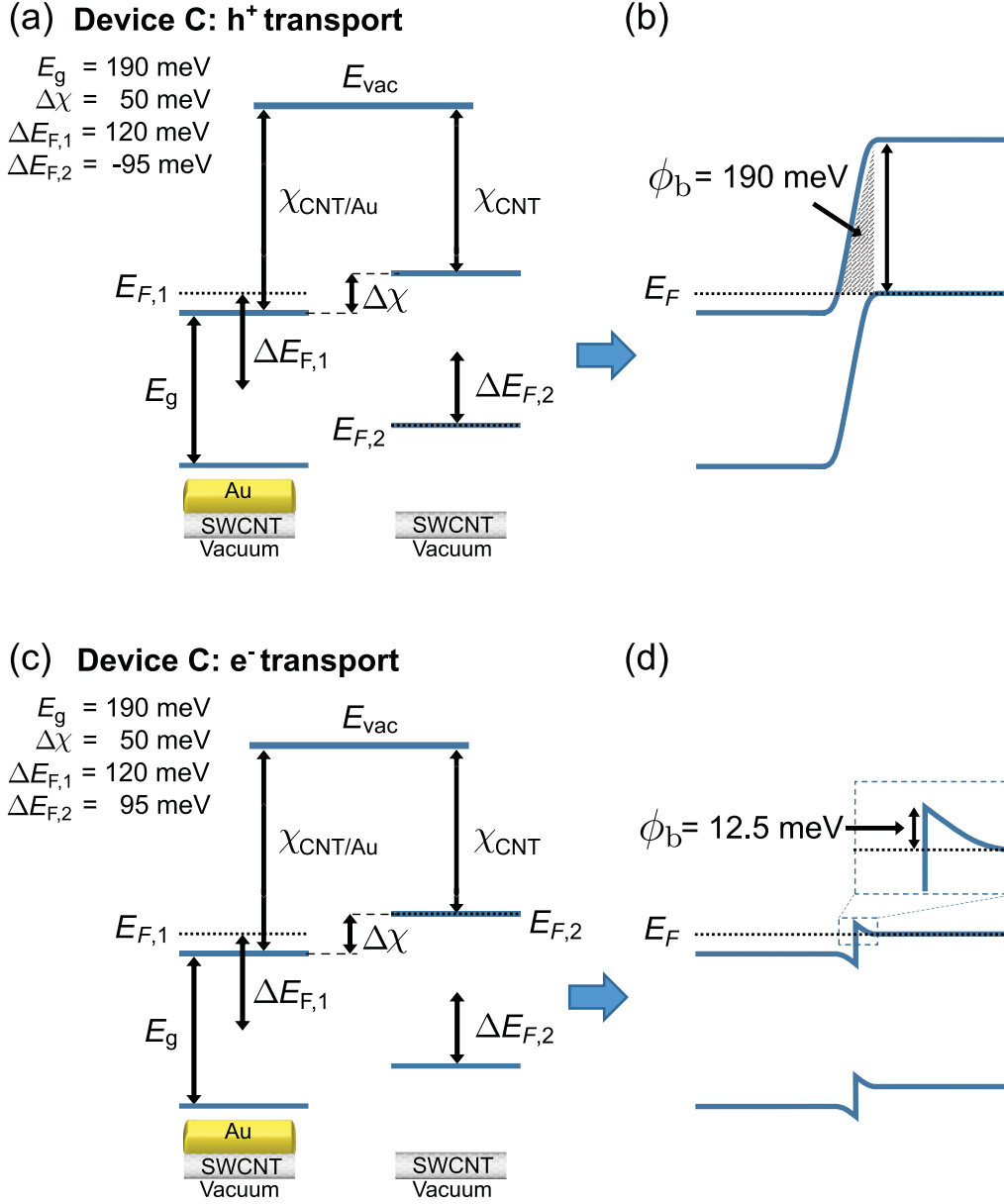


Figure 4.6: Schematic of the barriers between the naked and gold-covered SWCNT sections. (a) The electronic bands in the gold-covered (left) and naked (right) suspended tube sections for a hole-doped channel. The quantity E_g is the band gap. The quantities $E_{F,1}$, $E_{F,2}$, $\Delta E_{F,1}$, $\Delta E_{F,2}$ are the Fermi energies and the Fermi energy shifts from the center of the band gaps in the gold-covered and naked nanotube, respectively. $\chi_{CNT/Au}$ and χ_{CNT} are the electron affinities in the gold-covered and naked sections, while $\Delta\chi$ is the electron affinity difference between the two. Schematic of the barriers in Device C when the naked channel is (a)–(b) hole-doped, and (c)–(d) electron-doped. Panels (a) and (c) show the bands in the two SWCNT sections (gold-covered and naked) before they are allowed to equilibrate. The naked channel is doped using the back gate voltage, and there is a small electron affinity difference of $\Delta\chi$ between the two SWCNT sections. Panels (b) and (d) show the junctions when the two sections equilibrate. The bands are aligned using Andersons rule [125].

(Fig. 4.6(b) and(d), Figs. 4.7(a)–(b) and 4.8(a)–(b). There are two needed input parameters, which we do not directly measure, to draw these diagrams: $\Delta E_{F,1}$ and $\Delta\chi$. The former is the displacement of the SWCNTs Fermi level underneath the annealed-gold film. The exact amount of doping, $\Delta E_{F,1}$, varies depending on the crystalline orientation of the gold as well as the quality of annealing (oxygen content). The relevant values for our devices are reported to range from 0.05 to 0.2 eV [118, 119, 126], and we used a median value of 0.12 eV to draw our band diagrams. The gold film also modifies the nanotube’s electron affinity by $\Delta\chi$. This shift is expected to be around 0.03 – 0.05 eV [119, 126], and we used 0.05 eV to draw the bands. We note that our conclusions are valid over a broad range of values for $\Delta E_{F,1}$ and $\Delta\chi$; and the transport data presented and discussed in the main text offer strong support for the band alignments in Figs. 4.6, 4.7, and 4.8.

The other quantities needed to draw the band diagrams are E_g (measured in section 4.2.1), and the Fermi level displacement $\Delta E_{F,2}$ in the naked channel which was tuned experimentally using V_G to match $\Delta E_{F,2} = \pm E_g/2$. We note that the asymmetric barrier heights for holes and electrons (Table 4.5) correctly predicts the sign of the electron-hole charging energy asymmetry for all devices (Table 4.6). It also predicts correctly the presence or absence of a barrier in all devices, and the qualitative magnitude of the asymmetry is correctly captured. Our conclusions are insensitive to the quantitative details of the barrier shapes and heights.

Device	E_g (meV)	ϕ_b^e (meV)	ϕ_b^h (meV)
A	28	0	28
B	270	27.5	270
C	190	12.5	190
D	250	27.5	250
E	170	7.5	170

Table 4.5: Estimated barrier heights in each reported device. The barrier heights are ϕ_b^e and ϕ_b^h for e^- doping and h^+ doping of the channel, respectively. The qualitative asymmetries of the barrier heights agree with the observed charging energy asymmetries (Table 4.6) for all devices

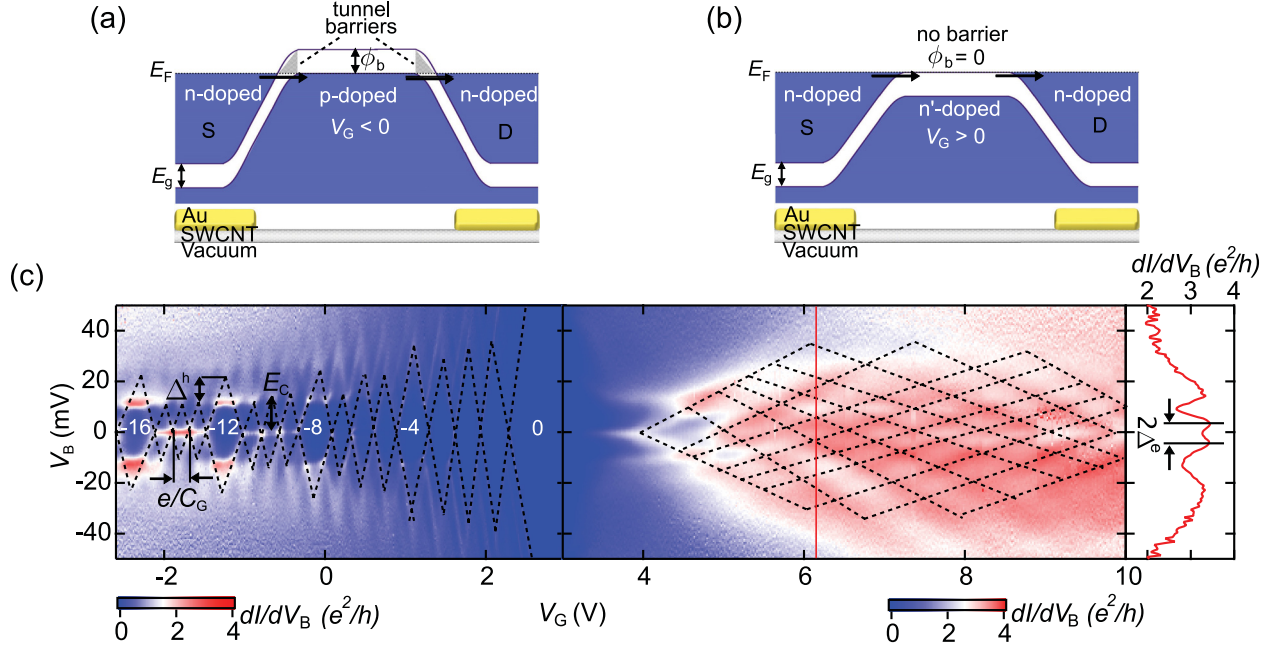


Figure 4.7: Electron-hole transport asymmetry and ballistic contacts. (a)-(b) Schematics of the bands at the junctions between the n-doped (gold-covered) nanotube contacts and naked channel in Device A ($E_g = 28$ meV) when the channel is (a) p-doped and (b) n-doped. Band-to-band tunnel barriers (shaded triangles) of height $\phi_b = E_g$ form between the nanotube contacts and the p-doped channel. On the other hand, when the naked channel is n-doped $\phi_b = 0$. (c) Charge transport data ($dI/dV_B - V_B - V_G$) for Device A at $T = 1.3$ K. The charge neutrality point of the channel is clearly visible around $V_G = 3$ V. A striking asymmetry is visible in the transport data between hole doping ($V_G < 3$ V) and electron doping ($V_G > 3$ V) of the channel. For hole doping, a four-fold Coulomb diamond structure indicates a single quantum dot (QD). The gate-to-QD capacitance C_G corresponds to a channel length of 102 ± 5 nm, closely matching L_{SEM} in Fig. 4.1(d). Under electron-doping, the transport data show clear Fabry-Pérot quantum interferences (see inset). The spacing between conductance maxima in V_B is 5 ± 1 mV, giving $L_{FP} = 330 \pm 70$ nm. This matches the suspension length of the gold film $L_{sus} = 350 \pm 70$ nm (Fig. 4.1(b)). It confirms that the transport in the suspended gold-covered nanotube sections is ballistic and preserves the quantum phase of the electrons travelling through the channel.

4.3 Ultra-short suspended SWCNT-QD transistors with ballistic contacts

Figure 4.7(a)–(b) show schematics of the homojunctions in Device A, $E_g = 28$ meV. Figure 4.7(a) shows the band alignment when the channel is hole doped, while Fig. 4.7(b) shows the electron doping configuration. Tunnel barriers form at the contacts when the channel is p-doped. The transport mechanism across the barriers in Fig. 4.7(a) is band-to-band tunnelling, and has been previously described for SWCNT transistors [101,128]. Approximating the shape of the bands at the homojunctions using the WKB (Wentzell-Kramers-Brillouin) model [129] (shaded triangular regions), the tunnel barrier height is $\phi_b = E_g = 28$ meV. When the channel is electron doped (Fig. 4.7(b)), the charge transport only involves the conduction band, and there is no tunnel barrier. Low-temperature ($T = 1.3$ K) transport data from Device A are shown in Fig. 4.7(c), where the color scales show the differential conductance dI/dV_B as a function of V_G and bias voltage V_B . The negative (positive) integer labels N indicate the number of holes (electrons) in the SWCNT channel. Under hole-doping of the channel, clear Coulomb blockade diamonds indicate quantum dot transport. When the channel is electron-doped, transport data along the V_G and V_B directions show strong Fabry-Pérot interferences characteristic of ballistic transport [29,124]. The dramatic asymmetry in quantum transport between holes (quantum dot) and electrons (ballistic channel) is a consequence of the different contact barriers for the two types of doping. A closer look at the data in Fig. 4.7(c) will confirm the device geometry shown in Fig. 4.5(b).

On the left hand side of Fig. 4.7(c), we observe four-fold quantum degeneracy [100] of the hole-doped QD energy levels. We extract an energy level spacing for holes of $\Delta^h \approx 12 \pm 1$ meV (height difference between neighbouring tall and short diamonds), and a charging energy $E_C^h = 11 \pm 1$ meV (height of short diamonds). The width of the Coulomb diamonds for holes is 0.21 ± 0.01 V $= e/C_G$, where C_G is the capacitance between the QD and back-gate. We obtain a QD length, $L_G = 102 \pm 5$ nm, from the measured C_G using the wire over a plane capacitor model discussed in section 4.2.2.

The length of $L_G = 102 \pm 5$ nm extracted using this model closely matches the length of the channel as measured by SEM, $L_{\text{SEM}} = 111 \pm 5$ nm. We note that on average in our samples $L_G < L_{\text{SEM}}$ is expected due to the two finite width p-n or n-n' junctions at each end of the QD. Comparing the measurements of L_G and L_{SEM} in all devices (Table 4.1), we find an average p-n junction length of $L_{\text{pn}} = 3 \pm 1$ nm. An independent estimate of L_{pn} is obtained from the SWCNT screening length [120], $\lambda = \sqrt{(\epsilon_{\text{CNT}}/\epsilon_{\text{vac}})d_{\text{CNT}}d_{\text{vac}}}$, where

$\epsilon_{\text{CNT}} \approx 10$ is the SWCNT permittivity [130], $d_{\text{CNT}} \sim 1.3$ nm is the tube diameter, $\epsilon_{\text{vac}} = 1$ is the permittivity of vacuum, and $d_{\text{vac}} \approx 0.3$ nm [119, 131] is the thickness of the vacuum dielectric between the tube and gold. This gives $\lambda \approx 2$ nm, matching the L_{pn} extracted above. It is remarkable that we can think of the suspended (annealed) gold film as a gate electrode for the SWCNT, with a dielectric spacer of 3 Å, offering the possibility to create extremely sharp p-n junctions. This capability will find applications in testing the ultimate downscaling of SWCNT transistors [91, 132], and creating nm-sized phase coherent electronic devices [100, 108, 133, 134] and NEMS [10, 11, 103–105].

While the suspended gold gates in Device A confine holes to a QD of length $L_G = 102$ nm, they do not confine electrons inside the naked channel. Using the transport data in the vertical line cut of Fig. 4.7, we measure an energy level spacing $\Delta^e = e\Delta V_B = 5 \pm 1$ meV between the interference maxima. We extract the length of the electron cavity as $L_{\text{FP}} = \hbar v_F / (2\Delta^e) = 330 \pm 70$ nm, where $v_F = 8 \times 10^5$ m s⁻¹ is the Fermi velocity. This cavity length matches the suspension length of the gold gates, $L_{\text{sus}} \approx 350 \pm 70$ nm (4.1(b) and Fig. 4.2(c)). The coherent FP interferences and cavity length confirm that the majority of the current in the contact sections ② flows through the SWCNT and not the gold film. This is expected due to the long charge injection length in ultra-clean SWCNTs [120, 122, 131]. The FP interferences also imply that the annealed gold covering sections ② does not prevent ballistic transport in the underlying SWCNT [135], and we do not detect any backscattering at the interfaces between sections ② and ③. Thus, the naked channel is very nearly ballistic and we extract a very conservative upper bound for its charging energy from the longer FP cavity. Using an open QD model [124] for the cavity formed by sections 2 and 3 together, we extract an approximate electron charging energy of $E_C^e \sim 0.1$ meV, giving a charging energy asymmetry ratio $\eta_{e-h} = E_C^h / E_C^e \gtrsim 100$. We note that previously reported SWCNT devices which showed QD to FP $e-h$ asymmetry [114, 123, 136] were not fabricated with suspended and annealed gold films, and thus had equal channel lengths for holes and electrons. The important new information in Fig. 4.7(c) are that the annealed gold film acts as a local top gate creating ballistic SWCNT contacts and a gate programmable QD-to-ballistic transistor with vastly different channel lengths under electron and hole doping. Specifically, applying a small V_G to Device A toggles between a 102 nm QD and a 330 nm ballistic wire. In the following section, we demonstrate in SWCNT-QD transistors, whose L_G ranges down to 7 nm and E_g up to 270 meV, that a large $e-h$ transport asymmetry creates QDs with two E_C 's.

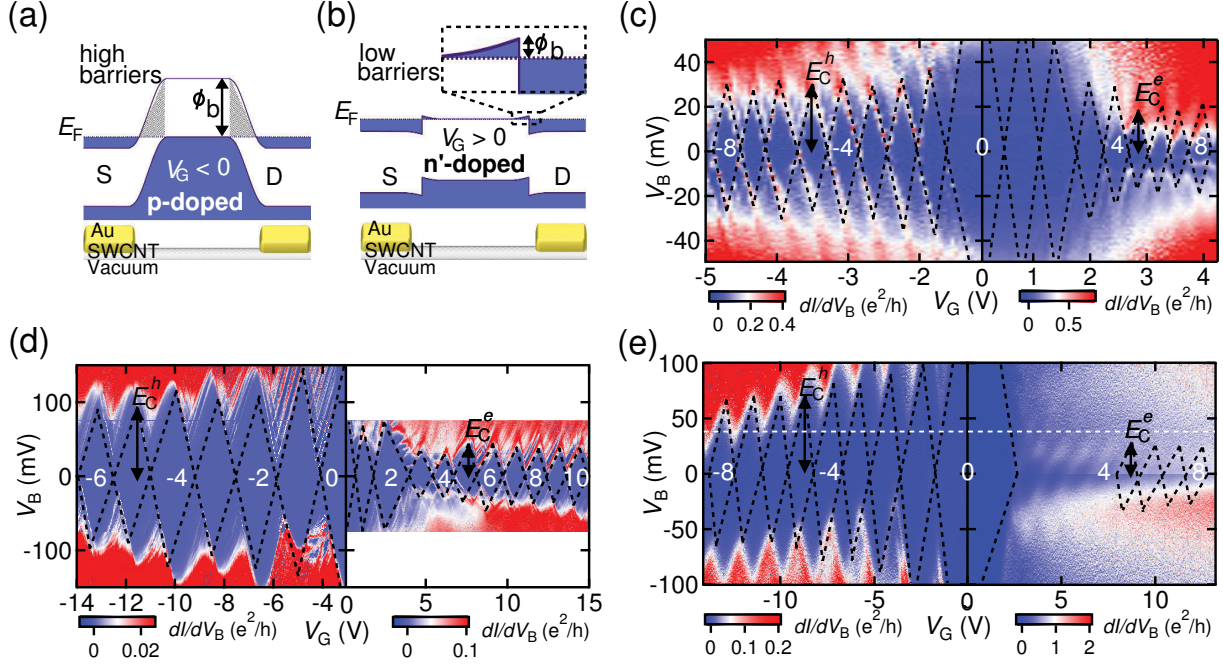


Figure 4.8: Giant $e-h$ charging energy asymmetry in 200 meV band gap nanotube quantum dots. (a)–(b) Schematics of the junctions between the n-doped nanotube contacts and naked tube channel in Device C, $E_g = 190$ meV. (a) When the channel is p-doped, the band-to-band tunnel barriers (shaded triangles) have a height $\phi_b = 190$ meV. (b) When the channel is n-doped, the tunnel barriers are much smaller, $\phi_b \sim 12$ meV (Fig. 4.6). (c)–(e), $dI/dV_B - V_B - V_G$ transport data for Devices C, D, and E respectively ($T = 4.0$ K, 1.3 K and 50 K). In all devices, clear Coulomb diamonds are visible for both hole and electron channel dopings, and show the formation of a single quantum dot in the channel. The charging energies, i.e. heights of the odd-labelled diamonds, are much larger for holes than for electrons due to the tunnel barrier asymmetry.

4.4 Giant $e-h$ charging energy asymmetry in 200 meV band gap SWCNT-QDs

For room-temperature applications and to explore many-body QD physics, we would like to extend the ability to create large $e-h$ transport asymmetry to SWCNT transistors whose E_g 's are larger than in Device A. We studied four larger E_g devices whose naked channels host single QDs whether they are doped with holes or electrons. The heights of the QD contact barriers for the two doping configurations are vastly different and lead to two different E_C 's.

Figure 4.8(a)-(b) show the homojunctions forming at the interfaces between the contacts and channel in Device C. When the channel is hole doped (Fig. 4.8(a)), tall tunnel barriers

of $\phi_b \approx E_g = 190$ meV form where the contacts (sections ②) meet the SWCNT channel (sections ③). Figure 4.8(b) shows the configuration when the channel is electron doped. The transport across the n-n' junctions only involves the conduction band, and the barriers are much smaller, $\phi_b \approx 12$ meV. This $e-h$ barrier height asymmetry creates an $e-h$ asymmetry of the source-QD and drain-QD capacitances, C_S and C_D respectively. It follows that the QD charging energy $E_C = e/(C_S + C_D + C_G) = e/C_\Sigma$, depends on whether the QD is populated with holes or electrons. This is visible in Fig. 4.8(c)–(e) where $dI/dV_B - V_B - V_G$ data for Devices C, D and E are shown. The Coulomb diamond heights in Fig. 4.8(c)–(e), i.e. the addition energies $E_{\text{add}} = E_C + \Delta$, are much larger for holes (left) than for electrons (right).

We use the data in Fig. 4.8 to quantify both the $e-h$ charging energy asymmetry $\Delta E_C^{e-h} = E_C^h - E_C^e$ and in turn the asymmetry ratio $\eta_{e-h} = E_C^h/E_C^e$. We first extract the addition energy, E_{add} , versus N for all five devices from the data in Fig. 4.8 and show these numbers in Fig. 4.9. The black circles in Fig. 4.9 show E_{add}^h , while the red circles show E_{add}^e . We then interpolate (dashed lines) E_{add} using only the odd- N values, because $E_{\text{add}} = E_C$ for odd N , and Devices C, D, and E show a two-fold degenerate energy spectrum. These interpolations show the values of E_C^h and E_C^e vs. N (except for E_C^e in Device A which must be calculated using an open-QD model [124]). We observe that E_C first drops quickly with increasing N and then stabilizes, converging to a roughly constant value at large N . To avoid this strong dependence at low N , we extract E_C^h and E_C^e at $N = 5$ for all devices, except Device B where we use $N = 1$ since the data set does not include $N = 5$. We calculate the relative charging energy asymmetry, $\eta_{e-h} = E_C^h/E_C^e$, as shown in Table 4.6. We verified that

Device	$\eta_{e-h}(N = 5)$
A	$\gtrsim 100$
B	2.6
C	1.5
D	2.1
E	2.5

Table 4.6: Electron-hole charging energy asymmetry ratios for the five studied SWCNT devices $\eta_{e-h} = E_C^h/E_C^e$.

the η_{e-h} asymmetry is not strongly dependent on the details of the analysis. For instance we find almost identical η_{e-h} if we compare the charging energies corresponding to diamonds located around $V_G = \pm 6$ V instead of at $N = 5$.

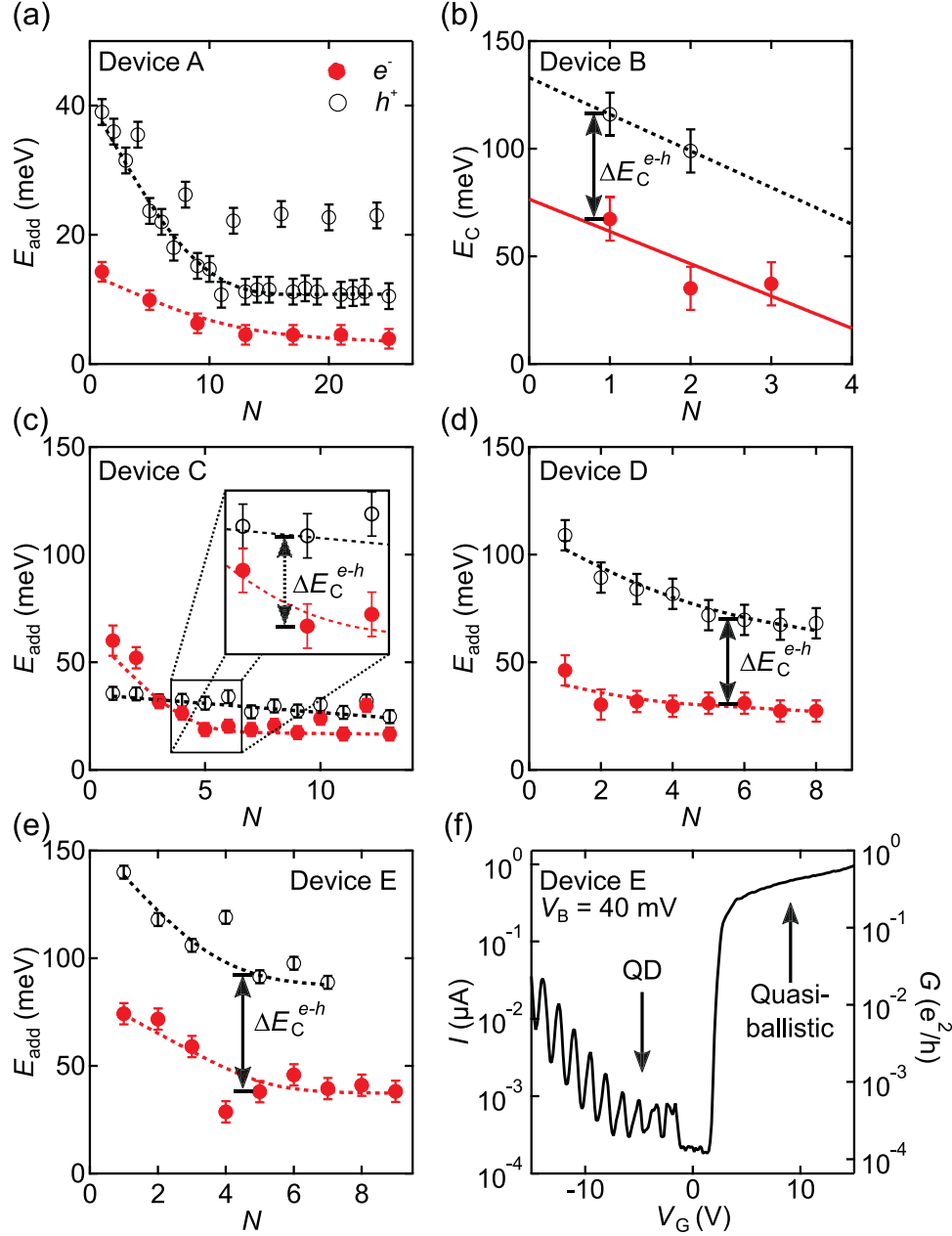


Figure 4.9: Extraction of addition and charging energies from each device vs. charge number. (a)–(e) E_{add} = height of diamonds, versus charge number, N , for both holes (open black data) and electrons (filled red data) in Devices A–E respectively. The data for odd N , for which $E_{\text{add}} = E_C$, are interpolated with dashed lines except in panel (b) where they are linear fits to the data. The charging energies decrease with increasing N , and a clear offset, ΔE_C^{e-h} is visible between hole and electron data. The value of ΔE_C^{e-h} becomes roughly constant at large N . The error bars represent the uncertainty in the extracted E_{add} , and stem from the limited resolution of the Coulomb diamond heights in Figs. 4.3 and 4.8)(c)–(e). The relative charging asymmetry η_{e-h} is calculated from the interpolations at $N = 5$ ($N = 1$ for Device B). (f) $I - V_G$ data for Device E at $V_B = 40$ meV (along white dashed line in Fig. 4.8).

While the E_g for all three of these devices are comparable, the channels in Devices D and E are three times shorter than in Device C. Both Devices D and E have significantly larger η_{e-h} than Device C, and this correlation is also confirmed by Device B (Table 4.3). We thus conclude that η_{e-h} scales inversely with length. This explains why we can observe large η_{e-h} in ultra-short QDs whose band gaps range up to 270 meV, while previous experiments [30] on much longer QD devices (few 100s of nm) showed $\eta_{e-h} \approx 1$ in devices with similar band gaps. Figure 4.9(f) shows $I - V_G$ data for Device E at $V_B = 40$ meV. We observe that similarly to Device A (Fig. 4.7), it is possible to toggle this large band gap, $E_g = 170$ meV, and very short, $L_G = 15$ nm, device from behaving as a QD to a nearly ballistic bus by applying modest V_G . To further understand the length dependence of η_{e-h} , it is useful to analyze the capacitances of the SWCNT-QDs versus L_G .

4.5 Origin and length dependence of the electron-hole asymmetry

In Fig. 4.10(a)–(b), the data in black (red) are for hole (electron)-doped channels. Figure 4.10(a) shows C_G extracted from the widths of the $N = 5$ Coulomb diamonds for all devices versus L_G (except for Device B, where only $N = 1$ is available). C_G is the same for hole or electron occupations of the QD and ranges from ≈ 0.05 to 0.6 aF. As expected, C_G scales linearly with L_G . Figure 4.10(b) shows the total QD capacitance $C_\Sigma = C_S + C_D + C_G$ extracted from the slopes of the diamonds in Figs. 4.7 and 4.8 as a function of L_G (Table 4.3). There is a marked $e - h$ asymmetry between the total capacitances for holes and electrons, which we label $\Delta C_\Sigma^{e-h} = C_\Sigma^e - C_\Sigma^h$. Figure 4.10(c) shows that both the relative capacitance asymmetry $\Delta C_\Sigma^{e-h}/C_\Sigma^h$ (left axis) and the resulting η_{e-h} (right axis) decrease rapidly with L_G for Devices B, C, D, and E which all have similar band gaps.

We can also isolate the qualitative effect of E_g on η_{e-h} . A length change of a factor of three between Devices C, D, and E (similar E_g 's) changes η_{e-h} by less than a factor of 2. An even smaller length difference between Devices A (Fig. 4.7(c)) and C (Fig. 4.8(c)), but coupled with an order of magnitude change in E_g , leads to a difference of two orders of magnitude in η_{e-h} . The change in η_{e-h} between Devices A and C can thus be predominantly ascribed to their different E_g 's. This inverse dependence of η_{e-h} on E_g can be understood by inspecting Fig. 4.7(a)–(b). The relative $e - h$ barrier height asymmetry decreases rapidly as E_g increases and becomes larger than the doping $\Delta E_{F,1}$ induced by the gold gates.

Because the values of E_C and ϕ_b in our SWCNT-QD transistors are large compared to

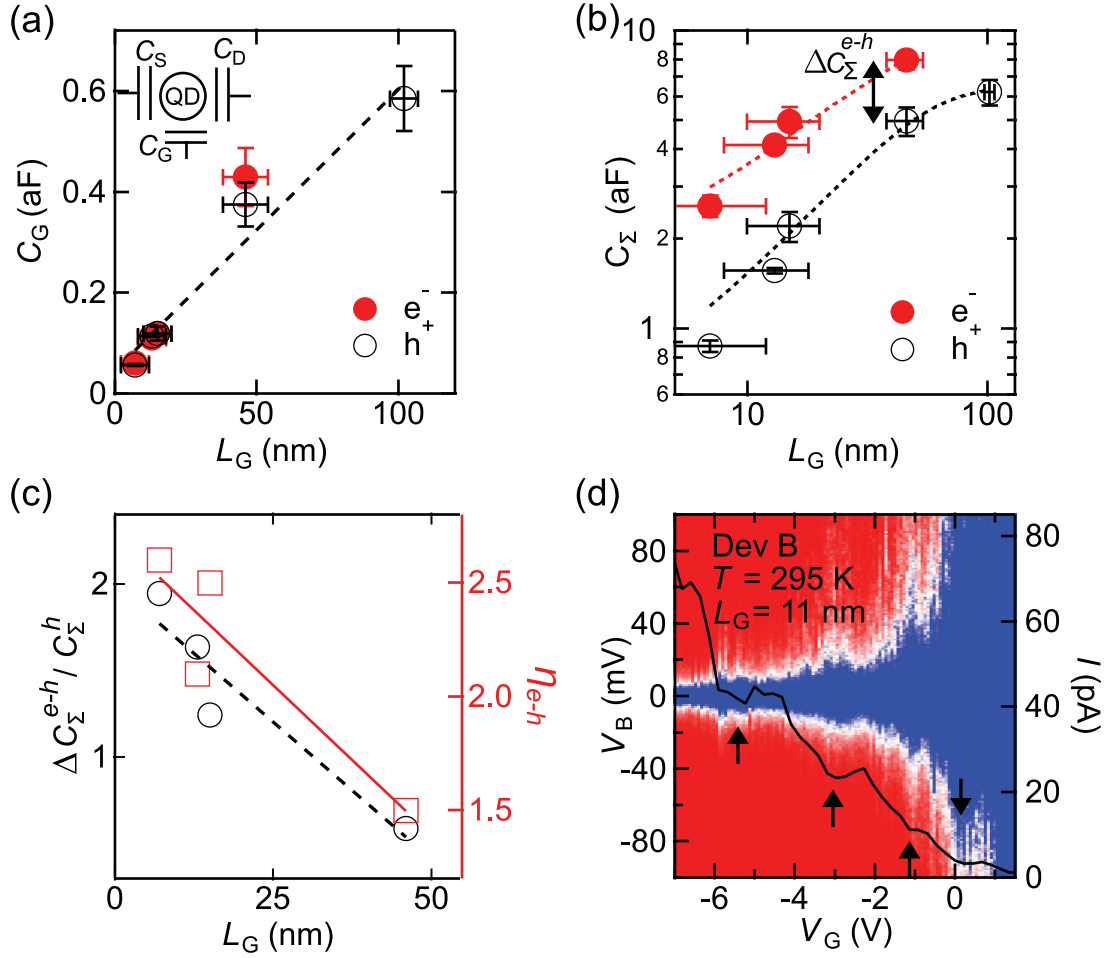


Figure 4.10: Origin of the $e-h$ charging energy asymmetry. (a) The gate-to-dot capacitance, C_G , in our devices is $e-h$ symmetric and scales linearly with L_G . The inset cartoon of the quantum dot (QD) devices shows the lumped element interpretation of C_G , C_S , and C_D . The error bars represent the uncertainty in the widths of the Coulomb diamonds in the transport data of Fig. 4.8 and 4.8. (b) The total QD capacitance C_Σ increases approximately linearly as a function of L_G in our devices. A clear capacitance offset ΔC_Σ^{e-h} is visible between the hole and electron data due to the $e-h$ tunnel barrier asymmetry. This offset is at the origin of the $e-h$ charging energy asymmetry. The error bars represent the uncertainty in the total QD capacitance stemming from the uncertainties in the slopes of the Coulomb diamonds in the transport data of Figs. 4.8 and 4.8. (c) The relative $e-h$ capacitance asymmetry $\Delta C_\Sigma^{e-h}/C_\Sigma^h$ decreases with increasing L_G , and explains why $\eta_{e-h} = E_C^h/E_C^e$ also decreases with increasing L_G . The dashed and solid lines are linear fits of the data. (d) $I - V_B - V_G$ data in Device B at 295 K with a superimposed $I - V_G$ data cut, $V_B = 10$ mV. The spacing of the conductance oscillation (black arrows) gives $L_G \approx 11$ nm.

$k_B T_{\text{room}}$, we can envision making use of the $e-h$ transport asymmetry in room temperature QD devices. Figure 4.10(d) shows $I-V_B-V_G$ data for Device B at 295 K, with a superimposed $I-V_G$ trace taken at $V_B = 10$ mV. The SEM image of Device B in Fig. 4.1(d) shows a channel length of only 14 nm, and transport data a bandgap of 270 meV. During the warm up from 1.3 K to room temperature, Device B was exposed to oxygen (Fig. 4.2) leading to p-doped SWCNT contact sections (Fig. 4.5). In Fig. 4.10(d), remnants of conductance oscillations are visible when the channel is p-doped. The spacing of these oscillations matches the L_G measured at low temperature, and suggests the formation of a QD with an $E_C^h \sim 25$ meV. The data in Fig. 4.2 are consistent with $E_C^e > E_C^h$ at 295 K, and we expect the $e-h$ asymmetry to survive at room temperature.

4.6 Conclusions

In summary, we used suspended annealed gold films as local gates to create $e-h$ asymmetric suspended SWCNT-QD transistors (Fig. 4.5(b)). Using transport measurements, we showed that the gold gates permit ballistic (coherent) charge transport in the underlying SWCNT sections, and create nm-sharp tunnel barriers at the edge of the SWCNT channels. These barriers were of vastly different heights whether a channel was hole or electron doped. This produced a giant $e-h$ transport asymmetry in the five SWCNT transistors studied. We used this asymmetry to create two types of SWCNT quantum devices with dual functionality. We first showed a low- E_g SWCNT device where a small gate voltage could switch the device from being a 330 nm long quantum bus, under electron doping, to a 102 nm long QD, for hole doping. Secondly, we reported four devices with $E_g \gtrsim 200$ meV where a small V_G could switch the QD between two charging energies whose values differed by a factor up to 2.6, or switch the transport from QD to nearly ballistic. The size of the $e-h$ transport asymmetry in these devices scaled inversely with the length of the channel and the band gap of the tube. In a 14-nm long channel device, we measured low-temperature charging energies for holes and electrons exceeding 100 meV and 50 meV respectively, which suggests that the $e-h$ asymmetry could survive in room temperature devices. Nanotube transistors with a giant $e-h$ transport asymmetry could find applications in exploring the physics of near molecular size SWCNT-NEMS [137], to shrink down SWCNT qubits [108, 138], and to create SWCNT THz detectors [111] or gate programmable transistors [112].

In studying quantum electromechanics, it is crucial to have a detailed understanding of

contact effects and charge injection mechanisms. These play an important role for transmission in graphene transistors, as we will explore in the following chapter.

Chapter 5

Graphene Quantum Strain Transistors (GQSTs): an Applied Theory

Through uniaxial strain it is possible to completely suppress conductivity in graphene, creating a new type of device which we call a graphene quantum strain transistor (GQST). In this chapter, we develop an applied theory for these GQSTs, accounting for experimental realities, such as contact doping and distortions in the strained lattice, which have been left out of previous theoretical studies of this effect. The work presented in this chapter is in preparation for submission to *Nano Letters*.

5.1 Introduction

High on/off ratio transistors based on pristine bulk graphene have been long sought after, and were previously proposed in idealized ballistic devices under uniaxial strain [32, 35, 139]. We name these proposed devices graphene quantum strain transistors. Their conductivity can be turned off, not due to band gap formation, but because uniaxial strain can tailor the energy, momentum, and quantum transmission of graphene's ballistic electrons [2]. GQSTs are technologically relevant given that ballistic transport in graphene can persist up to a micron in length, even at room temperature [68, 140]. A state-of-the-art transistor behaviour in graphene would be a paradigm shift for transparent, flexible electronic devices [141], and the quantum engineering of 2D heterostructures [142]. Unfortunately, a full decade after the first proposal of GQSTs [32], there is no clear path forward to realize them experimentally. This bottleneck is widespread amongst many proposals of quantum transport strain engineering (QTSE) in graphene and 2D materials [4, 22, 31, 32, 143, 144]. We see two main causes

for the slow experimental realization of QTSE proposals in 2D materials. First, there is no established experimental platform with *in situ* tunable mechanical strain suited for quantum transport measurements. Secondly, due to the hypersensitivity of 2D materials to their environment, there are large quantitative discrepancies between the predictions of idealized models and experimental results. As a concrete example, previous theoretical predictions of the GQST effect were far too optimistic [32, 35, 139] because they treated metal films covering graphene as either not affecting or setting to infinity its Fermi level, and omitted important components of the vector potential arising from mechanical strain [54, 55].

Graphene is an ideal system to first bridge the present experiment-theory divide in QTSE of 2D materials. Its extreme mechanical strength, flexibility, and elastic deformation range makes graphene's electronics vastly tunable via mechanical strain [1, 2, 4, 22, 143], while its defect-free lattice allows ballistic (quantum) transport [68, 140]. It has been shown that static strain can add extreme pseudomagnetic fields [4] ~ 100 T to graphene's Dirac Hamiltonian. Uniaxial strains can be applied to graphene deposited on flexible [47] or nanoengineered [48] substrates, as well as in suspended devices [145]. In the short term, uniaxial strain engineering of graphene could demonstrate GQSTs. These would be ideal transistors for flexible electronics due to their high on/off ratio and fast transition frequency [141], with potential use in hypersensitive strain sensors [38, 146], and permit the development of valley filters for valleytronics [147, 148]. Beyond uniaxial strain, there are ongoing efforts to use strain-engineering in graphene to explore zero-magnetic field quantum Hall physics and valleytronics [21, 22, 31, 45, 149], and topological phase transitions [144, 150].

Here, we first present a powerful experimental platform for uniaxial strain engineering of quantum transport in graphene or other 2D materials. We provide all relevant experimental parameters of both the mechanical strain instrumentation and suspended graphene devices to realize GQSTs. We calculated the mechanically-tunable, thermally-induced, and gate-induced strains in our devices, and predict a widely tunable total mechanical strain ($2.6\% < \varepsilon_{\text{total}} < 5.1\%$). We show that $\varepsilon_{\text{total}}$ and the Fermi energy, E_F , in the graphene channel can be independently controlled. We then present a complete model of the ballistic charge conductivity in uniaxially strained graphene, matching parameters from the proposed experimental platform. We included all dominant effects of uniaxial strain, such as the scalar potential due to modulation of next-nearest-neighbor hopping [58], and vector potentials from changes to the three nearest-neighbor hoppings and spacings, γ_n and δ_n ($n = 1, 2, 3$) [4, 54]. We used experimentally realistic parameters, such as the Fermi level in graphene under a metal [96], a wide channel boundary condition [69], and realistic device dimensions, crystal

orientations, and strain values. The main purpose of our detailed calculations is to properly guide experimentalists toward the realization of GQSTs. As such, we detail all needed ingredients to make major quantitative (order of magnitude) improvements to the accuracy of previous models in calculating the strain-dependent conductivity. We find four quantitative transport signatures of the model: a shift in gate voltage of the conductivity curves, a dramatic conductivity suppression, a tunable set of Fabry-Pérot interferences, and a large modulation of the electron-hole conductivity asymmetry. Finally, we demonstrate that a strong GQST effect ($\sigma_{\text{on/off}} > 10^4$) is broadly realistic. The transistors can be turned on/off via a simple gate voltage, while strain is held constant. The simplicity, and detailed description, of the experimental proposal should permit a short-term demonstration of GQSTs. More broadly, we believe that this type of experiment-ready proposal can accelerate the development of QTSE in 2D materials.

5.2 Proposed experimental platform for strain engineering of 2D quantum transport

We propose in Fig. 5.1 a device geometry and instrumentation to realize graphene quantum strain transistors. This platform combines many important features to connect measurements to a simple theory. The suspended graphene channel is shown in Fig. 5.1(a)–(b), and its dimensions, $L = 100$ nm and $W = 1000$ nm, can be readily fabricated [151]. The length of the naked graphene channel is defined by gold films directly deposited on top of the graphene. It was previously reported that such gold films, when annealed, act as local gates for the ballistic graphene underneath [53, 152]. These gold-covered graphene regions act as contacts to the naked graphene channel. Few-nm sharp $p-n$ junctions form between these graphene contacts and the naked channel [53, 152]. The high aspect ratio $W/L \gg 1$ ensures that quantum transport is not significantly affected by the atomic disorder at the edges of the graphene crystal, such that a smooth boundary condition along the y -axis is justified [69]. Additionally, because the suspended channel is mechanically clamped across its entire width and $W/L \gg 1$, there cannot be significant scrolling (mechanical turning up) of the free edges, or slippage of the graphene sheet [153]. The channel closely matches an ideal rectangle, which can be described with a simple analytic ballistic transport model.

The zoomed-in part of Fig. 5.1(a) shows the graphene lattice with nearest-neighbour spacing $a = 1.42$ Å, the 2-atom basis (A, B), primitive lattice vectors $\mathbf{a}_{1,2}$, and nearest-neighbor vectors δ_n . Also pictured is the crystal orientation, θ , defined as the angle between

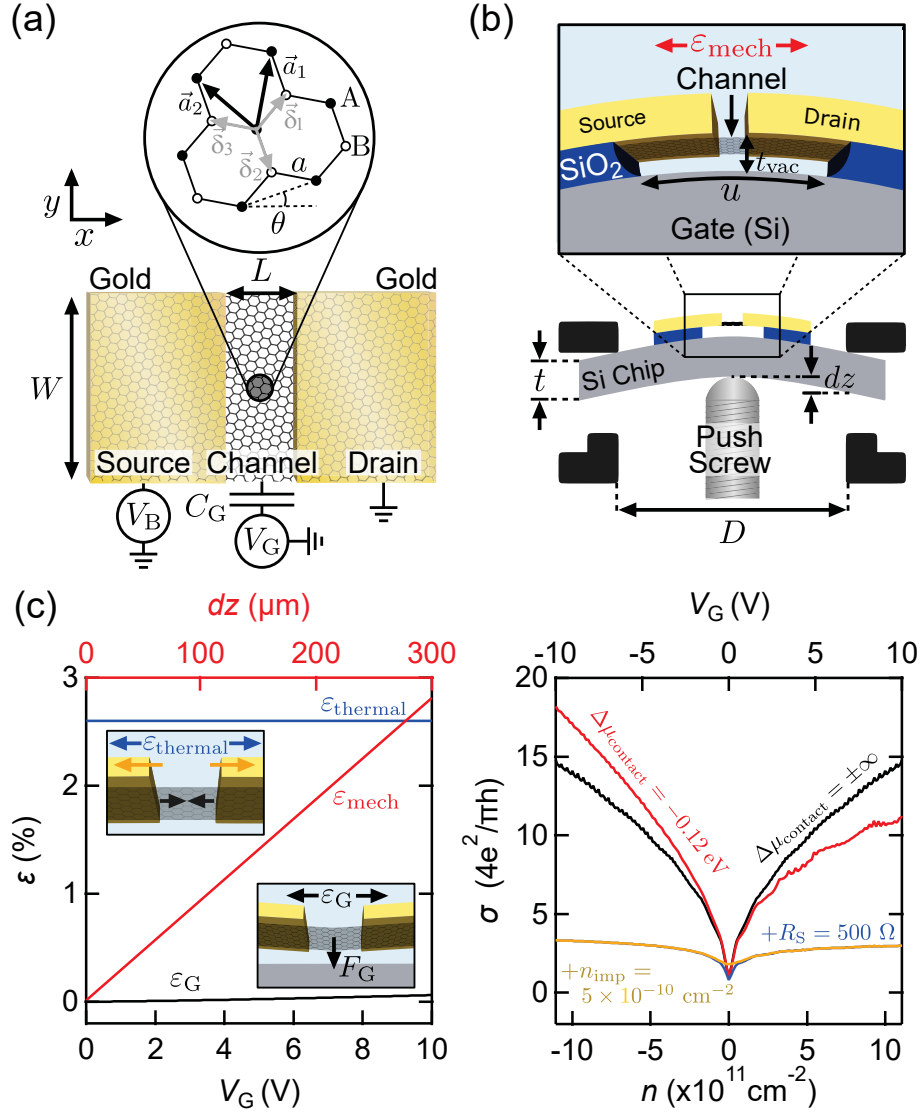


Figure 5.1: Platform for uniaxial quantum transport strain-engineering (QTSE) in graphene. (a) Top-down view of the proposed ballistic graphene transistor geometry. Inset: the graphene lattice, showing the crystal orientation θ with respect to the x -axis of the device. (b) Side view of the proposed graphene device and mechanical strain instrumentation. The mechanical assembly bends the substrate, which strains the suspended channel. The inset shows a close-up view of the suspended device geometry. (c) The three sources of strain in the channel: the thermal contraction (blue) at ~ 1 Kelvin, the mechanical motion (red, top axis) of the push screw, and electrostatic strain (black, bottom axis) from the gate voltage, V_G . Insets: visualizing the strain imparted by the gold and graphene thermal expansion (top left), and electrostatic pulling (bottom right). (d) Conductivity versus charge density, n (bottom axis), or V_G (top axis). The data are for an unstrained channel of $L = 100 \text{ nm}$, $W = 1000 \text{ nm}$, with contact doping $\Delta\mu_{\text{contact}} = \infty$ (black) and -0.12 eV (red, blue, gold). The series resistances, R_S , are 0 (black, red), and 500Ω (blue, gold). The charge impurity density n_{imp} is 0 (black, red, blue) and $5 \times 10^{10} \text{ cm}^{-2}$ (gold).

the x -axis of the device and the zig-zag direction of the crystal. This angle can be measured prior to gold film deposition using polarized Raman spectroscopy [154], or scanning tunneling microscope (STM) imaging [155]. Figure 5.1(b) shows suspended gold beams, 100 nm thick, used to anchor the suspended graphene. Upon bending the silicon substrate, these suspended gold beams act as cantilevers, amplifying the uniaxial mechanical strain applied to the naked graphene channel without bending it. The total suspension length of the gold cantilevers and channel is $u = 1 \mu\text{m}$. This suspension length can be tuned by etching the SiO_2 under the gold with a standard anisotropic wet etch [151]. The suspension height of the channel above the doped-silicon back-gate is $t_{\text{vac}} = 50 \text{ nm}$. The gate capacitance per unit area between the back-gate and the suspended channel is then $c_{\text{G}} = \epsilon_0/t_{\text{vac}} = 1.8 \times 10^{-8} \text{ F/m}^2$, with the vacuum permittivity ϵ_0 . The channel's suspension enables *in situ* thermal annealing to reach the ballistic transport regime [40,60]. A standard dc transport circuit (pictured) can be used for both annealing and transport measurements. An important aspect of this device design is the large area of the gold mechanical anchors ($\sim \mu\text{m}^2$) to achieve slippage-free clamping of the graphene channel [153].

To give an experimentally relevant description of our devices, we must include a finite Fermi energy in the source and drain graphene contacts, $\Delta\mu_{\text{contact}} = -0.12 \text{ eV}$. The source and drain contacts are sections of the same graphene crystal as the naked channel, but are located under the gold cantilevers. The very long injection length of electrons from gold into graphene [53,122] ensures that the electrons entering the naked graphene channel come from the graphene electrodes, and not directly from the gold film. The $\Delta\mu_{\text{contact}}$ in the graphene contacts arises from the charge transfer due to the work function difference between the metal and graphene [96]. This contact doping determines how many subbands (ballistic modes) are occupied in the leads, and can therefore have a drastic effect on the transport behaviour. We chose gold as the metal because its work function is similar to that of graphene, leading to low contact doping [96] ($|\Delta\mu_{\text{contact}}| = 0.05 - 0.25 \text{ eV}$). The exact $\Delta\mu_{\text{contact}}$ depends on the oxygen content of the gold film, which modifies its work function. The oxygen content can be adjusted *in situ* via Joule annealing [53]. For the purpose of the present work we use a median value [53] of $|\Delta\mu_{\text{contact}}| = 0.12 \text{ eV}$ with the most common doping: p -type. Our main conclusion, that GQSTs are feasible, is preserved over a broad range of $\Delta\mu_{\text{contact}}$ as we will show in Section 5.5.

The proposed mechanical strain instrumentation shown in the lower portion of Fig. 5.1(b) is very similar to a previously reported mechanical break-junction assembly [79]. It was

shown to operate accurately over a broad range of mechanical separations at low temperatures and in high magnetic fields [14, 156]. It is better suited for quantum transport studies in 2D materials than currently used strain-engineering instrumentation [51, 157], allowing slippage-free low-temperature charge transport measurements. A finely polished macroscopic push screw is used to reversibly bend a 200 μm -thick silicon substrate between two anchoring points, spaced apart by $D = 8 \text{ mm}$. The expected channel strain from the motion of the push screw is given by [79], $\varepsilon_{\text{mech}} = (3ut/D^2)dz/L$, where L is the naked graphene channel length, u is the total suspended length of the gold cantilevers and channel, t is substrate thickness, D is the distance between the anchoring points, and dz is the vertical displacement of the push screw. Based on previous experiments [79], the range of dz is up to 300 μm , giving a maximum mechanical strain $= \varepsilon_{\text{mech}}^{\text{max}} = 2.8\%$. To account for variability in the structural integrity of the Si chip, we use a mechanical strain range of $0 \leq \varepsilon_{\text{mech}} \leq 2.5\%$. The strong mechanical adhesion of graphene on the sturdy gold cantilevers ensures that all of the mechanical strain is imparted to the naked graphene channel. Moreover, this instrumentation is modular, such that the clamping of the substrate and graphene flake could be modified to permit, for instance, triaxial strain engineering [22].

Figure 5.1(c) details the main sources of uniaxial strain in the suspended graphene channel. Because device nanofabrication is conducted at room temperature, a substantial amount of strain will be generated when cooling the devices to cryogenic temperatures necessary for quantum charge transport measurements. This thermal strain, $\varepsilon_{\text{thermal}}$, has two main contributions as shown in the top inset of Fig. 5.1(c), arising from the contraction of the gold cantilevers [158] and the expansion of graphene [159]. Adding these contributions, we find $\varepsilon_{\text{thermal}} = 2.6 \pm 0.1\%$ for devices near $\sim 1 \text{ Kelvin}$. As shown in Fig. 5.1(c), this $\varepsilon_{\text{thermal}}$ is independent of gate voltage, V_G , or mechanical displacement of the push screw, dz . At a fixed temperature, this constant thermal strain will not hinder the exploration of strain engineering proposals. A second source of strain in the channel is the stretching ε_G caused by the electrostatic force from V_G . Given the very short length of the graphene channel and the sturdiness of the gold cantilevers, we calculate that ε_G is extremely small ($\sim 0.01\%$) over the V_G range relevant for experiments. This leaves the mechanical push screw $\varepsilon_{\text{mech}} \leq 2.5\%$ as the only way to tune the total strain, $\varepsilon_{\text{total}} = \varepsilon_{\text{thermal}} + \varepsilon_G + \varepsilon_{\text{mech}} = 2.6 - 5.1\%$. The proposed experimental platform permits a broad, and independent, control of the uniaxial strain and charge density in the graphene channel.

Figure 5.1(d) shows the calculated ballistic conductivity, σ , as a function of the charge density in the channel, n , or equivalently $V_G = ne/c_G$ on the top axis, when $\varepsilon_{\text{total}} = 0$. We

based this calculation on the standard ballistic transport model for a $W/L \gg 1$ geometry [69]. To highlight the impact of contact doping on the $\sigma - V_G$ characteristics, we plot in Fig. 5.1(d) the calculated conductivity for both $\Delta\mu_{\text{contact}} = \infty$ (black) and -0.12 eV (red). The sign and value of the finite contact doping determines the electron-hole transport asymmetry [76]. The inclusion of a realistic $\Delta\mu_{\text{contact}}$ becomes critical when strain is applied, since an infinite contact doping allows infinite transmission modes, making σ completely insensitive to strain. The blue-coloured data in Fig. 5.1(d) show the impact of adding a finite series resistance R_S arising from the injection of carriers from the gold films into the graphene contacts. Based on reported R_S values [122, 160] and the geometry in Fig. 5.1(a), a $R_S \leq 500 \Omega$ is expected. This would cause only a global reduction of σ , with a negligible impact on the on/off ratio of the GQSTs. We therefore use a generic $R_S = 0$ in our calculations. The gold trace in Fig. 5.1(d), shows the impact on $\sigma - V_G$ of a charge impurity density of the same order of magnitude expected in suspended graphene $n_{\text{imp}} = 5 \times 10^{-10} \text{ cm}^{-2}$ [161]. As long as ballistic transport is maintained, the conductivity is largely unaffected by n_{imp} when V_G is far away from the conductivity minimum (Dirac point), V_D . The proposed GQSTs would be operated far away from V_D , as will become evident below. For this reason our conclusions are independent of the exact n_{imp} in a ballistic device.

5.3 Applied theory of the strain engineering of transport in ballistic graphene

In this section, we translate the above device and instrumentation design into an applied theoretical model to calculate the transmission probability of charge carriers across the device as it is uniaxially strained. We consider all strain effects to first order, given that $\varepsilon_{\text{total}} \ll 1$. We use the uniaxially-strained graphene Dirac Hamiltonian given in Eq. 5.1, derived from a tight binding model combining previous approaches [4, 54, 69, 139, 162]. Uniaxial strain has three major effects on graphene's band structure: a downward shift of graphene's work function which can be described by a scalar potential, a crystal momentum shift of the Dirac points, which can be described by a gauge vector potential, and an anisotropic warping the Dirac cones which corresponds to a direction-dependent Fermi velocity. In this section, we discuss the origin and magnitude of these three effects and their impact on the transmission probability of individual conduction modes, which are summed to obtain the device's conductivity. A detailed discussion of the device conductivity versus the experimental parameters will follow in the next section.

5.3.1 Strain-induced scalar and vector potentials in graphene

Using the smooth-edge boundary condition for wide aspect ratio devices, the Hamiltonians in the K and K' valleys are decoupled. Equation 5.1 is the Hamiltonian describing the graphene channel's K valleys, and can be modified to describe the K' valleys by reversing the sign of the gauge vector potential \mathbf{A}_i .

$$H_{K_i} = \hbar v_F (\bar{\mathbf{I}} + (1 - \beta) \bar{\boldsymbol{\varepsilon}}) \cdot \boldsymbol{\sigma} \cdot (\mathbf{k} - \mathbf{A}_i) + \Delta\mu_G + \Delta\mu_\varepsilon, \quad (5.1)$$

where the pseudospin operator $\boldsymbol{\sigma} = (\sigma_x, \sigma_y)$ is represented by the Pauli spin matrices and acts on the two-component spinor wave function, referring to the A and B sublattices. The pseudospin orientation is either parallel (up) or anti-parallel (down) with the generalized wavevector $\mathbf{k} - \mathbf{A}_i$, where the index $i = 1, 2, 3$ labels the three K . The matrices $\bar{\mathbf{I}}$ and $\bar{\boldsymbol{\varepsilon}}$ are respectively the identity matrix and strain tensor, which in the device's $x - y$ coordinates is $\bar{\boldsymbol{\varepsilon}}$, with elements $\varepsilon_{xx} = \varepsilon_{\text{total}}$, $\varepsilon_{yy} = -\nu \varepsilon_{\text{total}}$ and $\varepsilon_{xy} = \varepsilon_{yx} = 0$, where $\nu = 0.165$ is the Poisson ratio [4]. The term $\Delta\mu_G$ is the gate-induced electrostatic potential in the channel, and it is replaced by the gold-induced electrostatic doping $\Delta\mu_{\text{contact}}$ in the source/drain graphene contacts. As shown in Eq. 5.1, uniaxial strain has three main qualitative effects on graphene's band structure: an anisotropic warping the Dirac cones which corresponds to a direction-dependent Fermi velocity $\bar{\mathbf{v}}_F = \hbar v_F (\bar{\mathbf{I}} + (1 - \beta) \bar{\boldsymbol{\varepsilon}})$, crystal momentum shifts of the Dirac points which can be described by gauge vector potentials \mathbf{A}_i , and a downward shift of the Fermi energy which can be described by a scalar potential $\Delta\mu_\varepsilon$. The parameter $\beta = -\partial \ln \gamma / \partial \ln a \approx 2.5$ is the electronic Grüneisen parameter [4]. We discuss in Fig. 5.2 the origin and magnitude of two dominant effects, the scalar and vector potentials, and how they impact charge transport. We then calculate the transmission probability of individual conduction modes, and sum them to obtain the device's charge conductivity.

Figure 5.2(a)–(b) shows the low energy dispersion and Fermi circle around a Dirac point in the source/drain contacts and the strained channel respectively. The magnitude of the Fermi wave vector in Fig. 5.2(a) is set by the contact doping, $k_F = \Delta\mu_{\text{contact}} / \hbar v_F$. In the strained channel, as shown in Fig. 5.2(b), \tilde{k}_F depends on both the strain-induced scalar potential and the gate-induced doping, $\tilde{k}_F = (\Delta\mu_G + \Delta\mu_\varepsilon) / \hbar v_F$, where $\Delta\mu_G = \hbar v_F \sqrt{\pi c_G V_G / e}$, and $v_F = (3/2) \gamma_0 a / \hbar = 8.8 \times 10^5$ m/s is the Fermi velocity, and $\gamma_0 = -2.7$ eV is the unstrained hopping energy [2]. The term $\Delta\mu_\varepsilon$ arises from the strain-dependence of the next-nearest-neighbour hopping [58], $\gamma' \approx -0.3$ eV. This hopping does not connect lattice sites on sublattices A and B , and thus is not related to the pseudospin of charge carriers. However, the increase in the

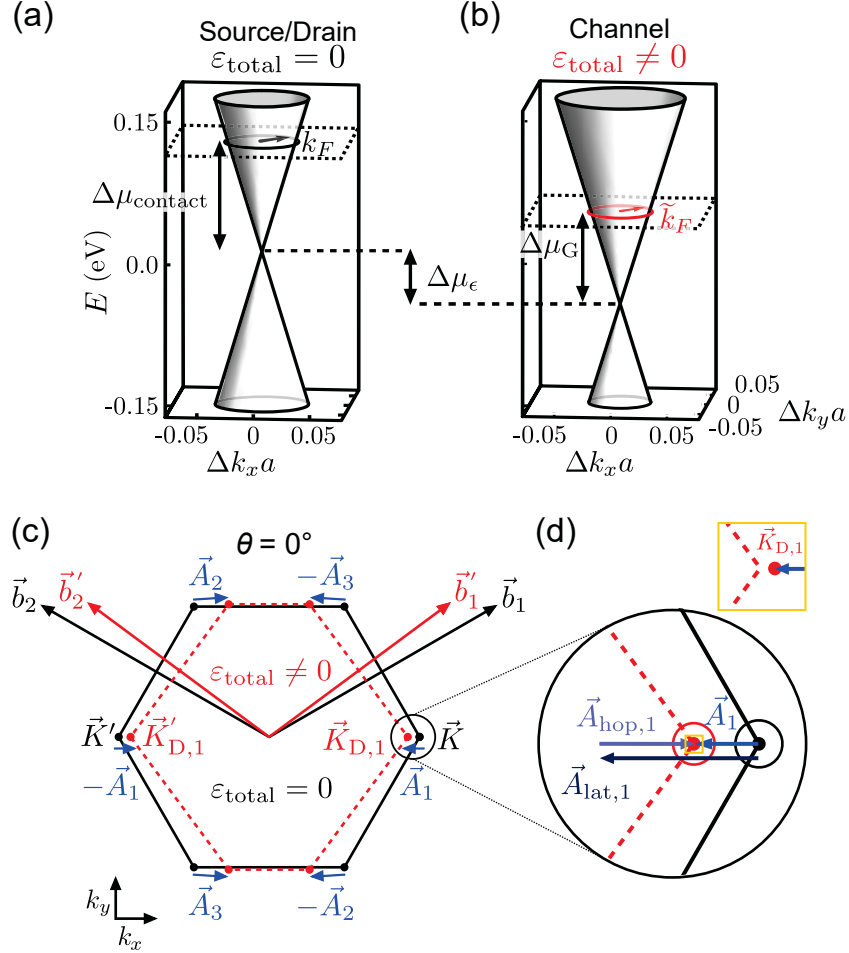


Figure 5.2: Applied theory for uniaxial strain tuning of graphene's band structure. (a) Dirac cone and Fermi circle in the unstrained source/drain graphene contacts, and (b) in the strained graphene channel. (c) Unstrained (black) and uniaxially strained (red) first Brillouin zone (FBZ) of graphene when $\theta = 0^\circ$. The strain value in this figure is exaggerated, $\epsilon_{\text{total}} = 20\%$, to make its effects clearly visible. (d) Under strain, the Dirac point shifts can be used to define gauge vector potentials (blue arrows), $\vec{A}_i = \vec{A}_{\text{lat},i} + \vec{A}_{\text{hop}}$. The inset shows that the corner of the FBZ does not coincide with the Dirac point when the device is under strain.

next-nearest-neighbour distance with strain leads to an increase in graphene's work function corresponding to a scalar potential [139], which can be expressed as $\Delta\mu_\varepsilon = g_\varepsilon(1-\nu)\varepsilon_{\text{total}}$ [163], where [164] $g_\varepsilon \approx 3.0$ eV.

The strain-induced changes to the nearest-neighbour hopping are incorporated in the Dirac Hamiltonian of graphene as gauge vector potentials \mathbf{A}_i . In Fig. 5.2c), we show the unstrained (black) and strained (red) first Brillouin zones (FBZs) with a uniaxial strain applied along the zig-zag direction ($\theta = 0^\circ$). To better visualize the \mathbf{A}_i in Fig. 5.2(c)–(d), we show $\varepsilon_{\text{total}} = 20\%$, but restate that we only studied $\varepsilon_{\text{total}} \leq 5.1\%$. To first order in strain, there are two main modifications to the tight-binding description of the Hamiltonian for unstrained graphene [4,54,55], $H_0 = -\gamma_0 \sum_k \sum_{n=1}^3 \exp[-i\mathbf{k} \cdot \boldsymbol{\delta}_n] a_k^\dagger b_k + \text{H. c.}$ Firstly, distortion of the lattice, stretching of the and nearest-neighbour distances $\boldsymbol{\delta}_n$, modifies the Hamiltonian with $\boldsymbol{\delta}_n \rightarrow (\bar{\mathbf{I}} + \bar{\boldsymbol{\varepsilon}}) \cdot \boldsymbol{\delta}_n$. Secondly, the value of the nearest-neighbor hopping is modified as $\gamma_0 \rightarrow \gamma_0 \exp[-\beta((\bar{\mathbf{I}} + \bar{\boldsymbol{\varepsilon}}) \cdot \boldsymbol{\delta}_n / a) - 1]$. Both of these effects can be re-written as gauge vector potentials in Eq. 5.1, respectively as $\mathbf{A}_{\text{lat},i} = -\bar{\boldsymbol{\varepsilon}} \cdot \mathbf{K}_i$, and $\mathbf{A}_{\text{hop}} = \beta/2a(\varepsilon_{xx} - \varepsilon_{yy}, -2\varepsilon_{xy})$. The total gauge potentials are then $\mathbf{A}_i = \mathbf{A}_{\text{lat},i} + \mathbf{A}_{\text{hop}}$. The signs of both components of the vector potentials are opposite in the K_i and K'_i valleys. To make this model applicable to real devices, we generalize the vector potentials in the lattice frame of reference aligned with the zigzag axis, $(x' - y')$ to an arbitrary crystal orientation θ with respect to the lab frame of reference $(x - y)$ aligned with the device axis. We find:

$$\mathbf{A}_{\text{hop}} = \frac{\beta\varepsilon(1+\nu)}{2a} \begin{pmatrix} \cos 3\theta \\ \sin 3\theta \end{pmatrix} \quad (5.2a)$$

$$\mathbf{A}_{\text{lat},1} = \frac{4\pi\varepsilon}{3\sqrt{3}a} \begin{pmatrix} -\cos \theta \\ \nu \sin \theta \end{pmatrix} \quad (5.2b)$$

$$\mathbf{A}_{\text{lat},2} = \frac{2\pi\varepsilon}{3a} \begin{pmatrix} \frac{1}{\sqrt{3}} \cos \theta + \sin \theta \\ -\frac{1}{\sqrt{3}} \nu \sin \theta + \nu \cos \theta \end{pmatrix} \quad (5.2c)$$

$$\mathbf{A}_{\text{lat},3} = \frac{2\pi\varepsilon}{3a} \begin{pmatrix} \frac{1}{\sqrt{3}} \cos \theta - \sin \theta \\ -\frac{1}{\sqrt{3}} \nu \sin \theta - \nu \cos \theta \end{pmatrix} \quad (5.2d)$$

Because of lattice symmetry, $0^\circ < \theta < 60^\circ$ and the $\mathbf{A}_{i,y}$ have a maximum at $\theta = 30^\circ$. An illustration of the vector potentials given by Eq. 5.2 are shown in Fig. 5.2(c) for $\theta = 0^\circ$. They represent the displacements from the original unstrained Dirac points to the strained ones. Figure 5.2(d) details the contributions from the terms $\mathbf{A}_{\text{lat},i}$ and \mathbf{A}_{hop} to the new Dirac point locations $\mathbf{K}_{D,i} = \mathbf{K}_i + \mathbf{A}_{\text{lat},i} + \mathbf{A}_{\text{hop}}$. As shown in the inset of Fig. 5.2(d), the new

Dirac points no longer coincide with the corners of the FBZ [162]. We remark that the two terms in the vector potential are of comparable magnitude, and both significantly affect the Hamiltonian and transport behaviour. However, in most previous work, the focus has been on studying the pseudomagnetic field $\mathbf{B}_{\text{sp}} = \nabla \times \mathbf{A}$ [22, 45]. Because $\mathbf{A}_{\text{lat},i}$ always has a zero curl [55], it was omitted. It is however crucial to include it in our present study which is reminiscent of an Aharonov-Bohm experiment, and depends directly on the full gauge vector potentials.

5.3.2 Transmission model for ballistic electrons in strained graphene

To clarify the connection between Eq. 5.1 and the ballistic conductivity in our devices, we show in Fig. 5.3(e) an example of a charge carrier's trajectory as it moves from the source (unstrained) to the channel (strained), and then the drain (unstrained). The trajectory is described by the momentum wavevector in the source, $k_F = \pm|k\hat{x} + q_n\hat{y}|$, and in the channel, $\pm|\tilde{k}_F = \tilde{k}\hat{x} + \tilde{q}_n\hat{y}|$, where the \pm symbol refers to electron or hole transport respectively. The transverse boundary condition conserves the y -momentum throughout the device [32], such that $\tilde{q}_n = q_n - A_{i,y}$. This strain-induced shift in y -momentum alters the propagation angle of the carrier, and its Klein transmission probability at the strained/unstrained interfaces. As mentioned above, we expect both the electrostatic potential steps and strain field steps, at the edges of the naked graphene channel, to be sharp ($\sim \text{nm}$) [53, 152]. Using Eq. 5.1 and matching the carrier's wave function at the potential steps along x , we solve for the transmission probability $T_{\xi,i,n}$ in conduction mode n and valley $\xi = \pm 1, i = 1, 2, 3$. We find

$$T_{\xi,i,n} = \frac{(v_x k \tilde{k})^2}{(v_x k \tilde{k})^2 \cos^2[\tilde{k}L] + (k_F \tilde{k}_F - v_y q_n (q_n - \xi A_{i,y}))^2 \sin^2[\tilde{k}L]}, \quad (5.3)$$

where $q_n = \frac{\pi}{W}(n + \frac{1}{2})$ is the quantized transversal momentum for the mode n , $k = (k_F^2 - q_n^2)^{1/2}$, $\tilde{k} = v_x^{-1}[v_F^2 \tilde{k}_F^2 - v_y^2 (q_n - \xi A_{i,y})^2]^{1/2}$, $v_x = v_{F,xx}/v_F = (1 + (1 - \beta)\epsilon_{\text{total}})$, and $v_y = v_{F,yy}/v_F = (1 - (1 - \beta)\nu\epsilon_{\text{total}})$. The values of $A_{i,y}$ in Eqs. 2 and 3 are in the device's $(x - y)$ coordinates. They coincide with the lattice coordinates $(x' - y')$ at $\theta = 0^\circ$. We calculate the charge conductivity of the device by properly summing the transmissions from all relevant modes:

$$\sigma = \frac{L}{W} \frac{2e^2}{h} \frac{1}{3} \sum_{\xi} \sum_i^3 \sum_n^N T_{\xi,i,n}, \quad (5.4)$$

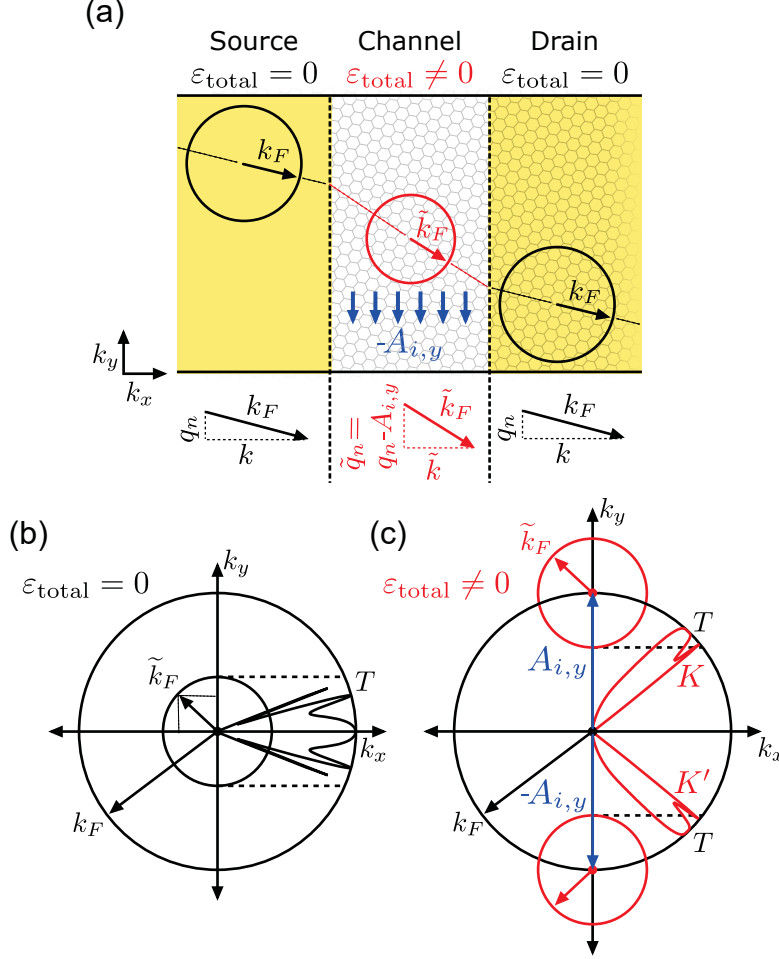


Figure 5.3: Applied theory for ballistic charge transport in strained graphene. (a) Charge carrier wavevectors in the source, channel, and drain of the uniaxially strained ballistic transistor. The transmission modes are labelled with their y -component wave number q_n . The addition of $A_{i,y}$ in the channel modifies the propagation angle, and transmission probability, of the carriers. (b)–(c) Transmission probability, T , of the conduction modes for a single vector potential $A_{1,y} = 0$ and $A_{1,y} = k_F$ respectively. The Fermi circles represent the Fermi surface in the contacts (big circles) and channel (small circles), for $\tilde{k}_F = k_F/2.5$, while the solid curves show the calculated transmission probabilities (origin = 0, outer circle = 1) vs. incidence angle (polar axis) when $\theta = 15^\circ$ and $\Delta\mu_{\text{contact}} = -0.12$ eV. The boundary condition in y imposes transversal momentum conservation (horizontal dashed lines), and explains the zero transmission at some propagation angles.

where $N = \text{Int}(k_F W / \pi + \frac{1}{2})$ is the number of energetically allowed modes set by the contact's Fermi energy, and the factor $\frac{1}{3}$ accounts for the lifting of the three-fold K and K' point degeneracy in strained graphene. Equations 5.2, 5.3, and 5.4 are similar to previously derived ones [32, 35, 139], but now permit the insertion of experimentally relevant $\Delta\mu_{\text{contact}}$, $\Delta\mu_{\varepsilon}$, θ , and $\mathbf{A}_{\text{lat},i}$.

We now describe the qualitative impact of uniaxial strain on the transmission, and how it sets the stage for GQSTs. Figure 5.3(f) and (g) show the Fermi circles in the contacts (big circles) and the channel (small circles) for channel strain $\varepsilon_{\text{total}} = 0$ and $\varepsilon_{\text{total}} \neq 0$ respectively. The dashed lines show the restrictions caused by y -momentum conservation, allowing transmission only where the lead and channel Fermi circles overlap. The overlaid solid curves in Fig. 5.3(f)–(g) show the transmission (radial axis ranges from 0 to 1) as a function of the angle of carrier propagation in the leads, $\phi = \sin^{-1}(q_n/k_F)$ (polar axis). The transmission is calculated using Eq. 5.3, and $A_{1,y}$ from Eq. 5.2 and parameters: $L = 100$ nm, $W = 1000$ nm, $\Delta\mu_{\text{contact}} = -0.12$ eV, and $\tilde{k}_F = k_F/2.5$. In Fig. 5.3(f), the channel is uniaxially strained and a vector potential $A_{i,y} = k_F$ is applied for $\theta = 15^\circ$. This $A_{i,y}$ vertically shifts the channel's Fermi circle in opposite directions for the two valleys. Strain modifies the allowed carrier injection angles, as well as the number of energetically allowed transmission modes. As strain increases, the overlap between the contact (black) and channel (red) Fermi circles shrinks, such that fewer modes permit the y -momentum conservation. When the circles no longer overlap ($A_{i,y} > k_F + \tilde{k}_F$), transmission is always energetically forbidden and $\sigma \rightarrow 0$. We emphasize that the drop in conductivity does not arise from a strain-induced band gap, which is only expected to occur at much larger uniaxial strains $\sim 20\%$ [162].

5.4 Conductivity signatures of strain-induced scalar and vector potentials

We set to map out the behaviour of ballistic conductivity from Eq. 5.4 as a function of experimentally tunable parameters. We predict four clear strain-tunable experimental transport signatures as shown in Fig. 5.4: a lateral shift in the $\sigma - V_G$ curves, an extreme reduction in conductivity, a rich set of ballistic conductivity resonances, and a sizeable electron-hole transport asymmetry. We quantify how these predictions depend on realistic values of the contact doping, crystal orientation, uniaxial strain, and gate voltage.

To calculate the σ data in Fig. 5.4 we used the MATHEMATICA code presented in Appendix A, along with the parameters introduced above: $\varepsilon_{\text{thermal}} = 2.6\%$, $\Delta\mu_{\text{contact}} = -0.12$ eV,

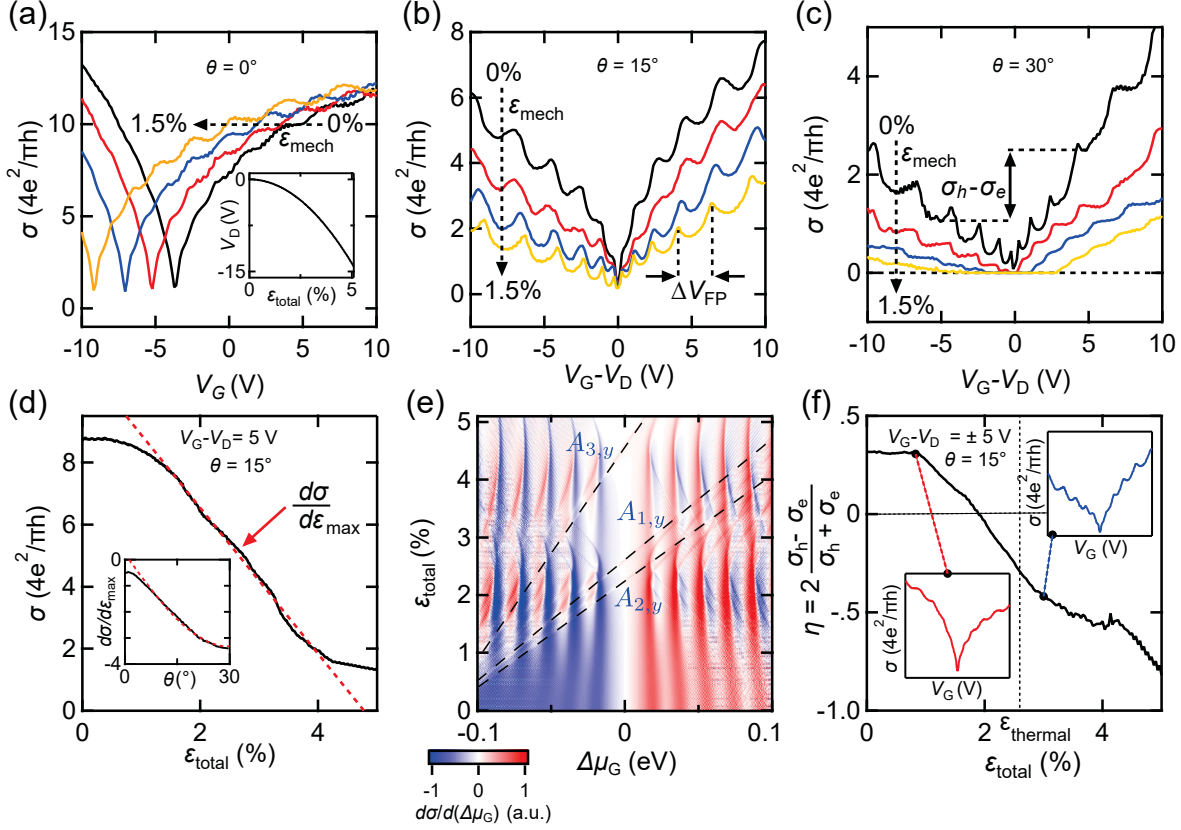


Figure 5.4: Conductivity signatures of uniaxial QTSE in graphene. Conductivity signatures of uniaxial QTSE in graphene. (a) $\sigma - V_G$ for $\varepsilon_{\text{mech}} = 0\%$, 0.5% , 1.0% , 1.5% (black, red, blue, gold) at $\theta = 0^\circ$. The strain-induced scalar potential shifts $\sigma - V_G$ curves towards negative V_G . The inset shows the gate-shift of the Dirac point, V_D , as a function of $\varepsilon_{\text{mech}}$ up to 1.5% . (b) $\sigma - (V_G - V_D)$ at $\theta = 15^\circ$. There is a rapid decrease in σ with strain. Fabry-Pérot resonances are clearly visible, and their spacing ΔV_{FP} is strain-dependent. (c) $\sigma - (V_G - V_D)$ data at $\theta = 30^\circ$ show a complete suppression of σ at higher strains. There is an asymmetry between hole (σ_h) and electron (σ_e) conductivities at opposite $(V_G - V_D)$. (d) $\sigma - \varepsilon_{\text{total}}$ for $\theta = 15^\circ$, at $(V_G - V_D) = 5$ V with a linear fit (red) to extract $(d\sigma/d\varepsilon)_{\text{max}}$. Inset: $(d\sigma/d\varepsilon)_{\text{max}} - \theta$ with a sinusoidal fit (red). (e) Colour map of $d\sigma/d(\Delta\mu_G)$ versus $\hbar v_F \tilde{k}_F$ and $\varepsilon_{\text{total}}$. Clear Fabry-Pérot resonances are visible, and the dashed lines identify the three $k_F = k_F + A_{i,y}$ resonances. (f) Relative electron-hole asymmetry, $\eta = 2(\sigma_h - \sigma_e)/(\sigma_h + \sigma_e)$, as a function of $\varepsilon_{\text{total}}$ at $\theta = 15^\circ$, at $(V_G - V_D) = 5$ V. Insets: $\sigma - V_G$ shows $\eta > 0$ at $\varepsilon_{\text{total}} = 1\%$ (bottom left), and $\eta < 0$ at $\varepsilon_{\text{total}} = 3\%$ (top right).

$L = 100$ nm and $W = 1000$ nm. We considered the experimentally relevant regime where $k_B T \sim 0.1$ meV $< eV_B < 1$ meV $\ll \Delta\mu_{\text{contact}} = 0.12$ eV, and $\hbar v_F A_{i,y}$ reaches up to 0.34 eV at maximum $\varepsilon_{\text{total}} = 5.1\%$ when $\theta = 30^\circ$. Based on the energy scales in the problem, we can safely neglect the minor impact of a small V_B and low temperature on the calculated σ . We remind the reader that the main objective of our applied theory is to include experimental considerations which have major impacts on the theoretical predictions. For instance, the inclusion of the thermally induced strain offset, the lattice distortions $\mathbf{A}_{\text{lat},i}$, and of realistic values of $\Delta\mu_{\text{contact}}$, lead to order of magnitude changes in the calculated σ at some V_G , and dramatically impact the predicted transistor on/off ratios. On the other hand, we verified numerically that an exhaustive list of other factors such as a modest impurity density, series resistance, gating of $\Delta\mu_{\text{contact}}$, thermal strain in the contacts, uncertainties on v_F , ν , β , L , W , etc..., lead to modest corrections to the calculated σ .

In Fig. 5.4(a), we plot σ - V_G for $\varepsilon_{\text{mech}} = 0, 0.5, 1.0$, and 1.5% (black, blue, red, gold) for $\theta = 0^\circ$. At this crystal orientation the $A_{i,y}$ are nearly zero, and the only significant consequence of strain is the scalar potential $\Delta\mu_\varepsilon = g_\varepsilon(1 - \nu)\varepsilon_{\text{total}}$. We remind the reader that even when $\varepsilon_{\text{mech}} = 0$, there is a built-in thermal uniaxial strain of $\varepsilon_{\text{thermal}} = 2.6\%$. A clear transport signature of uniaxial strain is apparent in Fig. 5.4(a): the $\sigma - V_G$ curves shift towards negative gate due to the strain-induced scalar potential. The shift of the V_D , gate-position of the Dirac point, is plotted in the inset of Fig. 5.4(a), and given by $V_D = -\frac{e}{C_G} \frac{g_\varepsilon^2}{\pi(\hbar v_F)^2} (1 - \nu)^2 \varepsilon_{\text{total}}^2$. The value of V_D is independent of θ and $\Delta\mu_{\text{contact}}$, and can be used in experiments to calibrate the thermal and mechanical strains applied by the instrumentation.

In Fig. 5.4(b)–(c), we plot $\sigma - (V_G - V_D)$ at various $\varepsilon_{\text{mech}}$. We subtracted V_D from the horizontal axis to remove the lateral shift arising from the scalar potential, and focus on the effects of the vector potentials. We set θ respectively to 15° and 30° in Fig. 5.4(b) and (c). The uniaxial strain dramatically decreases the conductivity, and this suppression is maximized at $\theta = 30^\circ$. We see that σ can reach ≈ 0 for $\varepsilon_{\text{mech}}$ as low as 0.5% . The range of V_G where a clear turning off of the conductivity is possible grows rapidly as $\varepsilon_{\text{mech}}$ increases to 1.5% .

In Fig. 5.4(d) we show the dependence of σ versus $\varepsilon_{\text{total}}$, where σ is calculated at $(V_G - V_D) = 5$ V and $\theta = 15^\circ$. The dashed red line is a linear fit of the steepest section of the curve, and defines $(d\sigma/d\varepsilon)_{\text{max}}$. This latter quantity is plotted and fit in the inset as a function of θ . The fit (dashed) is a sinusoidal function matching the form of the hopping vector potential from Eq. 5.1. The discrepancy between the data and fit below $\theta = 5^\circ$

indicates that \mathbf{A}_{hop} is no longer the main contribution to the \mathbf{A}_i at small angles. The strong, and single-valued, dependence of $(d\sigma/d\varepsilon)_{\text{max}}$ on θ makes it plausible to extract the crystal angle from transport data. This would relax the requirement to measure θ with polarized Raman spectroscopy [154] or STM imaging [155].

Another consequence of uniaxial strain on transport is the shifting of conductivity resonances, which are visible in Fig. 5.4(b), (c) and (e). These resonances arise from interferences of the ballistic carriers as they are transmitted or reflected at the channel-contact interfaces. The Fermi energy spacing of these Fabry-Pérot (FP) like resonances [70] is $\Delta E_{\text{FP}} = \pi \hbar v_F / (L \cos \tilde{\phi})$, where $\tilde{\phi}$ is the angle of propagation in the channel. As described in Fig. 5.4(e), $\tilde{\phi}$ is widely tunable with the strain-induced $A_{i,y}$, thus the FP resonances permit a measurement of the vector potentials. Figure 5.4(e) presents the calculated $d\sigma/d(\Delta\mu_G)$ versus $\Delta\mu_G$ and $\varepsilon_{\text{total}}$, showing a rich set of ballistic resonances. The dashed lines label peaks which are not related to the FP cavity, whose slopes relate to the $A_{i,y}$. The slopes of these dashed lines are determined by the formula $k_F = \tilde{k}_F + A_{i,y}$. For $\varepsilon_{\text{total}} = 0$, the vector potentials $A_{i,y} = 0$ and the three diagonal lines intersect at $k_F = \tilde{k}_F$. This allows the contact doping to be uniquely determined through extrapolation. At the intersections of the dashed lines with the Dirac point (highlighted by black circles), $\tilde{k}_F = 0$, and $k_F = A_{i,y}$. The three intersections depend on the crystal orientation and contact doping, allowing θ to be determined uniquely if polarized Raman spectroscopy is not available, or if the crystal orientation is known, this relationship gives an independent measurement of the contact doping.

A fourth effect of $\varepsilon_{\text{mech}}$ is to modify the electron-hole transport asymmetry, $\sigma_e \neq \sigma_h$. We extract σ_e and σ_h at $(V_G - V_D) = \pm 5$ V as shown in Fig. 5.4(c). We then define a relative electron-hole transport asymmetry as $\eta = 2(\sigma_h - \sigma_e)/(\sigma_h + \sigma_e)$. This relative asymmetry η is widely dependent on both $\varepsilon_{\text{mech}}$ and θ , and in Fig. 5.4(f) we plot $\eta - \varepsilon_{\text{mech}}$ at $\theta = 15^\circ$. The two insets display the asymmetric shape of $\sigma - (V_G - V_D)$ at respectively $\varepsilon_{\text{total}} = 1\%$ (bottom left), and 3% (top right). At $\varepsilon_{\text{total}} \approx 1.8\%$ the electron-hole asymmetry η reverses sign. The vertical dashed line in Fig. 5.4(f) shows the expected $\varepsilon_{\text{thermal}}$ in the devices, showing that for our device geometry, we expect the transport asymmetry to be reversed already. For a known θ , the dependence of η versus $\varepsilon_{\text{total}}$ could also be used to experimentally determine the value of $\Delta\mu_{\text{contact}}$. We remark that the strong tunability of σ via uniaxial strain implies that shot noise measurements of the Fano factor would provide another experimental signature of the model. We are now ready to assess the potential of the proposed devices for a practical demonstration of high on/off ratio graphene quantum strain transistors (GQSTs).

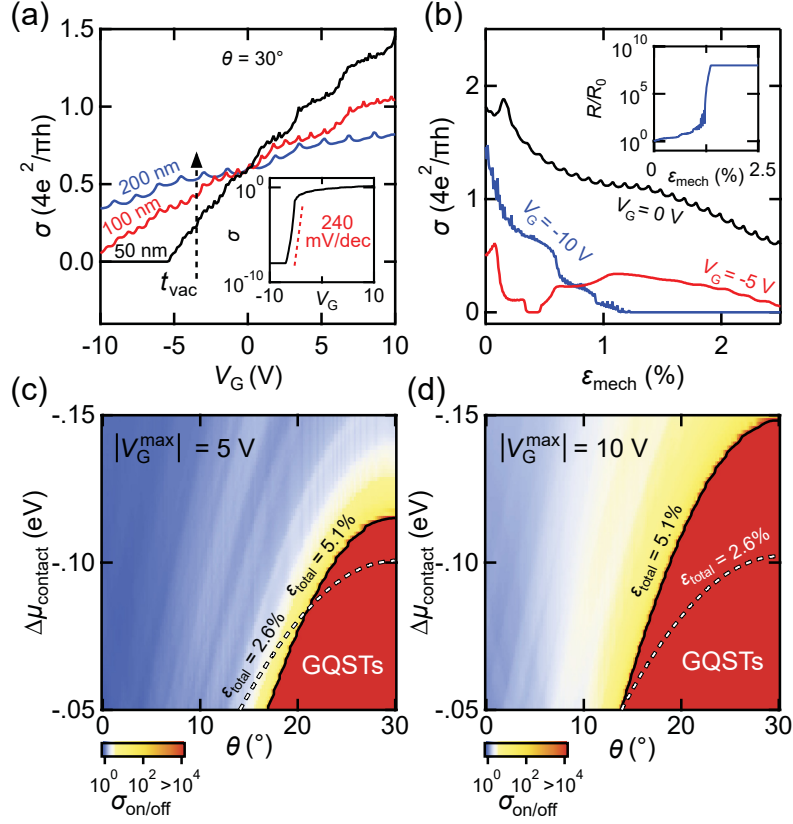


Figure 5.5: Graphene quantum strain transistors (GQSTs). (a) $\sigma - V_G$ for a gate-channel vacuum dielectric thickness $t_{\text{vac}} = 50$ nm (black), 100 nm (red), and 200 nm (blue) for $\varepsilon_{\text{total}} = 5.1\%$ and $\theta = 30^\circ$. The 50 nm gate spacing gives rise to a dramatic GQST effect with $\sigma_{\text{on/off}} \gg 10^4$. The inset shows a subthreshold slope of 240 mV/dec for $t_{\text{vac}} = 50$ nm. (b) $\sigma - \varepsilon_{\text{mech}}$ shows the extreme strain sensitivity of σ versus uniaxial strain at fixed $V_G = 0$ V, -5 V, and -10 V. Inset: Resistance-based strain sensitivity at $V_G = -10$ V. (c) and (d) $\sigma_{\text{on/off}} - \Delta\mu_{\text{contact}} - \theta$ colour maps for respectively $V_G^{\text{max}} = \pm 5$ V and ± 10 V and $\varepsilon_{\text{total}} = 2.6\%$. The solid and dashed lines show the $\sigma_{\text{on/off}} > 10^4$ boundaries for total strain values of $\varepsilon_{\text{total}} = 2.6\%$, and 5.1% respectively.

5.5 Graphene quantum strain transistors

We use our applied model to demonstrate the expected performance of GQSTs. We consider device operation at low temperature (~ 1 K), which imposes a minimum $\varepsilon_{\text{total}} = \varepsilon_{\text{thermal}} = 2.6\%$ to the suspended channel. As can be seen in Fig. 5.4(a), this built-in strain creates a scalar potential shift of the Dirac point to $V_G \approx -4$ V, for a gate-channel spacing of $t_{\text{vac}} = 50$ nm. Figure 5.5(a) shows $\sigma - V_G$ at $\varepsilon_{\text{mech}} = 2.5\%$ for $\theta = 30^\circ$, and t_{vac} respectively 50 nm (black), 100 nm (blue), and 200 nm (red). As the spacing is increased, larger V_G is needed to achieve high on/off ratios. For a realistic $t_{\text{vac}} = 50$ nm, very high on/off ratios ($\sigma_{\text{on/off}} > 10^4$) are possible even for modest V_G between -5 V and 0 V. The inset of Fig. 5.5(a) plots the

$\sigma - V_G$ data on a log scale, and shows a subthreshold slope of 240 mV/dec. The subthreshold slope is not limited by the thermionic limit, and we calculate subthreshold slopes below 60 mV/dec when $t_{\text{vac}} < 10$ nm. It could be reduced much further by using a gate-channel spacer with a higher dielectric constant than vacuum, and a shallow, but wide suspension.

Figure 5.5(b) demonstrates a second application for GQSTs as ultra-sensitive strain or pressure sensors. The turning on and off of the conductivity can be triggered entirely by mechanical actuation, while holding V_G constant. The data show respectively $\sigma - \varepsilon_{\text{mech}}$ at $V_G = 0$ V (black), -5 V (red), and -10 V (blue), with $t_{\text{vac}} = 50$ nm and $\theta = 30^\circ$. In the inset of Fig. 5.5(b), we show the expected relative resistance change, R/R_0 , of the graphene channel at $V_G = -10$ V. While previously demonstrated graphene strain sensors [38, 146] have shown a roughly linear resistance change with strain, these GQSTs have a range where they are exponentially sensitive. The location in $\varepsilon_{\text{mech}}$ of this exponential sensitivity region is tunable with V_G .

In Fig. 5.5(c)–(d), we plot colour maps of the highest $\sigma_{\text{on/off}}$ ratio extracted from data similar to Fig. 5.5(a) within a range $V_G = \pm 5$ V and $V_G = \pm 10$ V respectively. We map the on/off ratio as a function of the contact doping $\Delta\mu_{\text{contact}}$, and the lattice orientation θ , when $t_{\text{vac}} = 50$ nm. For $\varepsilon_{\text{total}} = 5.1\%$ and $|\Delta\mu_{\text{contact}}| \leq 0.12$ eV, a $\sigma_{\text{on/off}} > 10^4$ is achieved with a 5 V gate range in devices where $\theta \geq 16^\circ$. This defines a broad region (red) of parameter space for an excellent GQST effect, and makes it plausible that this platform can lead to an experimental demonstration. For instance, for $|\Delta\mu_{\text{contact}}| \approx 0.1$ eV, and using crystals with random θ orientations, we expect a strong GQST effect in half of the devices. Moreover, the prediction is robust to variations in the exact value of the applied mechanical and thermal strains. To show this, we draw an additional contour line in Fig. 5.5(c)–(d) corresponding to $\sigma_{\text{on/off}} > 10^4$ for $\varepsilon_{\text{total}} = 2.6\%$.

Contact resistance and extrinsic impurity doping of the channel are relevant experimentally, but would not modify significantly Fig. 5.5(c)–(d). For realistic series resistances ($R_S < 1000 \Omega$) [122, 160], we calculate a $\sigma_{\text{on/off}}$ reduction of $< 20\%$ for $V_G = \pm 5$ V. A realistic charge impurity density of $n_{\text{imp}} = 5 \times 10^{10} \text{ cm}^{-2}$ [151, 161] is equivalent to the doping created by $(V_G - V_D) = 0.45$ V, when $t_{\text{vac}} = 50$ nm. From Fig. 5.2(a), we see that the location of the charge degeneracy point V_D is significantly below $V_G = -10$ V at $\varepsilon_{\text{total}} = 5.1\%$. In Fig. 5.5, the doping of the channel is consequently largely dominated by the electrostatic gate doping, and the impact of n_{imp} is negligible.

5.6 Conclusions

In conclusion, we presented an experimental platform able to realistically implement proposals for uniaxial strain-engineering of quantum transport in 2D materials. Some of the key aspects of the proposed devices and instrumentation are a wide aspect ratio of the transistor channels, which removes the need for ordered crystal edges, and an independent control over the mechanical strain and the charge density in the devices. This platform provides a wide experimental tunability for low-temperature transport experiments.

We then reported an applied theoretical model describing quantitatively QTSE in graphene. The model includes the effect of strain on the Fermi energy (scalar potential), on the position of the Dirac points in k -space (gauge vector potentials), and the anisotropy of the Fermi velocity. We included the dominant experimental parameters such as contact doping, the reciprocal lattice distortion for an arbitrary crystal orientation, and the thermally and mechanically generated strains. We showed that the calculated $\sigma - V_G$ as a function of $\varepsilon_{\text{total}}$ gives four experimentally observable signatures as follows: a gate-shift of the charge conductivity curves, a dramatic decrease in conductivity, a rich set of Fabry-Pérot resonances, and a tunable electron-hole conductivity asymmetry.

Finally, we assessed the performance of the proposed GQST devices. We found that comfortably within experimental capabilities, the charge conductivity in graphene can be completely suppressed by uniaxial strain. We mapped out the parameter space for contact doping, crystal orientation, and applied strain where a robust GQST effect with $\sigma_{\text{on/off}} > 10^4$ can be achieved using small V_G . This transistor effect is purely a result of the quantum (ballistic) nature of the transport, and does not arise from a bandgap generation. Recent progresses in making room-temperature ballistic graphene devices [140], and building controlled strain fields into substrates [47, 48], pave the way for GQSTs to be used in flexible electronics [141], and in valleytronics [31, 147]. More immediately, the proposed platform and model should lead to a demonstration and optimization of GQSTs.

Chapter 6

Experimental Evidence for Strain-Induced Scalar and Vector Potentials in Graphene

In this chapter, we show experimental results from electron transport measurements in strained suspended graphene, using our instrumentation for quantum transport strain engineering (QTSE). Here, we will show strong evidence for the observation of strain-induced scalar and vector potentials in graphene, causing transport features consistent with pseudo-magnetic field generation in graphene quantum dots (QDs), and with predictions from our applied transport model (Chapter 5) in a ballistic graphene device. These unique transport signatures allow us to use strain as a tool to measure the contact doping and crystal orientation of the ballistic graphene device. The strain-tunable vector potentials we observe in these devices have applications in studying the quantum nature of graphene through Aharonov-Bohm experiments, where the quantum phase of electrons lead to interference, or as graphene quantum strain transistors. The devices discussed here were constructed using the fabrication methods discussed in Chapter 3.

6.1 Introduction

Total suppression of conductivity in graphene has been long sought after in condensed matter research, and is instrumental in the realization of high switching frequency dc graphene transistors, which could be used for integrated quantum circuits in graphene [39,165]. To this end, there has been much focus on gap generation in graphene's band structure [36]. However,

this approach reduces carrier mobility and eliminates relativistic carrier behaviour which are fundamental to graphene’s interest, in the scientific community [37]. A less conventional approach involves applying uniaxial strain to graphene, which is predicted to lead to a quantum transport gap while maintaining ballistic transport [32,35,56]. Such devices could be used in room temperature quantum circuits, for high-quality transistor function or highly sensitive strain sensors, owing to their long coherence lengths [9]. We refer to these devices as graphene quantum strain transistors (GQSTs). The GQST transport gap, discussed in detail in Chapter 5, arises from a strain-induced vector potential which changes the carrier trajectories in the graphene sheet and is predicted to lead to the extremely high on/off ratios [35,56].

Here, we present our experimental findings on strain-tunable scalar and vector potentials in graphene, and test the validity of our realistic applied transmission model, presented in Chapter 5. We fabricate suspended graphene gap junction and break junction devices using our fabrication methods, discussed in Chapter 3, using wafers with 300 nm SiO₂. This allows us to establish that our methodology and instrumentation can produce measurable strain-induced scalar and vector potentials, rather than use the ideal set fabrication parameters (50 nm SiO₂) used in Chapter 5, which would require more advanced fabrication methods. We measure strain-tunable electron transport in four suspended graphene devices, using our instrumentation for quantum transport strain engineering.

In two suspended graphene quantum dot devices, we observe shifting of the quantum dot energy states with strain. We show that these were unlikely to have originated from the strain-induced scalar potential, but rather are consistent with the presence of pseudomagnetic fields (B_{ps}). These pseudomagnetic fields are likely a product of non-uniform strain profiles, caused by the irregular geometry and small size (~ 10 nm) of our quantum dots. In a suspended ballistic graphene device, we measured and quantified all four predicted signatures of the strain-mediated scalar and vector potentials: a gate-shift in conductivity associated with the strain-induced scalar potential, and a decrease in conductivity, modification of electron-hole transport asymmetry, and shift of Fabry-Pérot (FP) resonances associated with the strain-induced vector potential. We quantify these signatures, and use them to determine the crystal orientation and contact doping of the device. Using these extracted parameters, we simulate transport data using our applied model, finding very good semi-quantitative agreement between experiment and theory. This indicates that GQSTs are realistically achievable, and further study is warranted; particularly with the use of wafers with thinner oxide spacing (~ 50 nm), and the use of polarized Raman spectroscopy [50,154],

or a scanning tunnelling microscope (STM) [155] to measure crystal orientation.

6.2 Evidence for strain-tunable pseudomagnetic fields in graphene quantum dots

In this section, we will discuss two suspended graphene devices which exhibit quantum dot transport behaviour. We found that straining these devices caused a smooth and continuous shift of their quantized energy levels, showing that our QTSE instrumentation functions properly. We attribute these shifting levels to pseudomagnetic fields caused by non-uniform strains in these devices, rather than strain-induced scalar potentials. Finally, we show that the observed gate-shift in our data moves the entire Coulomb diamond quantum dot spectrum, not just the Coulomb peaks.

6.2.1 Suspended graphene quantum dots

To generate extreme uniaxial strains in graphene, we fabricated ultra-short graphene break junctions using our electromigration procedure (see Section 3.4). One such device, Device 1, is shown in a false coloured scanning electron microscope (SEM) image in Fig. 6.1(a), with source and drain contacts under the gold films (yellow), and gate electrode under the oxide (blue). The graphene channel is not visible, indicating that a short electromigrated gap was closed due to thermal expansion of the gold films upon warming the device to room temperature. In the top-right inset, we show a zoom-in of the break junction, from which we estimate a channel width of $W = 70 \pm 30$ nm. In the top-left inset, we show a tilted SEM image of this device at 70° tilt, showing a total suspended length of $u = 1.0 \pm 0.1$ μm . The vacuum and oxide spacings under the graphene channel in Device 1 were measured after suspension by ellipsometry and reflectometry: $t_{\text{vac}} = 97$ nm, and $t_{\text{ox}} = 201$ nm, giving $c_{\text{G}} = 0.60$ F/cm². Using $u = 1.0 \pm 0.1$ μm , we calculate the displacement ratio for Device 1 using Eq. 6.3, $dx/dz = 4.5 \times 10^{-6}$.

In Fig. 6.1(b) we show our measured $dI/dV_{\text{B}} - V_{\text{G}} - V_{\text{B}}$ transport data from Device 1, taken at $T = 1.3$ K, as with all data in this section. We observe clear Coulomb diamonds in Device 1, indicating formation of a graphene QD. The irregular pattern of the diamonds is consistent with chaotic Dirac billiard behaviour [166], not unexpected given the small, non-circular shape of the QD. We can calculate the total gate capacitance from their average widths: $C_{\text{G}} = e/\Delta V_{\text{G}} = e/0.7$ V = 0.2 aF, corresponding to an area of ≈ 3000 nm².

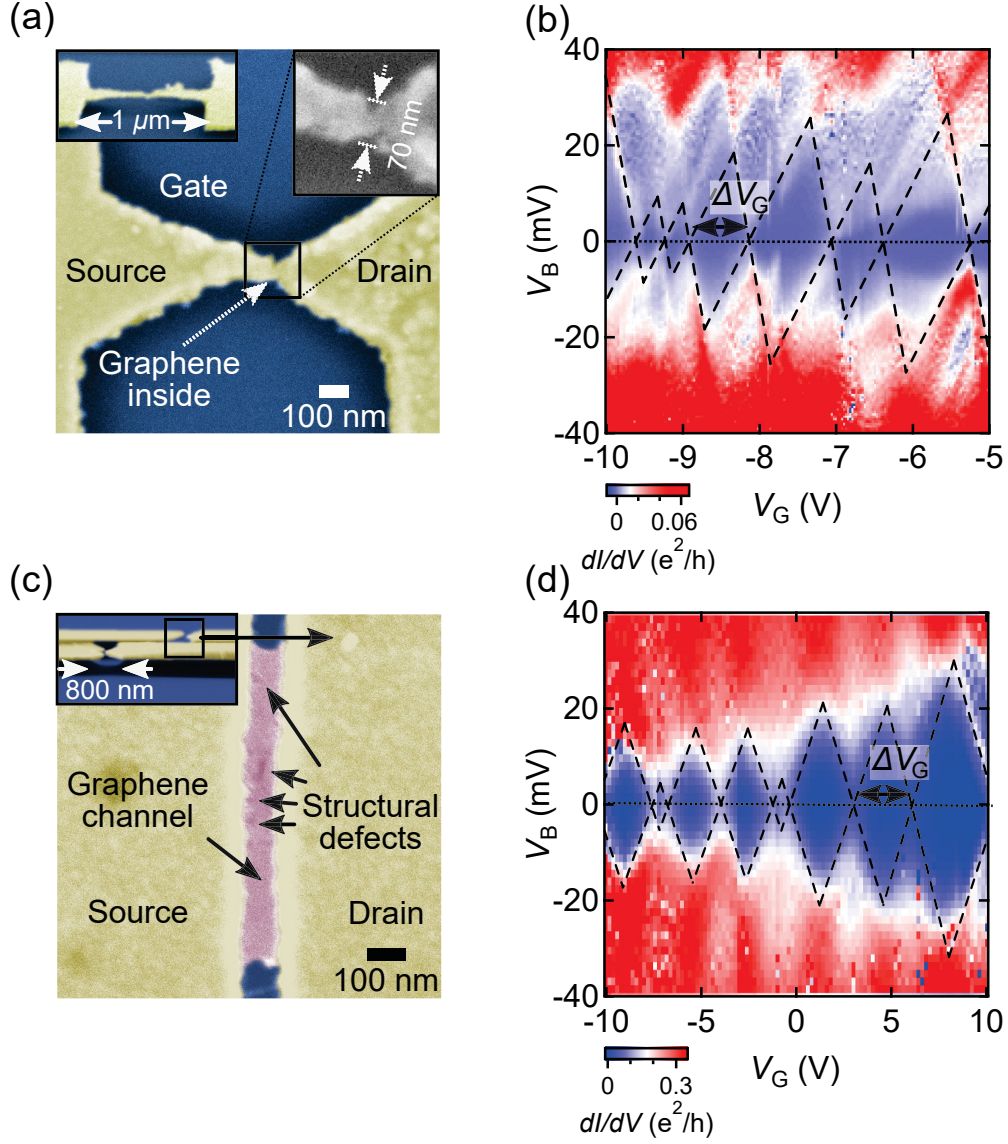


Figure 6.1: Suspended graphene quantum dots. (a) False coloured SEM image of Device 1, a graphene break junction. The top left inset shows a tilted SEM image (70°) of the suspended break junction. The top right inset shows a close-up view of the break junction which has width $W \approx 70$ nm. The graphene channel is not visible as thermal expansion of the gold films caused the gap to grow together. (b) $dI/dV_B - V_B - V_G$ data from Device 1, showing irregular Coulomb blockade diamonds, indicative of chaotic Dirac billiard behaviour. (c) False coloured SEM image of Device 2, a graphene gap junction. Structural defects in the graphene sheet are clearly visible. The inset shows a tilted SEM image (80°) of the device, highlighted with the black square. (d) $dI/dV_B - V_B - V_G$ data from Device 2, showing irregular Coulomb blockade diamonds, indicative of chaotic Dirac billiard behaviour.

Using $W \approx 70$ nm as measured from the SEM image, this corresponds to a device length of $L \approx 40$ nm.

In addition to this break junction device we observed QD transport in one of our gap junction devices, Device 2. This device is pictured in the false coloured SEM in Fig. 6.1(c), where the graphene channel (pink) has dimensions $W = 770 \pm 10$ nm, and $L = 85 \pm 10$ nm. There are clear discolourations in the graphene sheet, a result of structural defects such as small tears in the graphene lattice, potentially from reactive ion etching (RIE). In the inset, we show a tilted SEM image of Device 2 (80° tilt), behind an additional pair of suspended gold films, highlighted by the black square. Using ellipsometry and reflectometry after suspension, we measured the vacuum and oxide spacing in Device 2 $t_{\text{vac}} = 274$ nm and $t_{\text{ox}} = 36$ nm, giving $c_G = 0.31$ F/cm². From the visible suspended Au films we measured a total device suspension length of $u = 0.8 \pm 0.1$ μ m. As the gold films are the same in this device, we expect this number to accurately describe the suspension of Device 2. This gives a displacement ratio $dx/dz = 3.6 \times 10^{-6}$ (Eq. 6.3).

In Fig. 6.1(d), we show $dI/dV_B - V_B - V_G$ transport data from Device 2. This device also exhibits an irregular Coulomb blockade pattern indicative of a chaotic Dirac billiard system. Therefore, it appears that the structural defects visible in Fig. 6.1(c) disrupt transport in the graphene channel, resulting in confinement of the charge carriers. This is unexpected in the short and wide graphene gap junction, which is an ideal candidate for ballistic transport. A precedent for this defect-induced QD behaviour in graphene is graphene anti-dot lattices, where missing lattice sites in the graphene sheet have been shown to open a band gap [167, 168]. Measuring the diamond widths from the transport data yields a measure of the gate capacitance $C_G = e/\Delta V_G = e/2.6$ V = 0.06 aF, corresponding to an area of ≈ 2000 nm², indicating that despite the large size of the graphene sheet, the defect-induced quantum dot has an average radius of ≈ 25 nm.

6.2.2 Strained graphene QDs: evidence for tunable pseudomagnetic fields

Here, we will present our findings on electron transport in strained graphene quantum dots. We will first calculate the expected strain magnitude for Devices 1 and 2 using our QTSE geometry. In Fig. 6.2(a) and (b), we show colour plots of $G - V_G - dz$ data, measured in Devices 1 and 2 respectively, at $V_B = 1$ mV. On the right axes, we plot estimated mechanical strains calculated using the displacement ratios of the two devices, and the maximum position of the push screw: in Device 1 $dz = 107$ μ m corresponds to a lateral

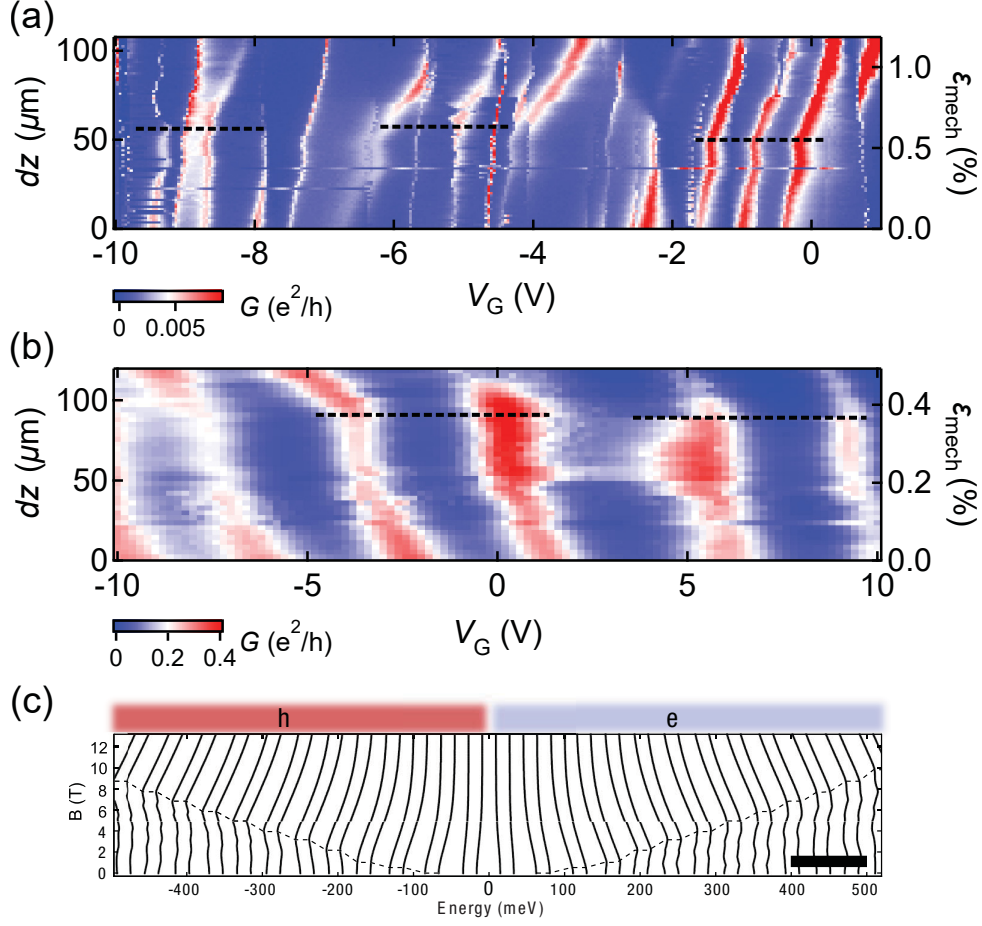


Figure 6.2: Energy level shifts in strained graphene quantum dots. (a) and (b) show $G - dz - V_G$ transport data from Devices 1 and 2 respectively, taken at $V_B = 1$ mV. Estimated mechanical strains are marked on the right axes. Both datasets show kinks in the shifting of the QD levels, indicated by the dashed black lines. (c) Simulated quantum dot energy levels as a function of perpendicular magnetic field for a 50×80 nm QD from Ref. [169], showing remarkable similarity to the data above. The dashed line marks the positions of kinks in the data associated with level crossings at the $\nu = 2$ filling factor.

strain of $\varepsilon_{\text{mech}} = dx/L = 0.48 \text{ nm}/40 \text{ nm} = 1.2\%$, while in Device 2 $dz = 118 \text{ }\mu\text{m}$, yields $\varepsilon_{\text{mech}} = dx/L = 0.42 \text{ nm}/85 \text{ nm} = 0.5\%$, where strain is applied to the entire suspended flake, not just the QD. In the data, we observe clear shifting of the energy levels (Coulomb peaks, red data) with increasing motion of the push screw. We quantify this shift by the difference in gate between minimum and maximum strain, following a single Coulomb peak. In Devices 1 and 2, this shift is $\approx 1 \text{ V}$ and $\approx -2 \text{ V}$ respectively. In both cases, we observe a kink in the gate-shifts of the blockade peaks with strain, as highlighted by the horizontal dashed lines.

Initially it seems that the gate-shift could arise from the strain-induced scalar potential discussed in Chapter 5. However, on closer inspection this seems unlikely. Firstly, the scalar potential caused by uniaxial strain always lowers the graphene work function, causing negative gate-shifts of the features in the data. The observed strain-induced gate-shift is positive in Device 1. Secondly, we investigate the magnitude of the gate-shift in Device 1. Using Eq. 6.4 with parameters $g_{\varepsilon} = 3 \text{ eV}$ and $\varepsilon_{\text{mech}} = 1.2\%$, the measured gate-shift of $\approx 1 \text{ V}$ is much weaker than that predicted for the strain-induced scalar potential, requiring $\varepsilon_{\text{thermal}} < 0$ (slack in the graphene sheet). We know that this is not the case, as there is no slack-associated “delay” in the shifting of the Coulomb peaks as strain is applied. Thirdly, we see that there is some variance in the shape and magnitude of the motion of the Coulomb peaks. For a scalar potential induced by uniaxial strain, we would expect the gate-shift to be completely uniform across the dataset, resulting in parallel behaviour of the blockade peaks with strain. The direction, magnitude, and shapes of the energy level shifts provide strong evidence that the gate-shift is not associated with a strain-induced scalar potential. This non-parallel gate-shift of the blockade peaks is also visible in Device 2.

If the strain-induced scalar potential is not the cause of the gate-shift observed in our QDs, the strain-induced vector potential is the next most likely candidate. Uniaxial strain generates a constant vector potential which causes a momentum shift of the carriers in the suspended graphene sheet, as discussed in Chapter 5. As this momentum shift is not associated with any change in energy, we do not expect a constant vector potential to have a strong effect on the energy levels of a graphene QD. Because we do not know the exact shape or orientation of the QDs in Devices 1 and 2, it is possible that non-uniform strains are created in the channel by bending the chip with our QTSE set-up. Non-uniform strains would create vector potentials with non-zero curl, and therefore potentially strong pseudomagnetic fields. The gate-shift of the Coulomb peaks with strain shares a striking resemblance to previous studies where graphene QDs were studied in terms of a perpendicular magnetic

field [169–171]. We show calculated QD energy level positions as a function of gate and magnetic field for a 50×80 nm QD from Ref. [169] in Fig. 6.2(c) for comparison, with hole states on the left at negative energy and electron states on the right at positive energy. From the data in Fig. 6.2(c), it is clear that the Coulomb peaks positions, indicated by the black lines, shift towards the charge neutrality point (Energy = 0) for increasing magnetic field. Kinks in the simulated data, marked by the dashed black lines, indicate level crossings at the $\nu = 2$ filling factor, and small oscillations in the peak positions at large energy indicate level crossings of the single particle levels for the $n=0$ and $n=1$ Landau levels. By analogy, a strain-induced pseudomagnetic field would show the same features, explaining why we observe a gate-shift in opposite directions in Devices 1 and 2; the visible charge states in Device 1 are holes and in Device 2 are electrons. In the transport data from Device 1 in Fig. 6.2(a), the predicted energy level fluctuations are visible in the charge states near $V_G = -10$ V. Moreover, we observe the predicted kinks in our experimental data, marked by the black dashed lines, providing compelling evidence that the observed gate-shift is a result of pseudomagnetic fields in strained graphene quantum dots.

By comparing the measured data from Device 1 in Fig. 6.2(a) to the simulated magnetic field data in Fig. 6.2(a), we can estimate the magnitude of the pseudomagnetic field in Device 1. Using the fact that we observe 20 charge states in our experimental data with positive motion of the Coulomb peaks, and comparing this to the simulated data in Fig. 6.2(a), gives a lower bound estimate of $B_{ps} \approx 8$ T at $\varepsilon_{mech} = 0.5\%$. In the measured data from Device 2, we do not have sufficient visible charge states to make any statements about the magnitude of B_{ps} , but the data match the qualitative picture of strain-induced pseudomagnetic fields.

Finally, we show that it is the entire Coulomb diamond spectrum that shifts with strain. In Fig. 6.3 we plot $dI/dV_B - V_B - V_G$ for $\varepsilon_{mech} = 0\%$, 0.6% , and 1.2% . Nearly the same Coulomb diamond pattern is repeated in all three datasets, simply shifted to a more positive gate position. The black arrows highlight this gate shifting motion.

We have shown evidence for strain-induced pseudomagnetic fields in graphene QDs. From our transport data, it is unclear how tunable this pseudomagnetic field is, or how much of it is due to built-in thermal strain in the system. However, we have shown evidence of large pseudomagnetic fields in graphene QDs, which bodes well for the study of graphene valleytronics and large pseudomagnetic fields using our QTSE instrumentation, and shows that further study of strained graphene QDs is warranted.

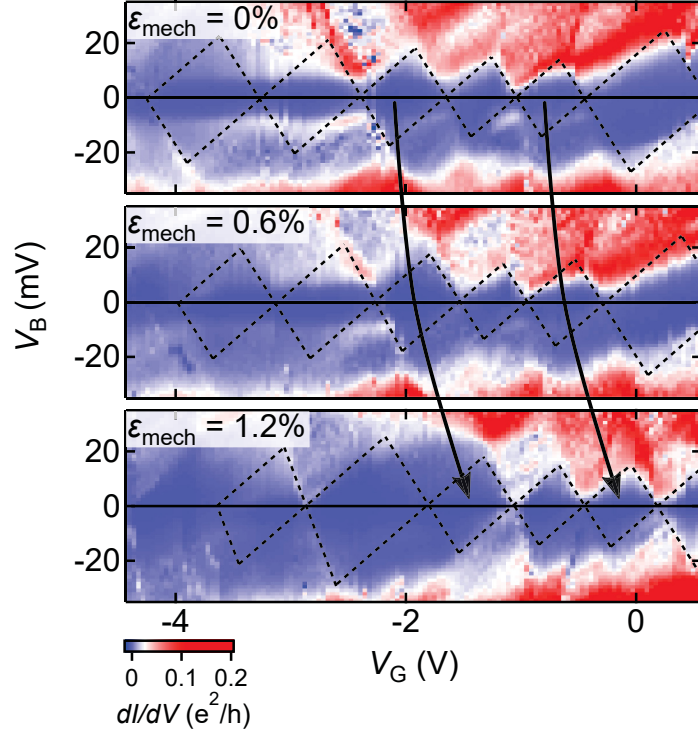


Figure 6.3: Strain-induced shifting of Coulomb diamonds in graphene QDs. $dI/dV_{\text{B}} - V_{\text{B}} - V_{\text{G}}$ from Device 1 at $\epsilon_{\text{mech}} = 0\%$, 0.6% , and 1.2% (top to bottom). The general trend is a shifting of the Coulomb blockade diamonds to positive gate with strain as indicated by the black arrows, with a slight change in shape of some of the blockade diamonds.

6.3 Suspended ballistic graphene: device geometry and electron transport

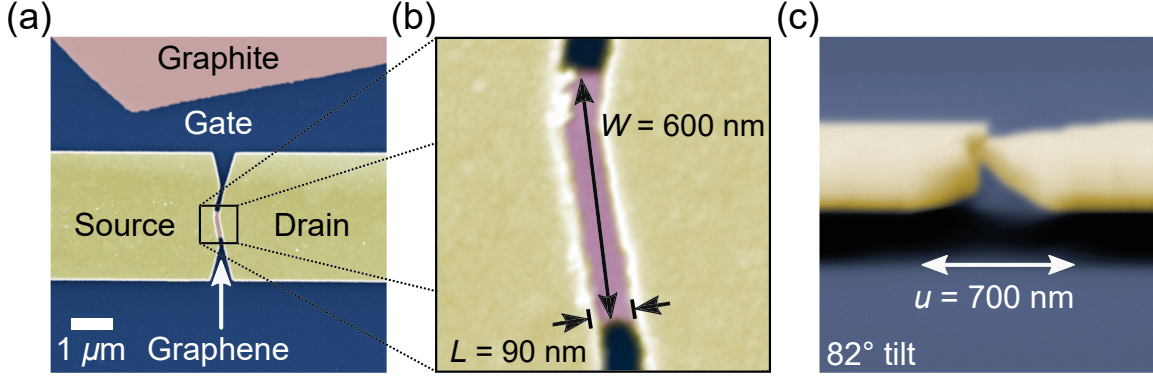


Figure 6.4: False colour SEM images of a suspended graphene device. (a) SEM image of Device 3, showing the Au films (yellow) covering the graphene source and drain electrodes, back gate under remaining oxide (blue) and graphene channel (pink). (b) Close-up view of Device 3, with graphene (pink) channel dimensions. (c) Tilted SEM image of Device 3, taken at 82° tilt, showing clear suspension, and undercut length.

In this section we show the channel and suspension geometry of a graphene device, and present transport measurements to show that it is ballistic, before showing the effects of strain on electron transport in this device. In Fig. 6.4 we show the geometry of a suspended graphene device, Device 3. In Fig. 6.4(a)–(b), we show false coloured top-down SEM images of Device 3, zoomed out and zoomed in respectively, showing the Au films (yellow) which cover the source and drain graphene contacts, as well as the global back gate electrode, which lies underneath the remaining oxide layer (blue) after buffered oxide etching. The graphene channel is pictured in pink, as well as a nearby piece of graphite, which has no effect on our sample. We measure the length and width of Device 3 to be $L = 90 \pm 10 \text{ nm}$ and $W = 600 \pm 20$ from the SEM images. The somewhat irregular shape of the gold films is a result of proximity effects during e-beam lithography. However, due to the parallel, nearly vertical edges at the gold-graphene junctions, and the long injection lengths in metal-carbon contacts [53], we do not expect this to alter transport significantly from that expected in our model for a rectangular graphene sheet.

Using reflectometry and ellipsometry measurements, we determined the vacuum and oxide thicknesses under the suspended device to be $t_{\text{vac}} = 211 \text{ nm}$ and $t_{\text{ox}} = 106 \text{ nm}$. From

this we calculate the gate capacitance per unit area:

$$c_G = \frac{\epsilon_{\text{vac}}\epsilon_{\text{ox}}}{t_{\text{ox}}\epsilon_{\text{vac}} + t_{\text{vac}}\epsilon_{\text{ox}}}, \quad (6.1)$$

treating the system as two capacitors in series, giving $c_G = 0.37 \text{ F/cm}^2$. In Fig. 6.4(c), we show the device suspension with tilted SEM imaging, taken at 82° tilt. The graphene channel is clearly suspended and shows the total suspension length of the device, $u = 700 \pm 50 \text{ nm}$.

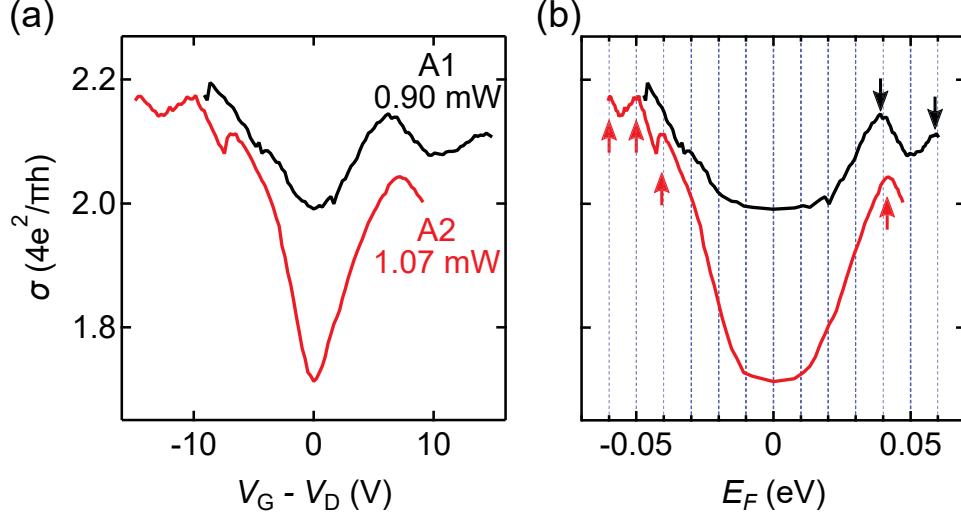


Figure 6.5: Ballistic transport in suspended graphene. (a) $\sigma - (V_G - V_D)$ data from Device 3 at 1.3 K and $V_B = 0.5 \text{ mV}$ after two different anneals, A1 at 0.9 mW (blue) and A2 at 1.07 mW (red). (b) Same data as in (a), plotted in terms of Fermi energy. In both anneals, evenly spaced conductance oscillations form as a result of coherent transport in the device. The resonance energy spacings for holes and electrons are $\Delta E_{\text{FP}}^e \approx 0.02 \text{ eV}$ and $\Delta E_{\text{FP}}^h \approx 0.01 \text{ eV}$. The smaller energy spacing for holes indicates p -type doping in the device contacts.

We now present electron transport measurements from Device 3. All data presented were taken at $T = 1.3 \text{ K}$ and bias voltage $V_B = 0.5 \text{ mV}$. In Fig. 6.5(a), we show $\sigma - (V_G - V_D)$ data from Device 3 after initial current annealing at 0.9 mW (A1, black), and secondary annealing (A2, red), where V_D is the gate voltage associated with the minimum conductivity at the Dirac point. For more information on the annealing process see Section 3.4. In Fig. 6.5(b), we plot the same conductance data from (a) in terms of the Fermi energy of the graphene sheet ($E_F = \text{sgn}(V_G - V_D)\hbar v_F \sqrt{\pi|V_G - V_D|c_G/e}$), with black and red arrows indicating the positions of conductance peaks. From these data, we observe two signatures which provide strong evidence that Device 3 is ballistic. The data in Fig. 6.5(a) follow the characteristic $\sigma \propto \sqrt{V_G}$ expected for ballistic transport, while the data in Fig. 6.5(b) show conductance peaks at regular intervals, indicative of coherent ballistic transport (see Section 2.3).

From Fig. 6.5, it is clear that current annealing the graphene channel lowers its conductivity, sharpens the conductivity minimum, and causes a gate-shift of the conductivity curves, indicating that the annealing process has removed charge impurities from the channel [60, 172]. However, the conductivity minimum is well above the expected ballistic minimum value for graphene, $\sigma_{\min} = 4e^2/\pi h$ [69], implying that the annealing is incomplete. Using strained transport data, we will later estimate the remaining impurity density n_{imp} .

From anneals A1 and A2 in Fig. 6.5(b) we measure the FP energy spacing for electrons and holes to be $\Delta E_{\text{FP}}^e \approx 0.02$ eV and $\Delta E_{\text{FP}}^h \approx 0.01$ eV respectively. We take the energy spacing to be that of a 1D channel $\Delta E_{\text{FP}} = \hbar v_F/2L$ [29], as the majority of transmission arises from normally incident charge carriers [71]. We calculate channel lengths for electrons and holes of $L_{\text{FP}}^e \approx 90$ nm and $L_{\text{FP}}^h \approx 180$ nm respectively, with the electron channel matching the SEM-measured channel length. The electron-hole channel length asymmetry is analogous to that measured in our ultra-short nanotube device in Chapter 4, this time with holes moving coherently in the graphene leads under the gold films, and electrons confined to the naked graphene channel. This indicates p-type doping in the graphene leads. For graphene covered by gold films, p-type doping indicates that there is oxygen content on the gold films which have either not been, or have only been slightly, annealed [53, 76]. As in our electromigrated carbon nanotube devices from Chapter 4, we expect the suspended gold contacts to be partially annealed by proximity to the channel annealing. On inspection of the SEM image in Fig. 6.4(b), we see that the gold films near the graphene channel have a polycrystalline texture, indicating that the gold films have not been strongly annealed. This is not unexpected as Joule heating is much less localized, and more heat sinking is provided by the wide and thick suspended contacts in gap junctions than in electromigrated break junctions.

6.4 Strain-tunable transport in ballistic graphene: scalar and vector potentials

We now calculate the expected uniaxial strain range for Device 3, before showing strained electron transport data. As discussed in Chapter 5, we expect the electrostatic strain from the gate electrode pulling on the graphene sheet to be negligible. However, thermal strain can be quite significant at low temperatures, and must be included. The thermal strain, $\varepsilon_{\text{thermal}}$, arises from contraction of the suspended gold films and expansion of the graphene sheet with decreasing temperature. We expect the thermal contraction in the Si/SiO₂ substrate to be

negligible [159]. The total thermal strain in the graphene sheet at temperature T is therefore given by the formula:

$$\varepsilon_{\text{thermal}} = -\frac{u - L}{L} \int_{300}^T \alpha_{\text{Au}}(t) dt - \int_{300}^T \alpha_{\text{g}}(t) dt, \quad (6.2)$$

where α_{Au} and α_{g} are the coefficients of thermal expansion for gold and graphene respectively. Using α_{Au} from Ref. [158] and α_{g} from Ref. [173], we calculate a net thermal strain of $\varepsilon_{\text{thermal}} = 1.9 \pm 0.1\%$ for $T = 0$ K.

We now calculate the expected mechanical strain applicable by our QTSE instrumentation for Device 3. The lateral stretching caused by pushing of the screw to bend the chip is the displacement ratio, given by the formula [79, 81]:

$$\frac{dx}{dz} = \frac{3ut}{2D^2}, \quad (6.3)$$

where the factor of $1/2$ comes from the QTSE calibration (Section 3.4.2), and is confirmed by previous experimental QTSE measurements [79]. Using the QTSE parameters discussed in section 3.3.1, wafer thickness $t = 200 \mu\text{m}$, and clamping distance $D = 8.18 \text{ mm}$, we calculate $dx/dz = 3.1 \pm 0.3 \times 10^{-6}$. We measure the $dz = 0$ position of the push screw by ramping the motor position back and forth and measuring current in the graphene device, and any other devices on the same chip. For $dz \leq 0$ there is no detectable change in current. At $dz = 0$ there is a detectable change in current, allowing this position to be determined accurately. We must be very careful in determining how far to displace the push screw, as the Si chips which hold our device can shatter if they are over-bent (see Section 3.3.1). In this device, we use a maximum displacement $dz_{\text{max}} = 173 \mu\text{m}$, as determined by rotations of the stepper motor; a mechanical strain $\varepsilon_{\text{mech}} = 0.6 \pm 0.1\%$ is expected in Device 3. This gives a total accessible strain range of $\varepsilon_{\text{total}} = \varepsilon_{\text{thermal}} + \varepsilon_{\text{mech}} = 1.9\text{--}2.5\%$.

We now introduce our main dataset from Device 1, which we will analyze in detail in Sections 6.4.1, 6.4.2. In Fig. 6.6(a) and (b) we show $\sigma - V_{\text{G}} - \varepsilon_{\text{mech}}$ data for forward and backward motion of the push screw respectively, as indicated by the black arrows. These data were collected after anneal A1 (see Fig. 6.5). The colours of the curves from blue to red represent an increase in mechanical strain. We note the impressive reproducibility for forward and backward motion of the push screw. Close inspection of the data reveal the four signatures of strain in ballistic graphene predicted in Chapter 5: scalar-potential-induced gate-shifting of the conductivity minima, and vector-potential-induced transport asymmetry modulation, conductivity suppression, and shifting of the Fabry-Pérot resonances. We will

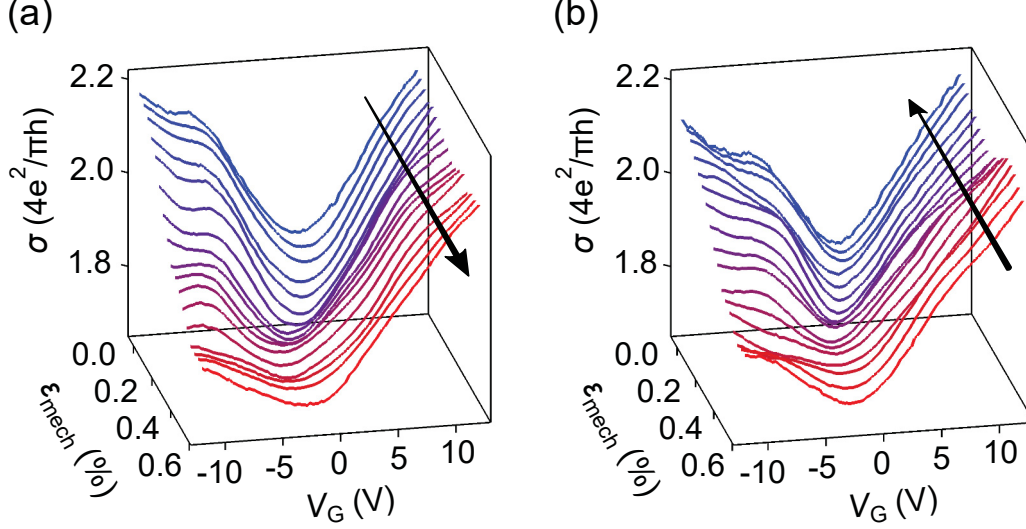


Figure 6.6: Strain-tunable conductivity, and GQST signatures in graphene. (a) and (b) $\sigma - V_G - \varepsilon_{\text{mech}}$ data from Device 3 at 1.3 K and $V_B = 0.5$ mV after anneal A1, for forward and backward motion of the push screw, showing good repeatability. Qualitatively, the four signatures of the strain-mediated scalar and vector potentials are visible in the data with increasing strain: scalar potential gate-shifting of the Dirac point, an overall decrease in conductivity, a change in electron-hole transport asymmetry, and shifting of coherent resonance peaks caused by the strain-induced vector potential.

focus on the scalar and vector potential effects separately in the following two sections.

6.4.1 Experimental measurement of the strain-induced scalar potential

Perhaps the most obvious feature in the main dataset from Device 3, shown in Fig. 6.6, is the shifting of the conductivity minimum (Dirac point) towards negative gate. This strain-tunable shift in the conductivity data was present in all six annealing states of Device 3, even in those where the conductivity minimum was not visible. In Fig. 6.7, we quantify this gate-shifting. In Fig. 6.7(a), we show a colour plot of differential transconductance data as a function of strain $dI/dV_G - dz - V_G$ in Device 3 before anneal A1. In these data, there is no visible Dirac point to track the gate-shift. However, a resonance peak, shown by the red part of the colour plot, shows a clear monotonic decrease in V_G as a function of $\varepsilon_{\text{mech}}$, as highlighted by the black dashed lines. We plot the data extracted along these two black dashed lines in Fig. 6.7(b) for forward and backward motion of the push screw as the filled and open symbols, showing good reproducibility. The data in the bottom part of Fig. 6.7(b) show the gate-shift as measured from the conductivity minimum from the main dataset in

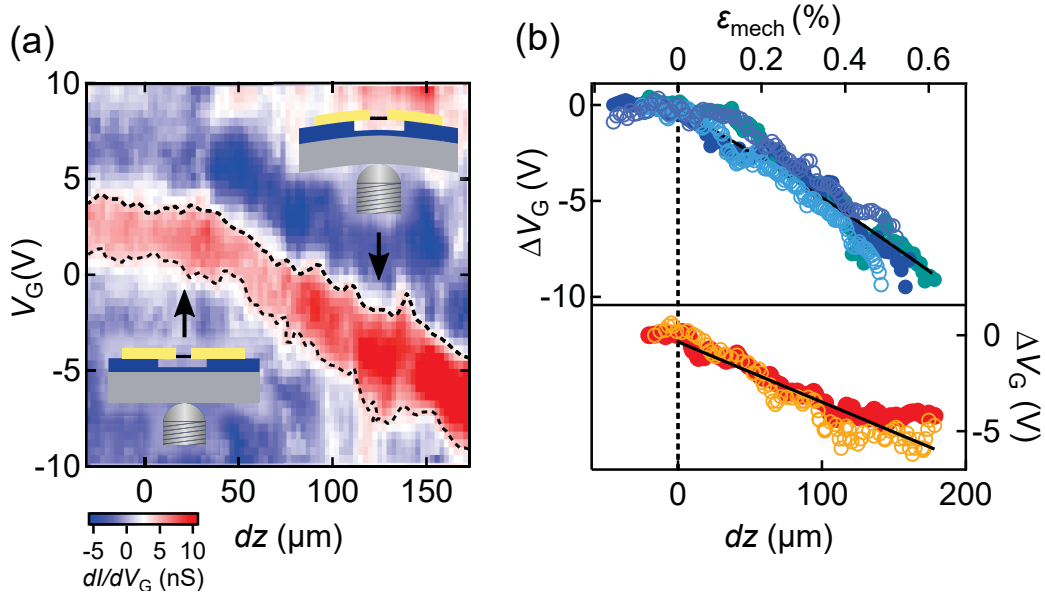


Figure 6.7: Scalar potential shift in strained graphene. (a) $dI/dV_G - dz - V_G$ data from Device 3 at 1.3 K and $V_B = 0.5$ mV before anneal A1. For increasing dz , the chip bends and the suspended devices are strained, as shown by the cartoon insets. The Dirac point is not visible in this data, but a discernable gate-shift of the differential transconductance features occurs with strain, such as the resonance peak outlined with dashed black lines. (b) Extracted gate-shift with strain before (top) and after (bottom) anneal A1, from panel (a) Fig. 6.6 respectively. The filled and open symbols represent forward and backward motion of the screw, showing good repeatability and the black lines are fits to Eq. 6.4 for $\Delta\mu_\epsilon$.

Fig. 6.6 for forward and backward motion of the push screw.

This gate-shift of the conductivity curves with strain is predicted by the GQST model discussed in Chapter 5, arising from the scalar potential associated with the strain-induced change in next-nearest-neighbour hopping. This scalar potential shifts graphene's work function downwards, causing a gate-shift in the conductivity data. The expected gate-shift caused by the scalar potential is:

$$\Delta V_G = -\frac{e}{c_G} \frac{g_\varepsilon^2}{\pi(\hbar v_F)^2} (1 - \nu)^2 ((\varepsilon_{\text{mech}} + \varepsilon_{\text{thermal}})^2 - \varepsilon_{\text{thermal}}^2). \quad (6.4)$$

Using this equation, we fit the data in Fig. 6.7(b), as shown by the solid black lines, giving $g_\varepsilon = 3.51 \pm 0.02$ eV and $g_\varepsilon = 2.93 \pm 0.03$ eV, for the top and bottom fits respectively. This is in good agreement with literature values ranging from 2–4.5 eV [56, 164, 174]. The similarity of these fits shows that even without seeing the Dirac point, it is possible to accurately measure the scalar potential effect in graphene. For the remainder of this section, we will use $g_\varepsilon = 2.9$ eV to match the main dataset.

We will now use this measurement of g_ε to estimate the impurity density in the graphene channel of Device 3. The Dirac point lies at $V_D = 1.92$ V in this device, as measured from the main dataset in Fig. 6.6, for both forward and backward motor motion. For thermal strain $\varepsilon_{\text{thermal}} = 1.9\%$, we use Eq. 6.4 to calculate the Dirac point gate-position $V_D = -8.7$ V, for $\varepsilon_{\text{mech}} = 0\%$. This discrepancy of 10.6 V between the experimental and theoretical Dirac point values corresponds to an impurity density of $n_{\text{imp}} = c_G V_G / e \approx -2.5 \times 10^{11} \text{ cm}^{-2}$, where the minus sign indicates that the channel impurities are p-type dopants. This shows that the scalar potential gate-shift can be used as a tool to calibrate thermal and mechanical strains, as well as measure the impurity density in graphene.

6.4.2 Experimental measurement of the strain-induced vector potential

We now quantify the three remaining predicted signatures of the vector potential observed in Fig. 6.6, and quantify them in terms of the vector potential which arises from the strain-modified hopping between nearest neighbours. These data, extracted from Fig. 6.6, are presented in Figure 6.8. To study only the effects of the vector potential, we subtract a scalar potential correction from all conductivity curves, using $V_G - V_D$.

We first quantify the observed decrease in conductivity as a function of strain, shown in Fig. 6.8(a). The bottom left inset shows unitless σ vs. $V_G - V_D$ data for $\varepsilon_{\text{mech}} = 0\%$ (blue)

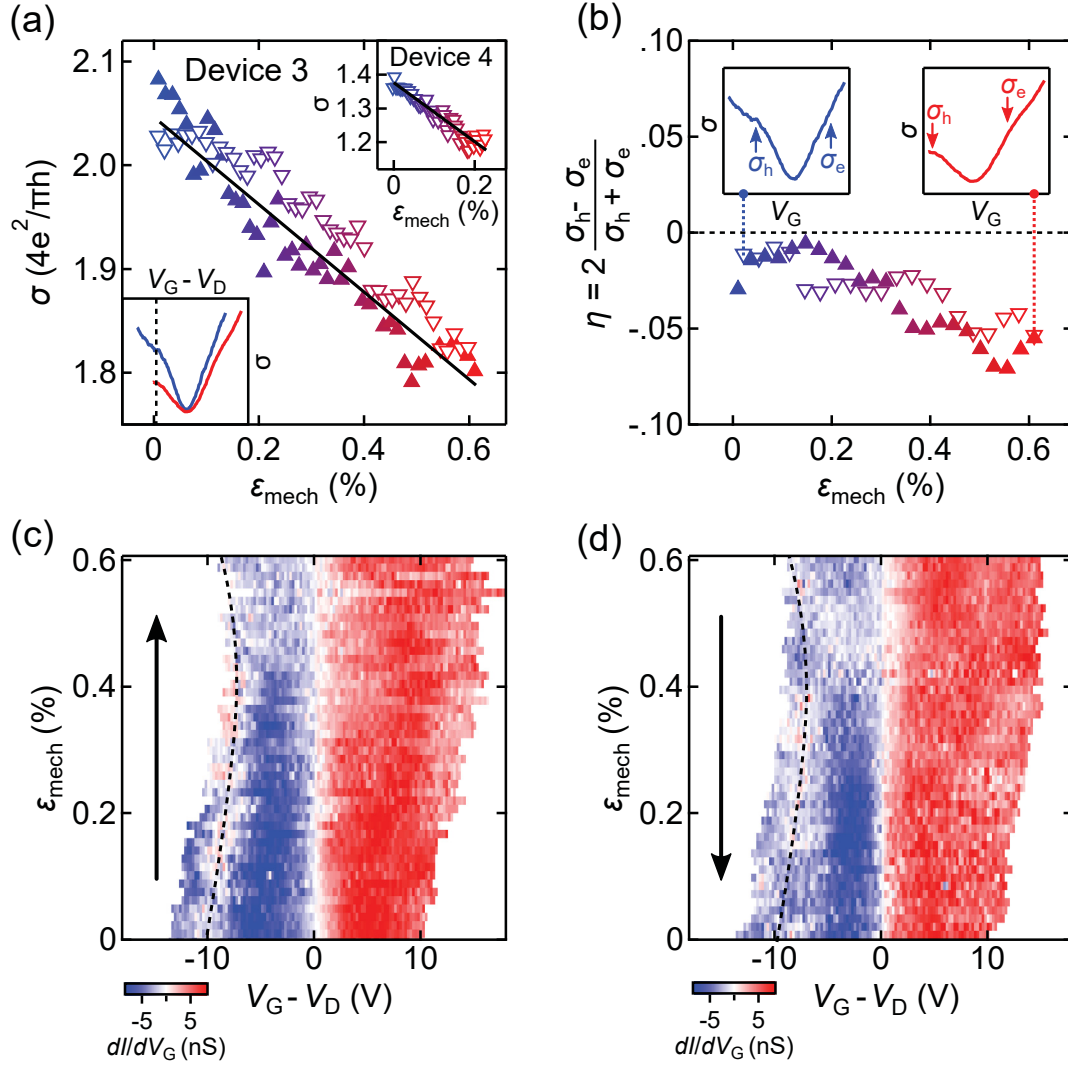


Figure 6.8: Transport signatures of strain-induced vector potentials. (a) $\sigma - \varepsilon_{\text{mech}}$ data from Device 3 at $V_G - V_D = -8.1$ V, with forward (closed symbols) and backward (open symbols) motion of the push screw. The black line is a linear fit of the data. The bottom left inset shows $\sigma - (V_G - V_D)$ data, with dashed line at -8.1 V where the data were extracted for $\varepsilon_{\text{mech}} = 0\%$ (blue) and $\varepsilon_{\text{mech}} = 0.6\%$ (red). Top right inset shows supporting strain-tunable conductivity data from Device 4. (b) Relative transport asymmetry, $\eta = (\sigma_h - \sigma_e)/(\sigma_h + \sigma_e)$ as a function of mechanical strain. The left and right insets correspond to $\varepsilon_{\text{mech}} = 0\%$ and $\varepsilon_{\text{mech}} = 0.6\%$ showing higher conductivity for electrons than holes in both cases, and a greater transport asymmetry at larger strain. (c)–(d) $dI/dV_G - \varepsilon_{\text{mech}} - (V_G - V_D)$ data from the same device, for forward and backward screw motion respectively. The progression of a strong resonance peak is highlighted with black dashed lines, showing significant curvature, with a turning point at $\varepsilon_{\text{mech}} \approx 0.4\%$.

and $\varepsilon_{\text{mech}} = 0.6\%$ (red), showing clear conductivity reduction over the entire gate range. To avoid the influence of impurities in the channel, we study conductivity as far from the Dirac point as possible while retaining as much conductivity data as possible in our gate range. To this end, we investigate our conductivity data at $V_G - V_D = -8.1$ V, indicated by the vertical dashed line in the inset. In the main panel of Fig. 6.8(a), we plot conductivity at $V_G - V_D = -8.1$ V as a function of applied mechanical strain, with filled and open triangles symbolizing forward and backward motion of the push screw, and colours change from blue to red for $\varepsilon_{\text{mech}} = 0\%$ to $\varepsilon_{\text{mech}} = 0.6\%$. In the top right inset we show the reduction in conductivity as a function of strain in a secondary supporting ballistic device, Device 4, which does not clearly show the other signatures of the strain-induced scalar and vector potentials. Device 4 was damaged during measurement, so SEM images are unavailable. As such, we use $L = 100$ nm and $W = 1000$ nm from the e-beam computer aided design (CAD) file, and $u = 800 \pm 100$ nm from adjacent gap junctions on the same chip. These data were taken at $V_G - V_D = -7.1$ V for Device 4. Both devices exhibit a linear decrease in conductivity, with fits shown as black solid lines, with slopes of $d\sigma/d\varepsilon_{\text{mech}} = -42 \cdot 4e^2/\pi h$ and $-88 \cdot 4e^2/\pi h$ for Devices 3 and 4 respectively. These data show that conductivity can be tuned reproducibly using uniaxial strain. This strain-tunable conductivity, caused by the strain-induced vector potential, is a major step towards total conductivity suppression, and realization of high-quality GQSTs.

Secondly, we quantify the change in the transport asymmetry predicted by our GQST model, shown in Fig. 6.8(b). The left and right insets show conductivity as a function of gate voltage from the main dataset for $\varepsilon_{\text{mech}} = 0\%$ (blue) and $\varepsilon_{\text{mech}} = 0.6\%$ (red), highlighting the transport asymmetry. There is a clear difference between the transport asymmetry at minimum and maximum $\varepsilon_{\text{mech}}$. Electron and hole conductivities (σ_e and σ_h) at $|V_G - V_D| = 8.1$ V are indicated by the arrows. We quantify the relative transport asymmetry as $\eta = 2(\sigma_h - \sigma_e)/(\sigma_h + \sigma_e)$, and show this quantity in the main panel, relating the strain magnitudes to the insets with dashed vertical lines. As before, the filled and open triangles symbolize forward and backward motion of the push screw, and blue to red signifying minimum and maximum mechanical strains. In Device 3, η is negative for all strains, and increases in magnitude with increasing strain. We have already established that the graphene leads are p-type doped, and would therefore expect η to be positive (higher conductivity for holes than electrons) for $\varepsilon_{\text{total}} = 0\%$. In Section 5.4, we predicted a monotonic change in η with strain, eventually causing transport asymmetry reversal as a result of the strong vector potential, as well as a monotonic change in η . The fact that η is negative in Device 3 and becomes more

negative with strain indicates that the built-in thermal strain is sufficient to have already reversed the sign of the transport asymmetry. This unconventional transport asymmetry behaviour provides strong evidence for strain-induced scalar and vector potentials in Device 3.

The final transport data signature expected from our GQST model is a rich spectrum of strain-tunable Fabry-Pérot resonances. In Fig. 6.8(c) and (d), we plot differential transconductance colour plots as a function of $\varepsilon_{\text{mech}}$ and $V_G - V_D$ for forward and backward motion of the push screw respectively, as indicated by the black arrows. Our gate and strain range is only sufficient to reveal one moving resonance peak (highlighted by the dashed black line), but it is reproducible in forward and backward motion of the push screw and it is extremely telling. The curvature of the resonance peak gate-position with increasing strain looks remarkably like those in Fig. 5.4(e), where the turning point of the dashed curve highlights the vector potential magnitude. In the data from Device 3, this turning point occurs at $\varepsilon_{\text{mech}} \approx 0.4\%$ and allows a relationship to be established between the vector potential, which depends on the total strain and crystal orientation, and the contact doping $A_{i,y}(\varepsilon_{\text{total}}, \theta) = \Delta\mu_{\text{contact}}/\hbar v_F$. In the following section, we will use this relationship to determine the crystal angle and contact doping of Device 3.

6.5 Strained ballistic graphene: transport simulations

In this section we will estimate the crystal angle and contact doping of Device 3 using the results from the previous section, and simulate its transport using our applied model from Chapter 5. There remain three major unknowns necessary to simulate transport in Device 3: the contact doping $\Delta\mu_{\text{contact}}$, crystal orientation θ , and series resistance R_S . In recent publications [89, 160], estimates of gold on graphene series resistance lie within the range $W \cdot R_S = 200\text{--}600 \text{ } \Omega \cdot \mu\text{m}$. For our $W = 600 \text{ nm}$ device, this gives $R_S = 120\text{--}360 \text{ } \Omega$. By analyzing our data in terms of differences in resistivity ($\rho = 1/\sigma$), rather than conductivity, we can eliminate R_S from our assessment as a constant offset, and reduce the problem to two unknowns, $\Delta\mu_{\text{contact}}$ and θ .

We show resistivity data from Device 3 in Fig. 6.9(a), selected from the main dataset in Fig. 6.6. From blue to red $\varepsilon_{\text{mech}} = 0\%, 0.15\%, 0.3\%, 0.45\%$, and 0.6% respectively. We extract a single unique value from each resistivity curve which is strain-dependent and independent of R_S , the absolute difference in resistivity between electrons and holes $\Delta\rho_{e-h} = \rho_h - \rho_e$ at $|V_G - V_D| = 8.1 \text{ V}$. This quantity is independent of R_S . In Fig. 6.9(a), we show

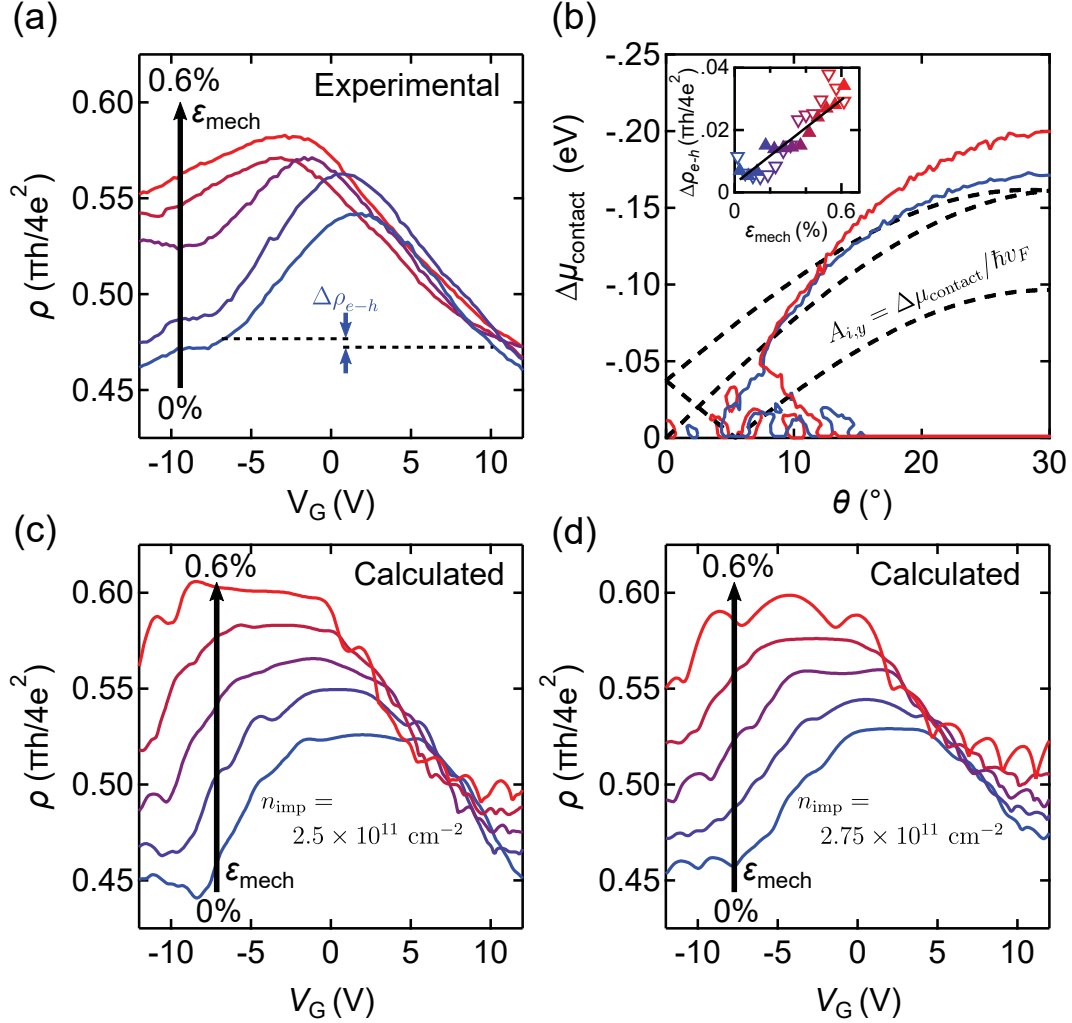


Figure 6.9: Measured and calculated transport data for strained ballistic graphene. (a) Selected experimental $\rho - V_G$ data from Device 3 for mechanical strains $\epsilon_{\text{mech}} = 0\%$, 0.15% , 0.3% , 0.45% , and 0.6% (blue to red). Same data as in Fig. 6.6(a). The electron-hole resistivity asymmetry ($\Delta\rho_{e-h}$, blue arrows) at $|V_G - V_D| = 8.1$ V is shown for $\epsilon_{\text{mech}} = 0$. (b) Inset: $\Delta\rho_{e-h}$ vs. ϵ_{mech} from experimental data for forward (filled) and backward (open) motion of the push screw, with linear fit (black). Main panel: calculated constant $\Delta\rho_{e-h}$ contours vs. $\Delta\mu_{\text{contact}}$ and θ for $\epsilon_{\text{mech}} = 0\%$ (blue) and 0.6% (red). The black contours plot $A_{i,y}(\epsilon_{\text{total}}, \theta) = \Delta\mu_{\text{contact}}/\hbar v_F$ at $\epsilon_{\text{mech}} = 0.4\%$. The three curves intersect at $\Delta\mu_{\text{contact}} = -0.062$ eV and $\theta = 7.8^\circ$. (c) Calculated $\rho - V_G$ data as a function of ϵ_{mech} , matching the data from panel (a), using parameters: $L = 90$ nm, $W = 600$ nm, $\epsilon_{\text{thermal}} = 1.9\%$, $\Delta\mu_{\text{contact}} = -0.062$ eV, $\theta = 7.8^\circ$, $R_S = 350$ Ω , and $n_{\text{imp}} = 2.5 \times 10^{11}$ cm^{-2} . (d) Calculated $\rho - V_G$ data as a function of mechanical strain, matching the data from panel (a), using modified parameters: $\Delta\mu_{\text{contact}} = -0.055$ eV, $\theta = 7.0^\circ$, $R_S = 360$ Ω , and $n_{\text{imp}} = 2.75 \times 10^{11}$ cm^{-2} .

this quantity with blue arrows.

In the inset of Fig. 6.9(b), we plot $\Delta\rho_{e-h}$ at $|V_G - V_D| = 8.1$ V as a function of the mechanical strain, where the filled and open symbols represent forward and backward motion of the push screw and the colours indicate minimum to maximum (blue to red) $\varepsilon_{\text{mech}}$. A linear fit to these data is overlaid in black, from which we extract $\Delta\rho_{e-h} = 0.0003$ and $0.0303 \pi\hbar/4e^2$ for $\varepsilon_{\text{mech}} = 0\%$ and $\varepsilon_{\text{mech}} = 0.6\%$ respectively. In the main panel, we use this information to estimate contact doping and crystal orientation in this device.

We calculate $\Delta\rho_{e-h}$ at $|V_G - V_D| = 8.1$ V as a function of $\Delta\mu_{\text{contact}}$ and θ using Equations 5.3 and 5.4 with parameters $L = 90$ nm, $W = 600$ nm, $c_G = 0.37$ F/cm², $n_{\text{imp}} = 2.5 \times 10^{11}$ cm⁻², $\varepsilon_{\text{thermal}} = 1.9\%$, $\varepsilon_{\text{mech}} = 0\%$ and 0.6% . In the main panel of Fig. 6.9(b) we plot calculated contours which match the values of $\Delta\rho_{e-h}$ at minimum (blue) and maximum (red) mechanical strain. In addition, we plot the relationship $A_{i,y}(\varepsilon_{\text{total}}, \theta) = \Delta\mu_{\text{contact}}/\hbar v_F$ at $\varepsilon_{\text{mech}} \approx 0.4\%$, as measured from Fig. 6.8. We obtain an estimate of the contact doping and crystal orientation of this sample by measuring the intersection of the three contours: $\Delta\mu_{\text{contact}} = -0.062$ eV and $\theta = 7.8^\circ$. The relatively small magnitude of p-type contact doping is consistent with partial annealing of the gold contacts [76] expected in this device.

We will now briefly discuss our treatment of impurity density in our simulations. To include the effects of n_{imp} we must calculate how the spatial variance of the charge impurities affects the total carrier density in the channel. At low temperature ($T \sim 0$ K), we expect the total charge density to be [63]:

$$n_{\text{tot}} = \text{sgn}(V_G - V_D) \sqrt{\frac{(V_G - V_D)c_G}{e}} + n_{\text{imp}}^2. \quad (6.5)$$

Including n_{imp} in our transport calculations introduces an unphysical discontinuity at the Dirac point, as the sign function does not accurately capture the smooth transition between hole and electron densities at the Dirac point. Because the spatial distribution of charge density is roughly Gaussian [175], we average our data using a Gaussian function of height $\frac{1}{2}$ and full-width-half-max n_{imp} , centered at the Dirac point carrier density $n_D = V_D c_G/e$:

$$g(n) = \frac{1}{2} e^{-4 \ln 2 \frac{(n - n_D)^2}{n_{\text{imp}}^2}}. \quad (6.6)$$

To smooth the electron-hole transition in our data, we perform the following operation: $\sigma(n_{\text{tot}}) = \sigma_+(n_{\text{tot}})[1 - g(n_{\text{tot}})] + \sigma_-(-n_{\text{tot}})g(n_{\text{tot}})$, with $\rho(n_{\text{tot}}) = \sigma^{-1}(n_{\text{tot}})$, and σ_+ and σ_- are calculated using Eqs. 5.3 and 5.4 for $+n_{\text{tot}}$ and $-n_{\text{tot}}$ respectively.

Using this Gaussian averaging over the impurity density and the device parameters extracted above, we calculated $\rho - V_G$ data plotted in Fig. 6.9(c). To match the experimental data, a constant series offset of $\rho_0 = 0.23 \pi h/4e^2$ was subtracted, corresponding to a series resistance $R_S = \rho_0 L/2W = 350 \Omega$, where the factor $\frac{1}{2}$ accounts for the two contacts. This is within the expected range of $R_S = 120\text{--}360 \Omega$ [160]. The simulated data reproduces the experimental data in Fig. 6.9(a) quite well. We can improve our simulation slightly by making small adjustments to the parameter values. Plotting contours such as those shown in panel Fig. 6.9(b) and comparing resistivity values across the entire dataset (not shown), we find $n_{\text{imp}} = 2.75 \times 10^{11} \text{ cm}^2$, $\Delta\mu_{\text{contact}} = -0.055 \text{ eV}$, $\theta = 7.0^\circ$ and $R_S = 360 \Omega$. We calculate $\rho - V_G$ data using these parameters, and plot them in Fig. 6.9(d), showing a remarkably good semi-quantitative fit to the experimental data in Fig. 6.9(a). The only major discrepancy between the experimental and simulated data are the strong resonances which arise in our calculated data, due to the addition of quantized transversal transmission modes to the device with gate voltage. These are not observed in the experimental data, due to the imperfect edges and non-uniform channel length which smear these resonances out.

6.6 Conclusions

In this chapter, we presented our experimental results from strained transport measurements of graphene devices at low temperature. In two graphene QDs, we showed that strain causes shifting of the quantized energy levels. We showed that these shifting levels are inconsistent with a scalar potential or constant vector potential caused by uniaxial strain, and are likely a result of pseudomagnetic fields induced by non-uniform strains. We estimate pseudomagnetic fields of $B_{\text{ps}} \approx 8 \text{ T}$ in an electromigrated graphene break junction device.

In a ballistic graphene gap junction device, we showed that the four signatures predicted from our applied transport model in Chapter 5 were present in our experimental data, including the gate-shift in our data arising from the scalar potential, and conductivity suppression, transport asymmetry modification and resonance peak shifting as a result of the vector potential. By quantifying these signatures in strained transport data, we determined the charge impurity density of the channel, the contact doping, the crystal orientation and series resistance of the device, reproducing our experimental data with good semi-quantitative agreement. This shows that our GQST model accurately captures the physics of strained ballistic graphene.

These two results show that future study of strain effects in ballistic graphene and

graphene quantum dots using our QTSE set-up are warranted to understand and develop the rich physics of strained graphene. With larger strains and thinner gate oxide, total conductivity suppression should be attainable in ballistic graphene using our set-up, with applications in high-quality graphene transistors for quantum circuits, or flexible and transparent sensors, while more controlled experiments on electromigrated graphene QDs could be used to explore Landau level physics and strong tunable pseudomagnetic fields at room temperature.

Chapter 7

Conclusions and Outlook

We have shown that through specific device design, and construction of unique quantum transport strain engineering (QTSE) instrumentation, we can tune the Hamiltonian of graphene and carbon nanotubes directly using mechanical strain. This gives us fine control over the energy, momentum, and quantum state of electrons in our carbon quantum nanoelectromechanical systems (QNEMS). Using uniaxial strain, we showed that we can tune vector and scalar potentials in graphene, providing proof-of-concept for future study of more complicated strain profiles. These could be used for generating large and tunable pseudomagnetic fields at room temperature to study Landau level physics, or valleytronics and quantum information processing. In this conclusion, we will first briefly summarize the main results described in the previous chapters, on our QTSE instrumentation, two-in-one ultra-short carbon nanotube quantum transistors, and theoretical and experimental findings on strain-induced scalar and vector potentials in graphene, leading towards graphene quantum strain transistors (GQSTs). We will then discuss possible improvements to our experimental microfabrication procedures to achieve greater strain-tunability, as well as our plans for future experiments in strained QNEMS.

7.1 Main results

In Chapter 1 we gave context to this thesis, based on recent results on strain engineering in graphene and carbon nanotubes, and explained how the intrinsic electronic and mechanical properties of graphene and carbon nanotubes make them ideal QNEMS. We showed how strain-induced scalar and vector potentials control the energy, momentum, and quantum

state of electrons in these systems. We discussed recent theoretical predictions and experimental findings on the effects of strain in carbon nanotubes and graphene, showing how non-uniform strains can produce strong pseudomagnetic fields to study the room temperature quantum Hall effect, or valleytronics for quantum information processing. We discussed how uniaxial strains can open a transport gap in graphene for GQST applications, and how resonators with time-dependent strains can be tuned with uniaxial strains for mass or force sensing. In carbon nanotubes, strain can be used to tune the band gap, which governs the two-in-one quantum transport behaviour observed in Chapter 4. Strain in nanotubes tune their intrinsic electron-vibron coupling and could lead to THz resonators. These many exciting prospects show that strain engineering in graphene and carbon nanotubes must be explored in further detail. We outlined recent experimental attempts to study strain effects in carbon nanotubes and graphene, but found no reliable instrumentation for large and tunable strains, compatible with low temperature electron transport measurements necessary for detailed and thorough exploration of strain in carbon nanotubes and graphene.

In Chapter 2 we gave the basic background in quantum electron transport in graphene and carbon nanotubes to understand the remainder of this thesis. We first detailed the real-space lattice and band structure of graphene, and showed how the hexagonal lattice structure leads to relativistic charge carrier behaviour. We then described electron transport in semi-classical diffusive graphene and quantum ballistic graphene devices, presenting an idealized transmission model for transport in unstrained graphene. In Chapter 5, we used this model as a basis for our realistic applied model to describe transmission in uniaxially strained graphene. We next detailed the real-space lattice and chirality-dependent band structure of carbon nanotubes, which follow directly from those of graphene. We showed how, for different band gaps, contact dopings and temperatures, carbon nanotube devices can exhibit a variety of transport behaviours, forming field effect transistors, single electron transistors (quantum dots), or 1D ballistic electron waveguides.

In Chapter 3, we presented our specialized fabrication methods and unique instrumentation design for large and tunable strains in suspended graphene and carbon nanotube devices, compatible with low temperature electron transport measurements. Our fabrication was designed to produce clean, high-quality, carbon nanotube and graphene devices, with device geometries capable of imparting large strains. We specifically designed our graphene devices with wide and short channels to eliminate edge effects, and suspended all devices to avoid substrate defects and to freely allow stretching of our device. Examples of suspended graphene (≈ 100 nm) and ultra-short (~ 10 nm) carbon nanotube devices are shown

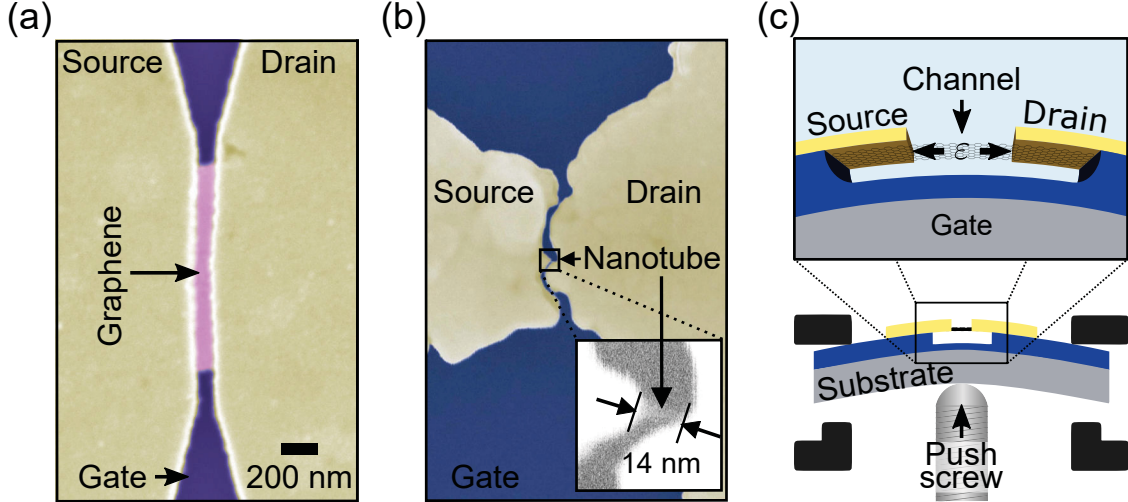


Figure 7.1: Strain instrumentation for ultra-short carbon nanoelectronic devices. (a)–(b) False coloured SEM images of suspended 100-nm graphene and 14-nm carbon nanotube devices respectively. The inset in panel (b) is a zoom-in on the nanotube in the main panel. (c) Schematic diagram of our QTSE instrumentation. (bottom) A push screw bends the sample substrate, imparting a strain on the suspended channel. (top) A more detailed view of the strained devices, shows the strained suspended channel, and source/drain/gate electrodes used for electron transport measurements.

in Fig. 7.1(a) and (b) respectively. We next presented the construction and design of our unique quantum strain transport engineering set-up, shown schematically in Fig. 7.1(c), used for applying large and tunable strains to our QNEMS. Our custom-built QTSE system uses a push screw to bend the wafer substrates, imparting large strains (theoretically $\lesssim 10\%$) through the suspended metal films which act as lever arms, which magnify the stretching of the channel. We then described our electromigration and annealing procedures for creating ultra-short (10–100 nm) and pristine carbon nanotube and graphene quantum electronic devices with ballistic contacts. Finally, we showed that our QTSE set-up affords tunable, controllable, and stable strains with picometer sensitivity, through gold tunnel junction calibration measurements.

In Chapter 4, we described the two-in-one quantum transistor behaviour we observed in ultra-short, suspended carbon nanotube devices with ballistic contacts. We showed that we can engineer the electron-hole transport asymmetry we observe in these devices with contact doping, bandgap, and device length. Understanding these contact effects is instrumental for realistic modeling of transmission in our QNEMS. A summary of our findings, published in Nature Communications [53], is shown in Fig. 7.2. In Fig. 7.2(a), we show a false coloured SEM image of a $L \approx 100$ nm carbon nanotube device, made using our electromigration

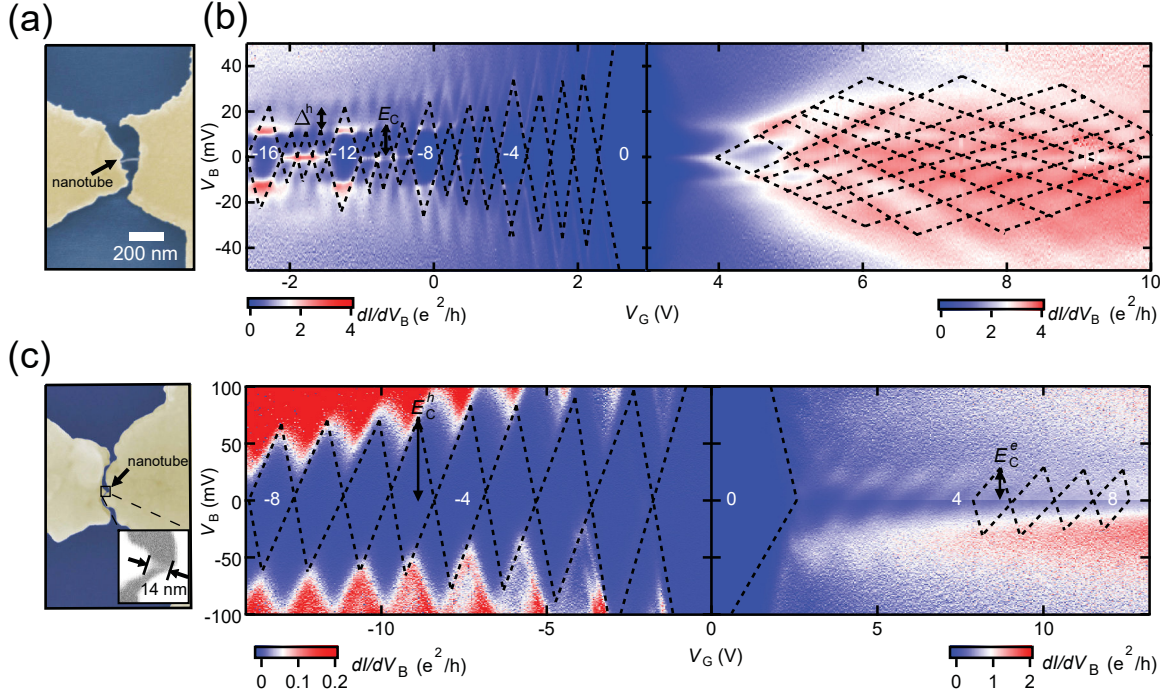


Figure 7.2: Ultra-short two-in-one quantum dot carbon nanotube transistors. (a) False colour SEM image of a $L \approx 100$ nm carbon nanotube device, produced by electromigration. (b) Transport data from the small bandgap device in (a), showing a strong electron-hole transport asymmetry, with quantum dot transport for holes and ballistic transport for electrons. (c) False colour SEM image of a $L \approx 14$ nm carbon nanotube device, produced by electromigration. (d) Transport data from a small bandgap device like the one shown in (c), showing electron-hole charging energy asymmetry, with larger charging energies for holes than electrons.

procedure. We showed that electromigration anneals the suspended gold films coating the nanotube. This causes our gold films to act as non-disruptive top gates to the nanotube sections underneath. These metal-coated sections of nanotube are the source and drain leads to the naked nanotube channel. We found that this extremely local top-gating of the nanotube leads created nm-sized p-n junctions at the edges of the naked nanotube channel, causing a drastic electron-hole transport asymmetry in our devices. Transport data from the devices from the 100 nm in panel (a) are shown in Fig. 7.2(b). From this transport data, we found that holes were confined to the naked channel, forming a quantum dot, while the electrons exhibited ballistic 1D waveguide behaviour, with wavefunctions extending into the metal-coated nanotube leads under the gold films. In larger band gap devices, like that shown in Fig. 7.2(c), we observed a different manifestation of the electron-hole asymmetry, as can be seen in the transport data shown in Fig. 7.2(d). In this case, both electrons and holes exhibit quantum dot transport, but require vastly different energies to be added to the device. We showed that this electron-hole asymmetry depends heavily on the length of the nanotube, explaining why it has not been previously observed in longer nanotube devices.

In Chapter 5, we developed a realistic applied model for transport in strained ballistic graphene, accounting for contact effects, and strain-induced lattice distortions neglected in previous studies. This model fully captures the physics of strain in graphene, and allows us to study in detail the effects of strain-induced scalar and vector potentials in strained graphene. We used this model to predict a strong and tunable graphene quantum strain transistor effect in graphene. This work is in preparation for submission to 2D Materials. A summary of our findings is shown in Fig. 7.3. We first determined the expected theoretical strain range applicable for realistic graphene devices using our QTSE set-up: $\varepsilon_{\text{total}} \approx 2.6\% - 5.1\%$. In Fig. 7.3(a), we show the expected strain magnitudes from thermal (blue), electrostatic (black) and mechanical (red) strains, as a function of gate voltage (bottom axis) and mechanical motion of the push screw (top axis). The effectively negligible electrostatic strain is a major advantage of our QTSE set-up, and allows independent tuning of charge density and mechanical strain. We next calculated conductivity in uniaxially strained ballistic graphene devices, using realistic contact doping estimates in the metal-coated graphene leads, and accounting for the crystal orientation of the graphene flake. In Fig. 7.3(b), we show calculated conductivity as a function of gate and mechanical strain for $\theta = 15^\circ$ and $\Delta\mu_{\text{contact}} = 0.12$ eV. From our conductivity data, we identified four major signatures of strain: a scalar potential gate-shift of the conductivity curves, the overall suppression of conductivity with strain, the change in electron-hole transport asymmetry, and the shifting of the coherent transport

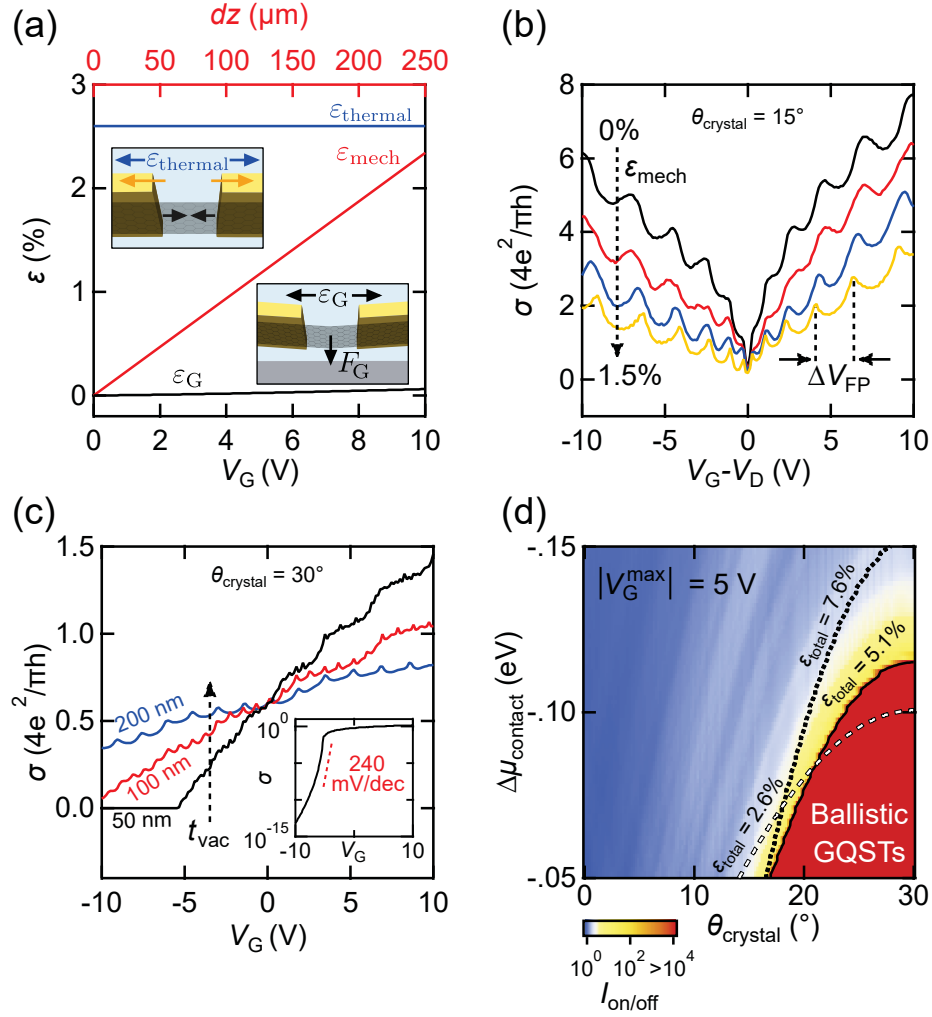


Figure 7.3: Graphene quantum strain transistors: theory. (a) Expected strains from our suspended graphene devices, constant thermal strain (blue), applied mechanical strain (red), and negligible contribution from electrostatic strain (black). (b) Calculated conductivity curves from our applied transmission model, showing the strain-induced reduction in conductivity, change in transport asymmetry, and change in Fabry-Pérot peak positions; signatures of the strain-induced vector potential. Scalar potential not shown here for clarity. (c) Graphene quantum strain transistor effect, for gate spacing $t_{\text{vac}} = 50, 100, 200$ nm in black, red, and blue respectively, showing conductivity suppression with on/off ratios $> 10^4$, tunable by gate and strain in the 50 nm case. The inset shows the same data for the 50 nm case on a log scale, indicating the large on/off ratio and small subthreshold slope. (d) Expected range of contact doping and crystal orientation for a large and tunable GQST effect for different total strain magnitudes.

(Fabry-Pérot) resonance peaks. These signatures can be used to prove the presence of scalar and vector potentials in strained graphene devices, and used as tools to quantify the strain, crystal orientation, and contact doping of our devices. For thin gate dielectric spacings ($t_{\text{vac}} \approx 50$ nm), we expect total suppression of conductivity using our realistic QTSE set-up, as shown in Fig. 7.3(c) (black curve). This conductivity suppression has large on/off ratios ($< 10^4$), and approaches the thermionic limit of subthreshold slope (240 mV/dec), as shown in the inset of Fig. 7.3(c), making our GQSTs excellent transistors, which could be used in graphene integrated circuits, or as highly sensitive transparent and flexible strain sensors. We investigated the dependence of the GQST effect on crystal orientation and contact doping, shown in Fig. 7.3(d), showing that the GQST is robust and should be readily attainable experimentally.

In Chapter 6, from experimental electron transport data, we observed unambiguous electron transport signatures of strain-tunable scalar and vector potentials in uniaxially strained graphene, using our QTSE instrumentation. These findings provide us confidence in our applied model, and pave the way for engineering of strain profiles in graphene for large pseudomagnetic fields or valleytronics. A summary of our findings is shown in Fig. 7.4. We measured strain-tunable transport in two graphene quantum dots. In Fig. 7.4(a), we show a false coloured scanning electron microscope (SEM) image of a graphene break junction quantum dot. The corresponding transport data are shown in Fig. 7.4(b), exhibiting Coulomb diamonds, signifying that this device forms a single electron transistor. In both devices, we observe gate-shifting of the energy levels of the quantum dot as we bend their Si chip substrates using our QTSE instrumentation, and straining the graphene channels. Kinks in the gate-shifts are consistent with strong pseudomagnetic fields ($B_{\text{ps}} \approx 8$ T) caused by non-uniform strains, arising from the irregular shape of the electromigrated device and structural defects in the graphene sheet. In addition to the QD devices, we measured strain-tunable electron transport in a suspended ballistic graphene device. In Fig. 7.4(c), we show a false coloured SEM image of the $L \approx 100$ nm, $L \approx 600$ nm graphene gap junction device. The corresponding transport data are shown in Fig. 7.4(d). We resolved and quantified all four expected transport signatures of the strain-induced scalar and vector potentials described in Chapter 5: gate-shifting of the conductivity curves from the scalar potential, and conductivity suppression, asymmetry modification, and Fabry-Pérot peak shifting from the vector potential. This shows the vast tunability of conductivity features with strain in ballistic graphene. We showed how to extract the impurity density, contact doping, crystal angle, and contact resistance from our data, and simulated transport in this device using our

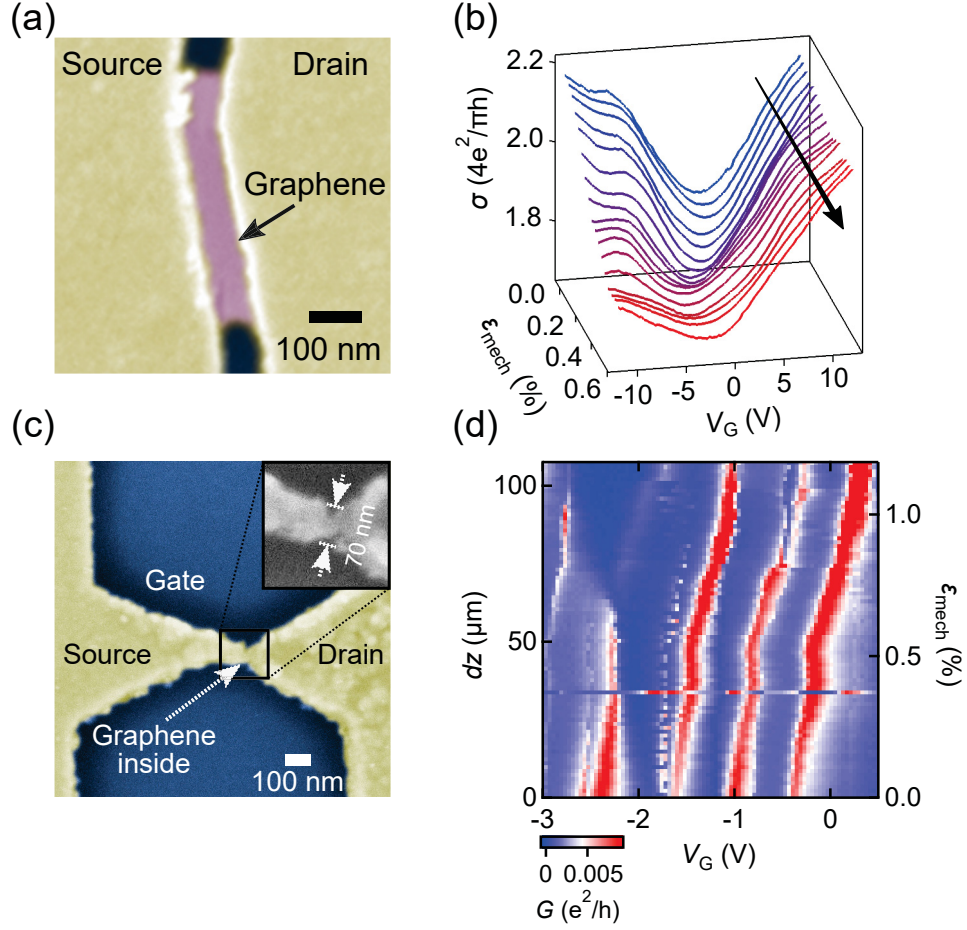


Figure 7.4: Strained graphene nanoelectronic devices. (a) False colour SEM image of a $L \approx 100$ nm graphene gap junction device. (b) Conductivity as a function of strain and gate from the device in panel (a), showing all 4 signatures of the strain induced scalar and vector potentials: gate-shift of the conductivity curves, conductivity suppression, asymmetry modification, and Fabry-Pérot peak shifting. (c) False colour SEM image of a graphene break junction device which formed a quantum dot. (d) Strain transport data from the device shown in (c), showing the quantum dot energy levels shifting with strain. The kinks in these data are indicative of Landau levels being formed by large pseudomagnetic fields.

model. We found a remarkably good semi-quantitative agreement between experiment and theory for this device. These results show that experimental realization of the GQST effect is within reach, by harnessing the strain-tunability of the vector potentials we measured in our devices.

In conclusion, we have developed instrumentation and fabrication methods for studying the effects of strain in ultra-short QNEMS with ballistic contacts. In unstrained, suspended carbon nanotube devices, we observed two-in-one quantum transistor behaviour with a striking transport asymmetry for electrons and holes. This asymmetry was caused by contact doping in the ballistic nanotube leads. We developed a realistic applied model to study GQSTs, accounting for this contact doping. We identified four transport signatures, arising from scalar and vector potentials in uniaxially strained graphene, and predicted a robust GQST effect with high on/off ratios for sufficient strains. We then studied electron transport in strained graphene devices, showing strain-tunable conductivity which matched our theoretical predictions.

7.2 Outlook for quantum strain engineering in carbon QNEMS

We have shown that we are able to tailor transport behaviour in suspended graphene and carbon nanotube devices through our fabrication procedures, electrostatic potentials, and mechanics, using instrumentation for quantum transport strain engineering. Our instrumentation, device design, and fabrication methods for suspended graphene and ultra-short carbon nanotube transistors, have allowed us to explore the physics of ballistic contacts for two-in-one quantum transistors in carbon nanotubes [53], as well as QTSE in graphene QNEMS. In this section, we will briefly describe the next steps forward in strained QNEMS research. For strain in monolayer graphene, we will discuss full realization of the GQST effect, large pseudomagnetic fields and room temperature pseudo Landau levels, and tunable THz resonators. In twisted bilayer graphene, we propose research on strain-tunable superconductivity. In carbon nanotubes we discuss strain-tunable electron-hole asymmetry, and THz nanoelectromechanical systems (NEMS).

Our transport measurements on strained monolayer graphene devices suggest that the GQSTs could be readily realized with a few small improvements to our fabrication methods. First, combining polarized Raman characterization to determine the crystal orientation of our graphene flakes [154] with dry stamping techniques [176] to orient our flakes, we can

ensure our devices always have armchair edges to maximize the effects of strain in our devices. Second, using a 50 nm SiO_2 wafer, suggested in Chapter 5, would provide the stronger gating required to observe the scalar-potential-shifted Dirac point, where the conductivity suppression is greatest. These improvements would make our QTSE instrumentation much more powerful and could allow us to fully realize GQSTs, and develop our understanding of strain effects in monolayer graphene. With this understanding, it may be possible to use specifically designed substrates [45,48] to strain graphene devices encapsulated in hexagonal boron nitride. Since encapsulated graphene has a long mean free path, exhibiting ballistic transport at room temperature, these would make ideal candidates for room temperature GQSTs which do not require complex instrumentation. Moreover, by developing tools to strain graphene using engineered substrates, complex strain-programmable circuits may become possible.

With strain-induced vector potentials, we can control the energy, momentum, and quantum state of electrons in graphene. For the right strain profile, these strain-tunable vector potentials can create large pseudomagnetic fields, for example with triaxial strain [22], or uniaxial strain with specific channel shapes [149]. Large pseudomagnetic fields can lead to the pseudo quantum Hall effect and pseudo Landau level physics [22,45,149] for room temperature quantum circuits with topologically protected edge states. Using a triaxial strain geometry with our QTSE instrumentation, and a reasonably achievable 100 nm graphene flake with 1% strain, we expect pseudomagnetic fields $B_{\text{ps}} \sim 4$ T, suitable for studying the pseudo quantum Hall effect in suspended graphene devices [45]. One application of this physics arises by combining both real magnetic fields and pseudomagnetic fields, precise control over the valley quantum number could lead to applications in valleytronics and quantum information processing in graphene [31].

By including ac actuation of the gate electrode, we can study strain-tunable, high frequency monolayer graphene resonators. Using the 100 nm long ideal graphene devices described in Chapter 5 as a starting point, with $\varepsilon_{\text{mech}} = 2.6\text{--}5.1\%$, and using the standard continuum model for graphene [33], we calculate a high, strain-tunable resonance frequency in graphene from 0.5–0.8 THz. By reducing the device length to 50 nm, we expect this range to increase to 1.1–1.5 THz, breaching the long sought-after terahertz regime. Such tunable high frequency NEMS have applications in extremely sensitive mass or force sensing [11]. These devices could also be used for valleytronics, with high resonance frequencies corresponding to larger charge-pumped bulk pure valley currents [41].

A recent notable result is the advent of superconductivity in magic angle twisted bilayer

graphene [98]. This intriguing effect arises due to hybridization of the bilayer structure when the two atomic layers are offset by the so-called “magic angle”. This effect is extremely sensitive to the proximity of the carbon atoms in the two layers. As the positions of the atoms in graphene are strain-tunable, the superconducting state of twisted bilayer graphene could be suppressed or enhanced by strain, although this prospect requires deeper theoretical analysis.

Carbon nanotubes have a strain-tunable band gap, allowing switching between metallic and semiconducting states with strain. Tuning the nanotube bandgap also changes the heights of the Schottky barriers which form at the nanotube/lead interfaces, resulting in a strongly strain-tunable electron-hole asymmetry. This would allow two-in-one quantum transistors, like those discussed in Chapter 4, which could be tuned between ballistic and quantum dot behaviour with gate, or with strain. Or, by enhancing the electron-hole transport asymmetry as much as possible using strain, it may be possible to achieve room temperature single electron transistor behaviour in graphene. Finally, as in graphene, stretching carbon nanotube devices while using ac actuation of the gate could be used for tunable THz carbon nanotube resonators for mass or force sensing. [10].

Bibliography

- [1] D. Akinwande et al., *A review on mechanics and mechanical properties of 2D materials- Graphene and beyond*, Extreme Mech. Lett.s **13**, 42 (2017).
- [2] A. H. Castro Neto, F. Guinea, N. M. R. Peres, K. S. Novoselov, and A. K. Geim, *The electronic properties of graphene*, Rev. Mod. Phys. **81**, 109 (2009).
- [3] R. Leturcq et al., *Franck-Condon blockade in suspended carbon nanotube quantum dots*, Nat. Phys. **5**, 327 (2009).
- [4] G. G. Naumis, S. Barraza-Lopez, M. Oliva-Leyva, and H. Terrones, *Electronic and optical properties of strained graphene and other strained 2D materials: a review*, Rep. Prog. Phys. **80**, 096501 (2017).
- [5] A. Bertoni, P. Bordone, R. Brunetti, C. Jacoboni, and S. Reggiani, *Quantum logic gates based on coherent electron transport in quantum wires*, Phys. Rev. Lett. **84**, 5912 (2000).
- [6] Y. Meir, N. S. Wingreen, and P. A. Lee, *Low-temperature transport through a quantum dot: The Anderson model out of equilibrium*, Phys. Rev. Lett. **70**, 2601 (1993).
- [7] D. Goldhaber-Gordon et al., *Kondo effect in a single-electron transistor*, Nature **391**, 156 (1998).
- [8] S. Wolf et al., *Spintronics: a spin-based electronics vision for the future*, Science **294**, 1488 (2001).
- [9] L. Banszerus et al., *Ballistic transport exceeding 28 μm in CVD grown graphene*, Nano Lett. **16**, 1387 (2016).
- [10] J. O. Island, V. Tayari, A. C. McRae, and A. R. Champagne, *Few-hundred GHz carbon nanotube nanoelectromechanical systems (NEMS)*, Nano Lett. **12**, 4564 (2012).

- [11] J. Chaste et al., *A nanomechanical mass sensor with yoctogram resolution*, Nat. Nanotechnol. **7**, 301 (2012).
- [12] A. Fennimore et al., *Rotational actuators based on carbon nanotubes*, Nature **424**, 408 (2003).
- [13] S. Savel'ev, X. Hu, and F. Nori, *Quantum electromechanics: Qubits from buckling nanobars*, New J. Phys. **8**, 105 (2006).
- [14] J. Parks et al., *Mechanical control of spin states in spin-1 molecules and the under-screened Kondo effect*, Science **328**, 1370 (2010).
- [15] H. Peng, C. Chang, S. Aloni, T. Yuzvinsky, and A. Zettl, *Ultrahigh frequency nanotube resonators*, Phys. Rev. Lett. **97**, 087203 (2006).
- [16] J. S. Bunch et al., *Electromechanical resonators from graphene sheets*, Science **315**, 490 (2007).
- [17] R. Karabalin et al., *Piezoelectric nanoelectromechanical resonators based on aluminum nitride thin films*, Appl. Phys. Lett. **95**, 103111 (2009).
- [18] Y. Hanlummyuang, X. Li, and P. Sharma, *Mechanical strain can switch the sign of quantum capacitance from positive to negative*, Phys. Chem. Chem. Phys. **16**, 22962 (2014).
- [19] B. A. Bernevig and S.-C. Zhang, *Quantum spin Hall effect*, Phys. Rev. Lett. **96**, 106802 (2006).
- [20] E. Mariani and F. von Oppen, *Electron-vibron coupling in suspended carbon nanotube quantum dots*, Phys. Rev. B **80**, 155411 (2009).
- [21] N. Levy et al., *Strain-induced pseudo-magnetic fields greater than 300 tesla in graphene nanobubbles*, Science **329**, 544 (2010).
- [22] F. Guinea, M. I. Katsnelson, and A. K. Geim, *Energy gaps and a zero-field quantum Hall effect in graphene by strain engineering*, Nat. Phys. **6**, 30 (2010).
- [23] S. M. Young et al., *Theoretical investigation of the evolution of the topological phase of Bi_2Se_3 under mechanical strain*, Phys. Rev. B **84**, 085106 (2011).

- [24] M.-F. Yu et al., *Strength and breaking mechanism of multiwalled carbon nanotubes under tensile load*, Science **287**, 637 (2000).
- [25] S. Chen et al., *Electron optics with p-n junctions in ballistic graphene*, Science **353**, 1522 (2016).
- [26] J. W. Wilder, L. C. Venema, A. G. Rinzler, R. E. Smalley, and C. Dekker, *Electronic structure of atomically resolved carbon nanotubes*, Nature **391**, 59 (1998).
- [27] A. Javey et al., *High performance n-type carbon nanotube field-effect transistors with chemically doped contacts*, Nano Lett. **5**, 345 (2005).
- [28] M. M. Shulaker et al., *Carbon nanotube computer*, Nature **501**, 526 (2013).
- [29] W. Liang et al., *Fabry-Pérot interference in a nanotube electron waveguide*, Nature **411**, 665 (2001).
- [30] P. Jarillo-Herrero, S. Sapmaz, C. Dekker, L. P. Kouwenhoven, and H. S. J. van der Zant, *Electron-hole symmetry in a semiconducting carbon nanotube quantum dot*, Nature **429**, 389 (2004).
- [31] M. Settnes, J. H. Garcia, and S. Roche, *Valley-polarized quantum transport generated by gauge fields in graphene*, 2D Mat. **4**, 031006 (2017).
- [32] M. M. Fogler, F. Guinea, and M. I. Katsnelson, *Pseudomagnetic fields and ballistic transport in a suspended graphene sheet*, Phys. Rev. Lett. **101**, 226804 (2008).
- [33] C. Chen et al., *Performance of monolayer graphene nanomechanical resonators with electrical readout*, Nat. Nanotechnol. **4**, 861 (2009).
- [34] M. Settnes, S. R. Power, and A.-P. Jauho, *Pseudomagnetic fields and triaxial strain in graphene*, Phys. Rev. B **93**, 035456 (2016).
- [35] Z.-Z. Cao, Y.-F. Cheng, and G.-Q. Li, *Strain-controlled electron switch in graphene*, App. Phys. Lett. **101**, 253507 (2012).
- [36] F. Schwierz, *Graphene transistors*, Nat. Nanotechnol. **5**, 487 (2010).
- [37] Y. Tan et al., *Graphene Klein tunnel transistors for high speed analog RF applications*, Sci. Rep. **7**, 9714 (2017).

- [38] S. Chun, Y. Choi, and W. Park, *All-graphene strain sensor on soft substrate*, Carbon **116**, 753 (2017).
- [39] Y.-M. Lin et al., *Wafer-scale graphene integrated circuit*, Science **332**, 1294 (2011).
- [40] V. Tayari et al., *Tailoring 10 nm scale suspended graphene junctions and quantum dots*, Nano Lett. **15**, 114 (2015).
- [41] Y. Jiang, T. Low, K. Chang, M. I. Katsnelson, and F. Guinea, *Generation of pure bulk valley current in graphene*, Phys. Rev. Lett. **110**, 046601 (2013).
- [42] E. D. Minot, Y. Yaish, V. Sazonova, and P. L. McEuen, *Determination of electron orbital magnetic moments in carbon nanotubes*, Nature **428**, 536 (2004).
- [43] N.-K. Chang, C.-C. Su, and S.-H. Chang, *Fabrication of single-walled carbon nanotube flexible strain sensors with high sensitivity*, Appl. Phys. Lett. **92**, 063501 (2008).
- [44] M. J. Biercuk, S. Ilani, C. M. Marcus, and P. L. McEuen, *Electrical transport in single-wall carbon nanotubes*, volume 111 of *Topics in Applied Physics*, chapter 15, pages 455–493, Springer Berlin Heidelberg, (2008).
- [45] Y. Jiang et al., *Visualizing strain-induced pseudomagnetic fields in graphene through an hBN magnifying glass*, Nano Lett. **17**, 2839 (2017).
- [46] A. Georgi et al., *Tuning the pseudospin polarization of graphene by a pseudomagnetic field*, Nano Lett. **17**, 2240 (2017).
- [47] K. S. Kim et al., *Large-scale pattern growth of graphene films for stretchable transparent electrodes*, Nature **457**, 706 (2009).
- [48] Y. Zhang et al., *Strain modulation of graphene by nanoscale substrate curvatures: a molecular view*, Nano Lett **18**, 2098 (2018).
- [49] C. Lee, X. Wei, J. W. Kysar, and J. Hone, *Measurement of the elastic properties and intrinsic strength of monolayer graphene*, Science **321**, 385 (2008).
- [50] T. M. G. Mohiuddin et al., *Uniaxial strain in graphene by Raman spectroscopy: G peak splitting, Grüneisen parameters, and sample orientation*, Phys. Rev. B **79**, 205433 (2009).

- [51] M. Goldsche et al., *Tailoring mechanically tunable strain fields in graphene*, Nano Lett **18**, 1707 (2018).
- [52] D. Metten, G. Froehlicher, and S. Berciaud, *Monitoring electrostatically-induced deflection, strain and doping in suspended graphene using Raman spectroscopy*, 2D Mat. **4**, 014004 (2016).
- [53] A. C. McRae, V. Tayari, J. M. Porter, and A. R. Champagne, *Giant electron-hole transport asymmetry in ultra-short quantum transistors*, Nat. Commun. **8**, 15491 (2017).
- [54] A. L. Kitt, V. M. Pereira, A. K. Swan, and B. B. Goldberg, *Lattice-corrected strain-induced vector potentials in graphene*, Phys. Rev. B **85**, 115432 (2012).
- [55] A. L. Kitt, V. M. Pereira, A. K. Swan, and B. B. Goldberg, *Erratum: Lattice-corrected strain-induced vector potentials in graphene [Phys. Rev. B85, 115432 (2012)]*, Phys. Rev. B **87**, 159909 (2013).
- [56] F. M. D. Pellegrino, G. G. N. Angilella, and R. Pucci, *Transport properties of graphene across strain-induced nonuniform velocity profiles*, Phys. Rev. B **84**, 195404 (2011).
- [57] M. J. Allen, V. C. Tung, and R. B. Kaner, *Honeycomb carbon: a review of graphene*, Chem. Rev. **110**, 132 (2009).
- [58] A. Kretinin et al., *Quantum capacitance measurements of electron-hole asymmetry and next-nearest-neighbor hopping in graphene*, Phys. Rev. B **88**, 165427 (2013).
- [59] M. Oliva-Leyva and G. G. Naumis, *Generalizing the Fermi velocity of strained graphene from uniform to nonuniform strain*, Phys. Lett. A **379**, 2645 (2015).
- [60] K. I. Bolotin et al., *Ultrahigh electron mobility in suspended graphene*, Solid State Commun. **146**, 351 (2008).
- [61] K. I. Bolotin, K. J. Sikes, J. Hone, H. L. Stormer, and P. Kim, *Temperature-dependent transport in suspended graphene*, Phys. Rev. Lett. **101**, 096802 (2008).
- [62] S. Adam, E. H. Hwang, V. M. Galitski, and S. Das Sarma, *A self-consistent theory for graphene transport*, **104**, 18392 (2007).
- [63] V. E. Dorgan, M.-H. Bae, and E. Pop, *Mobility and saturation velocity in graphene on SiO₂*, Appl. Phys. Lett. **97**, 082112 (2010).

- [64] A. K. Geim and K. S. Novoselov, *The rise of graphene*, Nat. Mater. **6**, 183 (2007).
- [65] F. Kusmartsev, W. Wu, M. Pierpoint, and K. Yung, Application of graphene within optoelectronic devices and transistors, in *Applied Spectroscopy and the Science of Nanomaterials*, pages 191–221, Springer, (2015).
- [66] M. Gibertini, A. Tomadin, F. Guinea, M. I. Katsnelson, and M. Polini, *Electron-hole puddles in the absence of charged impurities*, Phys. Rev. B **85**, 201405 (2012).
- [67] S. Samaddar, I. Yudhistira, S. Adam, H. Courtois, and C. B. Winkelmann, *Charge puddles in graphene near the Dirac point*, Phys. Rev. Lett. **116**, 126804 (2016).
- [68] A. S. Mayorov et al., *Micrometer-scale ballistic transport in encapsulated graphene at room temperature*, Nano. Lett. **11**, 2396 (2011).
- [69] J. Tworzydło, B. Trauzettel, M. Titov, A. Rycerz, and C. W. Beenakker, *Sub-Poissonian shot noise in graphene*, Phys. Rev. Lett. **96**, 246802 (2006).
- [70] P. Rickhaus et al., *Ballistic interferences in suspended graphene*, Nat. Commun. **4**, 2342 (2013).
- [71] M. I. Katsnelson, K. S. Novoselov, and A. K. Geim, *Chiral tunnelling and the Klein paradox in graphene*, Nat. Phys. **2**, 620 (2006).
- [72] J. R. F. Lima, A. L. R. Barbosa, C. G. Bezerra, and L. F. C. Pereira, *Tuning the Fano factor of graphene via Fermi velocity modulation*, Physica E **97**, 105 (2018).
- [73] J. Ding, X. Yan, and J. Cao, *Analytical relation of band gaps to both chirality and diameter of single-wall carbon nanotubes*, Phys. Rev. B **66**, 073401 (2002).
- [74] Y. Matsuda, J. Tahir-Kheli, and W. A. Goddard, *Definitive band gaps for single-wall carbon nanotubes*, J. Phys. Chem Lett. **1**, 2946 (2010).
- [75] X. Lu and Z. Chen, *Curved pi-conjugation, aromaticity, and the related chemistry of small fullerenes ($<C_{60}$) and single-walled carbon nanotubes*, Chem. Rev. **105**, 3643 (2005).
- [76] S. Heinze et al., *Carbon nanotubes as schottky barrier transistors*, Phys. Rev. Lett. **89**, 106801 (2002).

- [77] J. Park, *Electron transport in single molecule transistors*, PhD thesis, University of California, Berkeley, (2003).
- [78] J. Paaske et al., *Non-equilibrium singlet-triplet Kondo effect in carbon nanotubes*, Nat. Phys. **2**, 460 (2006).
- [79] A. R. Champagne, A. N. Pasupathy, and D. C. Ralph, *Mechanically adjustable and electrically gated single-molecule transistors*, Nano Lett. **5**, 305 (2005).
- [80] S. Caneva et al., *Mechanically controlled quantum interference in graphene break junctions*, arXiv:1803.05642 (2018).
- [81] N. Agrat, A. L. Yeyati, and J. M. Van Ruitenbeek, *Quantum properties of atomic-sized conductors*, Phys. Rep. **377**, 81 (2003).
- [82] H. Shioya, S. Russo, M. Yamamoto, M. F. Craciun, and S. Tarucha, *Electron states of uniaxially strained graphene*, Nano Lett. **15**, 7943 (2015).
- [83] T. Postek Michael, *An approach to the reduction of hydrocarbon contamination in the scanning electron microscope*, Scanning **18**, 269 (1996).
- [84] R. Y. Zhang, Y. Wei, L. A. Nagahara, I. Amlani, and R. K. Tsui, *The contrast mechanism in low voltage scanning electron microscopy of single-walled carbon nanotubes*, Nanotechnology **17**, 272 (2006).
- [85] R. Alizadegan, A. D. Liao, F. Xiong, E. Pop, and K. J. Hsia, *Effects of tip-nanotube interactions on atomic force microscopy imaging of carbon nanotubes*, Nano Res. **5**, 235 (2012).
- [86] T. Yamada et al., *Size-selective growth of double-walled carbon nanotube forests from engineered iron catalysts*, Nat. Nanotechnol. **1**, 131 (2006).
- [87] A. C. Ferrari et al., *Raman spectrum of graphene and graphene layers*, Phys. Rev. Lett. **97**, 187401 (2006).
- [88] A. C. Ferrari and D. M. Basko, *Raman spectroscopy as a versatile tool for studying the properties of graphene*, Nat. Nanotechnol. **8**, 235 (2013).
- [89] F. Giubileo and A. Di Bartolomeo, *The role of contact resistance in graphene field-effect devices*, Prog. Surf. Sci. **92**, 143 (2017).

- [90] C. Isaac, A. J. Luis, T. Jifa, and P. C. Yong, *Effect of oxygen plasma etching on graphene studied using Raman spectroscopy and electronic transport measurements*, New J. Phys. **13**, 025008 (2011).
- [91] J. O. Island, V. Tayari, S. Yiğen, A. C. McRae, and A. R. Champagne, *Ultra-short suspended single-wall carbon nanotube transistors*, Appl. Phys. Lett. **99**, 243106 (2011).
- [92] W. Jeong, K. Kim, Y. Kim, W. Lee, and P. Reddy, *Characterization of nanoscale temperature fields during electromigration of nanowires*, Sci. Rep. **4**, 4975 (2014).
- [93] G. K. Goswami and K. K. Nanda, *Electrical breakdown of carbon nanotube devices and the predictability of breakdown position*, AIP Adv. **2**, 022129 (2012).
- [94] G. Lene et al., *Graphene transport properties upon exposure to PMMA processing and heat treatments*, 2D Mat. **1**, 035005 (2014).
- [95] R. Wiesendanger, *Scanning probe microscopy and spectroscopy: methods and applications*, Cambridge University Press, (1994).
- [96] G. Giovannetti et al., *Doping graphene with metal contacts*, Phys. Rev. Lett. **101**, 026803 (2008).
- [97] P. Ghaemi, J. Cayssol, D. N. Sheng, and A. Vishwanath, *Fractional topological phases and broken time-reversal symmetry in strained graphene*, Phys. Rev. Lett. **108**, 266801 (2012).
- [98] Y. Cao et al., *Unconventional superconductivity in magic-angle graphene superlattices*, Nature **556**, 43 (2018).
- [99] X. He et al., *Strain engineering in monolayer WS_2 , MoS_2 , and the WS_2/MoS_2 heterostructure*, Appl. Phys. Lett. **109**, 173105 (2016).
- [100] E. A. Laird et al., *Quantum transport in carbon nanotubes*, Rev. Mod. Phys. **87**, 703 (2015).
- [101] G. A. Steele, G. Gotz, and L. P. Kouwenhoven, *Tunable few-electron double quantum dots and Klein tunnelling in ultraclean carbon nanotubes*, Nat. Nanotechnol. **4**, 363 (2009).
- [102] M. Jung et al., *Ultraclean single, double, and triple carbon nanotube quantum dots with recessed Re bottom gates*, Nano Lett. **13**, 4522 (2013).

- [103] A. Benyamini, A. Hamo, S. V. Kusminskiy, F. von Oppen, and S. Ilani, *Real-space tailoring of the electron-phonon coupling in ultraclean nanotube mechanical resonators*, Nature Phys. **10**, 151 (2014).
- [104] J. Moser, A. Eichler, J. Güttinger, M. I. Dykman, and A. Bachtold, *Nanotube mechanical resonators with quality factors of up to 5 million*, Nat. Nanotechnol. **9**, 1007 (2014).
- [105] P. Weber et al., *Switchable coupling of vibrations to two-electron carbon-nanotube quantum dot states*, Nano Lett. **15**, 4417 (2015).
- [106] F. Kuemmeth, S. Ilani, D. C. Ralph, and P. L. McEuen, *Coupling of spin and orbital motion of electrons in carbon nanotubes*, Nature **452**, 448 (2008).
- [107] F. Pei, E. A. Laird, G. A. Steele, and L. P. Kouwenhoven, *Valley-spin blockade and spin resonance in carbon nanotubes*, Nat. Nanotechnol. **7**, 630 (2012).
- [108] E. A. Laird, F. Pei, and L. Kouwenhoven, *A valley-spin qubit in a carbon nanotube*, Nat. Nanotechnol. **8**, 565 (2013).
- [109] J. P. Bergfield and M. A. Ratner, *Forty years of molecular electronics: Non-equilibrium heat and charge transport at the nanoscale*, Phys. Status Solidi B **250**, 2249 (2013).
- [110] M. Zonda, V. Pokorný, V. Janiš, and T. Novotný, *Perturbation theory for an Anderson quantum dot asymmetrically attached to two superconducting leads*, Phys. Rev. B **93**, 024523 (2016).
- [111] M. Rinzan, G. Jenkins, H. D. Drew, S. Shafranjuk, and P. Barbara, *Carbon nanotube quantum dots as highly sensitive terahertz-cooled spectrometers*, Nano Lett. **12**, 3097 (2012).
- [112] H. Yoo et al., *Reconfigurable complementary logic circuits with ambipolar organic transistors*, Sci. Rep. **6**, 35585 (2016).
- [113] C. C. Wu, C. H. Liu, and Z. H. Zhong, *One-step direct transfer of pristine single-walled carbon nanotubes for functional nanoelectronics*, Nano Lett. **10**, 1032 (2010).
- [114] J. Cao, Q. Wang, M. Rolandi, and H. J. Dai, *Aharonov-bohm interference and beating in single-walled carbon-nanotube interferometers*, Phys. Rev. Lett. **93**, 216803 (2004).

- [115] B. J. LeRoy, S. G. Lemay, J. Kong, and C. Dekker, *Electrical generation and absorption of phonons in carbon nanotubes*, Nature **432**, 371 (2004).
- [116] A. Jorio et al., *Structural (n, m) determination of isolated single-wall carbon nanotubes by resonant Raman scattering*, Phys. Rev. Lett. **86**, 1118 (2001).
- [117] K. H. Liu et al., *High-throughput optical imaging and spectroscopy of individual carbon nanotubes in devices*, Nat. Nanotechnol. **8**, 917 (2013).
- [118] X. D. Cui, M. Freitag, R. Martel, L. Brus, and P. Avouris, *Controlling energy-level alignments at carbon nanotube/Au contacts*, Nano Lett. **3**, 783 (2003).
- [119] M. Hasegawa and K. Nishidate, *Transfer doping of a metallic carbon nanotube and graphene on metal surfaces*, Phys. Rev. B **84**, 155435 (2011).
- [120] J. Knoch and J. Appenzeller, *Tunneling phenomena in carbon nanotube field-effect transistors*, Phys. Status Solidi A **205**, 679 (2008).
- [121] J. Tersoff, *Contact resistance of carbon nanotubes*, Appl. Phys. Lett. **74**, 2122 (1999).
- [122] R. S. Sundaram et al., *The graphene-gold interface and its implications for nanoelectronics*, Nano Lett. **11**, 3833 (2011).
- [123] A. Makarovski and G. Finkelstein, *$SU(4)$ mixed valence regime in carbon nanotube quantum dots*, Physica B **403**, 1555 (2008).
- [124] H. Jrgensen, K. Grove-Rasmussen, K. Flensberg, and P. Lindelof, *Critical and excess current through an open quantum dot: Temperature and magnetic-field dependence*, Phys. Rev. B **79** (2009).
- [125] J. H. Davies, *The physics of low-dimensional semiconductors: an introduction*, Cambridge university press, (1998).
- [126] P. A. Khomyakov et al., *First-principles study of the interaction and charge transfer between graphene and metals*, Phys. Rev. B **79**, 195425 (2009).
- [127] F. A. Chaves, D. Jiménez, A. W. Cummings, and S. Roche, *Physical model of the contact resistivity of metal-graphene junctions*, Journal of Applied Physics **115**, 164513 (2014).

- [128] J. Appenzeller, Y. M. Lin, J. Knoch, and P. Avouris, *Band-to-band tunneling in carbon nanotube field-effect transistors*, Phys. Rev. Lett. **93**, 196805 (2004).
- [129] M. Schmidt, *Fabrication, characterization and simulation of band-to-band tunneling field-effect transistors Based on Silicon-Germanium*, PhD thesis, RWTH Aachen University, (2013).
- [130] W. Lu, D. Wang, and L. W. Chen, *Near-static dielectric polarization of individual carbon nanotubes*, Nano Lett. **7**, 2729 (2007).
- [131] N. Nemec, D. Tomanek, and G. Cuniberti, *Contact dependence of carrier injection in carbon nanotubes: An ab initio study*, Phys. Rev. Lett. **96** (2006).
- [132] A. D. Franklin et al., *Sub-10 nm carbon nanotube transistor*, Nano Lett. **12**, 758 (2012).
- [133] F. Kuemmeth, H. O. H. Churchill, P. K. Herring, and C. M. Marcus, *Carbon nanotubes for coherent spintronics*, Materials Today **13**, 18 (2010).
- [134] S. Pecker et al., *Observation and spectroscopy of a two-electron Wigner molecule in an ultraclean carbon nanotube*, Nat. Phys. **9**, 576 (2013).
- [135] Y. Yang et al., *Coherent nonlocal transport in quantum wires with strongly coupled electrodes*, Phys. Rev. B **87**, 045403 (2013).
- [136] K. Grove-Rasmussen, H. I. Jørgensen, and P. E. Lindelof, *Fabry-Perot interference, Kondo effect and Coulomb blockade in carbon nanotubes*, Physica E **40**, 92 (2007).
- [137] P. S. Cornaglia, H. Ness, and D. R. Grempel, *Many-body effects on the transport properties of single-molecule devices*, Phys. Rev. Lett. **93** (2004).
- [138] B. Wunsch, *Few-electron physics in a nanotube quantum dot with spin-orbit coupling*, Phys. Rev. B **79**, 235408 (2009).
- [139] F. M. D. Pellegrino, G. G. N. Angilella, and R. Pucci, *Transport properties of graphene across strain-induced nonuniform velocity profiles*, Phys. Rev. B **84**, 195404 (2011).
- [140] L. Banszerus et al., *Ballistic transport exceeding 28 μm in CVD grown graphene*, Nano Lett **16**, 1387 (2016).
- [141] D. Akinwande, N. Petrone, and J. Hone, *Two-dimensional flexible nanoelectronics*, Nat. Commun. **5**, 5678 (2014).

- [142] G. Iannaccone, F. Bonaccorso, L. Colombo, and G. Fiori, *Quantum engineering of transistors based on 2D materials heterostructures*, Nat. Nanotechnol. **13**, 183 (2018).
- [143] B. Amorim et al., *Novel effects of strains in graphene and other two dimensional materials*, Phys. Rep. **617**, 1 (2016).
- [144] Y.-H. Wu, T. Shi, G. J. Sreejith, and Z.-X. Liu, *Fermionic symmetry-protected topological state in strained graphene*, Phys. Rev. B **96**, 085138 (2017).
- [145] F. Guan and X. Du, *Random Gauge Field Scattering in Monolayer Graphene*, Nano Lett **17**, 7009 (2017).
- [146] A. D. Smith et al., *Piezoresistive roperties of suspended graphene membranes under uniaxial and biaxial strain in nanoelectromechanical pressure sensors*, ACS Nano **10**, 9879 (2016).
- [147] T. Fujita, M. B. A. Jalil, and S. G. Tan, *Valley filter in strain engineered graphene*, App. Phys. Lett. **97**, 043508 (2010).
- [148] C. Yesilyurt, S. G. Tan, G. C. Liang, and M. B. A. Jalil, *Perfect valley filter in strained graphene with single barrier region*, AIP Adv. **6**, 056303 (2016).
- [149] S. Zhu, J. A. Stroscio, and T. Li, *Programmable Extreme Pseudomagnetic Fields in Graphene by a Uniaxial Stretch*, Phys. Rev. Lett. **115**, 245501 (2015).
- [150] M. R. Guassi, G. S. Diniz, N. Sandler, and F. Y. Qu, *Zero-field and time-reserval-symmetry-broken topological phase transitions in graphene*, Phys. Rev. B **92**, 075426 (2015).
- [151] S. Yigen and A. R. Champagne, *Wiedemann-Franz relation and thermal-transistor effect in suspended graphene*, Nano Lett **14**, 289 (2014).
- [152] Y. Q. Wu et al., *Quantum behavior of graphene transistors near the scaling limit*, Nano Lett. **12**, 1417 (2012).
- [153] W. Bao et al., *Controlled ripple texturing of suspended graphene and ultrathin graphite membranes*, Nature nanotechnology **4**, 562 (2009).
- [154] M. Huang et al., *Phonon softening and crystallographic orientation of strained graphene studied by Raman spectroscopy*, Proc. Natl. Acad. Sci. U.S.A. **106**, 7304 (2009).

- [155] E. Y. Andrei, G. Li, and X. Du, *Electronic properties of graphene: a perspective from scanning tunneling microscopy and magnetotransport*, Rep. Prog. Phys. **75**, 056501 (2012).
- [156] J. J. Parks et al., *Tuning the Kondo Effect with a Mechanically Controllable Break Junction*, Phys. Rev. Lett. **99**, 026601 (2007).
- [157] S. G. Sarwat et al., *Revealing strain-induced effects in ultrathin heterostructures at the nanoscale*, Nano Lett **18**, 2467 (2018).
- [158] F. C. Nix and D. MacNair, *The thermal expansion of pure metals: copper, gold, aluminum, nickel, and iron*, Phys. Rev. **60**, 597 (1941).
- [159] V. Singh et al., *Probing thermal expansion of graphene and modal dispersion at low-temperature using graphene nanoelectromechanical systems resonators*, Nanotechnology **21**, 165204 (2010).
- [160] L. Anzi et al., *Ultra-low contact resistance in graphene devices at the Dirac point*, 2D Mat. **5**, 025014 (2018).
- [161] S. Das Sarma and E. H. Hwang, *Density-dependent electrical conductivity in suspended graphene: Approaching the Dirac point in transport*, Phys. Rev. B **87**, 035415 (2013).
- [162] V. M. Pereira, A. H. Castro Neto, and N. M. R. Peres, *Tight-binding approach to uniaxial strain in graphene*, Phys. Rev. B **80**, 045401 (2009).
- [163] M. A. H. Vozmediano, M. I. Katsnelson, and F. Guinea, *Gauge fields in graphene*, Phys. Rep. **496**, 109 (2010).
- [164] S.-M. Choi, S.-H. Jhi, and Y.-W. Son, *Effects of strain on electronic properties of graphene*, Phys. Rev. B **81** (2010).
- [165] Y. M. Lin et al., *100-GHz transistors from wafer-scale epitaxial graphene*, Science **327**, 662 (2010).
- [166] L. Ponomarenko et al., *Chaotic Dirac billiard in graphene quantum dots*, Science **320**, 356 (2008).
- [167] T. G. Pedersen et al., *Graphene antidot lattices: designed defects and spin qubits*, Phys. Rev. Lett. **100**, 136804 (2008).

- [168] J. Eroms and D. Weiss, *Weak localization and transport gap in graphene antidot lattices*, New J. Phys. **11**, 095021 (2009).
- [169] J. Güttinger et al., *Electron-hole crossover in graphene quantum dots*, Phys. Rev. Lett. **103**, 046810 (2009).
- [170] S. Schnez, K. Ensslin, M. Sigrist, and T. Ihn, *Analytic model of the energy spectrum of a graphene quantum dot in a perpendicular magnetic field*, Phys. Rev. B **78**, 195427 (2008).
- [171] J. Güttinger, T. Frey, C. Stampfer, T. Ihn, and K. Ensslin, *Spin states in graphene quantum dots*, Phys. Rev. Lett. **105**, 116801 (2010).
- [172] Y.-C. Lin et al., *Graphene annealing: how clean can it be?*, Nano Lett. **12**, 414 (2011).
- [173] D. Yoon, Y. W. Son, and H. Cheong, *Negative thermal expansion coefficient of graphene measured by Raman spectroscopy*, Nano Lett. **11**, 3227 (2011).
- [174] D. Bahamon and V. M. Pereira, *Conductance across strain junctions in graphene nanoribbons*, Phys. Rev. B **88**, 195416 (2013).
- [175] M. Najafi and M. G. Nezhadhighi, *Scale-invariant puddles in graphene: Geometric properties of electron-hole distribution at the Dirac point*, Physical Review E **95**, 032112 (2017).
- [176] A. Castellanos-Gomez et al., *Deterministic transfer of two-dimensional materials by all-dry viscoelastic stamping*, 2D Mat. **1**, 011002 (2014).

Appendices

Appendix A

Details of Theoretical GQST Calculations

In this appendix, we show an example of the MATHEMATICA code used to calculate conductivity as a function of gate voltage, and applied mechanical strain. This code was modified to calculate data as a function of other variables, but the core code remains the same. The code has three parts, the first calculates the transmission equation based on the strained graphene Hamiltonian, following Refs. [56,69]. The second puts this transmission equation in terms of experimental variables. The third section performs the conductivity calculation and outputs the data. These sections are separated by lines of “+” symbols for easy identification.

```

In[1]:= (*Note: many lines have been commented out to keep the output briefer. To see specific outputs,
just delete the semicolon at the relevant line*)
(*First section is just to follow Tworzydło2006 + vector potentials to get to the Pellegrino2011 result*)

ClearAll["Global`*"] (*clear all variables and symbols*)

(*Pauli Spin Matrices*)
 $\sigma_x = \begin{pmatrix} 0 & 1 \\ 1 & 0 \end{pmatrix};$ 
MatrixForm[%]
 $\sigma_y = \begin{pmatrix} 0 & -i \\ i & 0 \end{pmatrix};$ 
MatrixForm[%]

(*Momentum Operators*)
 $p_x[\psi] := -i\hbar D[\psi, x];$ 
 $p_y[\psi] := -i\hbar D[\psi, y];$ 

(*Plane Wave Test Solution, transversal momentum can be positive or negative,
but we are only worried about positive x (right moving) solutions*)
 $\Psi[k_, x_, SGN_] := E^{i(kx)} E^{iSGN(qy)};$ 

(*Strained Hamiltonian*)
(*Note: To preserve time reversal symmetry, when q changes sign, so does A*)
 $H[\psi_, SGN_] := v_F \{ \{ \sigma_x (p_x[\psi] - \hbar A_x \psi) + \sigma_y (p_y[\psi] - SGN \hbar A_y \psi), 0 \}, \{ 0, \sigma_x (p_x[\psi] - \hbar A_x \psi) - \sigma_y (p_y[\psi] - SGN \hbar A_y \psi) \} \};$ 

(*Determine complete matrix to be diagonalized for positive q*)
Print["Final form of matrix for q>0:\r"];
MATp[k_, x_] = MatrixForm[ArrayFlatten[H[\Psi[k, x, 1], 1]] + (e*V + \gamma1) * IdentityMatrix[4]];
MatrixForm[FullSimplify[%]]

(*Calculate Eigenvectors for positive q*)
EVP = Eigenvectors[%];

(*Determine complete matrix to be diagonalized for negative q*)
Print["Final form of matrix for q<0:\r"];
MATn[k_, x_] = MatrixForm[ArrayFlatten[H[\Psi[k, x, -1], -1]] + (e*V + \gamma1) * IdentityMatrix[4]];
MatrixForm[FullSimplify[%]]

(*Calculate Eigenvectors for negative q*)
EVn = Eigenvectors[%];

(*Isolates a useful quantity, z (from Tworzydło), for simplification*)
zz = Factor[FullSimplify[PowerExpand[EVn[[2]][[1]]]]];
Print["Form of z:\r"];
Print["z=", zz]

(*Simplify q>0 eigenvectors and put in terms of z like Tworzydło*)
Refine[FullSimplify[PowerExpand[EVP]]];

(*2 of 4 vecors have a 1/z term instead of simply a z term, so we multiply
both components by z so all eigenvectors are the same length (normalization), and put solutions in terms of z*)
EVPz = Refine[FullSimplify[PowerExpand[EVP]]];
EVPz[[2]] = FullSimplify[EVPz[[2]] * zz];
EVPz[[4]] = FullSimplify[EVPz[[4]] * -zz];
EVPz = EVPz /. FullSimplify[PowerExpand[zz]] => z /. FullSimplify[PowerExpand[1/zz]] => 1/z /.
FullSimplify[PowerExpand[-1/zz]] => -1/z /. FullSimplify[PowerExpand[-zz]] => -z;
Print["Eigenvectors for q>0:\r"];
Print[MatrixForm[EVPz[[1]]], " ", MatrixForm[EVPz[[2]]], " ", MatrixForm[EVPz[[3]]], " ", MatrixForm[EVPz[[4]]]]

(*Simplify q<0 eigenvectors and put in terms of z*)
FullSimplify[PowerExpand[EVn]];

(*2 of 4 vecors have a 1/z term instead of simply a z term, so we multiply
both components by z so all eigenvectors are the same length (normalization), and put solutions in terms of z*)
EVnz = FullSimplify[PowerExpand[EVn]];
EVnz[[1]] = FullSimplify[EVnz[[1]] * zz];
EVnz[[3]] = FullSimplify[EVnz[[3]] * -zz];
EVnz = EVnz /. FullSimplify[PowerExpand[zz]] => z /. FullSimplify[PowerExpand[1/zz]] => 1/z /.
FullSimplify[PowerExpand[-1/zz]] => -1/z /. FullSimplify[PowerExpand[-zz]] => -z;
Print["Eigenvectors for q<0:\r"];
Print[MatrixForm[EVnz[[1]]], " ", MatrixForm[EVnz[[2]]], " ", MatrixForm[EVnz[[3]]], " ", MatrixForm[EVnz[[4]]]]

(* Therefore, plane wave solutions are: (taking z to be either positive or negative)*)
 $\Psi = E^{i(kx)} * (a * MatrixForm[EVPz[[4]]] * E^{i(qy)} +$ 
 $ap * MatrixForm[EVPz[[3]]] * E^{i(qy)} + b * MatrixForm[EVnz[[2]]] * E^{-i(qy)} + bp * MatrixForm[EVnz[[1]]] * E^{-i(qy)});$ 
Print["Plane wave solutions to the Hamiltonian Equation A2:\r\r \Psi =", \Psi, "\r"]

```

```

(*Note: There are four 4x1 eigenvectors, but we can make the system of equations
with just one of them, as they will be equivalent. (As they do in Tworzydło). We proceed using
the more general form of k's and q's rather than z's*)
(*System of equations vector from the eigenvector*)
SYS[k_, q_, Ax_, Ay_] := Evaluate[FullSimplify[PowerExpand[Delete[Delete[EVn[[2]], 4], 3]]]]
(*Print[SYS[kk, qq, aaax, aay]] (*Uncomment this line to see form of the system of equations*)*)

(*System of equations: This is eq.A8-A13 from Tworzydło
4 expressions that match up the left and right moving waves in the graphene channel and in the contacts*)
(*Have to change sign of Ax when we change sign of k, cause they go together*)
(*Need to include Ax in exponentials in the channel (α,β)*)
ex1 = FullSimplify[SYS[k1, q1, 0, 0][[1]]*W[k1, 0, 1] + r*SYS[-k1, q1, 0, 0][[1]]*W[-k1, 0, 1] ==
(α*SYS[k2*vxx, q2*vyy, Ax*vxx, Ay*vyy][[1]]*W[(k2 - Ax), 0, 1] +
β*SYS[-k2*vxx, q2*vyy, -Ax*vxx, Ay*vyy][[1]]*W[(-k2 + Ax), 0, 1]]];
ex2 = FullSimplify[SYS[k1, q1, 0, 0][[2]]*W[k1, 0, 1] + r*SYS[-k1, q1, 0, 0][[2]]*W[-k1, 0, 1] ==
(α*SYS[k2*vxx, q2*vyy, Ax*vxx, Ay*vyy][[2]]*W[(k2 - Ax), 0, 1] +
β*SYS[-k2*vxx, q2*vyy, -Ax*vxx, Ay*vyy][[2]]*W[(-k2 + Ax), 0, 1]]];
ex3 = FullSimplify[t*SYS[k1, q1, 0, 0][[1]]*W[k1, L - L, 1] = (α*SYS[k2*vxx, q2*vyy, Ax*vxx, Ay*vyy][[1]]*W[(k2 - Ax), L, 1] +
β*SYS[-k2*vxx, q2*vyy, -Ax*vxx, Ay*vyy][[1]]*W[(-k2 + Ax), L, 1]]];
ex4 = FullSimplify[t*SYS[k1, q1, 0, 0][[2]]*W[k1, L - L, 1] = (α*SYS[k2*vxx, q2*vyy, Ax*vxx, Ay*vyy][[2]]*W[(k2 - Ax), L, 1] +
β*SYS[-k2*vxx, q2*vyy, -Ax*vxx, Ay*vyy][[2]]*W[(-k2 + Ax), L, 1]]];
(*Solve the system of equations for t*)
tt = FullSimplify[Solve[{ex1, ex2, ex3, ex4}, {r, t, α, β}][[1]][[2]][[2]]]

(*Take modulus for total transmission, and substitute to put everything in terms of k's and q's t*)
(*This gives the answer from Pellegrino2011*)
TG = FullSimplify[Abs[t /. q1 => q /. q2 => q /. Sqrt[k1^2 + q^2] => kF1 /. Sqrt[vxx^2*(Ax - k2)^2 + vyy^2*(Ay - q)^2] => kF2 /. k1 => Sqrt[kF1^2 - q^2] /.
k2 => vxx^-1 * Sqrt[kF2^2 - vyy^2*(q - Ay)^2 + Ax^2]^2];
Print["\rGeneral Graphene transmission: \r", FullSimplify[%]]

Tφ[kF1_, kF2_, q_, L_, Ay_] := Evaluate[TG]; (*Make transmission into a function of the experimental variables*)

```

Out[3]/MatrixForm=

$$\begin{pmatrix} 0 & 1 \\ 1 & 0 \end{pmatrix}$$

Out[5]/MatrixForm=

$$\begin{pmatrix} 0 & -i \\ i & 0 \end{pmatrix}$$

Final form of matrix for q>0:

Out[12]/MatrixForm=

$$\begin{pmatrix} e^V + \gamma_1 & e^{i(kx+qy)}(-Ax + iAy + k - iq)\hbar v_F & 0 & 0 \\ e^{i(kx+qy)}(-Ax - iAy + k + iq)\hbar v_F & e^V + \gamma_1 & 0 & 0 \\ 0 & 0 & e^V + \gamma_1 & e^{i(kx+qy)}(-Ax - iAy + k + iq)\hbar v_F \\ 0 & 0 & e^{i(kx+qy)}(-Ax + iAy + k - iq)\hbar v_F & e^V + \gamma_1 \end{pmatrix}$$

Final form of matrix for q<0:

Out[16]/MatrixForm=

$$\begin{pmatrix} e^V + \gamma_1 & e^{i(kx-qy)}(-Ax - iAy + k + iq)\hbar v_F & 0 & 0 \\ e^{i(kx-qy)}(-Ax + iAy + k - iq)\hbar v_F & e^V + \gamma_1 & 0 & 0 \\ 0 & 0 & e^V + \gamma_1 & e^{i(kx-qy)}(-Ax + iAy + k - iq)\hbar v_F \\ 0 & 0 & e^{i(kx-qy)}(-Ax - iAy + k + iq)\hbar v_F & e^V + \gamma_1 \end{pmatrix}$$

Form of z:

$$z = \frac{Ax + i Ay - k - i q}{\sqrt{(Ax - k)^2 + (Ay - q)^2}}$$

Eigenvectors for q>0:

$$\begin{pmatrix} 0 \\ 0 \\ z \\ 1 \end{pmatrix} \quad \begin{pmatrix} 1 \\ z \\ 0 \\ 0 \end{pmatrix} \quad \begin{pmatrix} 0 \\ 0 \\ -z \\ 1 \end{pmatrix} \quad \begin{pmatrix} 1 \\ -z \\ 0 \\ 0 \end{pmatrix}$$

Eigenvectors for q<0:

$$\begin{pmatrix} 0 \\ 0 \\ 1 \\ z \end{pmatrix} \quad \begin{pmatrix} z \\ 1 \\ 0 \\ 0 \end{pmatrix} \quad \begin{pmatrix} 0 \\ 0 \\ 1 \\ -z \end{pmatrix} \quad \begin{pmatrix} -z \\ 1 \\ 0 \\ 0 \end{pmatrix}$$

Plane wave solutions to the Hamiltonian Equation A2:

$$\Psi = e^{i k x} \left(b p e^{-i q y} \begin{pmatrix} 0 \\ 0 \\ 1 \\ z \end{pmatrix} + a p e^{i q y} \begin{pmatrix} 0 \\ 0 \\ -z \\ 1 \end{pmatrix} + a e^{i q y} \begin{pmatrix} 1 \\ -z \\ 0 \\ 0 \end{pmatrix} + b e^{-i q y} \begin{pmatrix} z \\ 1 \\ 0 \\ 0 \end{pmatrix} \right)$$

$$\text{Out}[42] = (k1 (Ax - k2) vxx) \left/ \left(k1 (Ax - k2) vxx \cos[(Ax - k2) L] - i \left(q1 (Ay - q2) vyy + \sqrt{k1^2 + q1^2} \sqrt{(Ax - k2)^2 vxx^2 + (Ay - q2)^2 vyy^2} \right) \sin[(Ax - k2) L] \right) \right.$$

General Graphene transmission:

$$\text{Abs} \left[\left((kF1 - q) (kF1 + q) (kF2^2 - (Ay - q)^2 vyy^2) \right) \left/ \left(\sqrt{(kF1 - q) (kF1 + q)} \sqrt{kF2^2 - (Ay - q)^2 vyy^2} \cos \left[\frac{L \sqrt{kF2^2 - (Ay - q)^2 vyy^2}}{vxx} \right] - i (kF1 kF2 + (Ay - q) q vyy) \sin \left[\frac{L \sqrt{kF2^2 - (Ay - q)^2 vyy^2}}{vxx} \right] \right)^2 \right. \right]$$

(*****)

(*****)

(*****)

(*****)

(*****)

4 | MM_code_thesis_appendix.nb

```

In[46]:= Clear @@ Select[Names["Global`*"], ToExpression[#, StandardForm, Function[sym, OwnValues[sym] != {}, HoldAll]] &]
(*Clear all stored variables, but not functions*)

(* define x and y components of fermi wavenvector*)
(*Maximum number of modes available based on potential in the leads for smooth edges (Tworzydolo)*)
q[N_, W_] :=  $\pi / W * (N + 1/2)$ ;

(*Print transmission equation and put in terms of Fermi energies*)
Print["\rGeneral Graphene transmission: \r", T $\phi$ [kF1, kF2, q, L, Ay], "\rSimplified: \r",
Simplify[T $\phi$ [kF1, kF2, q, L, Ay]] /.  $\sqrt{kF1^2 - q^2} \Rightarrow k1 /. (kF1 - q) (kF1 + q) \Rightarrow k1^2 /. \sqrt{kF2^2 - (Ay - q)^2 vyy^2} \Rightarrow k2 * vxx /. (kF2^2 - (Ay - q)^2 vyy^2) \Rightarrow k2^2 * vxx^2$ , "\r"]

Tn[ $\mu$ l_,  $\mu$ c_, Nq_, L_, W_, Ay_] := T $\phi$ [ $\mu$ l / ( $\hbar * vF$ ),  $\mu$ c / ( $\hbar * vF$ ), q[Nq, W], L, Ay];

General Graphene transmission:
Abs[(((kF1 - q) (kF1 + q) (kF2^2 - (Ay - q)^2 vyy^2))) /

$$\left( \sqrt{(kF1 - q) (kF1 + q)} \sqrt{kF2^2 - (Ay - q)^2 vyy^2} \cos\left[\frac{L \sqrt{kF2^2 - (Ay - q)^2 vyy^2}}{vxx}\right] - i (kF1 kF2 + (Ay - q) q vyy) \sin\left[\frac{L \sqrt{kF2^2 - (Ay - q)^2 vyy^2}}{vxx}\right] \right)^2$$

Simplified:
Abs[
$$\frac{k1^2 k2^2 vxx^2}{(k1 k2 vxx \cos[k2 L] - i (kF1 kF2 + (Ay - q) q vyy) \sin[k2 L])^2}$$
]

(*****
*****
*****
*****
*****

In[50]:= (*Here, we run the transmission code to calculate conductivity*)

Clear @@ Select[Names["Global`*"], ToExpression[#, StandardForm, Function[sym, OwnValues[sym] != {}, HoldAll]] &]
(*Clear all stored variables, but not functions*)

(*Constants*)
kB = 1.4*10^(-23); (*Boltzman Constant J/K*)
e = 1.6*10^-19; (*Elementary Charge in C*)
 $\hbar$  = 1.05*10^(-34); (*Planck's constant /2 $\pi$  J.s*)
hbar =  $\hbar$ ;
h = 6.63* 10^(-34); (*J.s*)
t0 = 2.7*e;
a = 1.42*^-10; (*Lattice Constant in m*)
 $\beta$  = 2.5; (* Dimensionless electron-phonon coupling parameter*)
vF = 3/2*a*t0/hbar; (*Fermi velocity*)
(*****

(*Parameters*)
 $\Delta\phi$  = -0.12*e; (*Contact doping in eV*)
L = 100.0*10^(-9); (*Device Length in m*)
W = 1000.0*10^(-9); (*Device Width in m*)
 $\theta$  =  $\pi/6$ ; (*angle of flake (rel. to zigzag direction)*)
mins = 0.0/100.0; (*Minimum applied mechanical train*)
maxe = 2.5/100.0; (*Maximum applied mechanical train*)
Nstep = 3; (*Number of strain steps*)
eStep = (maxe - mins)/Nstep; (*Size of strain steps*)
e0 = 2.6/100.0; (*Built in strain*)
v = 0.165; (*Poisson Ratio in Graphene*)
(*****
dair = 50.0*10^(-9); (*Thicknes of vacuum under device(m)*)
dsio2 = 0*100.0*10^(-9); (*Thicknes of SiO2 under device (m)*)
eair = 8.85*10^(-12); (*Permittivity of Vacuum in F/m*)
esio2 = 3.9*8.85*10^(-12); (*Permittivity of SiO2 in F/m*)
Vdirac = 0.0; (*Dirac point position in V*)
VgateMax = 20.0; (*Maximum gate in V*)
Nstep = 300; (*Number of gate steps*)
VgateStep = (VgateMax*2)/Nstep; (*Gate step size*)
temp = 0*1.5; (*temperature of the sample (K)*)

```

Printed by Wolfram Mathematica Student Edition


```

Rc = 0*800.0; (*Contact Resistance (0 if want to take into acct later) in Ohms*)
Δφstr = 3.0*e; (*change in workfunction per % strain (choi2010) *)
nimp = 0*0.5*10.0^15; (*1/m2 Density of Impurities IF nimp=0, gaussmooth must =0, if nimp≠ Gaussmooth must =1*)
Gaussmooth = 0; (*Boolean, smooth over discontinuity at Dirac point caused buy nimp*)
Gauss[x_, FW_, H_, P_] := H*Exp[-4*Log[2]*(x - p)^2 / FW^2];
(*******)
Print["Gate capacitance (F/m^2)"]; cBG = 
$$\frac{\epsilon_{air} * \epsilon_{sio2}}{(\epsilon_{sio2} * \epsilon_{air}) + (\epsilon_{air} * \epsilon_{sio2})}$$

ntmp = 
$$\frac{\pi}{6} \left( \frac{kB * temp}{\hbar * vF} \right)^2$$
; (*Thermal carrier density*)
Nmax[EF_] := IntegerPart[
$$\frac{Abs[EF] * W}{\hbar * vF} * \frac{W}{\pi} + 0.5$$
]; (*Number of transmission modes, set by contact doping*)
(*******)
(*Build arrays to populate*)
Array[GG, (Nstep + 1) * (Nstep + 1) - 1];
Array[Fanum, (Nstep + 1) * (Nstep + 1) - 1];
Array[VVg, (Nstep + 1) * (Nstep + 1) - 1];
Array[εε, (Nstep + 1) * (Nstep + 1) - 1];
Array[μμ, (Nstep + 1) * (Nstep + 1) - 1];

(*Additional arrays needed for gaussian smoothing*)
If[Gaussmooth == 1, Array[GGn, (Nstep + 1) * (Nstep + 1) - 1], ];
If[Gaussmooth == 1, Array[GGS, (Nstep + 1) * (Nstep + 1) - 1], ];
If[Gaussmooth == 1, Array[Fanonum, (Nstep + 1) * (Nstep + 1) - 1], ];
If[Gaussmooth == 1, Array[Fanonums, (Nstep + 1) * (Nstep + 1) - 1], ];

(*For loop to increase strain*)
For[SStep = 0, SStep ≤ (Nstep), SStep += 1,

ε = (minε + (SStep) * εStep); (*Increment mechanical strain*)

(*Change Fermi velocity anisotropy*)
vxx = 1 - (β - 1) * (ε + ε0);
vyy = 1 + (β - 1) * v * (ε + ε0);

(*Define y vector potentials and calculate them*)
Ay1[ϕ_] := 
$$\frac{4 \pi (\epsilon + \epsilon_0)}{3 \sqrt{3} a} v \sin[\phi] + \frac{\beta (\epsilon + \epsilon_0) (1 + v)}{2 a} \sin[3 * \phi];$$

Ay2[ϕ_] := 
$$\frac{2 \pi (\epsilon + \epsilon_0)}{3 a} \left( -\frac{1}{\sqrt{3}} v \sin[\phi] + v \cos[\phi] \right) + \frac{\beta (\epsilon + \epsilon_0) (1 + v)}{2 a} \sin[3 * \phi];$$

Ay3[ϕ_] := 
$$\frac{2 \pi (\epsilon + \epsilon_0)}{3 a} \left( -\frac{1}{\sqrt{3}} v \sin[\phi] - v \cos[\phi] \right) + \frac{\beta (\epsilon + \epsilon_0) (1 + v)}{2 a} \sin[3 * \phi];$$


(*For loop to increase gate voltage*)
For[Step = 0, Step ≤ (Nstep), Step += 1,

Vgate = -VgateMax + (Step) * VgateStep; (*Increment gate voltage*)

(*carrier density from gate and scalar potential*)
nc = 
$$\frac{cBG}{e} * (Vgate - Vdirac) + \text{Sign}[\Delta\phi str] * \frac{(\Delta\phi str / \hbar * vF)^2}{\pi} * (1 - v)^2 * (\epsilon + \epsilon_0)^2$$
; (* nc=Number of carriers *)

(*Total Carrier Density (include impurities*)
ntot = 
$$\sqrt{nc^2 + 4 * \left( \left( \frac{nimp}{2} \right)^2 + (ntmp)^2 \right)}$$
;

(*Channel Fermi level*)
μc = 
$$\hbar * vF * \text{If}[nc \neq 0.0, \text{Sign}[nc], 1] * \sqrt{\pi * Abs[ntot]}$$
;

(*Define lead Fermi level, and calculatenumber of modes*)
μ1 = Δφ;
Nmodes = Nmax[μ1];

(*Initialize arrays*)
GG[Step + (SStep) * (Nstep + 1)] = 0;
If[Gaussmooth == 1, GGn[Step + (SStep) * (Nstep + 1)] = 0, ];
If[Gaussmooth == 1, GGS[Step + (SStep) * (Nstep + 1)] = 0, ];
Fanonum[Step + (SStep) * (Nstep + 1)] = 0;
If[Gaussmooth == 1, Fanonum[Step + (SStep) * (Nstep + 1)] = 0, ];
If[Gaussmooth == 1, Fanonums[Step + (SStep) * (Nstep + 1)] = 0, ];

```

```

(*Populate array with current strain, gate, and channel fermi level*)
VVG[Step + (SStep) * (Nstep + 1)] = Vgate;
εε[Step + (SStep) * (Nstep + 1)] = ε;
μμ[Step + (SStep) * (Nstep + 1)] = μc;

(*Additional arrays needed for gaussian smoothing*)
Array[TnA, Nmodes];
If[Gausssmooth == 1, Array[nTnA, Nmodes], ];

(*For loop to sum over all transmission modes*)
For[Nq = 0, Nq < (Nmodes), Nq += 1,

  (*Average transmission for all 6 vector potentials *)
  TnA[Nq] = (Tn[μ1, μc, Nq, L, W, Ay1[θ]] + Tn[μ1, μc, Nq, L, W, Ay2[θ]] + Tn[μ1, μc, Nq, L, W, Ay3[θ]] +
    Tn[μ1, μc, Nq, L, W, -Ay1[θ]] + Tn[μ1, μc, Nq, L, W, -Ay2[θ]] + Tn[μ1, μc, Nq, L, W, -Ay3[θ]]) / 6;

  (*Sum over transmission modes to get conductance*)
  GG[Step + (SStep) * (Nstep + 1)] +=  $\left(\frac{4 * e^2}{\pi * h}\right)^{-1} * \frac{4 * e^2}{h} * TnA[Nq]$ ;

  (*Calculate Fano factor*)
  Fanonum[Step + (SStep) * (Nstep + 1)] +=  $\left(\frac{4 * e^2}{\pi * h}\right)^{-1} * \frac{4 * e^2}{h} * TnA[Nq] * (1 - TnA[Nq])$ ;

  (*If Gaussian smoothing enabled, do the same for negative carrier density, and average using Gaussian function *)
  If[Gausssmooth == 1, nTnA[Nq] = (Tn[-μ1, μc, Nq, L, W, Ay1[θ]] + Tn[-μ1, μc, Nq, L, W, Ay2[θ]] + Tn[-μ1, μc, Nq, L, W, Ay3[θ]] +
    Tn[-μ1, μc, Nq, L, W, -Ay1[θ]] + Tn[-μ1, μc, Nq, L, W, -Ay2[θ]] + Tn[-μ1, μc, Nq, L, W, -Ay3[θ]]) / 6, ];
  If[Gausssmooth == 1, GGn[Step + (SStep) * (Nstep + 1)] +=  $\left(\frac{4 * e^2}{\pi * h}\right)^{-1} * \frac{4 * e^2}{h} * nTnA[Nq]$ , ];
  If[Gausssmooth == 1, GGs[Step + (SStep) * (Nstep + 1)] = GGn[Step + (SStep) * (Nstep + 1)] * Gauss[Vgate, 2 * nimp * e / cBG,
    0.5, Vdirac - Sign[Δφstr] *  $\frac{(\Delta\phi_{str} / \hbar v_F)^2}{\pi} * (1 - \nu)^2 * ((\epsilon + \epsilon_0)^2) * e / cBG$ ] + GG[Step + (SStep) * (Nstep + 1)] *
     $\left(1 - \text{Gauss}\left[Vgate, 2 * nimp * e / cBG, 0.5, Vdirac - \text{Sign}[\Delta\phi_{str}] * \frac{(\Delta\phi_{str} / \hbar v_F)^2}{\pi} * (1 - \nu)^2 * ((\epsilon + \epsilon_0)^2) * e / cBG\right]\right)$ , ];
  If[Gausssmooth == 1, Fanonum[Step + (SStep) * (Nstep + 1)] +=  $\left(\frac{4 * e^2}{\pi * h}\right)^{-1} * \frac{4 * e^2}{h} * nTnA[Nq] * (1 - nTnA[Nq])$ , ];
  ]
  If[Gausssmooth == 1, Fanonums[Step + (SStep) * (Nstep + 1)] = Fanonum[Step + (SStep) * (Nstep + 1)] * Gauss[Vgate, 2 * nimp * e / cBG,
    0.5, Vdirac - Sign[Δφstr] *  $\frac{(\Delta\phi_{str} / \hbar v_F)^2}{\pi} * (1 - \nu)^2 * ((\epsilon + \epsilon_0)^2) * e / cBG$ ] + Fanonum[Step + (SStep) * (Nstep + 1)] *
     $\left(1 - \text{Gauss}\left[Vgate, 2 * nimp * e / cBG, 0.5, Vdirac - \text{Sign}[\Delta\phi_{str}] * \frac{(\Delta\phi_{str} / \hbar v_F)^2}{\pi} * (1 - \nu)^2 * ((\epsilon + \epsilon_0)^2) * e / cBG\right]\right)$ , ];
  ]
]
AddRc[Rc_, Q_] :=  $\left(\left(\left(Q * \frac{4 * e^2}{\pi * h}\right)^{-1} + Rc\right)^{-1}\right) / \left(\frac{4 * e^2}{\pi * h}\right)$ ; (*Function to add contact resistance*)

(*Build table of data: Gate voltage, conductivity, mechanical strain, Fermi energy in the channel, and Fano factor*)
If[Gausssmooth == 1,
  TB2 = Table[{VVG[n], AddRc[Rc, Re[GGs[n]]] * L / W, εε[n], μμ[n], Re[Fanonums[n] / GGs[n]]}, {n, 0, (Nstep + 1) * (Nstep + 1) - 1, 1}],
  TB2 = Table[{VVG[n], AddRc[Rc, Re[GG[n]]] * L / W, εε[n], μμ[n], Re[Fanonum[n] / GG[n]]}, {n, 0, (Nstep + 1) * (Nstep + 1) - 1, 1}];

SetDirectory["C:\Users\Andrew\Desktop\Mathematica_data"] (*Define output directory*)
Export["Test(Fig4a).dat", TB2, "Table"] (*Define file name and export data directory*)

Gate capacitance (F/m^2)
Out[54]= 0.000177

Out[66]= C:\Users\Andrew\Desktop\Mathematica_data

Out[67]= Test(Fig4a).dat

```